



# TECHNISCHE UNIVERSITÄT MÜNCHEN

Department of Chemistry and Catalysis Research Center  
Chair of Technical Electrochemistry

## **Synthesis and Characterisation of Noble-Metal-Free and Low-Loaded Platinum Catalysts for Oxygen Reduction in Proton Exchange Membrane Fuel Cells**

Pankaj Madkikar

Vollständiger Abdruck der von der Fakultät für Chemie der Technischen Universität München zur Erlangung des akademischen Grades eines

Doktors der Naturwissenschaften

genehmigten Dissertation.

Vorsitzender

Priv.-Doz. Dr. Friedrich Esch

Prüfer der Dissertation

1. Prof. Dr. Hubert A. Gasteiger

2. Prof. Dr. Klaus Köhler

Die Dissertation wurde am 15.05.2018 bei der Technischen Universität München eingereicht und durch die Fakultät für Chemie 18.06.2018 angenommen.



# Abstract

One of the major hindrances in the commercialisation of proton-exchange-membrane fuel cell (PEMFC) technology is its high cost. This thesis addresses two approaches which lead to reducing PEMFC cost, namely i) developing inexpensive noble-metal-free catalysts (also referred to as platinum-group-metal (PGM)-free catalysts); and ii) reducing the mass-transport losses associated with low cathode platinum loading.

In the first approach, we have developed zirconia-based catalysts as an alternative for platinum as oxygen reduction reaction (ORR) catalyst. Although the here developed catalysts are not yet capable of replacing platinum, the observed activity enhancement of Fe-substituted  $ZrO_2$  catalysts, has unveiled a knob that could be turned in the future to develop PGM-free catalysts with higher activities.

In the second approach, we were successful in revealing a process to reduce the mass-transport losses (in the high current density region) at the Pt/ionomer interface. It is also shown that a delicate balance between a good ionomer distribution and low ionomer/carbon ratio (but high enough for adequate proton conductivity) is of paramount importance for high performance in low platinum loaded PEMFC cathodes.

## Kurzfassung

Eine der größten Hürden für die Kommerzialisierung von Protonen-Austausch-Membran Brennstoffzellen (PEMFC) ist deren hohe Kosten. Diese Arbeit verfolgt zweierlei Ansätze um diese Kosten zu reduzieren, i) die Entwicklung von preiswerten Katalysatoren frei von Metallen der Platingruppe (PGM) und ii) die Reduzierung von Stofftransportverlusten, die mit niedriger Platinbeladung in Kathoden einhergehen. Im ersten Ansatz haben wir Katalysatoren auf Basis von Zirconiumdioxid für die Sauerstoffreduktion als Alternative zu Platin entwickelt. Obwohl die hier beschriebenen Katalysatoren noch nicht in der Lage sind Platin zu ersetzen, konnten wir mit der Dotierung des Oxids mit Eisen einen Faktor ausmachen, welcher sich in zukünftigen Studien gezielt einstellen lässt, um PGM-frei Katalysatoren mit höherer Aktivität zu entwickeln. Im zweiten Ansatz konnte erfolgreich ein Vorgehen dargestellt werden, in dem die Stofftransportverluste (bei hohen Stromdichten) an der Platin/Ionomer Grenzfläche reduziert werden konnten. Weiterhin wurde gezeigt, dass eine feine Balance zwischen guter Ionomerverteilung und niedrigem Ionomer/Kohlenstoff Verhältnis (unter Beibehaltung

ausreichender Protonenleitfähigkeit) für hohe Leistungen bei niedrig Pt beladenen PEMFC Kathoden von höchster Wichtigkeit ist.

This Ph.D. thesis is a cumulative integration of four published and one ready to submit manuscript that emerged from my work at the Chair of Technical Electrochemistry and the Catalysis Research Center, at the Technical University of Munich. An introduction will be followed by a brief overview and description of the main experimental methods applied. Results of the conducted studies are presented in accordance to the aforementioned challenges in PEMFC technology.



# Content

<b>Abstract</b> .....	<b>iii</b>
<b>Content</b> .....	<b>v</b>
<b>List of Acronyms &amp; Abbreviations</b> .....	<b>vii</b>
<b>1. Introduction</b> .....	<b>1</b>
<b>2. Theoretical Concepts and Experimental Methods</b> .....	<b>9</b>
<b>2.1. Background on PEMFC Electrochemistry</b> .....	<b>9</b>
2.1.1. Relevant Electrochemical Reactions and Electrocatalysis .....	9
2.1.2. State-of-the-Art ORR Electrocatalysts.....	13
2.1.3. Noble-Metal-Free and Low-Loaded Platinum Catalysts: Challenges they Face .....	16
<b>2.2. Synthesis of Noble-Metal-Free and Low-Loaded Platinum Catalysts</b> .....	<b>18</b>
2.2.1. Synthesis of Noble-Metal-Free Phthalocyanines.....	18
2.2.2. Synthesis of Carbon Supported Noble-Metal-Free Catalysts .....	22
2.2.3. Synthesis of Low-Loaded Platinum Catalysts .....	23
<b>2.3. Structural-Morphological Characterisation</b> .....	<b>23</b>
2.3.1. X-ray Powder Diffraction .....	23
2.3.2. Mössbauer Spectroscopy .....	25
2.3.3. X-ray Photoelectron Spectroscopy.....	26
2.3.4. N <sub>2</sub> Physisorption Measurements .....	27
2.3.5. Thermogravimetric Analysis combined with Mass Spectrometry.....	28
2.3.6. Transmission Electron Microscopy.....	29
2.3.7. Fourier-Transform Infrared Spectroscopy .....	30
2.3.8. Proton Nuclear Magnetic Resonance Spectroscopy .....	31
<b>2.4. Electrochemical Characterisation</b> .....	<b>31</b>
2.4.1. Rotating (Ring) Disc Electrode Voltammetry .....	31
2.4.2. Single Cell PEMFC Measurements.....	34
<b>3. Noble-Metal-Free Electrocatalysts</b> .....	<b>39</b>
<b>3.1. Synthesis Optimization of Carbon-Supported ZrO<sub>2</sub> Nanoparticles from Different Organometallic Precursors</b> .....	<b>40</b>
<b>3.2. ZrO<sub>2</sub> Based Oxygen Reduction Catalysts for PEMFCs: Towards a Better Understanding</b> .....	<b>63</b>
<b>3.3. Synergistic Effect on the Activity of ZrO<sub>2</sub>-Fe as PGM-Free ORR Catalysts for PEMFCs</b> .....	<b>77</b>
<b>3.4. Nanometric Fe-Substituted ZrO<sub>2</sub> on Carbon Black as Novel PGM-Free ORR Catalyst for PEMFCs</b> .....	<b>82</b>
<b>3.5. Noble-Metal-Free Electrocatalysts – Conclusions</b> .....	<b>108</b>
<b>4. Low-Loaded Platinum Catalysts in PEMFCs</b> .....	<b>111</b>

*Content*

4.1. The Key to High Performance Low Pt Loaded Electrodes .....	112
4.2. Low-Loaded Platinum Catalysts in PEMFCs – Conclusions.....	124
5. Conclusions .....	125
References .....	127
List of Figures .....	139
List of Schemes .....	143
List of Tables.....	145
Acknowledgements .....	147
Curriculum Vitae .....	149
List of Scientific Contributions .....	151

## List of Acronyms & Abbreviations

APS	Average particle size
ATR	Attenuated total reflection
BET	Brunauer-Emmett-Teller
BEV	Battery electric vehicle
CC	Current collector
CCM	Catalyst coated membrane
DBU	1,8-Diazabicyclo[5.4.0]undec-7-en
DFT	Density functional theory
DOE	U.S. Department of Energy
EIS	Electrochemical impedance spectroscopy
FCEV	Fuel cell electric vehicle
FTIR	Fourier-transform infrared
FWHM	Full width at half maximum
G	Gasket
GC	Glassy carbon
GDL	Gas diffusion layer
GHG	Greenhouse gas
HCD	High current density
HER	Hydrogen evolution reaction
HOR	Hydrogen oxidation reaction
I/C	Ionomer to carbon mass ratio
ICE	Internal combustion engine
ICP	Inductively coupled plasma
IPCC	Intergovernmental Panel on Climate Change

*List of Acronyms & Abbreviations*

KB	Ketjenblack
KB <sub>graph</sub>	Graphitized Ketjenblack
MEA	Membrane electrode assembly
MS	Mass spectrometer
MWCNT	Multi-wall carbon nanotube
NDC	Nationally determined contribution
NEXAFS	Near-edge X-ray absorption fine structure
NMR	Nuclear magnetic resonance
NSTF	Nanostructured thin film
OEM	Original equipment manufacturer
OER	Oxygen evolution reaction
ORR	Oxygen reduction reaction
PEMFC	Proton exchange membrane fuel cell
PFSA	Perfluorinated sulfonic-acid
PGM	Platinum-group-metal
PHEV	Plug-in hybrid electric vehicle
PMMA	Poly(methyl methacrylate)
PO	Partial oxidation
PTFE	Polytetrafluoroethylene
QSDFT	Quenched solid density functional theory
R&D	Research and development
R(R)DE	Rotating (ring) disc electrode
RED	Reducing
RHE	Reversible hydrogen electrode
RT	Room temperature
SD	Standard deviation

SHE	Standard hydrogen electrode
TEM	Transmission electron microscopy
TF	Thin-film
TGA	Thermogravimetric analysis
XPS	X-ray photoelectron spectroscopy
XRPD	X-ray powder diffraction
ZEV	Zero emission vehicle



# 1. Introduction

## Political and environmental needs to curtail emissions

Year 2015 was the starting point for the first-ever global efforts towards climate change: the United Nations Climate Change Conference (21<sup>st</sup> Conference of the Parties), held between 30<sup>th</sup> November – 12<sup>th</sup> December 2015 in Paris [1]. 195 countries adopted a universal and legally binding global climate agreement. With regard to the meeting, the EU Commission quoted that the Paris Agreement acts as a “bridge between today's policies and climate-neutrality before the end of the century” [2]. A majority of the countries that participated in the Paris climate conference submitted a comprehensive collection of nationally determined contributions (NDCs), which contains the post-2020 climate actions that will be taken [3]. This agreement set the path and guidelines in order to achieve the target of keeping global warming below 2 °C. This also included mitigation strategies towards minimizing global warming effects, mainly focuses on reducing greenhouse gas (GHG) emissions from all possible sources.

Following are the main points on which the governments agreed as mitigation strategies in reducing emissions [4]:

- Have a long-term goal of keeping the increase in global average temperature to <2 °C above pre-industrial levels
- Aim to limit the increase to 1.5 °C, as this would reduce risks and the impacts of climate change significantly
- The need for global emissions to peak as soon as possible, and recognize that this will take longer for developing countries
- Undertake rapid reductions thereafter in accordance with the best available science

Figure 1 shows the global GHG emissions categorised by their various sources [5]. The largest single source (25%) of emissions is the burning of coal, natural gas, and oil for electricity and heat. The second largest contribution (24%) to GHG emissions originates from agriculture, forestry, and other land use. However, the above estimate does not include the CO<sub>2</sub> that is removed from the atmosphere by transformation of carbon into biomass, dead organic matter, and soils. Thus, by taking the latter into consideration offsets approximately by 20% of the emissions from this sector.

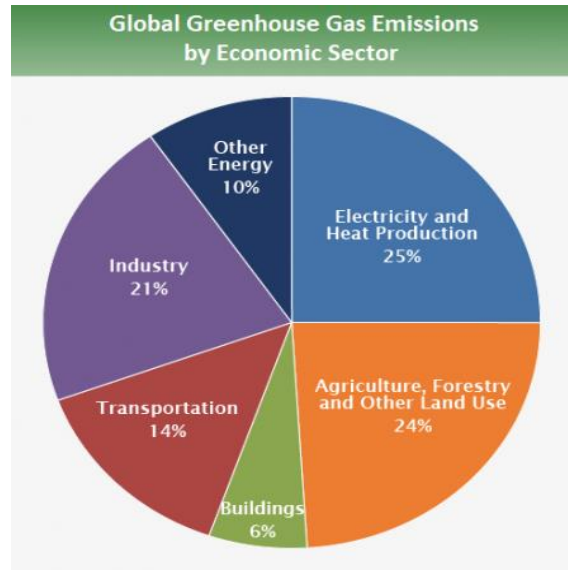


**Figure 1.** Global GHG emissions from 2010, categorised by economic sectors. Pie chart taken from United States Environmental Protection Agency [6], and the data for these estimates can be found in the Contribution of Working Group III to the Fifth Assessment Report of the Intergovernmental Panel on Climate Change [5].

The third largest contribution (21%) comes from the industry that primarily uses fossil fuels for energy production. The contribution to GHG from this sector also includes emissions from chemical, metallurgical, and mineral transformation processes. Buildings contribute to emissions by 6%, which includes onsite energy generation and burning fuels for heat in buildings or cooking in homes (emissions from electricity use in the buildings are part of the Electricity and Heat Production sector). Additional 10% of GHG emissions are due to indirect emissions from the energy sectors that are not directly related with the electricity or heat production, namely fuel extraction, refining, processing, and transportation. Lastly, we come to the transportation sector, which is of our concern. It constitutes 14% of the global GHG emissions, which includes fossil fuels burned in road, rail, marine, and air transportation. This is due to the fact that petroleum-based fuels are still the energy source for 95% of the world's transportation. In addition, the total emissions by road transport are still increasing, namely  $\approx 12\%$  from 1970 to 2010 (Figure 2), and in western countries the transportation sector is responsible for up to 26% of total CO<sub>2</sub> emissions [7].



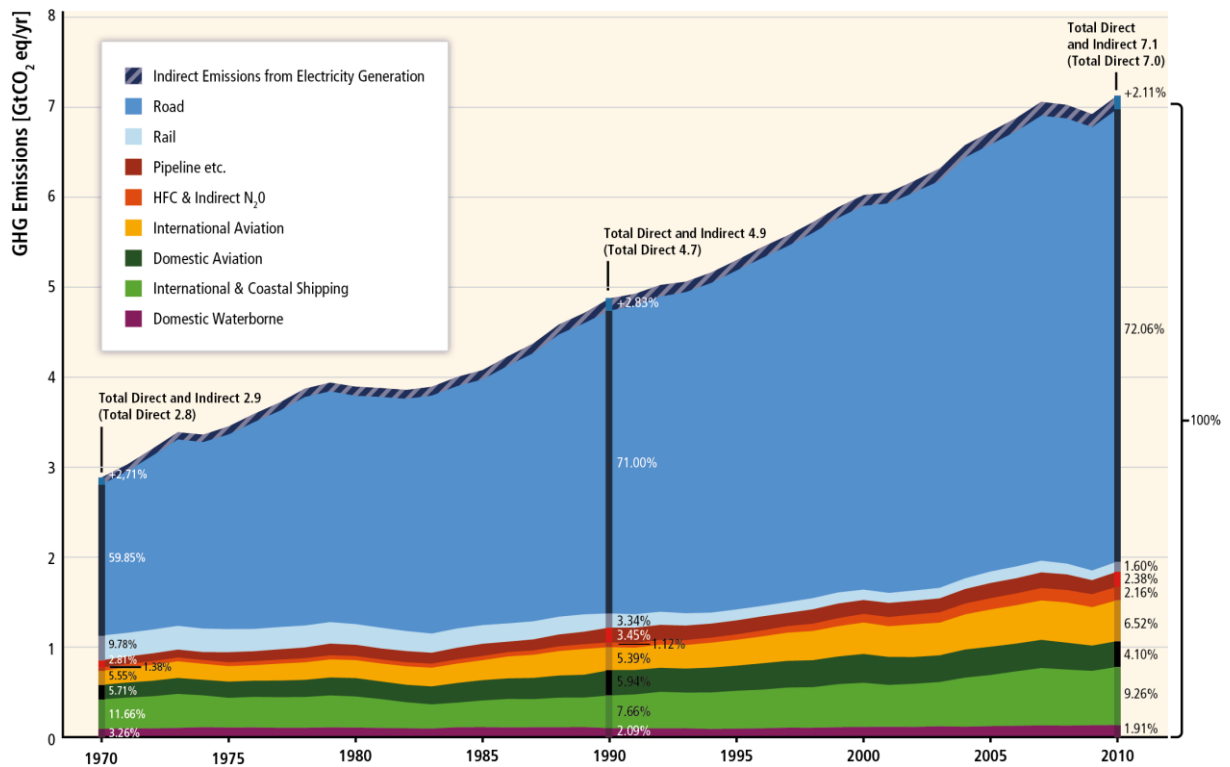


**Figure 2.** Direct GHG emissions from the respective transport modes, which rose from 2.8 Gt in 1970 to 7.0 Gt CO<sub>2</sub>eq worldwide in 2010. Graphic obtained from Sims R., R. Schaeffer, F. Creutzig, X. Cruz-Núñez, M. D’Agosto, D. Dimitriu, M.J. Figueroa Meza, L. Fulton, S. Kobayashi, O. Lah, A. McKinnon, P. Newman, M. Ouyang, J.J. Schauer, D. Sperling, and G. Tiwari, 2014: Transport. In: *Climate Change 2014: Mitigation of Climate Change. Contribution of Working Group III to the Fifth Assessment Report of the Intergovernmental Panel on Climate Change* [5].

GHG emissions are expected to grow because of the global population and economic growth. Experts fear that if no additional mitigation strategies towards curtailing GHG emission are taken, then the global mean surface temperature will increase by 3.7 to 4.8 °C by 2100 (compared to pre-industrialization level) [5].

### Strategies to decrease CO<sub>2</sub> emission from transportation

In 2009, EU and G8 leaders declared that CO<sub>2</sub> emissions must be cut by at least 80% (from 1990 levels) by 2050 in order for atmospheric CO<sub>2</sub> to stabilize at 450 parts per million (ppm) and to keep global warming below 2 °C [8]. Based on the 2014 UN Intergovernmental Panel on Climate Change (IPCC), if no action takes place to reduce emissions, it is estimated that the CO<sub>2</sub> emissions from the global transportation sector will double by 2050 [5]. On the other hand, taking aggressive and sustained measures would lead to 15-40% CO<sub>2</sub> emission reduction. Those measures would include higher fuel and vehicle efficiency. It is stated in the transport chapter of the IPCC report ‘without aggressive and sustained policies (to cut CO<sub>2</sub> from cars and trucks), transport emissions could increase at a faster rate than emissions from any other sector’ [5]. Commenting on the same report, Mr. Greg Archer, director of Transport & Environment’s Clean Vehicles said, “Thanks to EU regulations CO<sub>2</sub> emissions from new cars

1. Introduction

are now falling, but the progress on trucks and vans is glacial. The IPCC report stresses the urgency of taking new initiatives to tackle vehicle emissions, but the European Commission’s response is to repeatedly delay promised strategies to regulate car and van emissions after 2020 and to start addressing soaring emissions from trucks” [9]. Since the publication of the IPCC report, legislative bodies all over the world have started to discuss the measures to radically decrease CO<sub>2</sub> emissions.

Currently discussed regulations demand that vehicles manufacturers (Original Equipment Manufacturers, OEMs) should improve the average fuel economy of their new car fleet. For instance, the EU has demanded an average of 130 g of CO<sub>2</sub> per km for new passenger cars from 2015 on, and is set to lower it to 95 g CO<sub>2</sub> per km for 2020. However, this is an extremely ambitious target especially for manufacturers of larger premium vehicles. Table 1 summarises several technical possibilities that have been proposed to reduce vehicle emissions, many of which have already emerged in the market. Each solution can be implemented either solely or in combinations with others to decrease the emissions.

**Table 1.** Overview over technology improvements that reduce fleet emissions as reported by Wansart et al. [10].

Vehicle efficiency	Drivetrain efficiency	Low-emission fuels	Alternative drivetrains
Reduce vehicle size	Gasoline motor	Biofuels	Hydrogen
	✓ Downsizing		✓ Combustion
	✓ Hybrid		✓ Fuel Cell
Weight reduction through new materials	Diesel motor	Compressed natural gas	Electric storage
	✓ Downsizing		✓ Lithium-Ion battery
	✓ Hybrid		✓ Capacitor
Air resistance	Combined Combustion System		✓ Combined with
Introduce small cars			

While Table 1 only lists some strategies to reduce GHGs in automotive applications, it is up to the OEMs to decide which of these options to choose, and to decide about the timing of introducing the measures in order to keep up with the legislated CO<sub>2</sub> emission limits. Table 2 summarises the operative measures employed by OEMs to reduce emissions. The short-,

medium-, and long-term measure(s) is(are) employed either solely or in combination with others, similarly as in Table 1.

**Table 2.** Measures undertaken by OEMs to meet the emission targets as reported by Wansart et al. [10].

Short-term	Medium-term	Long-term
Increase tire pressure	Use more efficient tyres	Total electrification
Reduce vehicle weight	Use more efficient power steering	✓ Hydrogen fuel cell
Use more efficient transmission	Use automated ideal running mode	✓ Battery support
Reduce fuel consumption in ideal running mode	Improve motor efficiency	
	Weight reduction by new materials	
	Reduce air resistance by closing openings vehicle's front	
	Lithium battery	
	Biofuels	
	Compressed natural gas	
	Flexfuel	
	✓ Mild hybrid with NiMH batteries	
	✓ Full hybrid	

The level of decarbonisation mentioned in the beginning of this chapter would demand for 95% decarbonisation of the road transport. The average fuel economy can be improved in two ways: a) either emissions of existing drivetrains are reduced uniformly or b) a certain number of Zero Emission Vehicles (ZEVs, which do not emit any CO<sub>2</sub> during operation) are introduced to compensate the high emissions of the inferior ones. Unfortunately, the efficiency of Internal Combustion Engines (ICEs) is not expected to improve beyond 30% during that timescale and the compatibility and availability of biofuels is uncertain. Based on the limited potential of conventional engines to further reduce GHG emissions (see discussion above), there is an indisputable need for zero-emission solutions across the full range of vehicle types in order to reach future fleet emission goals. Based on the severity of the future challenge, most of the big OEMs have already invested in the long-term solutions and are launching demonstrations or small fleets of either battery or fuel cell based vehicles available to be purchased by

customers worldwide. Clearly, the market for ‘green’ ZEVs (hydrogen and battery powered) is expanding gradually.

Need for fuel cell vehicles

Both battery and fuel cell vehicles use electric drivetrains. A battery electric vehicle (BEV) uses a battery pack to power its motor, while in a fuel cell electric vehicle (FCEV) the motor is powered by a hydrogen fuel cell supported by with a small (typically few kWh) battery. Figure 3 shows a projection with different drivetrains for their well-to-wheel CO<sub>2</sub> emissions vs. their driving range. Battery electric vehicles are best suited for smaller cars where a continuous driving range of less than 300 kilometres is required. Restricted driving range and considerable recharging times (from 30 min to few hours) make BEVs best suitable for, e.g., city transport [11, 12].

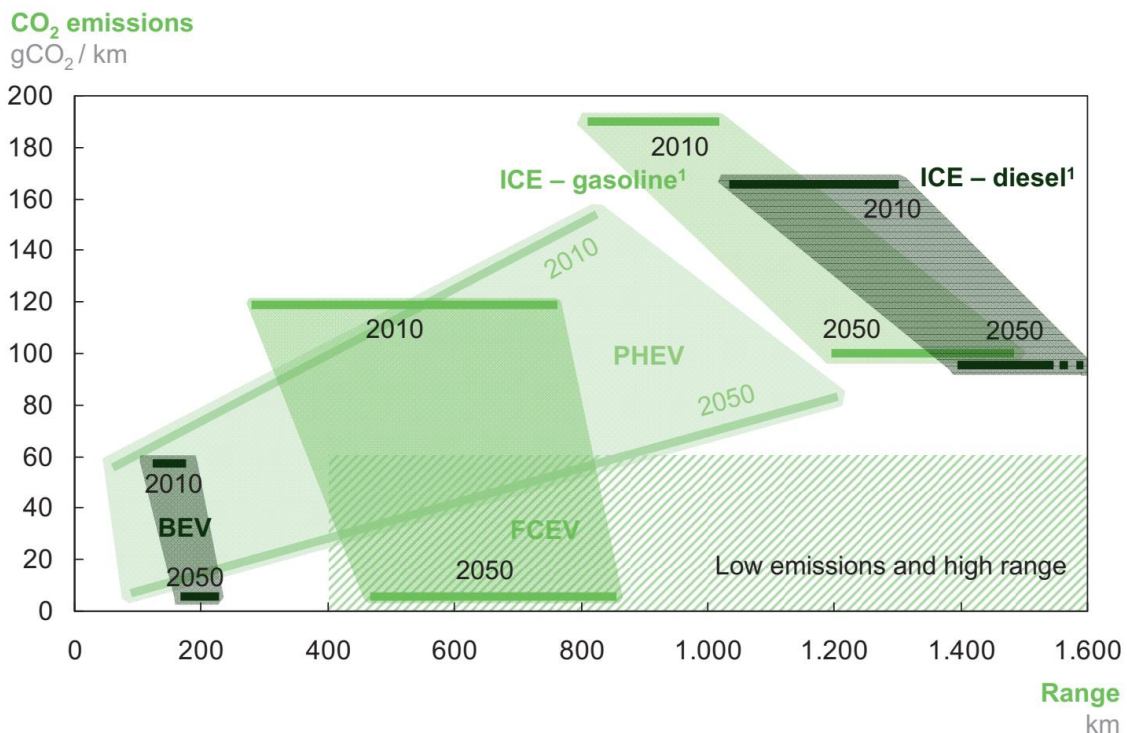


**Figure 3.** Powertrain ranges (kilometres) versus carbon emissions (gCO<sub>2</sub> (well-to-wheel)/kilometre) 2010 – 2050. Graphic obtained from a fact-based analysis of BEVs, PHEVs, and FCEVs [13]. <sup>1</sup>ICE range for 2050 based on fuel economy improvement and assuming tank size stays constant; Assuming 6% CO<sub>2</sub> reduction due to biofuels by 2020, and 24% by 2050. Reproduced from a study made for the FCH JU with their permission [13].

Plug-in hybrid electric vehicles (PHEVs) provide a bridging technology between the conventional and electric vehicles, as they allow for purely electric drive (limited to typically ≤50 km), but provide a high overall range using an internal combustion engine and a petrol (or diesel) tank. The PHEVs have the convenience of using conventional fuel with an electric drivetrain, but they can never be truly zero-emission. FCEVs on the other hand have all the benefits of electric vehicles (zero emission), with the great advantage of fast refuelling

(≈3.3 minutes) like a conventional vehicle [14] and a typical driving range of about 500 kilometres. Thus, after comparing the available options, FCEV technology is a compelling alternative for personal zero emission transportation. This is also confirmed from Figure 3, which clearly shows that in the long-run (2050), FCEVs offer low carbon emissions with highest range.

### Market introduction

Two basic requirements need to be met in order to introduce FCEVs in the market: i) an increased production of FCEVs to reducing manufacturing cost and ii) a sufficiently large number of hydrogen refuelling stations [15]. Fortunately, with the financial support of the EU, numbers of hydrogen refuelling stations in Europe have been increasing over the past years [16]. However, the numbers are still low at present due to the low numbers of FCEVs on the road (68 in operation, and 35 in progress in the EU as of 2018 [17]). However, the numbers will increase in the future, by looking into the fact that there is a gradual consumer acceptance especially after introduction of the Toyota Mirai ('future', in Japanese) FCEV in 2015 [18]. Once the H<sub>2</sub> fuelling infrastructure density increases, it is estimated that the attractiveness of FCEVs and their increasing market penetration will reduce the manufacturing cost and cost of the H<sub>2</sub> supply [19].

### PEMFC limitations

As for every new technology, FCEVs, specifically proton-exchange membrane fuel cell (PEMFC) technology faces some challenges. These hurdles need to be overcome for a long-term market penetration of FCEVs. Kongkanand and Mathias summarised these challenges in their perspective article [20]. The 2020 U.S. Department of Energy (DOE) target for platinum-group-metal (PGM)-based catalysts used per FCEV is ≈11.3 g<sub>PGM</sub> (currently ≈30 g of Pt are used [21]) per midsize sedan vehicle (90 kW<sub>gross</sub>). In a 2016 report by Strategic Analysis Inc. it was made clear that the PGM-based catalyst costs will be significant (≈43%) even if 500,000 systems/year are produced [22]. In addition, a study by Roland Berger indicated that PEMFC technology could not be commercialized on a mass-scale unless and until the amount of Pt per vehicle would be reduced to <10 g [23]. This upper limit is also based on considering Pt supply constraints when compared to the amount of PGM in ICEs (<5 g<sub>PGM</sub>), a target of ≈6 g<sub>PGM</sub>/vehicle appears reasonable. Thus, not only short-term cost reduction but also long-term Pt availability is the motivation behind the use of less platinum. At ≈6 g<sub>PGM</sub>/vehicle, platinum availability is not anymore considered a constraint to large-scale FCEV deployment as the Pt required for the rising number of FCEVs will become available from the declining number of internal combustion engine (ICE) cars. Many approaches have been followed to

## 1. Introduction

decrease the PGM content either by developing highly active Pt-based catalysts (e.g., Pt-alloys [24] or nanostructured thin film (NSTF) [25]) or catalysts by completely replacing PGM-based catalysts with PGM-free catalysts (e.g., Fe-N-C [26] or partially-oxidized valve-metal oxide compounds [27, 28]). Among the PGM-free catalyst systems, so-called Fe-N-C catalysts have reportedly the highest activity but their long-term operational stability is still insufficient. On the other hand, partially-oxidized valve-metal-oxide compounds have been reported to have a reasonably high ORR activity, and interestingly possess intrinsic stability in acidic medium. Development of partially-oxidized valve-metal-oxide compounds, in particular carbon-supported zirconia-based catalysts for the oxygen reduction reaction (ORR) [29], is the focus of this thesis. Another challenge, which has gained attention in the fuel cell community, is the voltage loss at high current density (HCD,  $>1 \text{ A/cm}^2$ ) with low Pt-loaded cathodes ( $<0.125 \text{ mg}_{\text{Pt}}/\text{cm}^2$ ) [30]. Minimizing these voltage losses by using  $-\text{NH}_x$  functionalised Pt/C catalysts is the second part of this thesis. The aforementioned challenges with PGM-free catalysts and low Pt-loaded electrodes will be further discussed in detail in chapter 2.1.3.

## 2. Theoretical Concepts and Experimental Methods

This chapter briefly describes the theoretical concepts and details of experimental methods relevant to this thesis.

### 2.1. Background on PEMFC Electrochemistry

'Electrochemistry is a discipline that deals with chemical reactions that involve an exchange of electric charges between two substances. Both chemical changes generating electric currents and chemical reactions triggered by the passage of electricity can be considered electrochemical reactions' [31]. An electrochemical reaction consists of an (or several  $v$ ) oxidized active species Ox in an electrolyte which are reduced to reduced species Red by gain of electron(s) ( $z$ ) from the electrode surface (typically solid), or vice versa:



Electrochemical reactions occur at the electrode–electrolyte interface.

#### 2.1.1. Relevant Electrochemical Reactions and Electrocatalysis

All potentials reported in this thesis are referenced to the potential of the following reaction,



at the pH of the given electrolyte. It is the reversible hydrogen electrode (RHE), which is a subtype of standard hydrogen electrode (SHE). It can be used directly with the actual electrolyte solution, which makes the measured reversible potentials independent of pH.

Four electrochemical reactions, namely the hydrogen oxidation reaction (HOR), the hydrogen evolution reaction (HER), the oxygen reduction reaction (ORR), and the oxygen evolution reaction (OER) are central to the use of  $\text{H}_2$  as energy carrier in fuel cells and to the generation of  $\text{H}_2$  by water electrolysis (Figure 4).

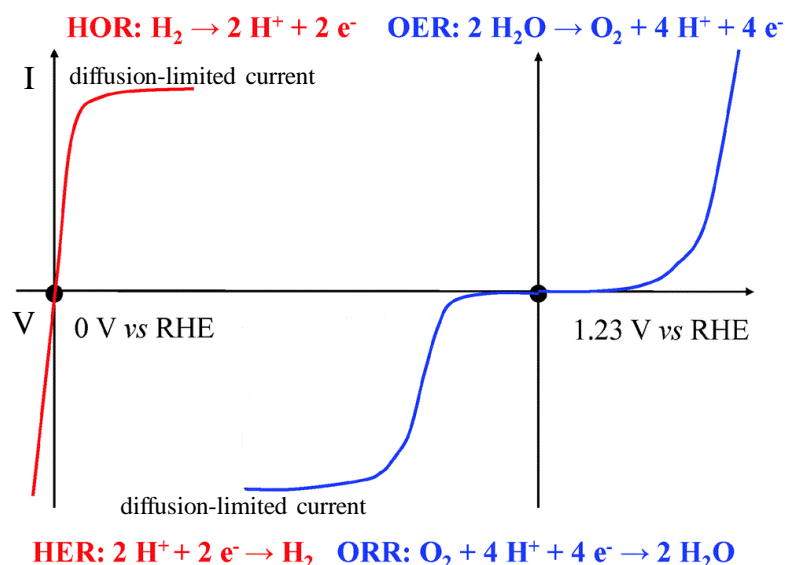
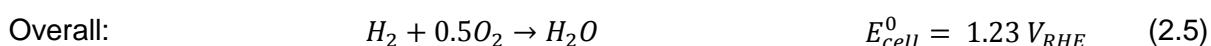
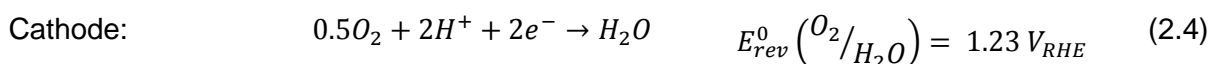
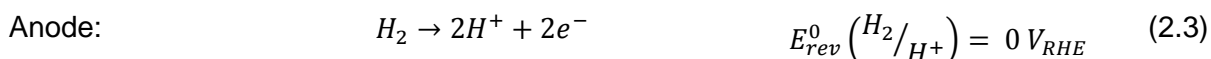


**Figure 4.** The polarization curves from rotating disc electrode technique (not to scale) for the key energy-related electrochemical reactions. Red and blue curves refer to the hydrogen- and oxygen-involving reactions, respectively. Reproduced (in part) from [32] with permission of The Royal Society of Chemistry.

The above reactions constitute the basis for two technologies, namely fuel cells technology which are galvanic cells, and electrolyzers which are electrolytic cells. The proton exchange membrane fuel cell (PEMFC) is based on the HOR and the ORR, which take place at the anode and cathode, respectively.



Here  $E_{cell}^0$  is the purely thermodynamic reversible cell potential. In reality, three voltage penalties, namely kinetic overpotentials ( $\eta_k$ ), ohmic losses ( $\eta_\Omega$ ), and mass-transport resistances ( $\eta_{mt}$ ) affect the overall cell potential [33, 34].  $\eta_k$  is related to the activity of an electrocatalyst towards a reaction, which could be a complex sequence of possibly many steps, namely adsorption of reactants, desorption of products, decomposition of some intermediate products etc. In terms of kinetics, the ORR is much more sluggish and complex than the HOR [35-37]. From Figure 4, the region that is close to the thermodynamic potential of a reaction, where the geometric currents are between  $\approx 5$  to 20% of the diffusion limited current is defined as kinetic region. In addition, the diffusion limited current as the name suggests is where the transport of reactants to the electrode happens only due to molecular diffusion, and its value is dependent on the rotation rate of the electrode.



Figure 5 depicts possible reaction pathways during the ORR. Platinum-based catalysts follow a direct reduction ( $4e^-$ ) to  $H_2O$ , while the typical highly active PGM-free catalysts (Fe-N-C) produce mainly  $H_2O_2$  [38]. For Fe-N-C catalysts with a thick catalyst layer, produced  $H_2O_2$  has a long diffusion path through the electrode; during this,  $H_2O_2$  can be electrochemically reduced to water ( $k_3$  followed by  $k_2$ ,  $2 + 2e^-$ ) and/or disproportionate to produce  $O_2$  on reactive centres. This “recycled”  $O_2$  can then again be electrochemically reduced to  $H_2O_2$ . This whole process is termed as quasi-four-electron process [38].

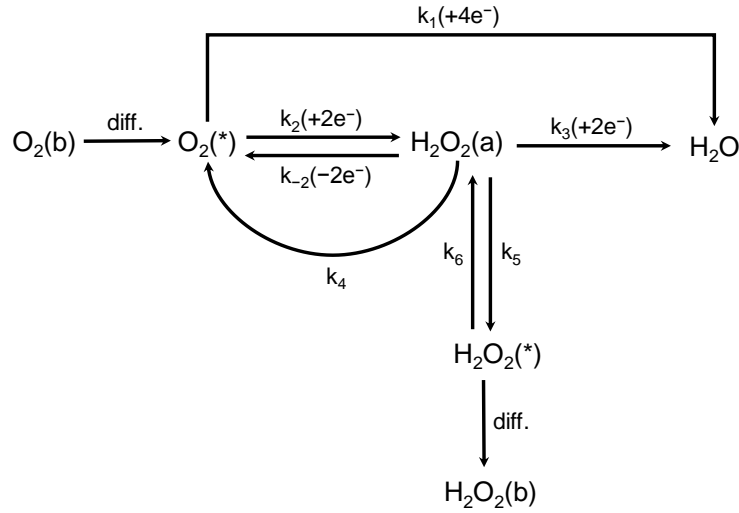


**Figure 5.** General scheme of ORR. Indices (b), \*, and (a) designate the bulk, vicinity of the disc electrode, and adsorbed species, respectively. The rate constant  $k_i$  pertains to the  $i$ -th reaction according to the following index notation: (1) direct reduction to  $H_2O$  ( $+4e^-$ ); (2) reduction to  $H_2O_2$  ( $+2e^-$ ); (-2) oxidation of  $H_2O_2$  to  $O_2$  ( $-2e^-$ ); (3) reduction of  $H_2O_2$  to  $H_2O$  ( $+2e^-$ ); (4) disproportionation of  $H_2O_2$  yielding  $O_2$ ; (5) desorption of adsorbed  $H_2O_2$ ; (6) adsorption of  $H_2O_2$  [36].

Electrochemical kinetics are usually described by the Butler-Volmer equation, which describes the overall current as the sum of both anodic and cathodic contributions. Equation 2.6 represents its  $\log_{10}$  form,

$$i = i_0 \cdot r f \cdot \left( 10^{\frac{\eta_k}{b_a}} - 10^{-\frac{\eta_k}{b_c}} \right) \quad (2.6)$$

The terms in Equation 2.6 are depicted as follows,  $i_0$  represents the exchange current density (extracted at zero overpotential), a kinetic reaction rate constant which depends on the specific electrocatalyst (usually given in terms of  $A/cm^2_{real}$ ).  $r f$  is the electrode roughness factor, which relates the real surface area of the catalyst to the geometric area of the electrode (usually given in terms of  $cm^2_{real}/cm^2_{electrode}$ ).  $\eta_k$  represents the kinetic overpotential (V), which describes the deviation of the electrode potential from the reversible potential of the reaction.  $b_{a,c}$  is the anodic and cathodic Tafel slope, which represents the overpotential increase required for a decade increase in the current (usually given as V/decade) and defined as in Equation 2.7.

$$b_{a,c} = \frac{2.303 \cdot R \cdot T}{\alpha_{a,c} \cdot F} \quad (2.7)$$

Whereby  $\alpha_{a,c}$  represents the anodic or cathodic dimensionless transfer coefficient, reflecting the symmetry of the energy barrier and the number of electrons in the rate determining step, and F and T are the Faraday constant and the temperature (in Kelvin), respectively.

In short,  $i_0$  and  $b_{a,c}$  are the two descriptors that are used to compare the performance of an electrocatalyst. The higher the  $i_0$  value, the faster are the electrode kinetics. Also, the smaller  $b_{a,c}$ , the lower is the overpotential needed to increase the current density by a factor of 10. A detailed discussion of Butler-Volmer equation and the Tafel-slope is out of scope of this thesis, and can be read elsewhere [39].

Ohmic potential losses are due to proton conduction through the polymer electrolyte membrane ( $\eta_{iR\text{-mem}}$ ) and through the catalyst layer ( $\eta_{H^+\text{-ele}}$ ), as well as due to the electrical contact resistances ( $\eta_{iR\text{-cont}}$ ) [40]. Mass transport resistances originate from reactant transport resistances in the flow channels, through the gas diffusion layer, through the porous electrode, and finally at the Pt/ionomer interface. The latter becomes significant with low Pt-loaded electrodes and at high current densities ( $>1 \text{ A/cm}^2_{\text{geo}}$ ) [41, 42]. The voltage losses due to the discussed overpotentials are depicted in Figure 6.

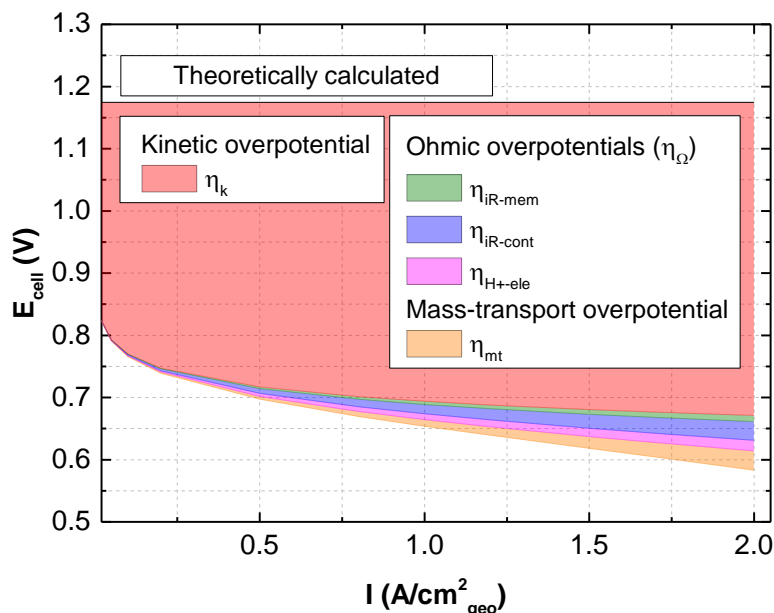


**Figure 6.** Graph representing various voltage losses due to the three overpotentials (kinetic, ohmic, and mass-transport) in comparison to the theoretical cell potential calculated at the same conditions [ $\text{H}_2$  ( $P_{\text{H}_2}$ :150 kPa<sub>abs</sub>)/Air ( $P_{\text{Air}}$ : 21 kPa<sub>abs</sub>), cathode: 0.1 mg<sub>Pt</sub>/cm<sup>2</sup><sub>geo</sub>, 80 °C]. Parameters considered in calculation of voltage losses are, mass activity at 0.9 V: 110 A/g<sub>Pt</sub>, electrochemically active surface area: 50 m<sup>2</sup>/g<sub>Pt</sub>, Tafel slope: 76 mV/decade, membrane conductivity: 0.1 S/cm, membrane thickness: 10 μm, membrane resistance: 0.005 Ωcm<sup>2</sup>, contact resistance: 0.015 Ωcm<sup>2</sup>, oxygen transport resistance: 1 s/cm, sheet resistance: 0.031 Ωcm<sup>2</sup>. The voltage losses are calculated based on equations 1 and 20 from Neyerlin et al. [40] and equation 5 from Zihrul et al. [43].

The work reported in this thesis mainly relates to  $\eta_k$  (specifically,  $\eta_{\text{ORR}}$ ) and  $\eta_{\text{mt}}$  (specifically, Pt/ionomer interface)

### 2.1.2. State-of-the-Art ORR Electrocatalysts

For any technology to be commercially sustainable, reducing its cost is one of the major challenges, and fuel cell technology is no exception to that. As already mentioned,  $\approx 43\%$  of the cost in a PEM fuel cell stack comes from the platinum-based catalyst layers [22], thus to decrease the stack cost, it is necessary to reduce the amount of Pt used, and to develop highly active and durable Pt-based catalysts. Another approach to decrease the cost is to use inexpensive PGM-free cathode catalysts, since  $\approx 80\%$  of the Pt-based catalysts are used in a PEMFC cathode.

In the R&D of Pt-based cathode catalysts, several approaches are followed to produce highly active electrocatalysts and thus lower the amount of material needed to achieve the same performance compared to conventional Pt catalysts. Specific approaches are; i) making nanostructured catalysts with a high surface-to-volume ratio; ii) alloying Pt with non-precious metals ( $\text{Pt}_y\text{M}_x$ ,  $M = \text{Ni, Cu, Co}$ ); iii) texturing nanostructures (Pt-skin or Pt monolayer catalysts). Based on the aforementioned approaches, extensive amount of research has been done, and the most important results are summarised here. Platinum has a face-centred cubic (fcc) crystal structure with a lattice parameter of 3.93 Å. Truncated octahedra or cuboctahedra are the thermodynamically favoured shapes, comprising the low-index facets Pt{100} and Pt{111}. Smaller nanoparticle size leads to an increased Pt utilization with a greater number of available catalytic sites as compared to bulk Pt single crystals. It has been experimentally shown by rotating ring disc measurements (a commonly used technique in screening electrocatalysts) on low-index single-crystal surfaces that in a  $\text{H}_2\text{SO}_4$  electrolyte Pt{100} possesses a higher ORR activity than Pt{111}. This is due the strong adsorption and the inhibiting effect of the (bi)sulphate anion [44]. They can adsorb on Pt{111} in a wider potential range and much more strongly compared to Pt{100}. On the contrary, the catalytic activity in non-adsorbing  $\text{HClO}_4$  (often used to mimic a PEMFC environment [37]) increases in the order: Pt{110} > Pt{111} > Pt{100} [45]. Hence, synthesising nanoparticles with favoured catalyst morphologies and crystal facets is of high importance.

However, the highly active Pt{110} and Pt{100} facets are not stable during long-term fuel cell operation, and their ageing usually results in a more stable and densely packed surface structure [46-48]. Thus, alloying with a non-precious metal ( $\text{Pt}_y\text{M}_x$ ,  $M = \text{Ni, Cu, Co}$ ) was started in order to increase stability and apparent activity of the catalysts [49, 50]. There are reports that these alloyed catalysts have a two- to four- fold higher mass activity than the pure Pt

catalysts. Changes in the surface electronic structure (downshift of Pt d-band centre or change in the d-band vacancy) and a favourable weaker adsorption of Pt–O and Pt–OH intermediates (shorter Pt–Pt bond distances leading to compressive strains) are the reasons for this activity enhancement [51-55]. It was also found that in Pt<sub>y</sub>M<sub>x</sub> alloys (M = Co, Fe, Ni, Cu) a Pt : M ratio of 3 : 1 exhibited much higher activity and stability, and Pt<sub>3</sub>Co had the highest specific activity [51, 56]. However, the main drawback of these catalysts is their deactivation after leaching or dissolution of the non-precious metal component. To reduce this deactivation, alloyed catalysts are often subjected to post-synthetic treatments like acid washing or heat-treatment. It has been shown that the acid-washed catalysts are more stable than catalysts without this pre-treatment [57, 58]. In addition, heat-treatment induces a higher degree of alloying and crystallinity in the structures, which could further improve their activity and stability [37, 59].

Further investigation of Pt<sub>y</sub>M<sub>x</sub> catalysts by DFT-based computational screening by the Nørskov group led to an observation that the alloyed catalysts exhibit Pt surface segregation and are more active than pure Pt. These investigations affirm the experimental findings that these so-called Pt skins have higher catalytic activity than pure Pt [60]. Around that same time, Stamenkovic et al. extensively studied bulk PtNi and PtCo surfaces, particularly the formation of so-called Pt skeleton structures upon acid leaching as well as Pt skin formation upon high temperature annealing [61]. From their study it was concluded that the ORR kinetics are dependent on the surface structural arrangement. The catalytic activity of Pt surfaces was found to vary substantially: Pt<sub>skin</sub> > Pt<sub>skeleton</sub> > Pt<sub>bulk</sub>. They also showed that various PtNi alloy skins had different ORR activities: Pt<sub>3</sub>Ni{111} > Pt<sub>3</sub>Ni{110} > Pt<sub>3</sub>Ni{100}. This unusually high activity of Pt<sub>3</sub>Ni{111}-skin was attributed to the low OH<sub>ad</sub> coverage during ORR, which was a result of altered electronic surface properties and their effect on OH adsorption strength. Last but not the least, all these developments of ≈30 years in Pt-based catalysts have resulted in the successful integration of PtCo alloy catalysts into the Toyota Mirai FCEV [62].

As mentioned in the beginning of this chapter, another way to decrease the cost of PEMFCs is to use PGM-free catalysts instead of Pt on the cathode. They can be further grouped into three main categories: i) transition metal-nitrogen-carbon catalysts (M-N<sub>x</sub>/C (M = Co, Fe, Ni, Mn, etc., and x = 2 or 4)); ii) non-precious transition metal chalcogenides (M(a)<sub>z</sub>M(b)<sub>3z</sub>X<sub>4</sub> thiospinels, where M(a) = Mn, Fe, Co, Ni, Cu or Zn, M(b) = Ti, V, Cr, Fe, Co or Ni and X = S, Se or Te); iii) transition metal oxides, carbides, nitrides, oxynitrides, and carbonitrides (Zr, Ta, Ti, Nb, W based compounds). Transition metal nitrogen carbon catalysts have been investigated for more than five decades, when it was initially demonstrated in 1964 by Jasinski that cobalt phthalocyanine (CoPc) could act as a ORR electrocatalyst in alkaline electrolyte [63]. In the following years, it was found that it was impossible to use the metal phthalocyanine

(MPc) as catalysts in acidic fuel cells, due to their poor stability in acidic medium [64]. This issue was resolved by heat treatment of Pcs ( $\approx 400 - 1000$  °C) [65-67]. Heat treatment not only increased their catalytic activity but also their stability. However, the exact nature of the active site(s) (M-N<sub>4</sub>/C, M-N<sub>2</sub>/C, N-C) in these types of catalysts is still under debate and its discussion is out of scope of this thesis [68-72]. Nevertheless, through the extensive exploration of various synthetic routes, it was found that to synthesise a M-N<sub>x</sub>/C catalyst, the use of expensive MPcs is not imperative. The only critical requirement is the simultaneous presence of a metal salt (e.g., metal halide), a nitrogen source (e.g., ammonia, melamine etc.), and a carbon source (e.g., the carbon support itself, a carbon rich (biomass) precursor etc.) during the heat treatment step in inert atmosphere [73-75]. It was also observed that in acidic medium, Fe- and Co- based catalysts had the highest activity. In 2011, Wu et al. demonstrated that a polyaniline-FeCo-based catalyst had a very high ORR performance in a fuel cell setup and only 3% performance degradation after 700 h at 0.4 V [76]. Despite these breakthroughs, long-term operational stability (5000 h) of M-N<sub>x</sub>/C catalysts is an ongoing pursuit. A recent study by Choi et al. has suggested that long-term stability could be achieved if a PEMFC is operated within a window between 0.7 to 0.9 V [77]. According to their research, operation at <0.7 V leads to de-metalation of Fe species and at >0.9 V leads to carbon oxidation (carbon corrosion), both resulting in the destruction of active sites. In addition, it is well-known that catalysts containing metallic Fe and FeC impurities exhibit inferior stability and that iron oxides have very low ORR activity [78, 79]. Based on this knowledge, researchers across the globe are trying to design M-N<sub>x</sub>/C catalysts that possess long-term operational stability in a wider operational voltage window, and without any metal, metal carbide, and metal oxide impurities.

Non-precious transition metal chalcogenides have been studied over the past few decades as possible ORR catalysts. In 1975, Behret et al. prepared various M(a)<sub>2</sub>M(b)<sub>32</sub>X<sub>4</sub> thiospinels, where M(a) = Mn, Fe, Co, Ni, Cu or Zn, M(b) = Ti, V, Cr, Fe, Co or Ni and X = S, Se or Te [80], finding that the ORR activity was directly related to the type of metal utilized (Co > Ni > Fe). In 2006 and 2007, Susac et al. investigated CoSe, FeS<sub>2</sub> (pyrite), and (Fe/Co)S<sub>2</sub> [81, 82]. Sulphide with both Fe and Co showed the highest open circuit potential (OCP; 0.8 V vs. RHE). At about the same time, Lee et al. also reported W-Co-Se chalcogenide materials as ORR catalysts [83]. Although transition metal chalcogenides demonstrate reasonably high ORR activity, compared to Pt their activity and stability is still inferior.

Transition metal carbides, nitrides, partially oxidized carbonitrides, and oxides from Zr, Ta, Ti, Nb, W, etc. have been reported to be ORR active [28]. Tungsten carbide (WC) was reported to possess similar electronic properties as platinum [84], but due to the limited stability of carbide materials in highly corrosive acidic medium, the use of pure WC and other metal

carbides seemed to be unfeasible. Transition metal nitrides have a relatively good stability in acidic conditions, but most of the reported catalysts are prepared by heat treatment in  $\text{NH}_3$  [85-87]. Thus, the exact nature of active sites (metal nitride, carbon nitrogen, or Fe-N-C active centres from minor Fe impurities) is yet unclear. Partially oxidized carbonitrides of Ta, Nb, and Zr have reportedly high ORR activity and stability [88-90]. It has been further concluded that partially oxidized Ta- and Zr- carbonitrides (Ta-CNO and Zr-CNO) have the highest activity within this sub-class [28]. It is hypothesized that partial oxidation of carbonitrides produces oxygen defects, which are formed by the release of C and/or N. The ORR activity was then linked to the degree of oxygen defected states [88, 90]. However, the ORR activity of materials was comparatively low where no carbon and/or nitrogen was involved. Potentially, this could be due to the insulating properties (wide band-gap) [91] and low inherent activity of oxygen vacancy-free metal oxides [92, 93]. Thus, the future steps in research are towards increasing the activity of partially oxidized carbonitrides. Recent research has demonstrated the synthesis of ORR active nanometric carbon supported  $\text{ZrO}_2$ -based catalysts by using an organometallic precursor (zirconium oxyphthalocyanine, ZrOPc) [29]. However, more work needs to be expended to identify the exact nature of the active sites in these type of catalysts, so that they can be tuned to develop catalysts with a higher activity.

### 2.1.3. Noble-Metal-Free and Low-Loaded Platinum Catalysts: Challenges they Face

Some of the PGM-free catalysts [ $\text{M-N}_x/\text{C}$  ( $\text{M} = \text{Co}, \text{Fe}$  and  $x = 2$  or  $4$ )] have demonstrated ORR performance comparable to Pt-based catalysts in the low current density ( $<0.1 \text{ A/cm}^2$ ) region [74, 76]. However, these highly active PGM-free catalysts suffer from some technical challenges: the typical thickness of a Pt-based cathode is  $\approx 10 \mu\text{m}$ , but the thickness of a PGM-free-based cathode is necessarily substantially higher (on the order of  $\approx 100 \mu\text{m}$ ) in order to obtain a sufficient ORR activity and to keep the  $\text{H}_2\text{O}_2$  production to a minimum. These thick cathodes make it challenging to design and manufacture a reasonable catalyst layer morphology. Challenges are both ohmic (proton and electron conduction) and mass-transport (oxygen and water) losses through those thick electrodes [94]. A recent modelling study has identified that a thick catalyst layer should possess a higher hydrophobicity (for low liquid water saturation) and lower ionomer tortuosity (for high conductivity) [95]. Apart from the aforementioned research in circumventing the technical challenges, the oldest shortcoming of  $\text{M-N}_x/\text{C}$  ( $\text{M} = \text{Co}, \text{Fe}$  and  $x = 2$  or  $4$ ) catalysts, i.e., the lack of long-term operational stability still remains unresolved. Thus, for our study of PGM-free catalysts we chose valve metal oxides, especially carbon supported  $\text{ZrO}_2$ , due to their intrinsic stability in acidic medium. Extensive research was spent in order to understand the active sites present in them (see chapters 3.1 and 3.2). In the later part (chapters 3.3 and 3.4), a successful attempt was made to boost the

activity of the ZrO<sub>2</sub>-based catalysts. This boost was achieved by substitution of Zr<sup>4+</sup> in ZrO<sub>2</sub> by Fe<sup>3+</sup>. It is shown that an iron content between 7 – 17 at% decreased the overpotential (measured at a catalyst mass normalised current of  $-1 \text{ A/g}_{\text{cat}}$ ) by  $\approx 200 \text{ mV}$  in comparison to pure ZrO<sub>2</sub> catalysts.

With low-loaded Pt-cathodes ( $0.1 \text{ mg}_{\text{Pt}}/\text{cm}^2$ ), the voltage losses at high current densities ( $>1 \text{ A/cm}^2$ ) are significantly larger than expected from the compromised kinetics due to lower loading. These unexplained voltage losses have been rationalized by suggesting complex ORR kinetics (variable Tafel slope), by an interfacial resistance (at the ionomer/Pt interface), and/or by unusually high oxygen transport resistances through a homogeneous thin ionomer film assumed to cover the Pt particles [42, 96-98]. This thesis has also addressed the aforementioned challenge with the low loaded Pt cathodes. We successfully managed to decrease the mass transport related voltage losses at high current densities by optimising the ionomer distribution on the catalyst. In addition, a major part of the unassigned voltage losses was also explained.

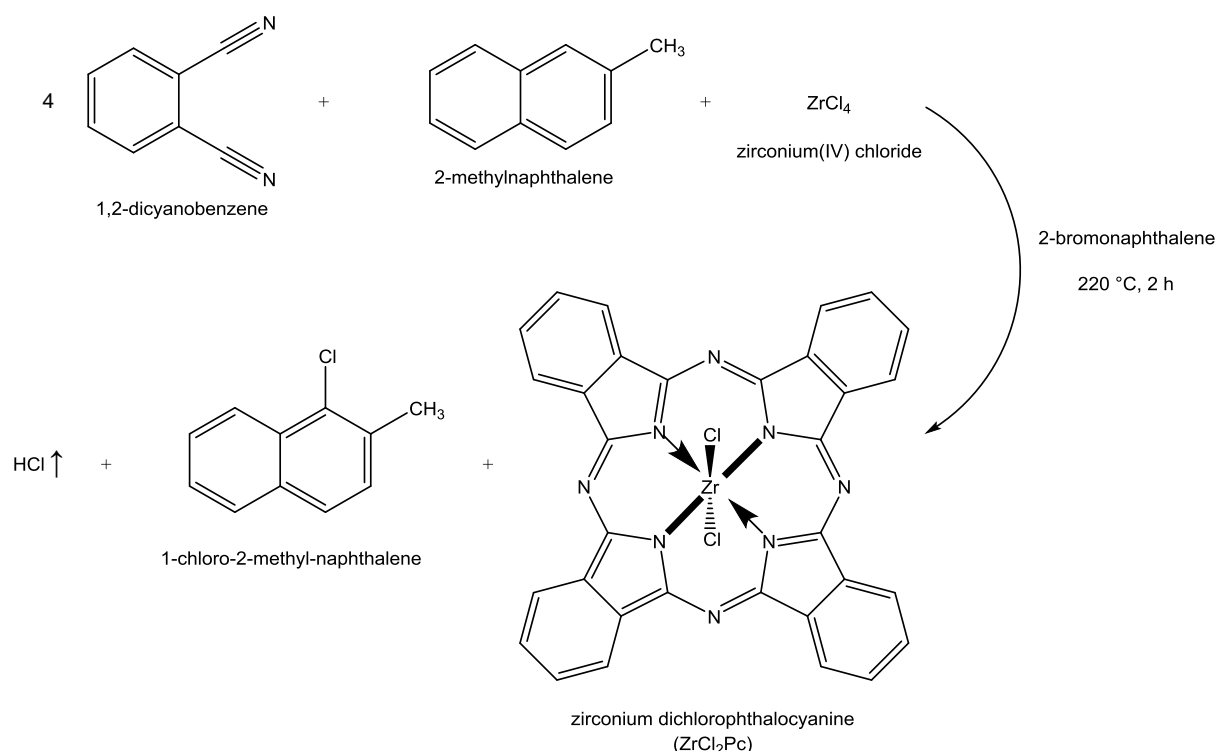
## 2.2. Synthesis of Noble-Metal-Free and Low-Loaded Platinum Catalysts

### 2.2.1. Synthesis of Noble-Metal-Free Phthalocyanines

Metal phthalocyanines (MPcs) were chosen as precursors in the synthesis of  $ZrO_2$  based catalysts. This was because of their relatively high thermal stability, low oxygen content and the presence of mainly carbon and nitrogen in the molecule. Intrinsically,  $ZrO_2$  is ORR inactive due to its high band gap [91]. However, past research had shown that the presence of nitrogen/carbon and of low oxygen concentrations during synthesis allows the formation of ‘oxygen vacancies’ or ‘uncoordinated metal sites’ which could act as ORR active centres [90, 99]. In the initial part of the synthetic procedure of  $ZrO_2$  catalysts, ZrOPc was used as a precursor, which was synthesised as reported by Tomachynskii et al. [100].

The synthesis envisages two steps. In the first step, zirconium dichloro-phthalocyanine ( $ZrCl_2Pc$ ) was synthesised (Scheme 1), which was then hydrolysed in the second step to ZrOPc (Scheme 2).

First step:



**Scheme 1.** Synthesis route of  $ZrCl_2Pc$  from  $C_6H_4(CN)_2 + C_{10}H_7CH_3 + ZrCl_4$ .

The chemicals utilized in ZrOPc synthesis are: zirconium (IV) chloride ( $ZrCl_4$ ,  $\geq 99.5\%$ ), 1,2-dicyanobenzene ( $C_6H_4(CN)_2$ , 98.0%), 2-methylnaphthalene ( $C_{10}H_7CH_3$ , 97.0%),



2-bromonaphthalene ( $C_{10}H_7Br$ , 97.0%), acetonitrile ( $CH_3CN$ ,  $\geq 99.9\%$ ), and pyridine ( $C_5H_5N$ ,  $\geq 99.0\%$ ), all procured from Sigma-Aldrich. Acetone ( $CH_3COCH_3$ ) (technical grade) was used as received from the in-house material management of TUM Chemistry department. De-ionized water ( $H_2O$ ) ( $\rho = 18\text{ M}\Omega\cdot\text{cm}$ ) was obtained from a Milli-Q ultrapure water system.

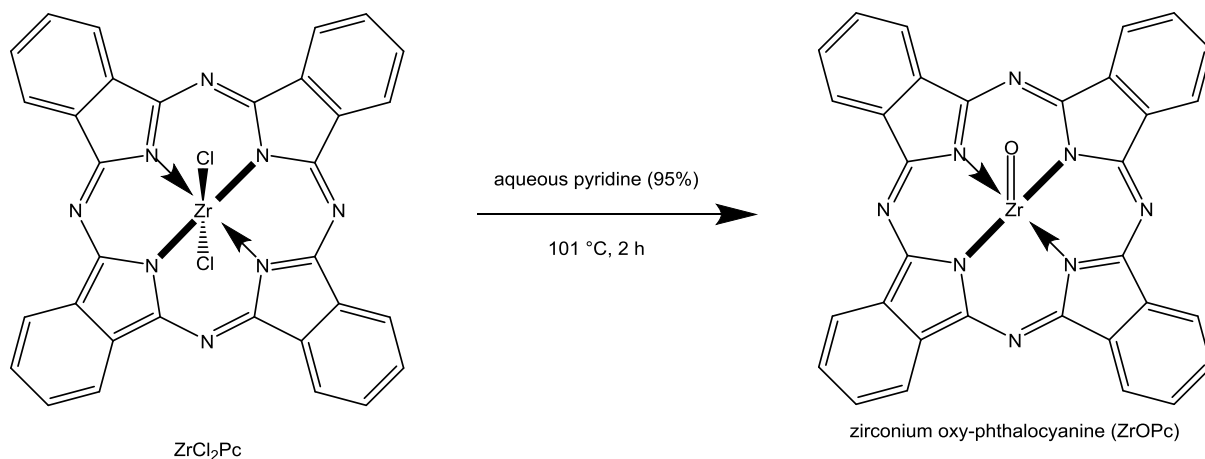
In a typical synthesis, 24.08 g of 2-bromonaphthalene ( $C_{10}H_7Br$ , m.p.  $58\text{ }^\circ\text{C}$ ) was added as solvent into a 100 ml three-necked round-bottom flask. To this, 12.80 g (0.1 mol) of 1,2-dicyanobenzene ( $C_6H_4(CN)_2$ ) and 3.55 g (0.025 mol) of 2-methylnaphthalene ( $C_{10}H_7CH_3$ ) were added. Afterwards, the flask was heated to  $220\text{ }^\circ\text{C}$  in an oil bath under magnetic stirring (750 rpm). At this point, 4.75 g (0.025 mol) of zirconium(IV) chloride ( $ZrCl_4$ ) were added under constant stirring and it was observed that the flask temperature would overshoot to  $235\text{ }^\circ\text{C}$ . This implies the start of the exothermic macrocycle formation from the  $C_6H_4(CN)_2$  units. The system was finally maintained at  $220\text{ }^\circ\text{C}$  under continuous stirring at 750 rpm. After about 15 min, a dark slurry was observed inside the flask and the colour of the reaction mixture changed from dark black at the beginning to bright blue at the end. This also indicates the formation of the phthalocyanine macrocycle, which is typically blue coloured. The reaction mixture was maintained at the same conditions for the following 2 h, and then removed from the hot oil bath to cool down to room temperature (RT). Unsubstituted phthalocyanines are practically insoluble in common organic solvents. This is due to strong intermolecular pi-bonding, Van der Waals forces, and hydrogen bonding, which causes stacking between individual molecular levels. Based on the aforementioned fact, the product purification was done by centrifuging with hot acetone (3 times with 25 ml) and acetonitrile (3 times with 25 ml) to remove all organic impurities, and finally with de-ionized water (3 times with 25 ml) to remove unreacted  $ZrCl_4$ . Before each washing, the product was sonicated until a homogeneous suspension was formed, then centrifuged (10000 rpm, 10 min,  $40\text{ }^\circ\text{C}$ ). The residue was dried overnight at RT. Dried residue was ground to a fine powder, and then heated in a glass oven (Büchi, B-585) under dynamic vacuum at  $250\text{ }^\circ\text{C}$  for 30 min and afterwards at  $200\text{ }^\circ\text{C}$  for 16 h. This step was to remove any traces of volatile impurities. The colour of the final product was dark green and its yield was 44%. The product was characterised with IR and  $^1H$  NMR spectroscopies, and elemental analyses were conducted to confirm the formation of  $ZrCl_2Pc$ .

Second step:

In the second step, 3.47 g of  $ZrCl_2Pc$  were mixed into a 100 ml three-necked round-bottom flask containing 50 ml mixture of 95 vol% pyridine ( $C_5H_5N$ ) and 5 vol% water (Scheme 2). The obtained mixture was heated under continuous stirring (1000 rpm), until the aqueous  $C_5H_5N$

## 2. Theoretical Concepts and Experimental Methods

solution started to boil ( $\approx 100\text{ }^{\circ}\text{C}$ ). Further on, the reaction mixture was refluxed for 2 h, afterwards the reaction flask was removed from the oil bath and cooled to RT. The product was washed, similarly to  $\text{ZrCl}_2\text{Pc}$ , initially with hot acetonitrile (3 times) and then with deionized water (3 times) with centrifugation at each step. The product was dried overnight at RT, and then further hand ground to a fine powder and finally heated in a glass oven (Büchi, B-585) under dynamic vacuum at  $100\text{ }^{\circ}\text{C}$  for 16 h.



**Scheme 2.** Hydrolysis of  $\text{ZrCl}_2\text{Pc}$  to  $\text{ZrOPc}$ .

The bright-blue coloured product (yield: 98%) was further analysed with IR and  $^1\text{H}$  NMR spectroscopies, and elemental analyses were conducted to confirm the formation of  $\text{ZrOPc}$ .

As mentioned before,  $\text{ZrOPc}$  is not soluble in common organic solvents. However, in order to get Fe-substituted  $\text{ZrO}_2$ -based catalysts to create more oxygen vacancies, soluble precursors were required. This solubility was crucial, as it enables a homogenous mixing of the Fe and Zr precursors, the necessary condition to obtain a successful substitution of Fe in  $\text{ZrO}_2$ .

To synthesise soluble Pcs it was decided to use 4-tert-butylphthalonitrile ( $\text{C}_{12}\text{H}_{12}\text{N}_2$ ,  $\geq 98.0\%$ , obtained from TCI) instead of 1,2-dicyanobenzene. This alternative precursor yields four t-butyl groups on the Pc ring, resulting in a soluble form (in acetone, chloroform, dichloromethane etc.) of the Pc macrocycle. Additionally, hexane ( $\text{C}_6\text{H}_{14}$ ) (technical grade) was acquired from TUM Chemistry department in-house material management, while chloroform ( $\text{CHCl}_3$ ,  $\geq 99.9\%$ ) and hydrochloric acid ( $\text{HCl}$ , 37.0%) were bought from Sigma-Aldrich. The synthesis of zirconium (IV) tetra-tert-butyl-dichlorophthalocyanine ( $\text{ZrCl}_2\text{Pc}(\text{t-Bu})_4$ ) was done very similarly to that of  $\text{ZrCl}_2\text{Pc}$ . In short, 25.00 g of  $\text{C}_{10}\text{H}_7\text{Br}$  were added into a 100 ml three-necked round-bottom flask. To this, 4.62 g (0.025 mol) of 4-tert-butylphthalonitrile ( $\text{C}_{12}\text{H}_{12}\text{N}_2$ ) and 1.78 g (0.0125 mol) of  $\text{C}_{11}\text{H}_{10}$  were added. Furthermore, the mixture was heated to  $200\text{ }^{\circ}\text{C}$  in an oil bath under continuous stirring. At this point, all the components formed a homogeneous solution. After that, 2.92 g (0.0125 mol) of  $\text{ZrCl}_4$  was added to the hot liquid mixture that was

finally kept at 230 °C under continuous stirring for 3 h. Finally, the flask was removed from the oil bath and was cooled down to RT. Product extraction was more complicated in the case of soluble Pcs. Initially, the residue was washed with  $\approx 2$  l of hexane, until the washings were colourless to remove all the solvent and unreacted reactants. Further, the product was washed with a solution of 0.2 M HCl in  $\text{CHCl}_3$ , in order to remove the unreacted  $\text{ZrCl}_4$ . Finally, the product was extracted with  $\text{CHCl}_3$ . The product was separated from the extractant by rotovaporation (Heidolph, Hei-VAP Value), initially dried overnight at 70 °C and then under dynamic vacuum at 175 °C for 48 h in a glass oven (Büchi, B-585). The colour of the dried residue was dark green and its yield was 57%. It was further subjected to characterisation by IR and  $^1\text{H}$  NMR spectroscopies. The Zr- content was estimated by TGA analysis. It is worth mentioning that it was decided not to hydrolyse  $\text{ZrCl}_2\text{Pc}(\text{t-Bu})_4$  in order to keep the molecular oxygen content at zero (Figure 7).

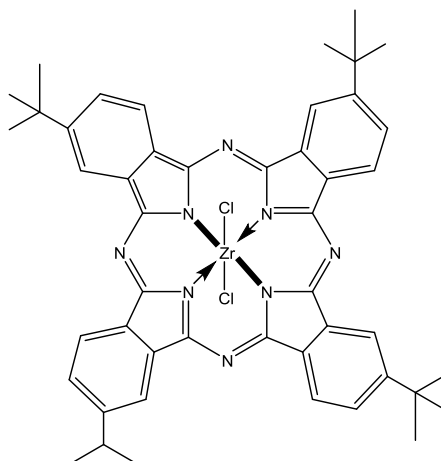


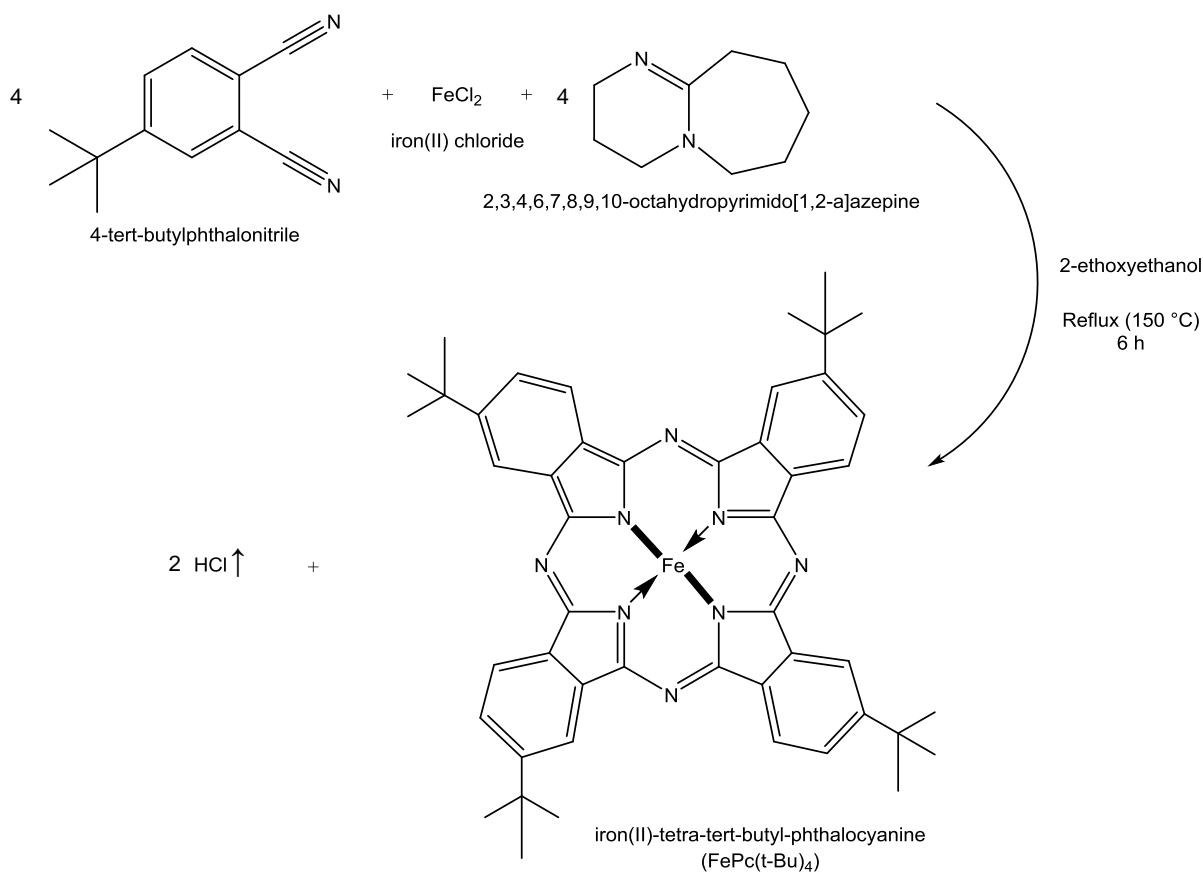
**Figure 7.** Zirconium (IV) tetra-tert-butyl-dichlorophthalocyanine ( $\text{ZrCl}_2\text{Pc}(\text{t-Bu})_4$ ) synthesised similarly to  $\text{ZrCl}_2\text{Pc}$ .

We would also like to mention that the obtained precursor contained a significant fraction of organic impurities, resulting in a Zr content  $\approx 3$  times smaller than expected for an ideal  $\text{ZrCl}_2\text{Pc}(\text{t-Bu})_4$ . Unfortunately, we were unable to remove the impurities from the precursor even after aforementioned rigorous purification. Hence, we used  $\approx 3$  times higher amount of this precursor in the catalyst synthesis. The exact origin of these organic impurities is not yet known, but it is hypothesised that the presence of minor water impurities in a reactant catalysed some organic side reaction(s).

Iron(II) tetra-tert-butyl-phthalocyanine ( $\text{FePc}(\text{t-Bu})_4$ ) was initially synthesised like in the publication by Tomachynskii et al. [100]. However, due to extremely low product yield ( $< 10\%$ ), this synthesis route was discarded.  $\text{FePc}(\text{t-Bu})_4$  in this thesis was synthesised similarly to Tomoda et al. (Scheme 3) [101]. Iron(II) chloride ( $\text{FeCl}_2$ , 98.0%), 2-ethoxyethanol ( $\text{C}_4\text{H}_{10}\text{O}_2$ , 99.0%), and 1,8-diazabicyclo[5.4.0]undec-7-ene (DBU,  $\text{C}_9\text{H}_{16}\text{N}_2$ ,  $\geq 99.0\%$ ) were purchased from Sigma-Aldrich. 2-Propanol ( $\text{CH}_3\text{CHOHCH}_3$ ) was acquired from TUM Chemistry

## 2. Theoretical Concepts and Experimental Methods

department in-house material management. In short, 3.68 g of  $C_{12}H_{12}N_2$  (0.02 mol) and 0.76 g of  $FeCl_2$  (0.006 mol) were dissolved in 50 ml of  $C_4H_{10}O_2$  using a three-necked round-bottom flask. To the mixture 3.1 ml of DBU (0.02 mol) was added and the mixture was refluxed ( $\approx 150^\circ C$ ) for 6 h. During this time, we witnessed the gradual precipitation of a blue coloured product. After the desired time, the reaction was stopped by removing the flask from the oil bath and cooling it to RT.



**Scheme 3.** Synthesis of  $FePc(t-Bu)_4$  from  $C_{12}H_{12}N_2 + FeCl_2 + DBU$ .

The product was collected by filtration and washed with 2-propanol, 3% HCl solution, and finally with de-ionized water. The final workup and characterisation of  $FePc(t-Bu)_4$  was done in a similar fashion as that of  $ZrCl_2Pc(t-Bu)_4$ . At the end, a product yield of 59% was obtained.

### 2.2.2. Synthesis of Carbon Supported Noble-Metal-Free Catalysts

The detailed route to synthesise carbon supported  $ZrO_2$  nanoparticles is reported in chapter 3.1 and 3.3. In short, the Pc supporting/impregnating process was done similarly to the examples described in the patent by Catanorchi and Piana [102]. The carbon-supported Pcs are heat treated based on the procedures reported previously [29, 103]. The key step in the heat treatment is the partial oxidation (PO), which is performed using a gas mixture of 2.5 vol%  $H_2$  in 0.5 vol%  $O_2$  with 95 vol% Ar and 2 vol%  $N_2$  as carrier gas. Even though the overall

atmosphere remains reducing, it is a controlled oxidation process, which is reportedly important to form the so-called ORR-active oxygen vacancies. In addition, the temperature increase and decrease was carried out in 5 vol% H<sub>2</sub>/Ar to avoid carbon oxidation due to minor oxygen intrusion because of the imperfect sealing of the furnace. Lastly, the temperature was ramped up with a variable rate to avoid overshooting and, after the constant temperature step, it was decreased to RT.

### 2.2.3. Synthesis of Low-Loaded Platinum Catalysts

Chapter 4.1 contains the details of the carbon functionalisation and platinum deposition. Briefly, the carbon was initially functionalised with oxygen-containing functional groups (mainly carboxylic and hydroxylic) by refluxing with conc. HNO<sub>3</sub> (at 70 °C for 30 min). This oxidized carbon was further heated under a stream of pure NH<sub>3</sub> (at 200 °C for 4 h). Thus, the obtained carbon was functionalised with amine containing groups (imides/lactams/amides). Platinum nanoparticles on the (un)functionalised carbon were synthesised by the polyol approach, to get a final loading of ca. 20 wt% Pt/carbon.

## 2.3. Structural-Morphological Characterisation

### 2.3.1. X-ray Powder Diffraction

X-ray powder diffraction (XRPD) was the first structural characterisation technique used to identify the phases and their crystallite size in the catalysts. The instrument was a STOE double-beam, double-goniometer XRPD with a MoK<sub>α1</sub> X-ray source (wavelength of 0.7093 Å, operated at 50 kV and 40 mA) as shown in Figure 8c. The instrument is based on STOE Stadi MP technology with a Dectris Mythen 1K detector. Initially, the samples were crushed to a fine powder in an agate mortar. For XRPD sample preparation, a suitable amount of the sample (ca. 2 – 5 mg) was compactly filled into a borosilicate glass capillary ( $\varnothing = 0.7$  mm) (Figure 8a). This capillary was fixed onto a goniometer, which was further mounted on the diffractometer (Figure 8b). In the instrument, Mo K<sub>α1</sub> radiation leaving the tube is further narrowed down by a collimator before reaching the sample. A beam stop prevents the damage of the detector by the transmitted radiation, and is located exactly opposite to the collimator.

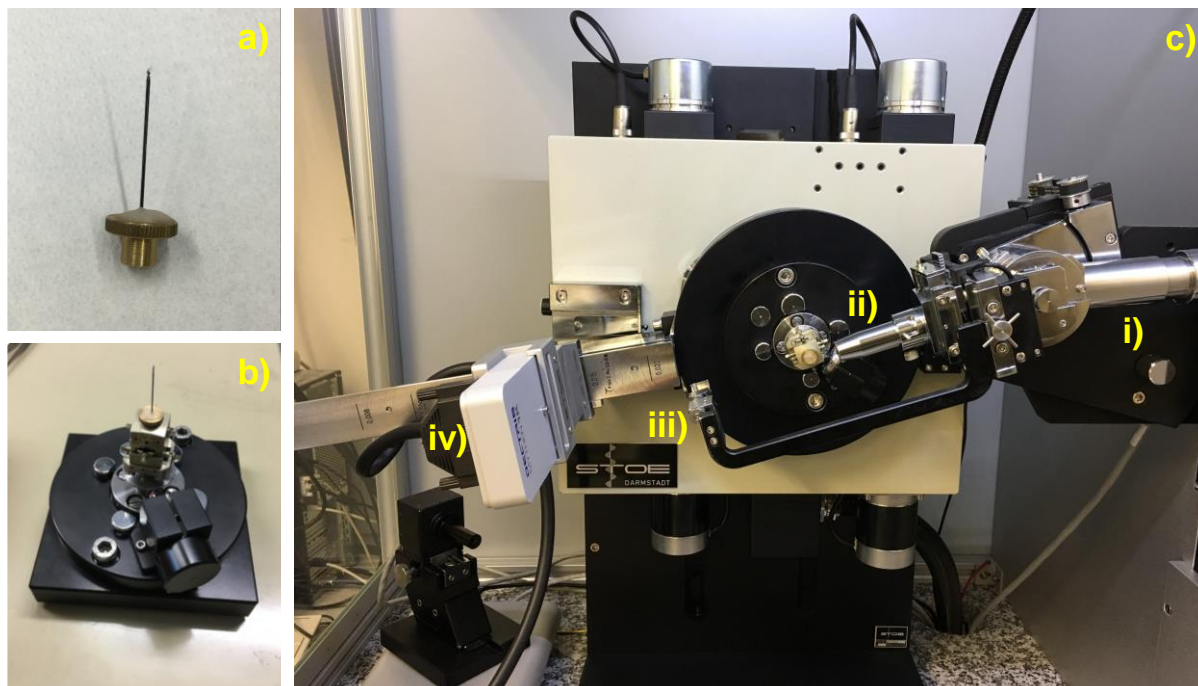


**Figure 8.** a) Sample holder with capillary; b) Goniometer; c) XRPD instrument; i) Mo  $K_{\alpha 1}$  radiation source; ii) Collimator; iii) Beam stop; iv) Detector.

Diffracted rays are collected by the detector. Samples were measured for 14 h to get a good signal-to-noise ratio. Measurement details can be found in Table 3 below. The small difference (0.004) between the  $2\theta$  values of consecutive ranges increases the number of the data points along the  $2\theta$  scale, thus increasing the resolution of the measurement.

**Table 3.** XRPD scan parameters used to characterise the catalysts.

Range	$2\theta_{\text{begin}}$ (°)	$2\theta_{\text{end}}$ (°)	Step (°)
1	2.000	50.000	0.015
2	1.996	49.996	0.015
3	2.004	50.004	0.015
4	2.000	50.000	0.015
5	1.996	49.996	0.015
6	2.004	50.004	0.015

WinXPOW was used for data acquisition and analysis. With this software, data treatments like background subtraction, addition of diffractograms and peak search were performed. In addition, with the function called search/match the detected peaks were compared with reference data to get information about the phases present in the samples. The crystallite size was estimated using the Scherrer equation (2.8).

$$L = \frac{K\lambda}{\beta \cos\theta} \quad (2.8)$$

Whereby  $L$  is the mean crystallite size,  $K$  is the dimensionless shape factor (here 0.94 for spherical crystals with cubic symmetry [104]),  $\lambda$  is the X-ray wavelength, and  $\beta$  is the full width at half maximum (FWHM) in radians of the line with the maximum intensity (after subtracting the instrumental line broadening) and  $\theta$  is the Bragg angle.

### 2.3.2. Mössbauer Spectroscopy

The Fe-containing catalysts were also characterised by Mössbauer spectroscopy. It can provide very useful information about the chemical composition, the oxidation state, and the spin-state of Fe, even at rather low concentrations ( $\approx 0.18$  wt%). Mössbauer spectra were recorded on powder samples placed in poly(methyl methacrylate) (PMMA) based holders (Figure 9a). The sample (absorber) together with the  $\gamma$ -ray source  $^{57}\text{Co}$  in rhodium (ca. 1 Giga Becquerel) were attached to a motor via a long connector (Figure 9b). Both absorber and source were immersed in a liquid helium bath cryostat where the measurements were performed at 4.2 K.

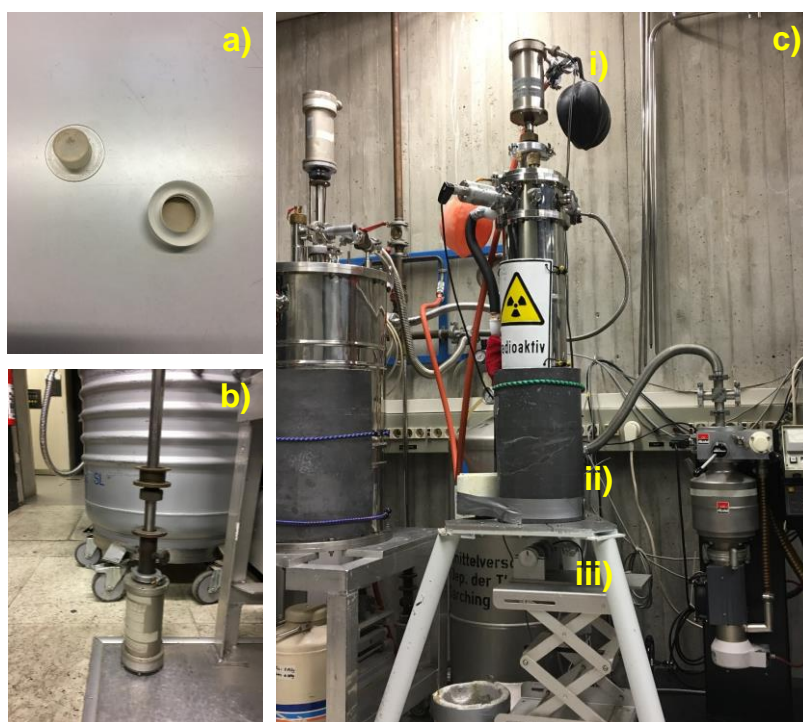


**Figure 9.** a) PMMA sample holder; b) Connector between motor and absorber; c) Mössbauer instrument; i) Motor; ii) Position of absorber and source; iii) Detector.

The detector was filled with krypton gas, which was ionized by the gamma rays transmitted through the absorber (Figure 9c). The electrons from the ionized krypton were further collected on a wire at  $\approx +2$  kV. During this collection, a pulse is recorded which is further transmitted as data through a set of electronics. Data treatment of the spectra was performed by fitting with Lorentzian functions grouped into sextets using the MOS90 software (version 2.2). The fitted



## 2. Theoretical Concepts and Experimental Methods

components often show broadened lines, which are representing distributions of magnetic hyperfine fields. The measured isomer shifts were not influenced by any temperature differences, because the source and the absorber were at the same temperature. Lastly, 0.245 mm/s was added to each isomer shift so that it can be referenced to  $\alpha$ -Fe.

### 2.3.3. X-ray Photoelectron Spectroscopy

X-ray photoelectron spectroscopy (XPS) was performed on selected samples to determine the oxidation state of Zr and Fe, as well as to confirm the functional groups on carbon. The data were collected on different instruments, but only one instrument (Kratos Axis Supra) (Figure 10c) is shown as an example here. XPS sample preparation starts with pressing the sample onto a carbon or copper tape, followed by outgassing for  $\approx 12$  h in an ultrahigh vacuum chamber (Figure 10a, b). This was to remove any unwanted atmospheric moisture and contaminants from the samples.

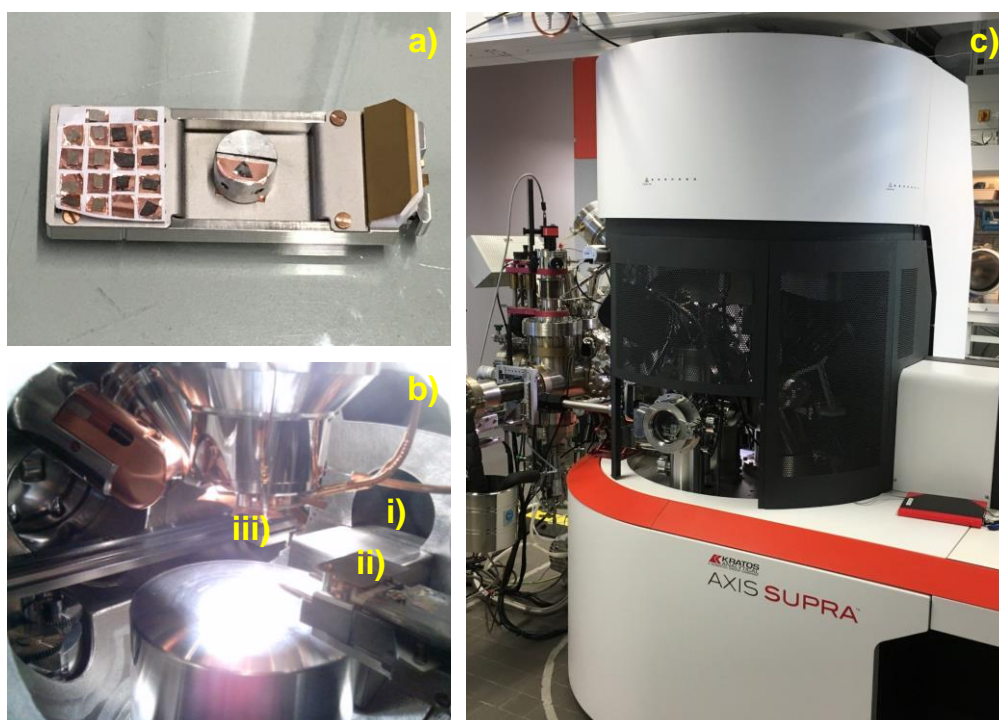


**Figure 10.** a) Sample holder with copper tapes; b) Analysis chamber of the XPS; i) X-ray beam; ii) Samples; iii) Detector; c) XPS instrument.

The samples were then transferred into the main analysis chamber, where they are irradiated with X-rays. The pressure in the chamber during the analysis was  $<1.0 \times 10^{-8}$  Torr. Kinetic energy of the electrons escaping from the surface ( $<10$  nm) and their number were detected. The binding energy is obtained by subtracting the kinetic energy and the analyser work function from the incoming photon energy. All reported binding energies were corrected, using the carbon signal from the support as a reference. Sample charging in the case of samples with



limited conductivity was avoided by using a charge neutralizer. The recorded data were initially background corrected (Shirley type) and then fitted with Gaussian and Lorentzian components.

#### 2.3.4. N<sub>2</sub> Physisorption Measurements

N<sub>2</sub> physisorption measurements were performed on platinum-based catalysts at 77 K (liquid N<sub>2</sub> temperature) using a Quantachrome Autosorb-iQ instrument (Figure 11b). The specific surface area and pore size distribution were calculated by the Brunauer-Emmett-Teller (BET) and the quenched solid density functional theory (QSDFT) method, respectively. The samples were initially filled in a glass tube ( $\varnothing = 9$  mm) (Figure 11a). A glass rod was used in the actual measurements to reduce the dead volume in the tube. Initially, the samples were outgassed under vacuum at 90 °C for 15 h. A cold trap was always used in order to trap moisture from the sample, preventing it from entering the pump. The measurements were executed in the relative pressure ( $p/p_0$ ) range between  $10^{-5}$  to 0.995, where  $p$  represents the gas pressure and  $p_0$  the saturation pressure.

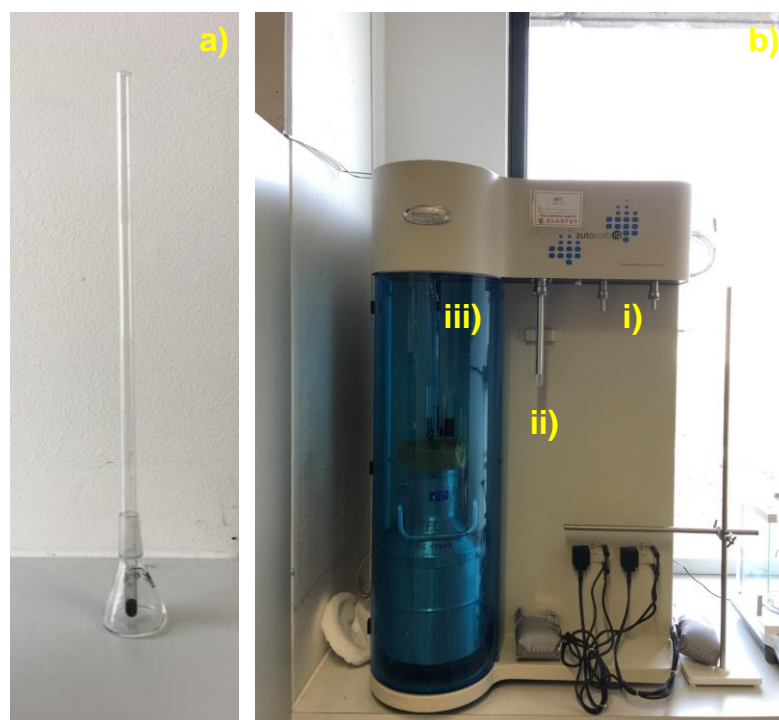


**Figure 11.** a) Glass tube with sample; b) N<sub>2</sub> physisorption instrument; i) Outgassing ports; ii) Cold trap; iii) Physisorption port.

This pressure range increases the resolution in the micro and mesopore region. It is important to mention that in every measurement the minimum sample amount was calculated based on the absolute surface area of the sample in the tube. To keep the measurement errors negligible, sample amounts corresponding to a minimum of 10 m<sup>2</sup> of absolute surface area

was used. The AsiQwin software was used for data treatment, with which BET surface area and pore size distribution analyses were performed.

### 2.3.5. Thermogravimetric Analysis combined with Mass Spectrometry

Thermogravimetric analysis combined with mass spectrometry (TGA-MS) is a powerful tool with which thermal degradation under various gas atmospheres can be studied. The identification of the fragments via MS makes detailed studies about degradation mechanisms possible. We studied the thermal degradation of our organometallic precursors, both carbon-supported and unsupported, in our Mettler Toledo TGA/DSC 1 instrument, which was equipped with a Pfeiffer Vacuum Thermostar mass spectrometer (Figure 12c). The samples were placed in  $\text{Al}_2\text{O}_3$  crucibles and heated to temperatures as high as 1000 °C under Ar and 5 vol%  $\text{H}_2/\text{Ar}$  atmosphere (Figure 12a, b).

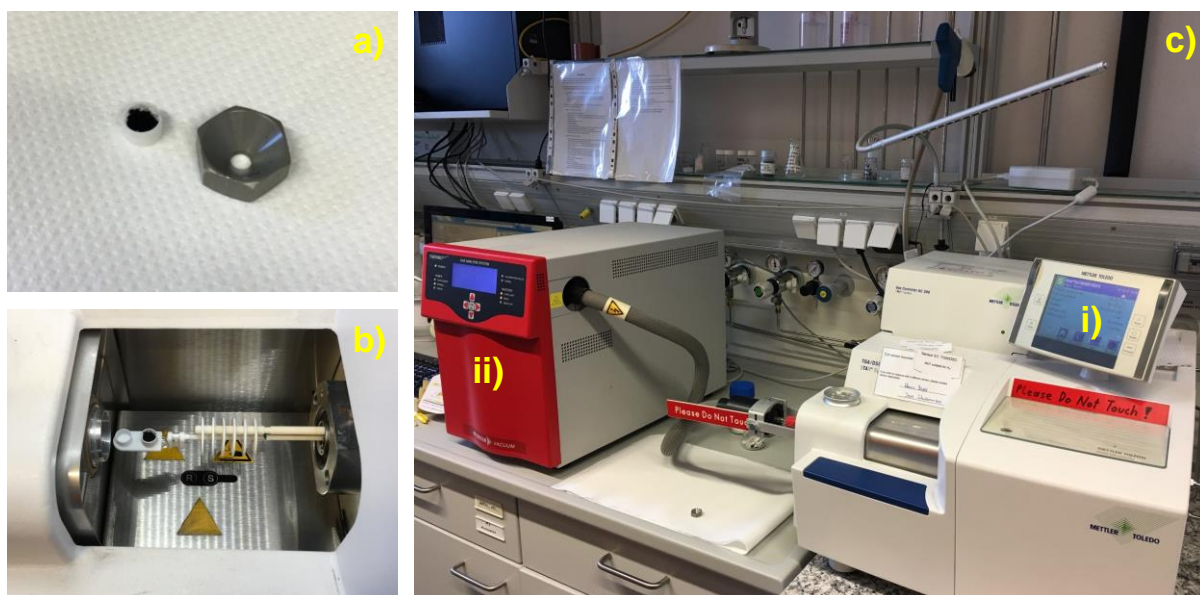


**Figure 12.** a)  $\text{Al}_2\text{O}_3$  crucible and funnel; b) Furnace with sample and reference crucible; c) TGA-MS instrument; i) TGA; ii) MS.

During the ramp-up, the MS scanned the masses between  $m/z = 12$  and 135 with a dwell time of 50 ms for each  $m/z$  channel. The unsupported precursors were heated at 10 °C/min under Ar atmosphere. In addition, TGA was used for quantitative analysis of the metal content in the precursors and catalysts. For this purpose the PGM-free catalysts or precursors were heated at 20 °C/min up to 1000 °C under 67 vol%  $\text{O}_2$  in Ar. The residual weight of the combusted sample (metal oxide) was measured to calculate the metal content. For the platinum catalysts, a slightly different approach was followed. The catalysts were first pre-dried under Ar flow at 120 °C for 1 h, and then the temperature was ramped up to 1000 °C under 67 vol%  $\text{O}_2$  in Ar, followed by cooling in the same atmosphere. The residual weight (platinum oxide) was

measured to estimate the platinum content of the catalyst. Softwares STAR<sup>e</sup> and QUADERA were used in data recording and analysis.

### 2.3.6. Transmission Electron Microscopy

Transmission electron microscopy (TEM) measurements were conducted to characterise the shape and size of the supported catalyst particles. The measurements were performed with a JEOL JEM 1400-Plus microscope equipped with a tungsten cathode. Holey carbon-coated TEM grids were used for sample mounting.



**Figure 13.** a) Dilute dispersion of sample; b) Copper grid with sample; c) TEM instrument; i) Electron gun; ii) Grid holder; iii) Fluorescent screen.

A small amount of catalyst was mixed in 2-propanol. This dispersion was sonicated in an ice-bath for 10 min to form a homogeneous dispersion (Figure 13a). Afterwards, one drop ( $\approx 10 \mu\text{l}$ ) of the dispersion was placed onto a holey carbon-coated copper grid. The grid was placed on a filter paper, so that there would be no excess dispersion around the grid (Figure 13b). Finally, the TEM grid with the sample was dried for 20 min at RT under ambient atmosphere. The measurements were performed with an acceleration voltage of 120 kV and the images were collected at different magnifications ranging from 100,000 to 500,000 with a CCD camera (Figure 13c). The software ImageJ<sup>®</sup> was used for particle size distribution analysis [105]. The diameter of at least 100 individual particles was measured. Further, the number average diameter ( $D_{\text{average}}$ ) and its standard deviation (SD) were computed. The Sauter diameter

( $D_{\text{Sauter}}$ ) (surface-volume diameter) was calculated using Equation 2.9, where  $l_i$  is the number of particles having a diameter ( $d_i$ ).

$$D_{\text{Sauter}} = \frac{\sum_{i=1}^n l_i d_i^3}{\sum_{i=1}^n l_i d_i^2} \quad (2.9)$$

The standard deviation for the Sauter diameter ( $SD_{\text{Sauter}}$ ) was calculated as per Equation 2.10, where  $SD$  is the above described standard deviation from the TEM particle size analysis.

$$SD_{\text{Sauter}} = \left( \frac{\partial D_{\text{Sauter}}}{\partial d} \right) \cdot SD \quad (2.10)$$

Which is further expressed in Equation 2.11

$$SD_{\text{Sauter}} = \left[ 3 - \frac{(2 \sum_{i=1}^n d_i^3)(D_{\text{average}})}{(\sum_{i=1}^n d_i^2)^2} \right] \cdot SD \quad (2.11)$$

$D_{\text{Sauter}}$  enlightens some aspects of the particle size distribution. For instance, in the calculation of  $D_{\text{average}}$ , if a few percent of particles have completely different size than the rest, no significant deviation will be evident in  $D_{\text{average}}$ . However, this difference will be predominant in  $D_{\text{Sauter}}$ . Thus, a comparison of  $D_{\text{Sauter}}$  and  $D_{\text{average}}$  is always advisable [106].

### 2.3.7. Fourier-Transform Infrared Spectroscopy

Fourier-transform infrared (FTIR) spectroscopy was employed to identify the characteristic vibrational frequencies in  $\text{ZrCl}_2\text{Pc}$ ,  $\text{ZrOPc}$ ,  $\text{ZrCl}_2\text{Pc}(\text{t-Bu})_4$ , and  $\text{FePc}(\text{t-Bu})_4$ . Common IR spectrometers operate between 4000 and 400  $\text{cm}^{-1}$  and most of the fundamental vibrations occur within this energy region. A PerkinElmer Spectrum Two FTIR spectrometer was employed. Before sampling, the attenuated total reflection (ATR) crystal and the press die were cleaned with acetonitrile. Afterwards, about 3 – 5 mg of sample was pressed onto the crystal by a mini hand press located above the crystal. 32 scans from 4000 to 400  $\text{cm}^{-1}$  with 4  $\text{cm}^{-1}$  resolution were recorded for each sample. After measurement, the ATR crystal and the press die were cleaned with acetonitrile. A blank measurement confirmed the cleanliness. The software Spectrum was employed in data acquisition and post-run analysis. Formation of the Pc ring and confirmation of metal insertion into the Pc was performed by FTIR spectroscopy. Formation of the Pc ring was confirmed by comparing the fingerprint region (1500 – 500  $\text{cm}^{-1}$ ), and metal insertion was confirmed by the absence of N-H stretching (1000 – 1006  $\text{cm}^{-1}$ ) based on a previous report [107].

### 2.3.8. Proton Nuclear Magnetic Resonance Spectroscopy

Proton nuclear magnetic resonance ( $^1\text{H}$  NMR) spectroscopy was performed for identification of characteristic aromatic protons in Pc compounds.  $^1\text{H}$  NMR spectra were recorded in  $\text{CDCl}_3$  solution with a Bruker AVHD400 (400 MHz) spectrometer. NMR analysis of unsubstituted phthalocyanine is not so common due to very poor solubility in common organic solvents. Taking the solubility limit of  $\text{ZrCl}_2\text{Pc}$  and  $\text{ZrOPc}$  in  $\text{CDCl}_3$  into consideration, about 5 mg of the complexes were dispersed in 0.7 ml  $\text{CDCl}_3$  and the dispersion was filtered through glass wool. The filtration was aimed to remove the undissolved sample. For the Pc compounds with t-butyl groups, solubility was not a problem, thus the samples were prepared in a standard NMR tube by dissolving 2 – 3 mg of sample in 0.7 ml  $\text{CDCl}_3$ . MestReNova software was used in post-run data analysis, including background correction, solvent referencing, phase correction, and spectra comparison.

## 2.4. Electrochemical Characterisation

The synthesised electrocatalysts were first characterised by rotating (ring) disc electrode R(R)DE voltammetry, where half-cell tests were done to determine their ORR mass activities and in some cases their hydrogen peroxide ( $\text{H}_2\text{O}_2$ ) yield. The catalyst with the highest mass activity was further tested in a PEMFC as cathode catalyst.

### 2.4.1. Rotating (Ring) Disc Electrode Voltammetry

Rotating (ring) disc electrode (R(R)DE) voltammetry was used as a primary tool for electrochemical characterisation of the synthesised catalysts. To be more specific, thin-film (TF) R(R)DE was used, which is a technique to obtain kinetic data from measured currents of an electrochemical reaction. The thin-film diffusion resistances become negligible at current densities far below the diffusion limited current density, so that the RDE data can be used to project the performance of PEMFC electrodes. Another practical advantage of the TF-R(R)DE method over PEMFC tests as screening technique is the sample amount. Typically, an R(R)DE experiment requires  $\approx 10$  mg of sample, while a test in PEMFC requires  $\approx 150$  mg in order to prepare membrane electrode assemblies (MEAs). Thus, considering the amounts commonly obtained in the synthesis of new catalysts, R(R)DE is a more practical screening technique. Moreover, a PEMFC measurement requires many more consumables (anode, membrane, sub-gasket layers, gas diffusion layers) in comparison to a R(R)DE (0.1 M  $\text{HClO}_4$  solution). Apart from being quick and inexpensive, the R(R)DE technique also has the advantage that

one can also employ the ring (here platinum) to detect the electrochemical reaction intermediates (e.g., hydrogen peroxide formed during the ORR).

A typical RRDE setup that was used in this work is depicted in Figure 14.

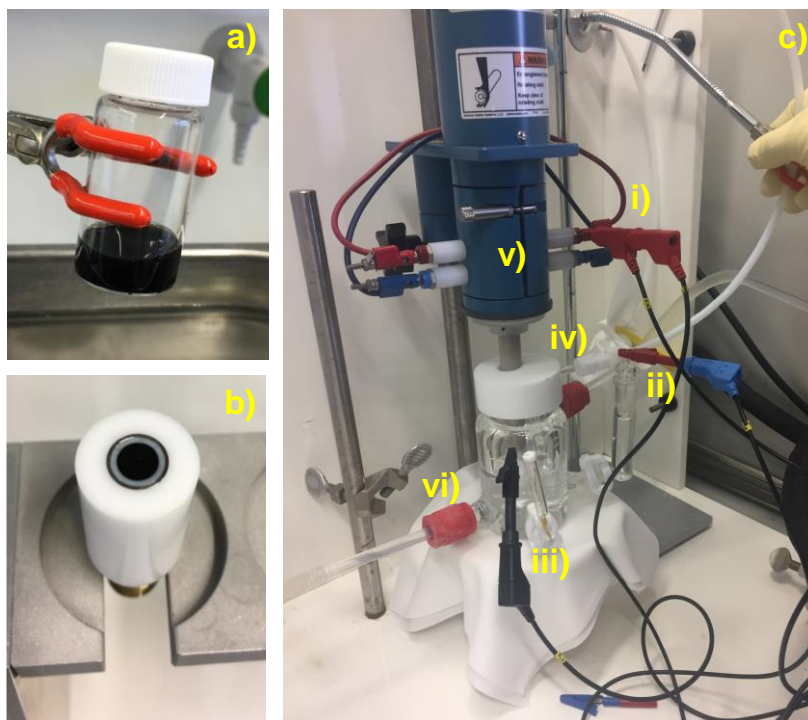


**Figure 14.** a) Ice-bath-sonicated homogeneous catalyst dispersion; b) Glassy carbon (GC) disc coated with a thin film of the catalyst. Here, the disc is surrounded by a Pt-ring to perform RRDE voltammetry; c) Water-jacketed electrochemical glass cell; i) working electrode contact; ii) reference electrode (RHE) along with a Luggin-Haber capillary; iii) counter electrode (Au mesh); iv) gas inlet (Ar, O<sub>2</sub>, H<sub>2</sub>); v) rotator; vi) thermostat connections.

It consists of a conventional three-electrode set-up, where both disc and ring electrodes are under potential control against a reference electrode (RHE) via a bi-potentiostat (Autolab PGSTAT302N). The counter electrode was separated by a glass frit (porosity grade 3) and the reference electrode (and bridge) via a Vycor 7930. Controlled gas atmosphere was maintained by passing gas through a bubbler with a shield to allow for constant bubbling during measurements. The glass cell is water-jacketed, allowing for temperature control with an external thermostat. The cell and its electrodes, i.e., working, reference, and counter electrodes have to be maintained in a very clean state. In the preparation and during the experiment, fresh clean-room gloves and lint-free cloths (both ISO class 3) are used. Except for the working electrode, all other components when bought are first pre-cleaned with isopropanol (technical grade) to de-grease them. Then they are soaked for 36 h in a bath of Caro's acid (mixture of  $\approx 30 - 50$  vol% hydrogen peroxide (stabilizer-free) and concentrated sulphuric acid ( $\geq 85$  wt%)), followed by boiling 5 – 6 times in ultra-pure (18.2 M $\Omega$ -cm) water (fresh water in each step). This cleaning is necessary to remove most of the organic/metallic impurities, which might otherwise adsorb on the catalyst surface leading to erroneous results. Various



papers have reported on the influence of contaminants on the catalyst's electrochemical performance, which the reader is encouraged to read [108-111]. Details on working electrode preparation can be found in chapter 3.

The protocol used for electrochemical characterisation is summarised in Table 4.

**Table 4.** Steps followed in the electrochemical characterisation of the catalyst by the TF-RDE technique.

Step #	Potential window $V_{\text{RHE}}$ (Number of scans #)	Scan rate mV/s	Rotation rate rpm	Purging gas	Comments
1	0.05 – 1.2 (10 – 20)	50	200	Ar	Electrochemical cleaning
2	0.05 – 1.2 (3)	20	200	Ar	
3	1.0 – 0.05 (2)	20	1600	Ar	Currents in Ar
4	1.0 – 0.05 (2)	5	1600	Ar	
Purge with O <sub>2</sub> for ≈10 min					
5	1.0 – 0.05 (2)	20	1600	O <sub>2</sub>	Currents in O <sub>2</sub>
6	1.0 – 0.05 (2)	5	1600	O <sub>2</sub>	
7	1.0	-	0	O <sub>2</sub>	Measurement of impedance

Electrochemical cleaning is performed as the first step in order to strip-off any unwanted unstable species/contaminants/anions from the catalyst; typically a steady shape in a cyclic voltammogram is reached between 10 to 20 cycles. Then currents in Ar are measured which serve as baseline to be subtracted from currents in O<sub>2</sub> in order to get the 'true' ORR (faradaic) currents ( $\equiv$ capacitive correction). Lastly, impedance measurements between the working and reference electrode are performed to determine the uncompensated solution resistance (by taking the high-frequency intercept of Nyquist plots recorded from 1 MHz to 100 mHz). For data treatment, the following corrections are applied to the measured data, i) Reference electrode potential: calibration of the reference electrode vs. the RHE; ii) Uncompensated solution resistance: obtained from the impedance measurement; iii) Capacitive correction: the currents recorded in Ar saturated electrolyte are subtracted from the faradaic currents in O<sub>2</sub> saturated solution; iv) Mass transport resistance: correcting the measured current with the diffusion limited current according to Equation 2.13; or, where no diffusion limited current was observed, estimating  $i_{lim}$  by an idealized 2 or 4 e<sup>-</sup> reference value. Further details about these corrections can be read in chapter 3.2.

After getting the potential referenced to the RHE scale, correcting the potential  $E$  for the uncompensated solution resistance is performed as in Equation 2.12.

$$E_{iR-free} = E - i \cdot R \quad (2.12)$$

Here,  $E_{iR-free}$  is the potential corrected for the solution resistance (vs. RHE),  $E$  is the measured potential referenced vs. RHE,  $i$  is the measured ORR current (note that  $i$  for the cathode ORR is negative), and  $R$  is the uncompensated solution resistance.

True kinetic currents ( $i_k$ ) are obtained by correcting the measured currents ( $i$ ) by the limiting current ( $i_{lim}$ ) (2.13). Theoretical 4 (production of  $H_2O$ ) and 2 (production of  $H_2O_2$ )  $e^-$  limiting currents are considered when no limiting currents are reached. This type of correction yields erroneous results when performed excessively, i.e., when  $i_k/i > 10$  if true limiting currents are known, but  $> 2$  if not known [112].

$$i_k = \frac{i_{lim} \cdot i}{i_{lim} - i} \quad (2.13)$$

The so obtained kinetic currents can further be translated into mass-specific- or surface-specific- activities by dividing by the catalyst mass or the catalyst surface area, respectively.

#### 2.4.2. Single Cell PEMFC Measurements

The final goal in any PEMFC related catalyst R&D project is the implementation of the catalyst into an actual PEMFC. Thus, catalysts with the best activity in TF-RDE measurements were tested in single-cell PEMFCs. It is very important to include PEMFC testing in the early stages of catalyst development, since there are a number of examples in the literature in which very high activities obtained in aqueous electrolyte are reported for catalysts could not yet be realized in PEMFCs [113-115]. Another important point is catalyst stability, which is a deciding factor with regards to actual implementation. PEMFC measurements allow the user to test the catalyst under the operating conditions which are present in real applications. Many highly active shape-controlled PtNi alloy catalysts loose Ni after MEA fabrication, ruining their activity and stability [116-119]. Some shape-controlled catalysts loose their distinct shape after loss of transition metal [120].

The left side of Figure 15 shows a sketch of a typical PEMFC single cell where all the components are listed in the left part of the figure.



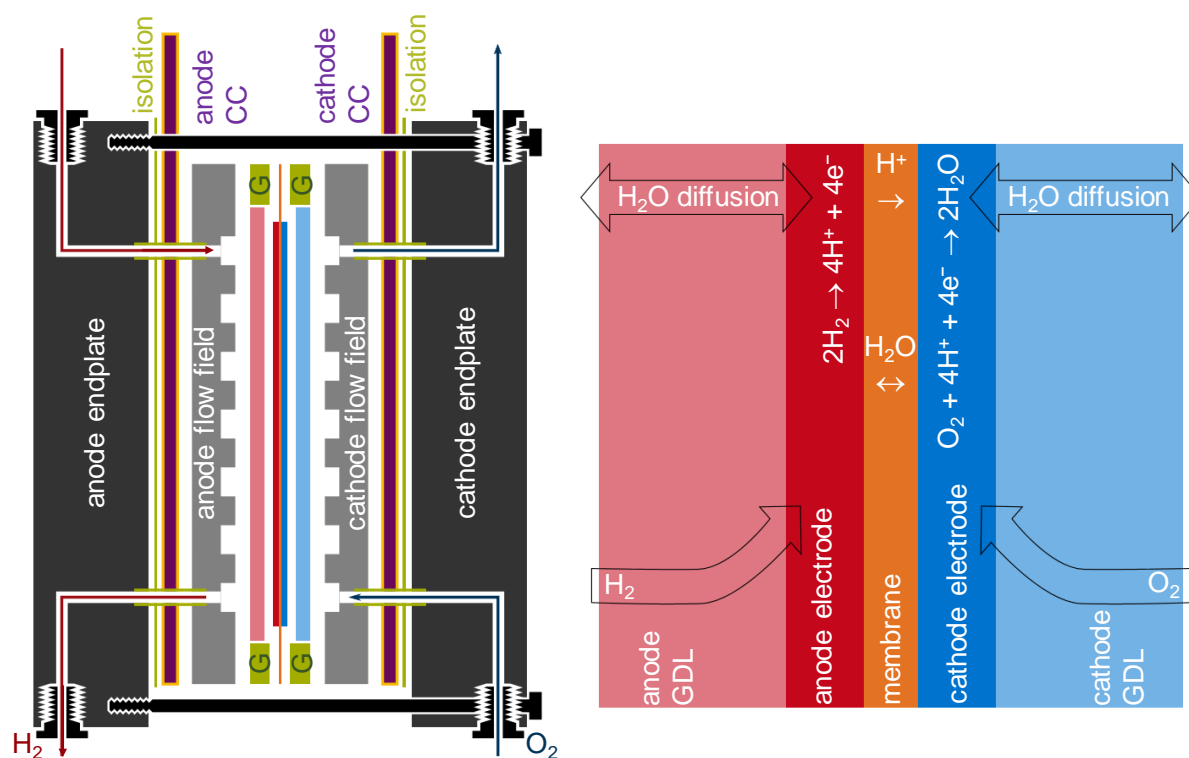


**Figure 15.** Schematic of a single PEMFC cell (not to scale). Components in the left figure (left to right): anode endplate with indicated gas flow path, insulating polymer, gold-coated anode current collector (CC), anode flow field, anode gasket (G) and MEA. A detailed sketch of the MEA is given in the right figure (left to right): anode gas diffusion layer (GDL), anode electrode, membrane, cathode electrode, cathode GDL. Reproduced (in part) by the permission of Cuvillier Verlag [121].

It is clearly seen that the membrane electrode assembly (MEA) is the heart of a PEMFC; it is sandwiched between flow fields (usually made of graphite for single-cells) which allow a convective supply of reactants and transport of water. It is worth mentioning that incompressible gaskets (G in Figure 15) are placed around the gas diffusion layer (GDL), so that the final GDL compression during cell assembly is  $\approx 20\%$ . This compression is the result of a compromise between high contact resistances at too low compression and puncturing of the membrane at too high compressions. The current collectors drive the electrical current provided by the PEMFC. The endplates (in our case made of aluminium) in the single-cell PEMFC experiments here are equipped with external heating and cooling elements. In addition, they also provide mechanical stability to the cell and facilitate a uniform compression over the active area of the cell. The right side of Figure 15 depicts a schematic of the MEA, which consists of a catalyst-coated membrane (CCM) sandwiched between two gas-diffusion layers (GDLs). The primary role of the GDLs is the effective transport of reactants towards the catalyst layers, water management, and electron transport. The CCM is comprised of a polymer electrolyte membrane (PEM), which is located between the anodic and cathodic electrode. The PEM is not only essential for the proton transfer from the anodic to the cathodic electrode, but has also the key role of separating the reacting gases ( $\text{H}_2$  and  $\text{O}_2$ ).

## 2. Theoretical Concepts and Experimental Methods

CCMs are commonly fabricated by the decal transfer method, where the catalyst layers are laminated under a defined temperature and pressure onto a PEM. However, the aforementioned way usually does not yield crack-free catalyst layers on the CCM when the catalyst loadings are higher than  $0.8 \text{ mg/cm}^2$ . In this scenario, a popular method is to coat the catalyst on GDLs, which are then pressed onto a PEM. Finally, any MEA is assembled in a PEMFC hardware for testing. The technical details of CCM manufacturing, MEA fabrication, and cell assembly can be found in chapters 3 and 4. Figure 16 is a pictorial summary of preparing CCMs and testing them in a single-cell PEMFC.

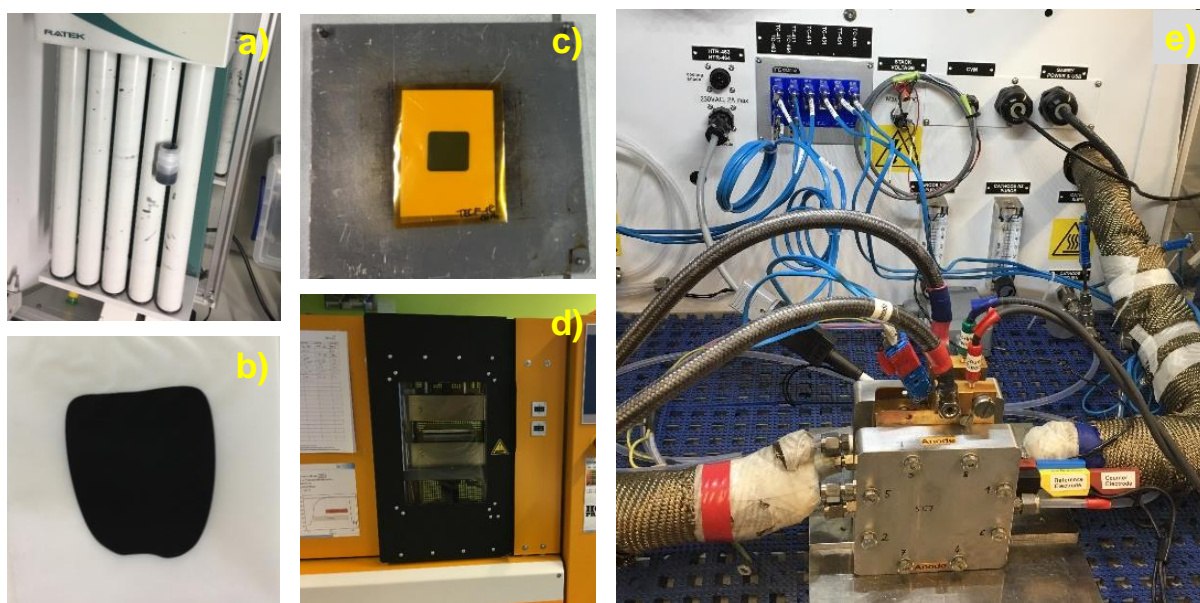


**Figure 16.** a) Ink preparation by roller mixing; b) Coating of the prepared ink onto a PTFE substrate using a Mayer rod; c) Preparing the decals for hot-pressing; d) Decal transfer by hot-pressing; e) Single-cell PEMFC in operation at the test station.

In short, the first step is catalyst ink preparation, where a defined amount of catalyst along with  $\text{ZrO}_2$  mixing beads (Glen Mills) is mixed with 1-propanol, water, and low-equivalent weight (equivalent weight:  $\frac{g_{\text{polymer}}}{\text{mol}_{\text{ionic-group}}}$ ) perfluorinated sulfonic-acid (PFSA) ionomer which provides both ion conductivity and mechanical stability. PFSA ionomer belongs to the class of ion-conductive polymers that comprises of an electrically neutral polytetrafluoroethylene (PTFE) polymer backbone which has  $\text{SO}_3^-$  groups linked along its side chain. Charge neutrality is maintained by an associated counter ion which in this case is  $\text{H}^+$ . Initially, the beads are added to a high-density polyethylene bottle, followed by catalyst, water, 1-propanol, and ionomer solution. This dispersion is further allowed to mix on a roller-mixer for a defined time and in a controlled temperature environment. After mixing, the ink is coated onto a virgin PTFE foil ( $50 \mu\text{m}$  thick) using the Mayer-rod technique (for  $<0.8 \text{ mg/cm}^2$  loadings) with a defined wet-film thickness, followed by drying at RT. After complete drying, the desired catalyst areas are cut from the sheets using appropriate cutting tools (Spahn). These catalyst

decals for both anode and cathode are laminated onto the PEM by hot-pressing. It not only ensures complete catalyst transfer, but also establishes an improved ionic contact between membrane and catalyst layers, since hot pressing temperatures are around the ionomer's glass transition point. The so produced CCMs are finally compressed between GDLs by assembly in a single-cell PEMFC and then tested.



### 3. Noble-Metal-Free Electrocatalysts

This chapter contains all the published research done on carbon supported ZrO<sub>2</sub>-based catalysts during this PhD thesis. The first two chapters, 3.1 and 3.2, focus on pure carbon supported ZrO<sub>2</sub> nanoparticles as ORR catalysts, presenting the details of the synthesis of the precursors and of the carbon supported catalysts. Synthesised catalysts were characterised mainly by XRPD, XPS, and TEM for their structure/morphology and finally by the thin-film R(R)DE technique and by single-cell PEMFC tests to assess their electrochemical performance. The last two chapters (3.3 and 3.4) focus on Fe substituted ZrO<sub>2</sub> as ORR catalysts. Carbon supported Fe substituted ZrO<sub>2</sub> nanoparticles are a new class of materials in the field of noble metal free catalysts. Detailed screening of the samples for the optimum Fe amount was conducted by comparing the ORR activity of each sample. Further, these catalysts were characterised by XPS, near-edge X-ray absorption fine structure (NEXAFS), and <sup>57</sup>Fe Mössbauer spectroscopy to get in-depth understanding about Fe coordination. Single-cell PEMFC tests were done and compared with the pure ZrO<sub>2</sub>-based catalysts. Density functional theory (DFT) calculations are also performed in chapter 3.4 to get better understanding about nature of active sites in the catalysts. Finally, the chapter is concluded by the summary of our results and the future scope of oxide based materials as ORR catalysts.

### 3.1. Synthesis Optimization of Carbon-Supported ZrO<sub>2</sub> Nanoparticles from Different Organometallic Precursors

P. Madkikar, X. Wang, T. Mittermeier, A. H. A. Monteverde Videla, C. Denk, S. Specchia, H. A. Gasteiger, and M. Piana

Journal of Nanostructure in Chemistry 2017, Volume 7, Issue 2, pp 133–147

Permanent weblink: <https://doi.org/10.1007/s40097-017-0225-6>

This article is distributed under the terms of the Creative Commons Attribution 4.0 International License (<http://creativecommons.org/licenses/by/4.0/>), which permits unrestricted use, distribution, and reproduction in any medium, provided appropriate credit is provided to the original author(s) and the source, and a link to the Creative Commons license is given, and that it is indicated if changes were made.

As already mentioned in the introduction, the use of PGM-free electrocatalysts is driven by the need to decrease the cost of PEMFCs. After an in-depth literature survey for possible routes to synthesise carbon supported ZrO<sub>2</sub> nanoparticles, we came across various publications regarding synthesis of un-supported ZrO<sub>2</sub> nanoparticles. However, owing to the possible complications of supporting them onto carbon after synthesis, we decided to adopt an approach in which ZrO<sub>2</sub> nanoparticles are synthesised directly onto carbon. On further search, we came across a handful of papers, which reported the in-situ synthesis of oxide nanoparticles but we could not find any article comparing the synthesis of carbon supported ZrO<sub>2</sub> nanoparticles from different precursors. The latter drew our attention in comparing the structure, size, oxidation state, and finally the ORR activity of ZrO<sub>2</sub> nanoparticles that are synthesised by completely different precursors.

For this work, we selected the articles by Yin et al. [29] and Lee et al. [122] as a starting point. Two precursors were used for this study; zirconium oxyphthalocyanine (ZrOPc) and zirconium acetylacetonate [Zr(acac)<sub>4</sub>]. These precursors were chosen due to their completely different composition and solubility in common organic solvents. In this chapter we compare primarily

the structure, size, and oxidation state of the resulting carbon supported ZrO<sub>2</sub> nanoparticles. And comparison of their ORR activities will be the focus of the next chapter.

Thermal stability of the precursors was characterised by thermogravimetric analysis (TGA). During thermal analysis, the released mass fragments were also measured by a coupled mass spectrometer (MS). TGA coupled with MS helped us to understand the mechanism in which the precursors will degrade during the actual heat-treatment. Thereafter, the precursors were supported on non-graphitized Ketjenblack (KB) carbon support according to a process reported by Catanorchi and Piana [102]. Further, based on the TGA results and an article by Yin et al., the heat treatment conditions for both samples were chosen. The samples were heat-treated at temperatures between 350 – 1000 °C in a quartz tube furnace in two different gas atmospheres: i) partial oxidation (PO) (0.5% O<sub>2</sub> in 2.5% H<sub>2</sub> in a mixture of N<sub>2</sub> and Ar), and ii) reducing (RED) (5% H<sub>2</sub> in Ar). The catalysts were characterised by XRPD in order to get a first information about the type of compounds synthesised after heat-treatment. ZrO<sub>2</sub> formation was confirmed in most of the samples. Further, the ZrO<sub>2</sub> particle size was estimated by the Scherrer equation. Samples were also subjected to TEM measurements, determining the average particle size (APS), particle size distribution, and Sauter diameter.

Based on the XRPD and TEM results it was concluded that samples heat-treated at temperatures  $\geq 750$  °C must have negligible amorphous phases and that the oxide nanoparticles are nanocrystals. It was also concluded that a phase pure ZrO<sub>2</sub> formation is easier when Zr(acac)<sub>4</sub> is used as a precursor. In addition, a loading variation study was also done with the ZrOPc precursor. Samples with three loadings of ZrO<sub>2</sub>/KB, i.e., 5, 10, and 15 wt%, were synthesised by heat treatment at 950 °C under PO conditions. It was clearly seen that the oxide loading affected the particle size of the ZrO<sub>2</sub> nanocrystals. Further, some selected catalysts were characterised by XPS to analyse the chemical state of Zr cations in ZrO<sub>2</sub>. From these measurements, it was confirmed that Zr species in the samples from different synthesis routes are in the pure ZrO<sub>2</sub> state. Unfortunately, we could not draw any clear trend between the Zr 3d<sub>5/2</sub> binding energy and the synthesis temperature or gas conditions due to the rather large standard deviation ( $\pm 0.4$  eV) of the 3d<sub>5/2</sub> peak energies.

### **Author contributions**


M. P. and H. A. G. conceived the project. P. M. performed the TGA-MS analysis. P. M., X. W., and C. D. synthesised and characterised (TEM and XRPD) the catalysts. A. H. A. M. V. and S. S. performed the XPS measurements. P. M. and M. P. wrote the manuscript. T. M., M. P.,

### 3. *Noble-Metal-Free Electrocatalysts*

and H. A. G. revised the manuscript. All authors discussed the results and commented on the manuscript.



# Synthesis optimization of carbon-supported ZrO<sub>2</sub> nanoparticles from different organometallic precursors

Pankaj Madkikar<sup>1</sup>  · Xiaodong Wang<sup>2</sup> · Thomas Mittermeier<sup>1</sup> ·  
Alessandro H. A. Monteverde Videla<sup>3</sup> · Christoph Denk<sup>1</sup> · Stefania Specchia<sup>3</sup> ·  
Hubert A. Gasteiger<sup>1</sup> · Michele Piana<sup>1</sup>

Received: 27 January 2017 / Accepted: 6 March 2017 / Published online: 4 April 2017  
© The Author(s) 2017. This article is an open access publication

**Abstract** We report here the synthesis of carbon-supported ZrO<sub>2</sub> nanoparticles from zirconium oxyphthalocyanine (ZrOPc) and acetylacetonate [Zr(acac)<sub>4</sub>]. Using thermogravimetric analysis (TGA) coupled with mass spectrometry (MS), we could investigate the thermal decomposition behavior of the chosen precursors. According to those results, we chose the heat treatment temperatures ( $T_{HT}$ ) using partial oxidizing (PO) and reducing (RED) atmosphere. By X-ray diffraction we detected structure and size of the nanoparticles; the size was further confirmed by transmission electron microscopy. ZrO<sub>2</sub> formation happens at lower temperature with Zr(acac)<sub>4</sub> than with ZrOPc, due to the lower thermal stability and a higher oxygen amount in Zr(acac)<sub>4</sub>. Using ZrOPc at  $T_{HT} \geq 900$  °C, PO conditions facilitate the crystallite growth and formation of distinct tetragonal ZrO<sub>2</sub>, while with Zr(acac)<sub>4</sub> a distinct tetragonal ZrO<sub>2</sub> phase is observed already at  $T_{HT} \geq 750$  °C in both RED and PO conditions. Tuning of ZrO<sub>2</sub> nanocrystallite size from 5 to 9 nm by varying the precursor loading is also demonstrated. The chemical state of zirconium was

analyzed by X-ray photoelectron spectroscopy, which confirms ZrO<sub>2</sub> formation from different synthesis routes.

**Keywords** Carbon-supported zirconia nanoparticles · Thermogravimetric analysis · X-ray diffraction · Transmission electron microscopy · X-ray photoelectron spectroscopy

## Introduction

Bulk zirconia has been explored over decades. ZrO<sub>2</sub> exists in three phases, viz., monoclinic (a room temperature stable phase), tetragonal (stable above 1100 °C), and cubic (stable above 2300 °C); the latter two are thus called high-temperature phases [1]. Various mechanisms are reported which explain the stabilization of high-temperature ZrO<sub>2</sub> phases at room temperature [2, 3]. ZrO<sub>2</sub> stabilized with dopants like yttria, magnesia, and alumina has a wide range of applications in solid-oxide fuel cells, thermal barrier coatings, and biomedical implants [4–6]. In comparison to the work done on bulk ZrO<sub>2</sub>, carbon-supported ZrO<sub>2</sub> nanoparticles are not much explored. Recently, works on the applications of carbon-supported ZrO<sub>2</sub> nanoparticles were reported. Sulfated ZrO<sub>2</sub> supported on multiwalled carbon nanotubes (MWCNTs) as a support for platinum is an example; the resulting catalyst is claimed to exhibit a higher methanol oxidation reaction (MOR) activity than unsulfated Pt-ZrO<sub>2</sub>/MWCNT and commercial Pt/C [7]. Sulfated-ZrO<sub>2</sub> acts as a co-catalyst of Pt, resulting in could be a relatively cheap anode catalyst in comparison to PtRu for MOR. Another example of application are ZrO<sub>2</sub>-C hybrid supports for Pt electrocatalysts to increase the stability of noble metal during the course of potential cycling [8]. Here it is reported, that the increase in durability is due to nanometric ZrO<sub>2</sub>

**Electronic supplementary material** The online version of this article (doi:10.1007/s40097-017-0225-6) contains supplementary material, which is available to authorized users.

✉ Pankaj Madkikar  
pankaj.madkikar@tum.de

- <sup>1</sup> Chair of Technical Electrochemistry, Department of Chemistry and Catalysis Research Center, Technische Universität München, 85748 Garching, Germany
- <sup>2</sup> Johnson Matthey Catalysts (Germany) GmbH, Bahnhofstr. 43, 96257 Redwitz, Germany
- <sup>3</sup> Department of Applied Science and Technology, Politecnico di Torino, Corso Duca degli Abruzzi 24, 10129 Turin, Italy

which inhibits the migration and aggregation of Pt during cycling. Similar ZrO<sub>2</sub>-C hybrid supports for Pd catalysts are reported to show higher activity and durability than Pd/C in formic acid electro-oxidation [9]. In the latter study, the authors concluded that the physical characteristics of ZrO<sub>2</sub> could promote dispersion of Pd nanoparticles and the presence of ZrO<sub>2</sub> could change the interaction of Pd with the support material, resulting in increased activity and reduced CO poisoning effect on Pd. There were also several other articles published which clearly indicated that ZrO<sub>2</sub> serves as co-catalyst in energy conversion [10–13]. In 2013, Seo et al. reported the synthesis of valve-metal-oxide nanoparticles by an electrodeposition technique as oxygen-reduction-reaction (ORR) electrocatalysts [14]. Sebastián et al. have also reported facile synthesis of Zr- and Ta-based ORR-active methanol-tolerant catalysts for direct alcohol fuel cells (DAFCs) [15]. In addition, Ota research group has also reported ORR activity for ZrO<sub>2</sub> [16, 17]. This material has been considered as a promising non-noble metal catalyst for PEMFCs (proton exchange membrane fuel cells) because of its availability, its observed ORR activity, and stability in the strong acidic environment of the PEMFC [18]. In a few conference proceedings articles, zirconium oxy-phthalocyanine (ZrOPc) has been used as a starting precursor for ZrO<sub>2</sub> nanoparticles synthesis [19–21], however, lacking detailed information and study of that synthesis. Carbon-supported ZrO<sub>2</sub> is not restricted to only DAFCs and PEMFCs applications; it has also used as a cathode in microbial fuel cell (MFC) as reported by Mecheri et al. [22].

Looking into this growing interest in carbon-supported valve-metal oxide nanoparticles like zirconia and lacking the scientific detailed information on its synthesis using ZrOPc as a precursor, this work provides a study on the preparation of ZrO<sub>2</sub> nanoparticles under different conditions. Two precursors, zirconium oxyphthalocyanine (ZrOPc) and zirconium acetylacetonate [Zr(acac)<sub>4</sub>], were chosen based on previous studies [19, 23] especially for their difference in atomic constitutions and solubility in organic solvents. ZrOPc contains less molecular oxygen but is nitrogen-rich, while, Zr(acac)<sub>4</sub> is an oxygen-rich but nitrogen-free precursor. Furthermore, ZrOPc is barely soluble in common organic solvents like chloroform, acetone, ethanol, etc., in contrast to Zr(acac)<sub>4</sub>, which is soluble [24, 25]. Starting from these highly different precursors, we aimed at comparing the structure, size, and ORR activity of the resulting carbon supported ZrO<sub>2</sub> nanoparticles.

The organometallic precursors were first supported on carbon. The obtained precursor was heat-treated at different temperatures ranging from 350 to 1000 °C, using two different gas conditions, i.e., reducing (RED) (5% H<sub>2</sub> in Ar) or partially oxidizing (PO) (0.5% O<sub>2</sub> in 2.5% H<sub>2</sub> in a mixture of N<sub>2</sub> and Ar). Additionally, ZrO<sub>2</sub> loading variation was also carried out by varying the starting amount of ZrOPc and its

effect on the oxide nanoparticles was checked. Our final aim was to check the ORR activity of the supported nanoparticles and find a possible correlation between their activity and size–structure. We have reported the electrochemical results in an electrochemistry-oriented journal [26].

## Experimental procedure

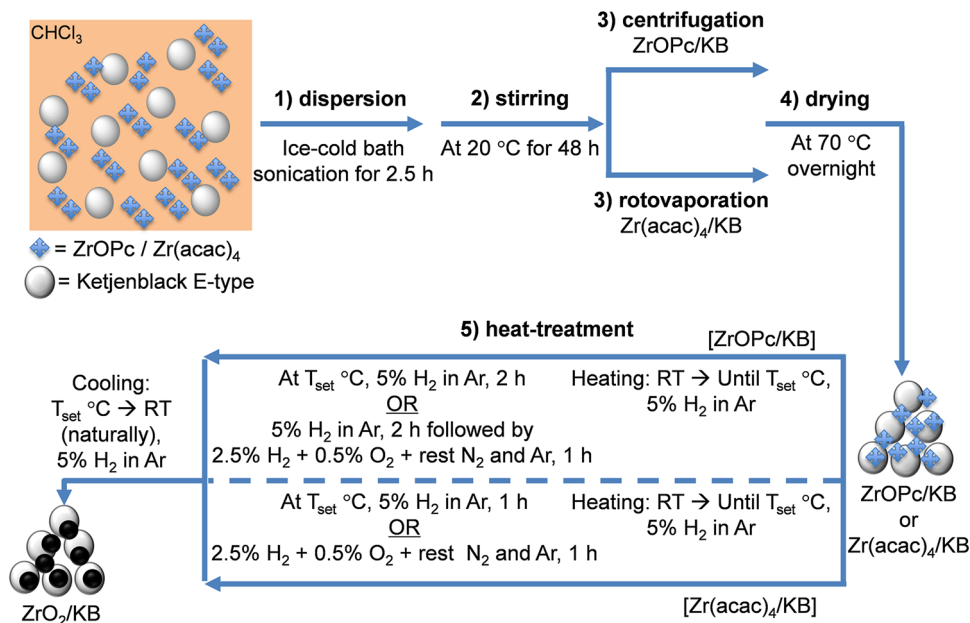
### Synthesis of carbon supported ZrO<sub>2</sub> nanoparticles

Zirconium oxy-phthalocyanine (ZrOPc) was synthesized as reported by Tomachynski et al. (Refer to the supplementary information for the chemical analyses of the produced ZrOPc) [27]. Zirconium acetylacetonate [Zr(acac)<sub>4</sub>, 98%] and chloroform (CHCl<sub>3</sub>, ≥99.9%) were purchased from Sigma-Aldrich. Ketjenblack E-type (KB) carbon support was bought from Tanaka Kikinokogyo K.K. Argon 5.0 (Ar, 99.999%), hydrogen W5 (5% H<sub>2</sub> in Ar), and synthetic air (a mixture of 20.5% O<sub>2</sub> and 79.5% N<sub>2</sub>) were supplied by Westfalen AG. All the commercial chemicals and gases were used as received without further purification.

For the synthesis of carbon-supported ZrO<sub>2</sub> nanoparticles, initially the precursors were deposited on KB by a method developed on the similar guidelines described in US 2011/0034325 A1 patent [28]. The general scheme is depicted in Fig. 1. Typically, 504 mg of ZrOPc (Zr = 0.8 mmol) or 220 mg of Zr(acac)<sub>4</sub> (Zr = 0.45 mmol) were added to 200 ml CHCl<sub>3</sub> in a 500 ml round-bottom flask. Considering different precursor losses in two different CHCl<sub>3</sub> separation methods for both precursors, the initial Zr mmoles are different to obtain similar Zr-loadings after supporting on carbon. The mixture was then sonicated for 5 min in an ice-cold ultrasonic bath. After this a uniform dispersion/solution was formed, which was dark blue colored in the case of ZrOPc and colorless in Zr(acac)<sub>4</sub>. Thereafter, 403 mg of KB and an additional 200 ml of CHCl<sub>3</sub> were added to the flask. Ice-cold bath sonication was continued for another 2.5 h and the dispersion was observed to be uniform. To ensure the maximum deposition of ZrOPc or Zr(acac)<sub>4</sub> on the carbon support, the sonicated dispersion was further kept under continuous stirring at 20 °C for 48 h. Afterwards, the carbon-supported precursor was isolated from CHCl<sub>3</sub> by centrifugation (*Eppendorf, Centrifuge 5810 R*) in the case of ZrOPc/KB and by rotovaporation (*Heidolph, Hei-VAP Value*) in the case Zr(acac)<sub>4</sub>/KB. The collected residue was dried at RT, then ground to fine powder in a mortar with pestle, and further dried in a temperature controlled vacuum oven at 70 °C overnight, to ensure complete removal of CHCl<sub>3</sub>.

Thermogravimetric analysis (TGA) of both ZrOPc/KB and Zr(acac)<sub>4</sub>/KB was performed on a *Mettler Toledo TGA/DSC 1* instrument to check the thermal stability and

**Fig. 1** Scheme of the steps and conditions involved in the synthesis of supported  $\text{ZrO}_2$  nanoparticles



degradation pattern of the precursors in both Ar and  $\text{H}_2/\text{Ar}$  atmospheres, adopting a heating rate of  $20\text{ }^\circ\text{C}/\text{min}$  in the analysis. In addition, TGA-MS analysis of unsupported  $\text{ZrOPc}$  and  $\text{Zr}(\text{acac})_4$  was carried out with *Pfeiffer Vacuum Thermostar* mass spectrometer (MS) in Ar atmosphere with a heating rate of  $10\text{ }^\circ\text{C}/\text{min}$  to obtain the fragmentation pattern of the precursors. Unsupported organometallic precursors were used in MS analysis to avoid signals from carbon, which might overlap with the signals from molecular fragments and cause possible complications in the data interpretation.

From the TGA of the carbon supported precursors (see discussion of Figs. 2, 5) we chose the desired gas conditions (PO or RED) and temperatures ( $350\text{--}1000\text{ }^\circ\text{C}$ ) for the final heat treatment in a quartz tube furnace (*HTM Reetz*). PO conditions were selected to be similar to those reported by Yin et al. [20].

In the above depositions of  $\text{ZrOPc}$  and  $\text{Zr}(\text{acac})_4$  on KB, the targeted  $\text{ZrO}_2$  loading on carbon was 13 wt.%  $\text{ZrO}_2/\text{KB}$  for both. Additionally, a loading variation study was conducted with carbon supported  $\text{ZrOPc}$ , to investigate its effect on the resulting particle size and structure. Samples with three loadings of  $\text{ZrO}_2$  on KB, i.e., 5, 10, and 15 wt.%, were synthesized by varying the relative amount of  $\text{ZrOPc}$  with respect to KB during the supporting process and heat-treating in PO conditions at  $950\text{ }^\circ\text{C}$ .

### Size-structural characterization of supported $\text{ZrO}_2$ nanoparticles

All heat-treated samples were analyzed by a *STOE* X-ray powder diffractometer (XRD), equipped with molybdenum

(Mo)  $\text{K}\alpha_1$  ( $\lambda = 0.7093\text{ \AA}$ , 50 kV, 40 mA) X-ray source and a one-dimensional silicon strip detector Mythen 1 K (*Dectris*). The measurements were conducted in a Debye-Scherrer geometry with a  $2\theta$  range of  $2^\circ\text{--}50^\circ$  and a step size of  $0.015^\circ 2\theta$ . Crystallite sizes were determined using the Scherrer equation on the (111) reflection ( $13.6^\circ\text{--}13.8^\circ 2\theta$ ), correcting the values for instrumental broadening. Transmission electron microscopy (TEM) measurements were conducted on the samples to evaluate their particle size and distribution. The measurements were performed with a *JEOL JEM 2010* transmission electronic microscope equipped with a tungsten cathode, operated at an acceleration voltage of 120 kV. Holey carbon-coated TEM grids were used for sample mounting. Several images were collected at magnifications from 100,000 to 500,000 with a CCD camera. The software ImageJ<sup>®</sup> was used for particle size analysis in which diameter of at least 100 individual particles was measured. Further the number average ( $D_{\text{average}}$ ) and the standard deviation (SD) were computed. Sauter's diameter ( $D_{\text{Sauter}}$ ) (surface-volume diameter) was calculated using Eq. 1, where  $l_i$  is the number of particles having a diameter ( $d_i$ ).

$$D_{\text{Sauter}} = \frac{\sum_{i=1}^n l_i d_i^3}{\sum_{i=1}^n l_i d_i^2} \quad (1)$$

Standard deviation for Sauter's diameter ( $\text{SD}_{\text{Sauter}}$ ) was calculated as per Eq. 2, where SD is the standard deviation from TEM particle size analysis.

$$\text{SD}_{\text{Sauter}} = \left( \frac{\partial D_{\text{Sauter}}}{\partial d} \right) \cdot \text{SD} \quad (2)$$

Which is further expressed in Eq. 3

$$SD_{\text{Sauter}} = \left[ 3 - \frac{(2 \sum_{i=1}^n d_i^3) (D_{\text{average}})}{(\sum_{i=1}^n d_i^2)^2} \right] \cdot SD \quad (3)$$

X-ray photoelectron spectroscopy (XPS) was performed on selected samples to determine the oxidation state of Zr in the synthesized catalysts. The analysis was carried out using a *Physical Electronics PHI 5000 Versa Probe* electron spectrometer system with monochromated aluminum (Al) K $\alpha$  X-ray source at 1486.60 eV operated at 25 W, 15 kV, and 1 mA anode current. To reduce any possible charging effects of X-rays, a dual-beam charge neutralization method was applied, combining both low energy ions and electrons. The samples were previously outgassed in an ultrahigh vacuum chamber at  $2.5 \times 10^{-6}$  Pa for 12 h. Survey scans, as well as narrow scans (high-resolution spectra) were recorded with a 100  $\mu\text{m}$  X-ray diameter spot size. The X-ray was used with a take-off angle of 45° for all samples. The survey spectra were collected from 0 to 1200 eV. The narrow Zr 3d spectra were collected from 174 to 194 eV. All of the spectra were obtained under identical conditions and calibrated against a value of the C 1s binding energy of 284.5 eV [29]. Measures on

selected samples were repeated at least three times on different spots; furthermore, on one sample the measurement was repeated from the beginning on a different portion of it, to estimate the precision of the values obtained. All measurements were affected by a standard deviation of about 0.4 eV. A commercial pure monoclinic nanometric (5–25 nm) ZrO<sub>2</sub> (*PlasmaChem GmbH*) was used as reference for the XPS data. Multipak 9.0 software was used to obtain semi-quantitative atomic percentage compositions. The peak position and areas were evaluated using symmetrical Gaussian–Lorentzian equations (in the fraction of 70 and 30%, respectively) with a Shirley-type background.

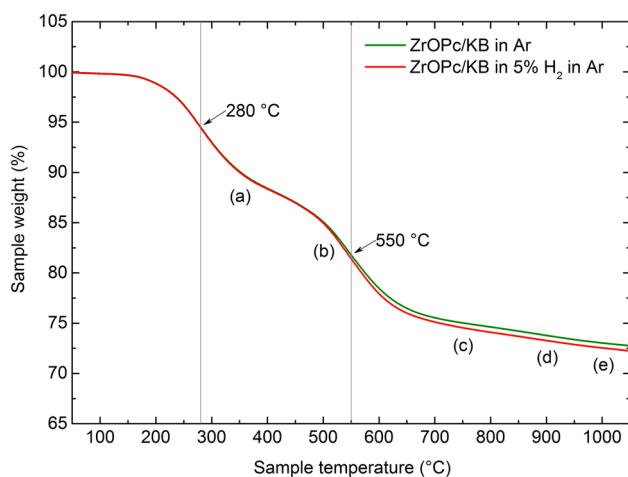
## Results and discussion

### Thermogravimetric analysis

#### ZrOPc/KB

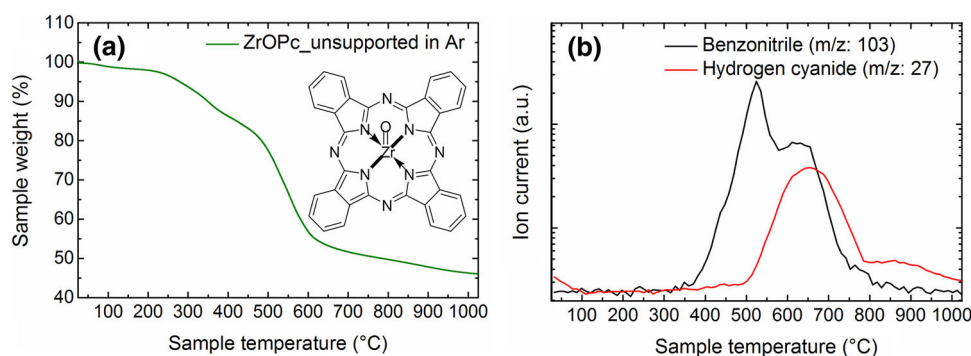
The TGA profiles of ZrOPc/KB in Ar and H<sub>2</sub>/Ar are shown in Fig. 2. No difference in ZrOPc decomposition was observed upon heat treatment under inert and reductive gas conditions. From both the weight loss curves a two-step decomposition process can be identified, with the first one between 180 and 350 °C, showing an inflection point (maximum weight loss rate) at 280 °C, and the second one between 450 and 650 °C and a maximum weight loss rate at 550 °C. It can be seen that after ~750 °C nearly all ZrOPc has degraded, with weight loss being practically independent of the temperature.

TGA-MS of unsupported ZrOPc is shown in Fig. 3. In the first step at ~300 °C benzonitrile (C<sub>6</sub>H<sub>5</sub>CN) ( $m/z = 103$ ) fragments from the skeleton start breaking. The observed typical fractionation pattern of benzonitrile ( $m/z = 104, 76, 63, 50$  not shown) [30] allows for a definite identification of  $m/z = 103$  with benzonitrile. When the temperature reaches ~500 °C, ZrOPc decomposition is still incomplete. This is confirmed by both TGA and MS signals which show rapid sample weight loss and C<sub>6</sub>H<sub>5</sub>CN signals, respectively. However, when the sample



**Fig. 2** Thermogravimetric analysis of ZrOPc/KB in pure Ar and 5% H<sub>2</sub>/Ar atmospheres

**Fig. 3 a** Thermogravimetric and **b** mass spectrometry analysis of evolution products from unsupported ZrOPc in pure Ar atmosphere



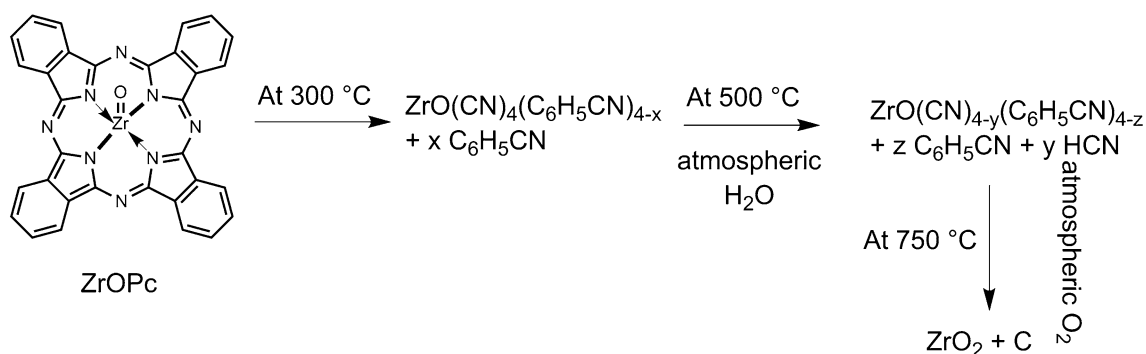


**Fig. 4** Proposed mechanism for ZrOPc thermal degradation in pure Ar atmosphere

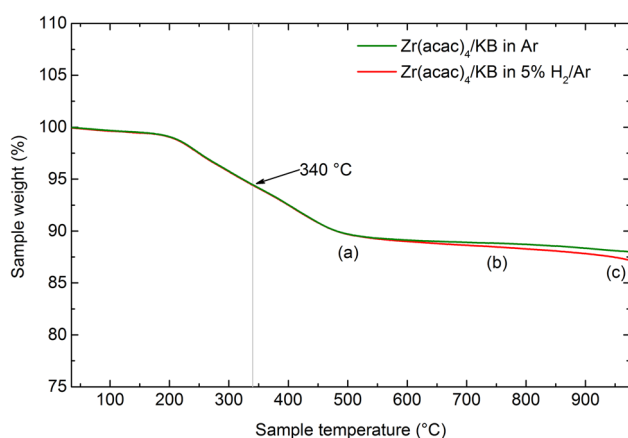


**Fig. 5** Thermogravimetric analysis of Zr(acac)<sub>4</sub>/KB in pure Ar and 5% H<sub>2</sub>/Ar atmospheres

temperature reaches  $\sim 750$  °C, nearly all the C<sub>6</sub>H<sub>5</sub>CN groups are detached from zirconium.

In addition to C<sub>6</sub>H<sub>5</sub>CN, hydrogen cyanide (HCN) ( $m/z = 27$ ) and its fragments ( $m/z = 26, 12, 13$  not shown) are detected between 500 and 800 °C [31], coming from the nitrile groups which chelate the zirconium atom. It can be concluded that molecular fragments in ZrOPc are stable until  $\sim 750$  °C. ZrOPc thermal degradation proceeds through the proposed mechanism (Fig. 4). After 750 °C, ZrO<sub>2</sub> (confirmed by XRD, refer to the supplementary

information), and carbon from degraded molecular fragments of the intermediates remains. Ideally, no ZrO<sub>2</sub> should be formed as the TGA was done in pure Ar atmosphere, but atmospheric H<sub>2</sub>O and O<sub>2</sub> through minor leaks in the instrument is the source of HCN and oxide formation.

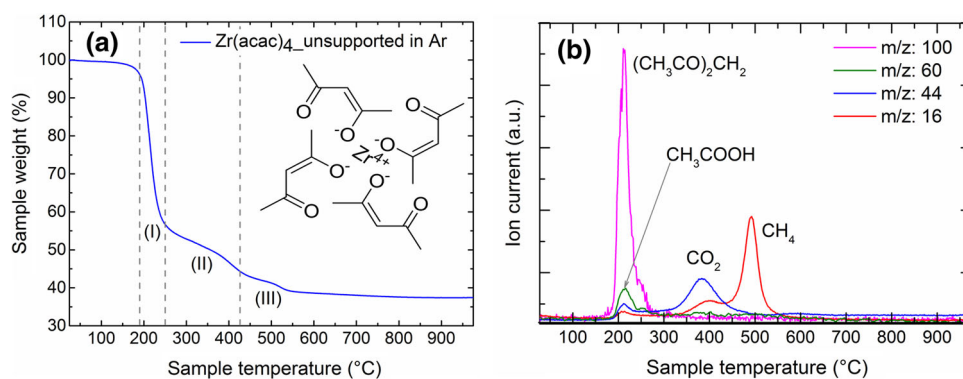
From Fig. 2, it is clear that at 500 °C, decomposition of ZrOPc is not complete but after around 700 °C ZrOPc/KB has relatively stable weight. Five different temperatures were selected (a) 350 °C (b) 500 °C (c) 750 °C (d) 900 °C, and (e) 1000 °C to study the effect of heat-treatment temperatures on ZrOPc/KB (as marked in Fig. 2).

#### Zr(acac)<sub>4</sub>/KB

Figure 5 shows the weight loss curve of Zr(acac)<sub>4</sub>/KB upon heating in Ar and 5% H<sub>2</sub>/Ar. One can easily see that the molecule degradation seems to follow the same path in both inert and reductive atmospheres. Only one-step degradation starting at  $\sim 200$  °C was observed here; with the maximum weight loss rate at  $\sim 340$  °C and a continuous weight loss until  $\sim 500$  °C.

Thus, it shows less thermal stability compared to ZrOPc (Fig. 2). Unsupported Zr(acac)<sub>4</sub> was also analyzed with TGA-MS (Fig. 6). Between  $\sim 180$  and  $\sim 250$  °C we observe the highest and rapid weight loss ( $\sim 45\%$  of the initial weight, Fig. 6a, region I), thus most of the

**Fig. 6 a** Thermogravimetric and **b** mass spectrometry analysis of evolution products from unsupported Zr(acac)<sub>4</sub> in pure Ar atmosphere





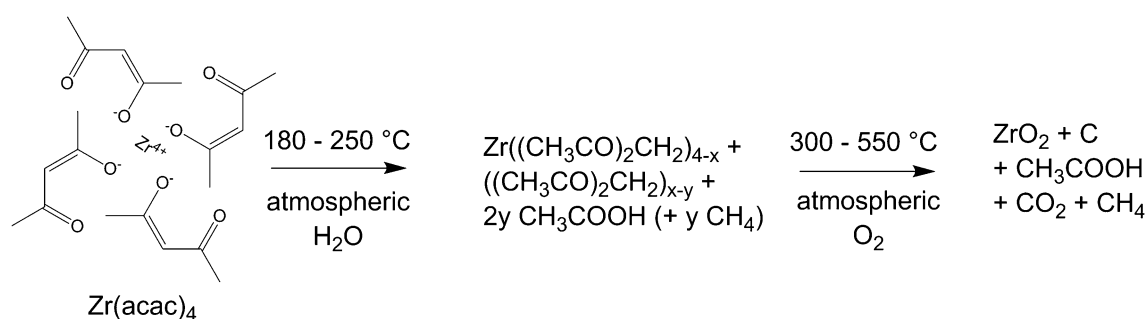


**Fig. 7** Proposed mechanism for  $\text{Zr(acac)}_4$  thermal degradation in pure Ar atmosphere

$\text{Zr(acac)}_4$  has degraded. From the MS-analysis we attribute this mainly to the detachment of acetylacetonate  $[(\text{CH}_3\text{CO})_2\text{CH}_2]$  ( $m/z = 100$ , Fig. 6b and  $m/z = 85, 72, 58, 43$  not shown) [32]. At the same temperature range acetic acid ( $\text{CH}_3\text{COOH}$ ) is unambiguously identified by the characteristic mass signal at  $m/z = 60$  (Fig. 6b), that in acetylacetonate MS-pattern has a comparably low intensity [33].

Mass signals at  $m/z = 44$  and 16 (Fig. 6b) are detected; they are attributed to acetylacetonate and/or acetic acid (part of their standard MS-pattern). We cannot exclude the evolution of acetone ( $\text{CH}_3\text{COCH}_3$ ) ( $m/z = 58$ ) since it has

a MS-pattern that almost completely superimposes on the lower  $m/z$  mass-pattern of acetylacetonate [34]. At a temperature slightly higher than  $\sim 250\text{ }^\circ\text{C}$  the acetylacetonate mass signal approaches zero (see Fig. 6b). Between 300 and  $450\text{ }^\circ\text{C}$ , carbon dioxide ( $\text{CO}_2$ ) ( $m/z = 44$ ) and acetic acid are observed as degradation products of  $\text{Zr(acac)}_4$  [35] (Fig. 6a, region II). In the same temperature range, a mass signal at  $m/z = 16$  (Fig. 6b) is detected; this is attributed to carbon dioxide and/or acetic acid as it is a part of their standard lower  $m/z$  MS-pattern. When the sample temperature reaches  $450\text{--}550\text{ }^\circ\text{C}$  there is a final weight loss of  $\sim 4\%$  which is attributed to methane ( $\text{CH}_4$ ) ( $m/z = 16$ ), confirmed by its fragments ( $m/z = 15, 14, 13$  not shown) [36] (Fig. 6a, region III). The observed molecular breakage pathway is in agreement with the reported literature [37].  $\text{Zr(acac)}_4$  degradation also yields  $\text{ZrO}_2$  (confirmed by XRD, refer to the supplementary information) and carbon (Fig. 7).

As with  $\text{ZrOPc}$ , residual carbon in  $\text{Zr(acac)}_4$  degradation is also attributed to the intermediate fragments.

At a temperature higher than  $500\text{ }^\circ\text{C}$ ,  $\text{Zr(acac)}_4/\text{KB}$  attains a stable weight. Three different temperatures were selected (a)  $500\text{ }^\circ\text{C}$  (b)  $750\text{ }^\circ\text{C}$ , and (c)  $950\text{ }^\circ\text{C}$  to study the effect of heat-treatment conditions on the final product (Fig. 5).

### Heat treatment of carbon-supported precursors

#### *ZrOPc/KB*

Due to the high thermal stability of  $\text{ZrOPc}$  (discussion from Figs. 2, 3, 4, 5, 6), we maintained 2 h of RED conditions before PO conditions. This was to ensure complete removal of the organic fragments from  $\text{ZrOPc}$ .

XRD patterns of the heat treated samples are shown in Fig. 8. For the sample heat treated at  $350\text{ }^\circ\text{C}$  under PO conditions no  $\text{ZrO}_2$  formation was observed (diffractogram not shown), which was further confirmed by TEM measurements, where no particles were found. For samples heat-treated in PO gas conditions, the formation of  $\text{ZrO}_2$  phase was observed for treatment at  $500\text{ }^\circ\text{C}$  and above.

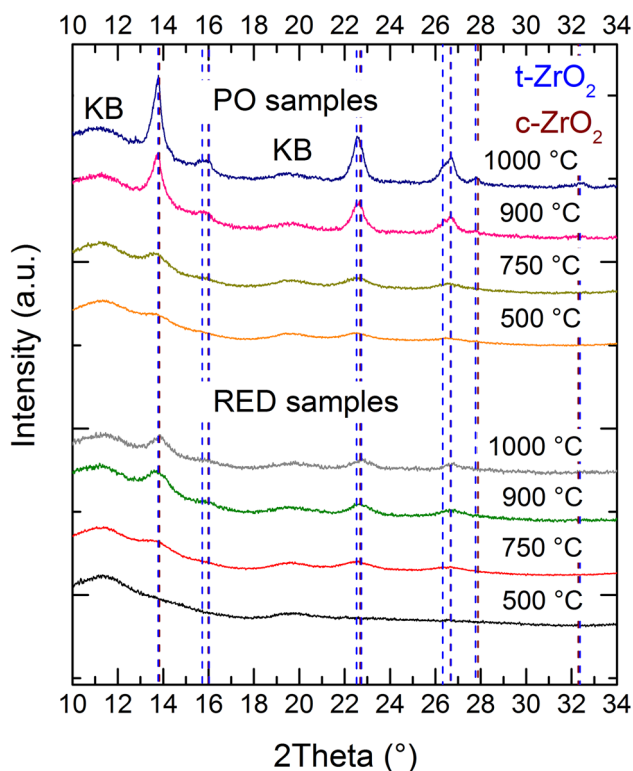


**Fig. 8** X-ray diffractograms of  $\text{ZrOPc/KB}$  heat-treated at different temperatures in PO and RED gas conditions. KB is Ketjenblack carbon support with reflexes at positions similar to graphite (PDF no. 00-056-0159)



With the increase in treatment temperature, full width half maximum (FWHM) of the reflections decreases, clearly indicating an increase in nanoparticle crystallinity.

For the samples heat-treated in RED conditions (Fig. 8), no diffraction pattern related to  $ZrO_2$  was detected for samples treated at 350 (diffractogram not shown) and 500 °C. This result fits well with the TGA data of ZrOPc/KB which clearly show that at 350 and 500 °C the phthalocyanine macrocycle degradation was incomplete with some organic residues remaining which might hinder oxidation of the metal center (see mass spectrometer data in Fig. 3). For higher synthesis temperatures ( $\geq 750$  °C), broad  $ZrO_2$  reflections were observed, which clearly indicated the formation of  $ZrO_2$ . In particular, for heat-treatment temperatures  $\geq 900$  °C,  $ZrO_2$  reflections from RED samples show higher FWHM compared to that of PO samples prepared at the same temperature. The results suggest that, at synthesis temperatures  $\geq 900$  °C PO gas conditions facilitates the formation of larger crystallites.

For the heat-treated samples correct phase assignment for the synthesized  $ZrO_2$  was not trivial.

This was because the reflections were broad and the standard tetragonal (t) and cubic (c) phase reflections were nearly overlapping. The main difference is only a shoulder reflection at  $26.32^\circ$  for t- $ZrO_2$  (marked by a red asterisk, Fig. 9). The reflections of the high temperature

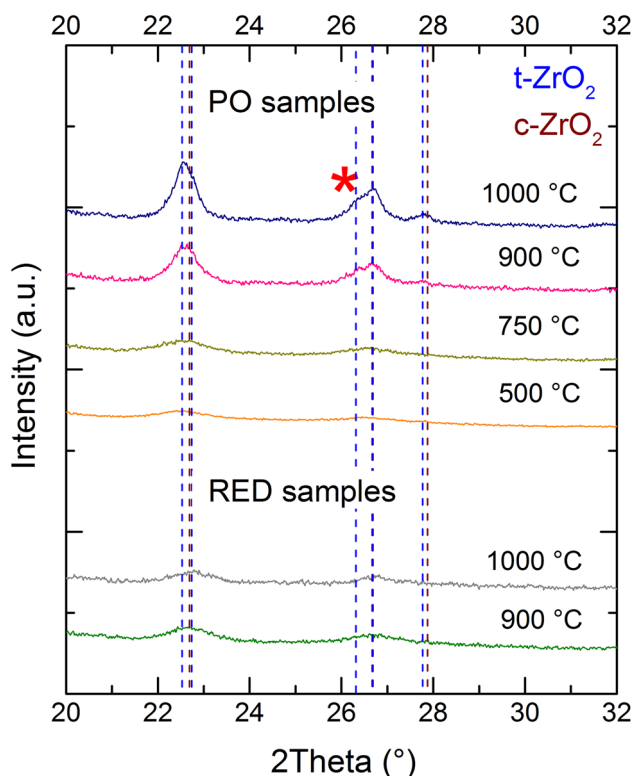


**Fig. 9**  $ZrO_2$  phase identification in heat-treated ZrOPc/KB samples

PO samples (900 and 1000 °C) fit very well with the reference data of a t- $ZrO_2$  phase (PDF no. 01-072-7115). The particle size is estimated to be dominantly below 20 nm based on the broadening of the reflections. No specific  $ZrO_2$  phase was assignable for the samples synthesized at lower temperatures (500 and 750 °C) in PO conditions due to broad reflections. Also for all the samples synthesized in RED conditions no definite  $ZrO_2$  phase is assignable. Thus, at synthesis temperatures  $\geq 900$  °C, PO gas conditions are important in formation of nanocrystals in which t- $ZrO_2$  phase can be clearly identified.

Figure 10 shows TEM micrographs of the supported  $ZrO_2$  nanoparticles prepared from ZrOPc/KB. For the samples prepared under PO gas conditions (Fig. 10a–d, f), a gradual increase in particle size with heat treatment temperature was observed. This is further confirmed in Table 1, showing that the average size of synthesized  $ZrO_2$  nanoparticles enlarged from 4 to 9 nm with an increase in synthesis temperature from 500 to 1000 °C. Comparing the heat-treated ZrOPc/KB sample under RED conditions at 1000 °C with samples heat-treated in PO conditions, it is observed that PO conditions clearly facilitate particle growth (Fig. 10d–f). Since Zr in phthalocyanine is chelated by  $N_4$  of the complex, a possible reason for the faster  $ZrO_2$  growth in PO heat treatment is the assistance of dilute oxygen in degrading the  $N_4$  chelate. Evaluation of TEM micrographs of PO samples confirms the particle size trend from XRD analysis (Figs. 8, 10).

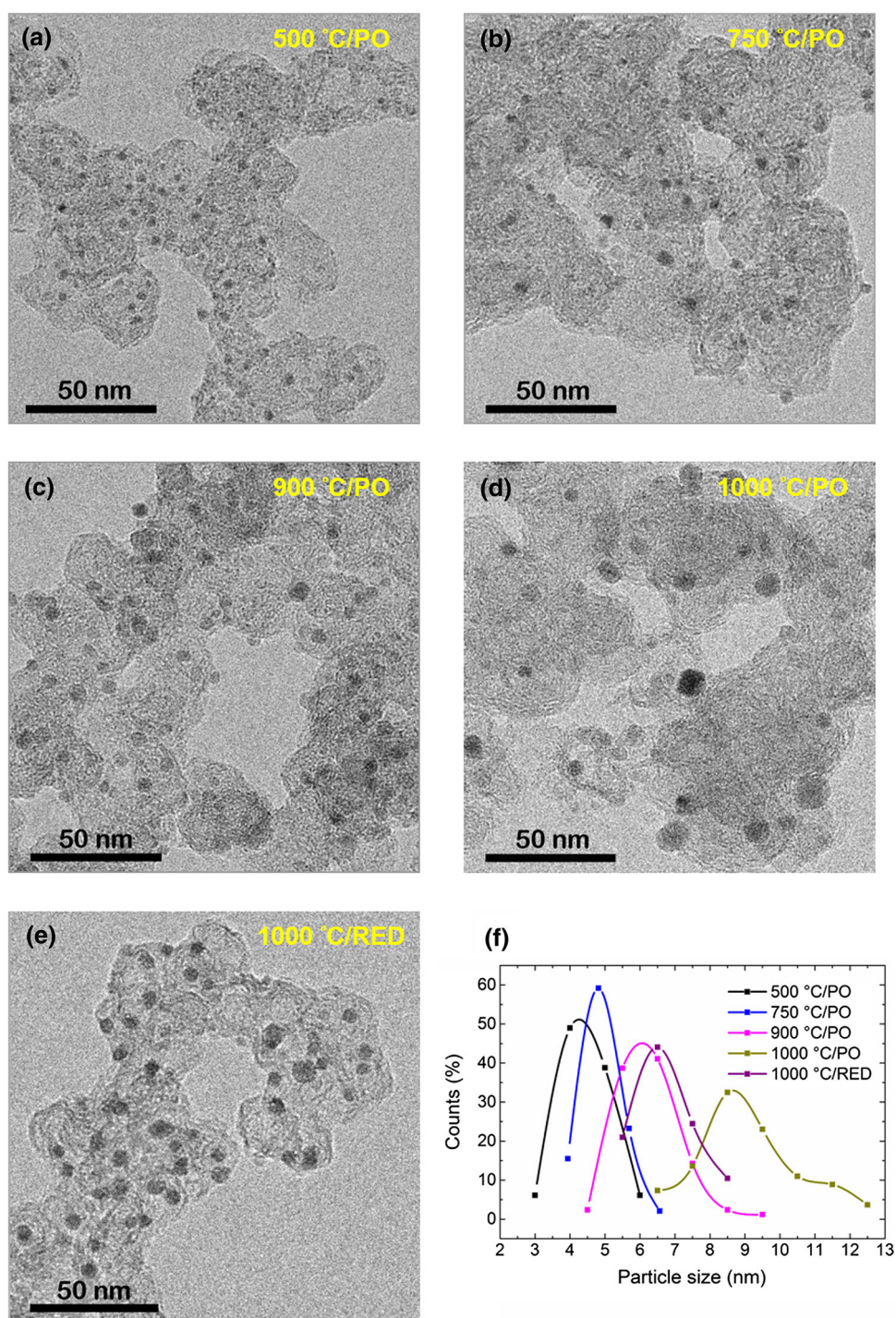
#### $Zr(acac)_4/KB$

From the diffractograms,  $ZrO_2$  formation is confirmed for samples synthesized in both PO and RED conditions (Fig. 11). These results fit well with the data obtained from TGA for  $Zr(acac)_4/KB$ , which clearly show that acetylacetonate degradation is nearly complete at 500 °C (Fig. 5). This means that at this temperature the metal atom can easily get oxidized. Thus, lower thermal stability and/or higher molecular oxygen from  $Zr(acac)_4$  makes  $ZrO_2$  formation easier.

Further, as the heat treatment temperature is increased, an increase in the  $ZrO_2$  crystallite size is observed. In addition, FWHM of  $ZrO_2$  reflections from samples heat-treated at 950 °C under PO and RED conditions seem very similar.

For the samples heat-treated at 750 and 950 °C in PO and RED conditions, a t-phase is assigned to the synthesized  $ZrO_2$  due to the presence of the shoulder reflection at  $26.32^\circ$  (PDF no. 01-072-7115) (marked by a violet asterisk, Fig. 12). No specific  $ZrO_2$  phase is assignable to samples synthesized at 500 °C in PO and RED conditions due to very broad reflections. Thus, from the observations on XRD patterns, we can conclude that  $ZrO_2$  synthesized from ZrOPc at  $\geq 900$  °C under

**Fig. 10** TEM images of supported  $\text{ZrO}_2$  nanoparticles from ZrOPc/KB heat-treated at different temperatures under PO conditions (a–d): **a** 500 °C; **b** 750 °C; **c** 900 °C; **d** 1000 °C; **e** under RED conditions 1000 °C and **f** particle size distribution plot of the samples shown here



PO conditions and from  $\text{Zr}(\text{acac})_4$  at  $\geq 750$  °C under both PO and RED conditions is isostructural.

In Fig. 13a, b, d, an increase in the average particle size from 6.5 to  $\sim 10$  nm can be observed in the samples as the heat-treatment temperature is increased from 750 to 950 °C. Comparing b and c, no major difference in the particle size is seen. The similarity in particle size is further confirmed in Fig. 13d and Table 1. This clearly indicates

that heat-treatment gas conditions are not influencing particle growth, which is in contrast with ZrOPc/KB samples Fig. 10f. This difference is attributed to lower  $\text{Zr}(\text{acac})_4$  thermal stability and its higher oxygen content. Observations from TEM analysis are in congruence with the trends observed in diffractograms of  $\text{Zr}(\text{acac})_4$  samples (Fig. 11). Dispersion of  $\text{ZrO}_2$  nanoparticles from  $\text{Zr}(\text{acac})_4$  and ZrOPc precursor is similar (Figs. 10, 13).





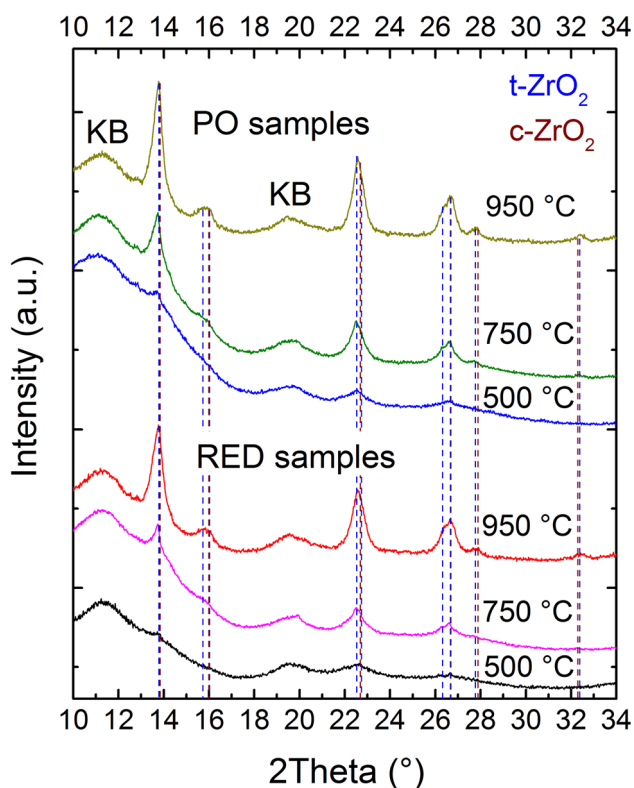


**Fig. 11** X-ray diffractograms of  $Zr(acac)_4/KB$  heat-treated at different temperatures in PO and RED gas conditions. KB is Ketjenblack carbon support with reflexes at positions similar to graphite (PDF no. 00-056-0159)

$ZrO_2$  crystallite size calculations, particle size analysis from TEM and its Sauter's diameter (surface-volume diameter) have been summarized in Table 1.

From Table 1, it is evident that crystallite size calculations from XRD and particle size analysis from TEM are significantly in agreement. This infers that  $ZrO_2$  nanoparticles are nanocrystals, and the amorphous phase should be negligible in the samples which are synthesized at temperatures  $\geq 750$  °C. There is also a good agreement between average particle size and Sauter's diameter calculations, which further confirms that all the samples have a narrow size distribution.

### Variation of $ZrO_2$ loading

t- $ZrO_2$  phase formation is apparent (PDF no. 01-072-7115) in 15 and 10 wt.%  $ZrO_2/KB$  samples, while it is not attributable in 5 wt.% sample due to very broad reflections (Fig. 14). As the loading increases, FWHM of  $ZrO_2$  reflections decreases. This infers an increase in the oxide particle size.

This increase in  $ZrO_2$  particle size is confirmed in the TEM analysis (see Fig. 15), with a particle size ranging

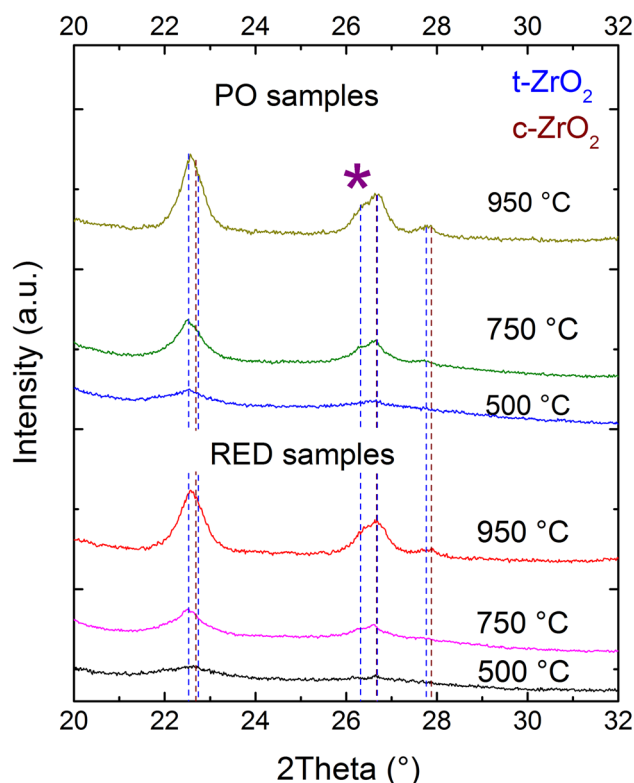


**Fig. 12**  $ZrO_2$  phase identification in heat-treated  $Zr(acac)_4/KB$  samples

from  $\sim 5$  to 8.5 nm in the samples as the loading increases from 5 to 15 wt.%. These observations are complementary with the FWHM trends from XRD (Fig. 14). Based on TEM micrographs the nanoparticles are well-dispersed on the support without obvious agglomeration and the dispersion looks similar for all the three samples. An attempt to calculate the average inter-particle distance (AID) for the above samples has been performed. In the literature about carbon supported platinum catalysts, several approaches have been followed to estimate the inter-particle distance on the support surface. Meier et al. proposed one of these methods, which as a rule-of-thumb is an estimate for AID (adapted here for carbon supported zirconia nanoparticles) (Eq. 4) [38]:

$$AID = \sqrt{\frac{\pi}{3\sqrt{3}} \cdot 10^{-3} \cdot \rho_{ZrO_2} \cdot \frac{100 - L_{ZrO_2}}{L_{ZrO_2}} \cdot A_{carbon} \cdot D_{average}^3} - D_{average} \quad (4)$$

where  $\rho_{ZrO_2} = 6.1$  g/cm<sup>3</sup> is the density of tetragonal zirconia,  $L_{ZrO_2}$  is the loading of  $ZrO_2$  on the catalyst powder in percent,  $A_{carbon} = 800$  m<sup>2</sup>/g for Ketjenblack E-type [39], and  $D_{average}$  has the same meaning as defined before.

**Fig. 13** TEM images of supported  $\text{ZrO}_2$  nanoparticles from  $\text{Zr}(\text{acac})_4/\text{KB}$  heat-treated at different temperatures under PO conditions (a, b): **a** 750 °C; **b** 950 °C; **c** under RED conditions 950 °C; **d** and particle size distribution plot of the samples shown here

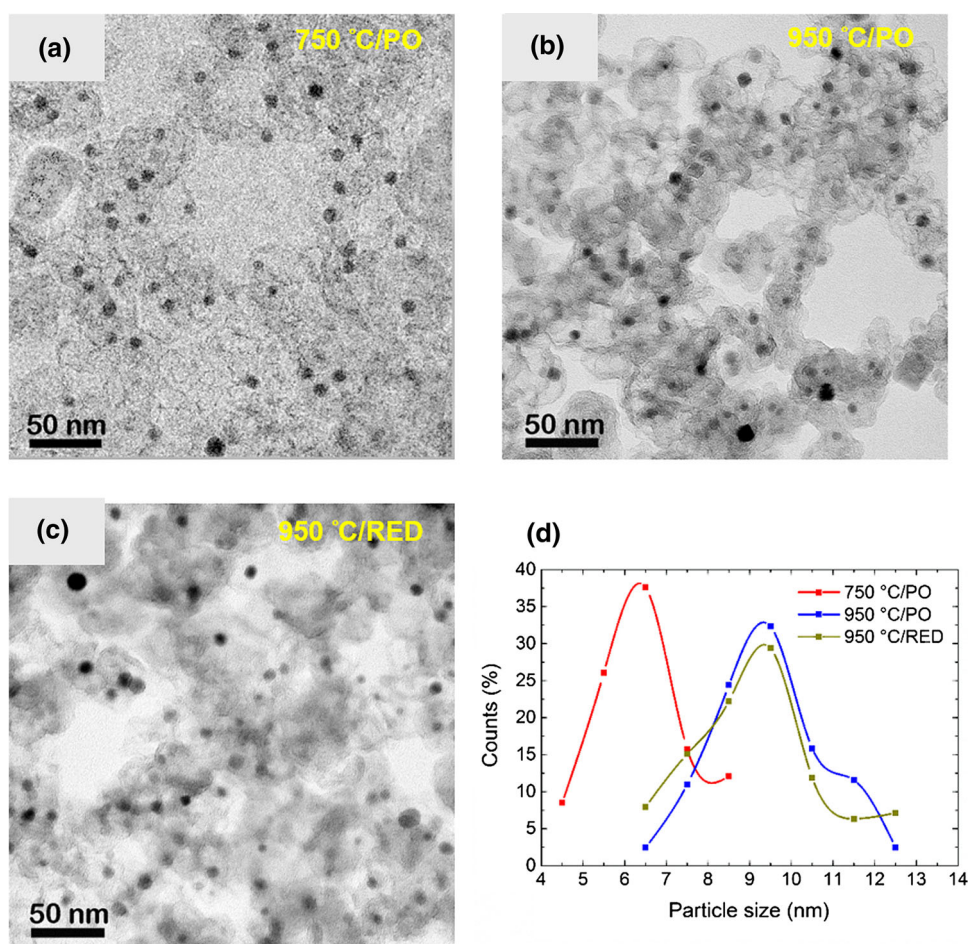


**Table 1** Crystallite size based on Scherrer equation ( $k = 0.94$ ) ( $D_{\text{Scherrer}}$ ), average particle size ( $D_{\text{average}}$ ) analysis with standard deviation (SD), and Sauter's diameter ( $D_{\text{Sauter}}$ ) with standard deviation for Sauter's diameter ( $SD_{\text{Sauter}}$ ) from particle size analysis of TEM images of  $\text{ZrOPc}/\text{KB}$  and  $\text{Zr}(\text{acac})_4/\text{KB}$  samples heat-treated at different temperatures and gas conditions

	Sample (°C)	$D_{\text{Scherrer}}$ (nm)	$D_{\text{average}} \pm \text{SD}$ (nm)	$D_{\text{Sauter}} \pm \text{SD}_{\text{Sauter}}$ (nm)
Heat-treated $\text{ZrOPc}/\text{KB}$				
PO	500	4	$4 \pm 1$	$5 \pm 1$
	750	4.5	$5 \pm 1$	$5 \pm 1$
	900	8	$6.5 \pm 1$	$7 \pm 1$
	1000	9	$9 \pm 2$	$10 \pm 2$
RED	500	–	–	–
	750	4	$4 \pm 1$	$4 \pm 1$
	900	4.5	$5.5 \pm 1$	$6 \pm 1$
	1000	5	$7 \pm 2$	$7 \pm 2$
Heat-treated $\text{Zr}(\text{acac})_4/\text{KB}$				
PO	500	5	$3.5 \pm 1$	$3.5 \pm 1$
	750	7	$6.5 \pm 2$	$7 \pm 2$
	950	8.5	$10 \pm 2$	$10 \pm 2$
RED	500	–	$3.5 \pm 1$	$3.5 \pm 1$
	750	5.5	$5 \pm 1$	$5 \pm 1$
	950	8	$9 \pm 2$	$10 \pm 2$



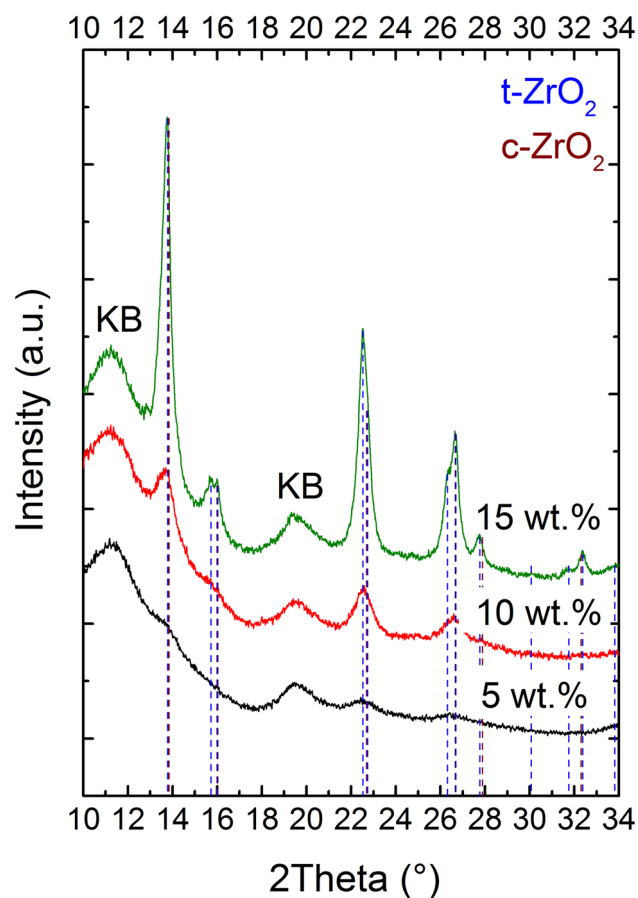


**Fig. 14** X-ray diffractograms of ZrOPc/KB heat-treated at 950 °C in PO gas conditions with varied ZrO<sub>2</sub> loadings. KB is Ketjenblack carbon support with reflexes at positions similar to graphite (PDF no. 00-056-0159)

If one calculates the AID for the samples shown in Fig. 15, the values range from  $\approx 80$ –95 nm (Table 2). Thus, although the loadings differ by a maximum factor of three, the apparent particle density on the support surface remains only weakly influenced.

From Table 2 we can also conclude in this case that the synthesized nanoparticles are nanocrystals which grow in size as ZrO<sub>2</sub> loading increases. Thus, metal loading could be used to tune the size of the supported nanocrystals.

### X-ray photoelectron spectroscopy

X-ray photoelectron spectroscopy (XPS) is a sensitive tool for analyzing the chemical state of Zr cations in ZrO<sub>2</sub>. Figure 16 shows the high-resolution Zr 3d spectra of samples prepared in various conditions. All of the spectra show the typical doublet structure in 3d<sub>5/2</sub> and 3d<sub>3/2</sub>

components, due to the spin–orbit splitting of the 3d level. The peaks resulted ranging from 182.3 to 183.4 eV for Zr 3d<sub>5/2</sub>, and from 184.7 to 185.7 eV for Zr 3d<sub>3/2</sub>, as shown in shaded bands in Fig. 16. In particular, sample ZrOPc/KB 900 °C/PO (which is one of the most interesting catalyst on the electrochemical point of view [26]) shows the measured spectra with Gaussian–Lorentzian fits and a Shirley type background. The deconvolution of the Zr 3d spin–orbit doublet is in agreement with the existence of Zr<sup>4+</sup> [40, 41]. Similar analyses has been performed for other samples. Zr 3d<sub>5/2</sub> values are extracted by taking the peak positions after data-fitting and reported in Fig. 17, together with the standard deviation ( $\pm 0.4$  eV).

After comparing the binding energy of Zr<sup>4+</sup> of pure monoclinic ZrO<sub>2</sub> (internal reference: 181.9 eV) with those reported in literature 181.9–182.1 eV [41–44] (green shaded band in Fig. 17), we could confirm that all the measurements were in agreement with reference values. The measured binding energies of Zr 3d<sub>5/2</sub> in all the samples lie inside or close to the range of Zr<sup>4+</sup> species in pure tetragonal ZrO<sub>2</sub> 182.1–182.8 eV [40, 41, 44–47] (yellow shaded band in Fig. 17).

Thus, the formation of ZrO<sub>2</sub> is confirmed by XPS for all the examined synthesis routes. Considering the trends of the binding energy of the Zr 3d<sub>5/2</sub> peak with the synthesis conditions (Fig. 17) and the standard deviation linked with the XPS measurements, it is not possible to obtain a clear trend between Zr 3d<sub>5/2</sub> with temperature, heat treatment gas conditions, and oxide particle size. In addition, it is impossible to link the shift of the binding energy with the presence of oxygen vacancies. The presence of suboxides must be excluded since in XRD we do not detect them and similar average ZrO<sub>2</sub> particle size from XRD and TEM demonstrate the only presence of pure ZrO<sub>2</sub> (Figs. 8, 11; Table 1).

### Conclusions

Successful synthesis of pure carbon supported ZrO<sub>2</sub> nanoparticles has been reported in this paper. A thorough comparative study on the synthesis of metal-oxide nanoparticles from two different precursors namely, ZrOPc and Zr(acac)<sub>4</sub> has been done. Our aim is to optimize the nanoparticle size and crystallinity of the samples for the possible application as electrocatalysts for the oxygen reduction reaction in PEMFCs. Using thermogravimetric analysis coupled with mass spectrometry, we could show and confirm the thermal-decomposition behavior of the



**Fig. 15** TEM images of carbon supported  $\text{ZrO}_2$  nanoparticles from ZrOPc/KB with different loadings: **a** 5 wt.%; **b** 10 wt.%; **c** 15 wt.% and **d** particle size distribution plot of the samples shown here

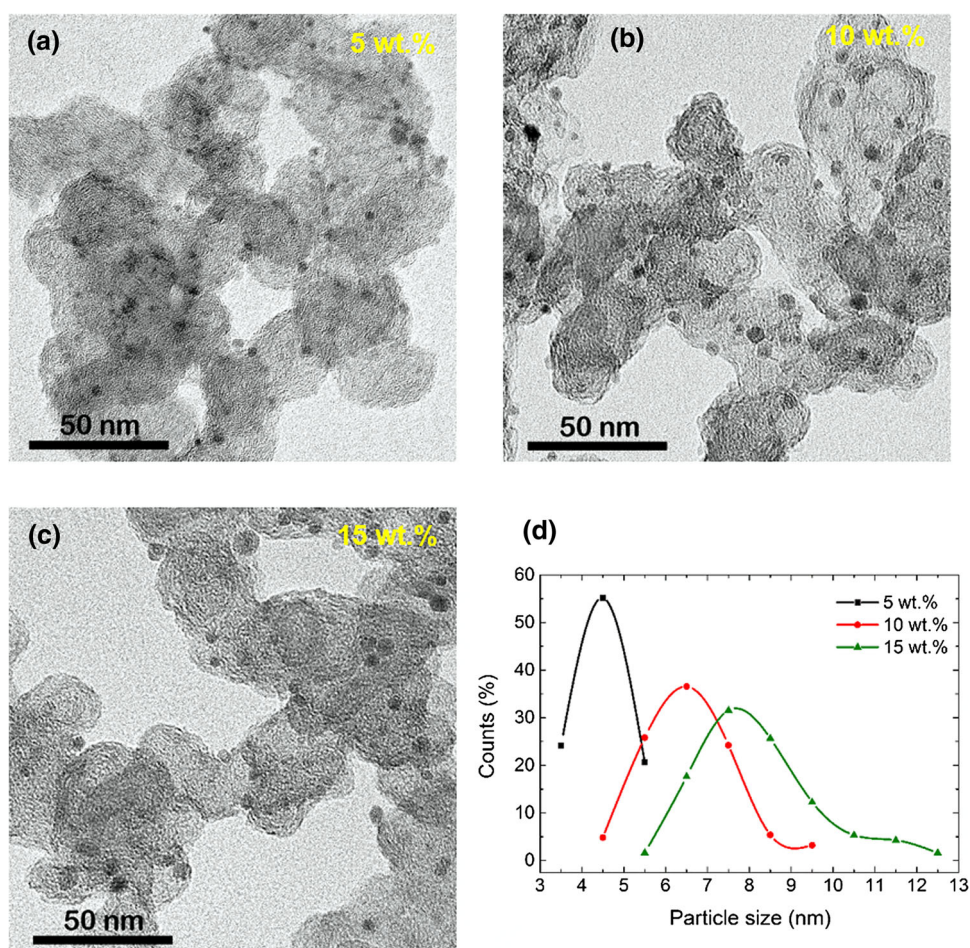


**Table 2** Crystallite size based on Scherrer equation ( $k = 0.94$ ) ( $D_{\text{Scherrer}}$ ), average particle size ( $D_{\text{average}}$ ) analysis with standard deviation (SD), and Sauter's diameter ( $D_{\text{Sauter}}$ ) with standard deviation for Sauter's diameter ( $SD_{\text{Sauter}}$ ) from particle size analysis

Sample (wt.%)	$D_{\text{Scherrer}}$ (nm)	$D_{\text{average}} \pm \text{SD}$ (nm)	$D_{\text{Sauter}} \pm \text{SD}_{\text{Sauter}}$ (nm)	AID $\pm \text{SD}_{\text{AID}}$ (nm)
5	4.5	$5 \pm 1$	$5 \pm 1$	$79 \pm 25$
10	5.5	$7 \pm 1$	$7 \pm 1$	$88 \pm 20$
15	8.5	$8.5 \pm 2$	$9 \pm 2$	$93 \pm 36$

chosen precursors. A clear correlation between the results from thermal analysis of precursors and the size- and structure of the nanoparticles obtained after heat-treatment at different temperatures was clearly seen. We showed that  $\text{ZrO}_2$  formation happens at a lower temperature with  $\text{Zr}(\text{acac})_4$  than with ZrOPc, due to the lower thermal stability of acetylacetonate precursor and a higher content of oxygen in comparison to phthalocyanine. With ZrOPc at heat-treatment temperatures  $\geq 900$  °C, PO conditions facilitate crystallite growth and formation of distinct t- $\text{ZrO}_2$ , but with  $\text{Zr}(\text{acac})_4$  a distinct t- $\text{ZrO}_2$  phase

of TEM images of ZrOPc/KB samples with varied loadings, but heat-treated at same conditions. Average inter-particle distance (AID) with standard deviation ( $SD_{\text{AID}}$ ) from Eq. 4

formation is observed already at temperatures  $\geq 750$  °C in both PO and RED conditions, due to the presence of a stoichiometrical excess of oxygen already in the precursor. The oxide nanoparticles in all the samples are well-distributed on the carbon support without evident agglomeration. After the size- and structural- analysis of the oxide nanoparticles, it is concluded that the oxide nanoparticles are nanocrystals and the amorphous phase is negligible in samples heat-treated at temperatures  $\geq 750$  °C. From the loading variation of zirconium, we show that metal loading can also be used to tune the size of oxide nanocrystals.



**Fig. 16** High resolution XPS spectra of Zr 3d core level of carbon supported ZrOPc and Zr(acac)<sub>4</sub> heat-treated at different temperatures in PO and RED gas conditions. The shaded bands highlight the binding energies variability of the samples

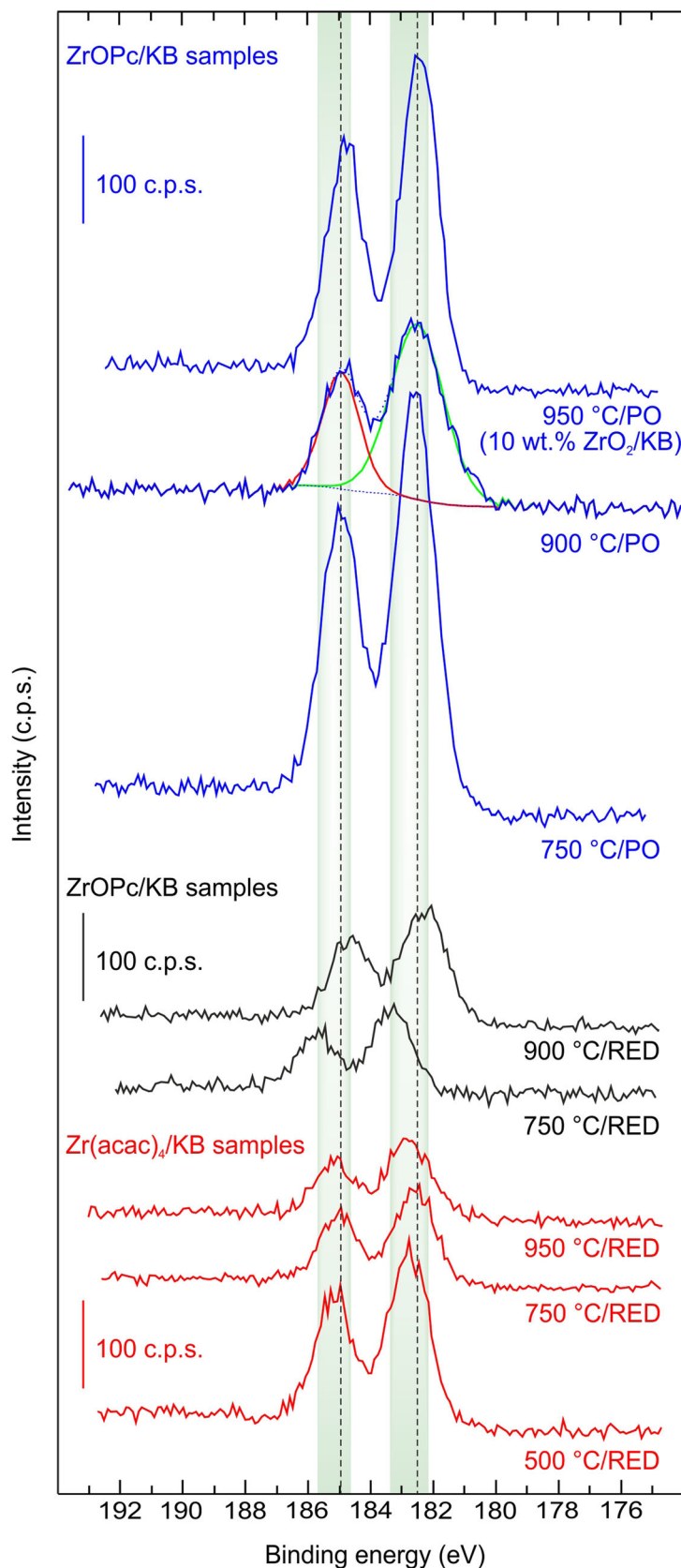
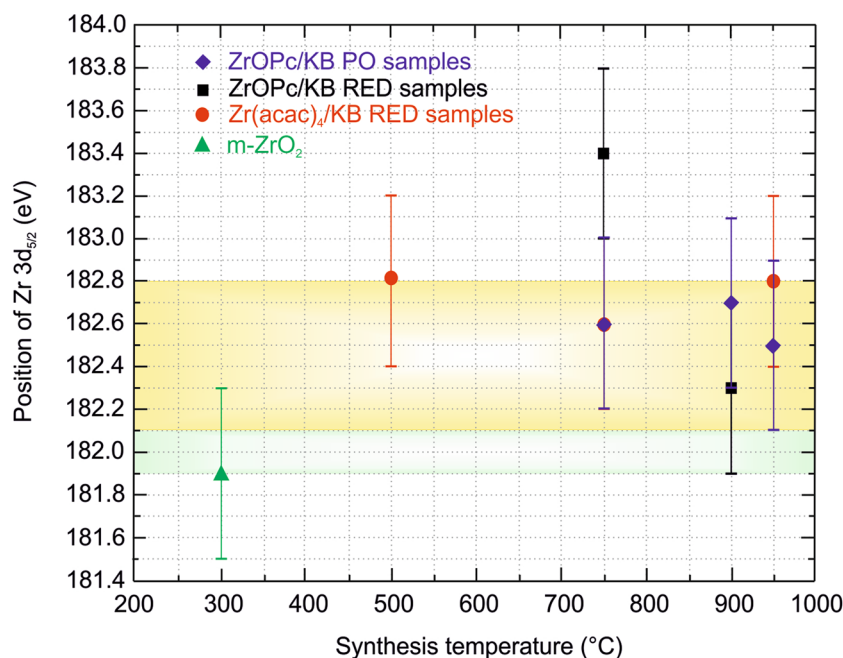


**Fig. 17** Binding-energy shift of the Zr 3d<sub>5/2</sub> peak of heat-treated samples as a function of the synthesis temperature and gas conditions, together with the measured value of the commercial m-ZrO<sub>2</sub>. The ranges of binding energies from the literature for m-ZrO<sub>2</sub> [41–44] and t-ZrO<sub>2</sub> [40, 41, 44–47] are depicted by the shaded green and yellow bands, respectively



From XPS analysis, it is clear that Zr species in samples from different synthesis routes are in the pure ZrO<sub>2</sub> state. No clear trend between Zr 3d<sub>5/2</sub> binding energy and synthesis temperature or gas conditions was found.

**Acknowledgements** For these results we acknowledge for funding the Fuel Cells and Hydrogen Joint Undertaking under Grant Agreement Duramet no 278054 as part of the Seventh Framework Programme of the European Community for research, technological development and demonstration activities (FP7/2007–2013). The authors are thankful to Dr. Viktor Ya. Chernii from Institute of General and Inorganic Chemistry (Ukraine) for his scholarly support on ZrOPc synthesis and purification. In addition, we thank Dr. Marianne Hanzlik for the superb TEM images. Sincere thanks to Dr. Hans Beyer and Michael Metzger for their assistance in TGA and MS, respectively. Dr. Salvatore Guastella is greatly acknowledged for XPS measurements.

**Open Access** This article is distributed under the terms of the Creative Commons Attribution 4.0 International License (<http://creativecommons.org/licenses/by/4.0/>), which permits unrestricted use, distribution, and reproduction in any medium, provided you give appropriate credit to the original author(s) and the source, provide a link to the Creative Commons license, and indicate if changes were made.

## References

- Earnshaw, A., Greenwood, N.: Chemistry of the elements, 2nd edn. Butterworth-Heinemann, Oxford (1998)
- Shukla, S., Seal, S.: Mechanisms of room temperature metastable tetragonal phase stabilisation in zirconia. *Int. Mater. Rev.* **50**, 45–64 (2005)
- French, R., Glass, S., Ohuchi, F., Xu, Y., Ching, W.: Experimental and theoretical determination of the electronic structure and optical properties of three phases of ZrO<sub>2</sub>. *Phys. Rev. B* **49**, 5133–5142 (1994)
- Minh, N.: Ceramic fuel cells. *J. Am. Ceram. Soc.* **76**, 563–588 (1993)
- Schulz, U., Leyens, C., Fritscher, K., Peters, M., Saruhan-Brings, B., Lavigne, O., Dorvaux, J.-M., Poulain, M., Mévrel, R., Caliez, M.: Some recent trends in research and technology of advanced thermal barrier coatings. *Aerosp. Sci. Technol.* **7**, 73–80 (2003)
- Kosmač T, Oblak Č, Jevnikar P, Funduk N, Marion L.: Strength and reliability of surface treated Y-TZP dental ceramics. *J. Biomed. Mater. Res.* **53**, 304–313 (2000)
- Guo, D., Qiu, X., Zhu, W., Chen, L.: Synthesis of sulfated ZrO<sub>2</sub>/MWCNT composites as new supports of Pt catalysts for direct methanol fuel cell application. *Appl. Catal. B* **89**, 597–601 (2009)
- Ly, H., Cheng, N., Peng, T., Pan, M., Mu, S.: High stability platinum electrocatalysts with zirconia–carbon hybrid supports. *J. Mater. Chem.* **22**, 1135–1141 (2012)
- Qu, W., Wang, Z., Sui, X., Gu, D., Yin, G.: ZrC-C and ZrO<sub>2</sub>-C as novel supports of Pd catalysts for formic acid electrooxidation. *Fuel Cells* **13**, 149–157 (2013)
- Malolepszy, A., Mazurkiewicz, M., Stobinski, L., Lesiak, B., Kövér, L., Tóth, J., Mierzwa, B., Borodzinski, A., Nitz, F., Wägberg, T.: Deactivation resistant Pd–ZrO<sub>2</sub> supported on multiwall carbon nanotubes catalyst for direct formic acid fuel cells. *Int. J. Hydrog. Energy* **40**, 16724–16733 (2015)
- Rutkowska, I., Kulesza, P.: Electrochemical oxidation of ethanol in acid medium: enhancement of activity of vulcan-supported platinum-based nanoparticles upon immobilization within nanostructured zirconia matrices. *Funct. Mater. Lett.* **7**, 1440005 (2014)
- Cheng-Lan, L., Yu-Chi, Y.: Platinum nanoparticles supported on zirconia–carbon black nanocomposites for methanol oxidation reaction. *Res. Chem. Intermed.* **40**, 2207–2215 (2014)
- Wang, R., Wang, K., Wang, H., Wang, Q., Key, J., Linkov, V., Ji, S.: Nitrogen-doped carbon coated ZrO<sub>2</sub> as a support for Pt nanoparticles in the oxygen reduction reaction. *Int. J. Hydrog. Energy* **38**, 5783–5788 (2013)
- Seo, J., Cha, D., Takanabe, K., Kubota, J., Domen, K.: Electrodeposited ultrafine NbOx ZrOx and TaOx nanoparticles on carbon black supports for oxygen reduction electrocatalysts in acidic media. *ACS Catal.* **3**, 2181–2189 (2013)





15. Sebastián, D., Baglio, V., Sun, S., Tavares, A., Aricò, A.: Facile synthesis of Zr- and Ta-based catalysts for the oxygen reduction reaction. *Chin. J. Catal.* **36**, 484–489 (2015)
16. Liu, Y., Ishihara, A., Mitsushima, S., Kamiya, N., Ota, K.: Zirconium oxide for PEFC cathodes. *Electrochem. Solid-State Lett.* **8**, A400–A402 (2005)
17. Ohgi, Y., Ishihara, A., Matsuzawa, K., Mitsushima, S., Ota, K.: Zirconium oxide-based compound as new cathode without platinum group metals for PEFC. *J. Electrochem. Soc.* **157**, B885–B891 (2010)
18. Shao, M.: *Electrocatalysis in fuel cells: A non- and low- platinum approach*. Springer, London (2013)
19. Yin, S., Ishihara, A., Kohno, Y., Matsuzawa, K., Mitsushima, S., Ota, K.: Preparation of highly active Zr Oxide-based oxygen reduction electrocatalysts as PEFC cathode. *ECS Trans.* **50**, 1785–1790 (2013)
20. Yin, S., Ishihara, A., Kohno, Y., Matsuzawa, K., Mitsushima, S., Ota, K.: Enhancement of oxygen reduction activity of zirconium oxide-based cathode for PEFC. *ECS Trans.* **58**, 1489–1494 (2013)
21. Okada, Y., Ishihara, A., Arao, M., Matsumoto, M., Imai, H., Kohno, Y., Matsuzawa, K., Mitsushima, S., Ota, K.: Improvement of the electrocatalytic activity of zirconium oxide-based catalyst for ORR. *ECS Trans.* **64**, 231–238 (2014)
22. Mecheri, B., Iannaci, A., D'Epifanio, A., Mauri, A., Licocchia, S.: Carbon-supported zirconium oxide as a cathode for microbial fuel cell applications. *ChemPlusChem* **81**, 80–85 (2016)
23. Lee, S., Zhang, Z., Wang, X., Pfefferle, L., Haller, G.: Characterization of multi-walled carbon nanotubes catalyst supports by point of zero charge. *Catal. Today* **164**, 68–73 (2011)
24. Leznoff, C., Lever, A.: *Phthalocyanines: properties and applications*. Wiley, New York (1989)
25. Sary, J., Liljenzin, J.: Critical evaluation of equilibrium constants involving acetylacetone and its metal chelates. *Pure Appl. Chem.* **54**, 2557–2592 (1982)
26. Mittermeier, T., Madkikar, P., Wang, X., Gasteiger, H., Piana, M.: ZrO<sub>2</sub> based oxygen reduction catalysts for PEMFCs: towards a better understanding. *J. Electrochem. Soc.* **163**, F1543–F1552 (2016)
27. Tomachynski, L., Chernii, V., Volkov, S.: Synthesis of dichloro phthalocyaninato complexes of titanium, zirconium, and hafnium. *Russ. J. Inorg. Chem.* **47**, 208–211 (2002)
28. Catanorchi S., Piana M.: High performance ORR (oxygen reduction reaction) pgm (pt group metal) free catalyst. Google Patents. <http://www.google.com.ar/patents/US20110034325> (2011). Accessed 17 April 2015
29. Liu, G., Li, X., Ganesan, P., Popov, B.: Studies of oxygen reduction reaction active sites and stability of nitrogen-modified carbon composite catalysts for PEM fuel cells. *Electrochim. Acta* **55**, 2853–2858 (2010)
30. National Institute of Standards and Technology. Benzonitrile. <http://webbook.nist.gov/cgi/cbook.cgi?ID=C100470&Units=SI&Mask=200#Mass-Spec>. Accessed 03 Mar 2015
31. Cornu, A., Massot, R.: *Compilation of mass spectral data/Index de Spectres de Masse*. Heyden & Sons, London (1966)
32. National Institute of Standards and Technology. Acetylacetone. <http://webbook.nist.gov/cgi/cbook.cgi?ID=C123546&Mask=200#Mass-Spec>. Accessed 17 April 2015
33. National Institute of Standards and Technology. Acetic acid. <http://webbook.nist.gov/cgi/cbook.cgi?ID=C64197&Mask=200#Mass-Spec>. Accessed 17 April 2015
34. National Institute of Standards and Technology. Acetone. <http://webbook.nist.gov/cgi/cbook.cgi?ID=67-64-1&Units=SI&CMS=on>. Accessed 17 April 2015
35. National Institute of Standards and Technology. Carbon dioxide. <http://webbook.nist.gov/cgi/cbook.cgi?ID=C124389&Units=SI&Mask=200#Mass-Spec>. Accessed 17 April 2015
36. National Institute of Standards and Technology. Methane. <http://webbook.nist.gov/cgi/cbook.cgi?Formula=CH4&NoIon=on&Units=SI&CMS=on>. Accessed 17 April 2015
37. Jasim, F.: Simultaneous thermal analysis of zirconium(IV) acetylacetonate in a helium atmosphere. *J. Therm. Anal.* **37**, 149–153 (1991)
38. Meier, J., Galeano, C., Katsounaros, I., Witte, J., Bongard, H., Topalov, A., Baldizzone, C., Mezzavilla, S., Schüth, F., Mayrhofer, K.: Design criteria for stable Pt/C fuel cell catalysts. *Beilstein J. Nanotechnol.* **5**, 44–67 (2014)
39. Meini, S., Piana, M., Beyer, H., Schwämmlein, J., Gasteiger, H.: Effect of carbon surface area on first discharge capacity of Li-O<sub>2</sub> cathodes and cycle-life behavior in ether-based electrolytes. *J. Electrochem. Soc.* **159**, A2135–A2142 (2012)
40. Ram, S., Mondal, A.: X-ray photoelectron spectroscopic studies of Al<sub>3</sub> + stabilized t-ZrO<sub>2</sub> of nanoparticles. *Appl. Surf. Sci.* **221**, 237–247 (2004)
41. Basahel, S., Ali, T., Mokhtar, M., Narasimharao, K.: Influence of crystal structure of nanosized ZrO<sub>2</sub> on photocatalytic degradation of methyl orange. *Nanoscale Res. Lett.* **10**, 1–13 (2015)
42. Majumdar, D., Chatterjee, D.: X-ray photoelectron spectroscopic studies on yttria, zirconia, and yttria-stabilized zirconia. *J. Appl. Phys.* **70**, 988–992 (1991)
43. Guittet, M., Crocombette, J., Gautier-Soyer, M.: Bonding and XPS chemical shifts in ZrSiO<sub>4</sub> versus SiO<sub>2</sub> and ZrO<sub>2</sub>: charge transfer and electrostatic effects. *Phys. Rev. B* **63**, 125117 (2001)
44. Kuratani, K., Uemura, M., Mizuhata, M., Kajinami, A., Deki, S.: Novel fabrication of high-quality ZrO<sub>2</sub> ceramic thin films from aqueous solution. *J. Am. Ceram. Soc.* **88**, 2923–2927 (2005)
45. Ardizzone, S., Bianchi, C.: XPS characterization of sulphated zirconia catalysts: the role of iron. *Surf. Interface Anal.* **30**, 77–80 (2000)
46. Alvarez, M., López, T., Odriozola, J., Centeno, M., Domínguez, M., Montes, M., Quintana, P., Aguilar, D., González, R.: 2,4-Dichlorophenoxyacetic acid (2,4-D) photodegradation using an Mn +/ZrO<sub>2</sub> photocatalyst: XPS, UV-vis, XRD characterization. *Appl. Catal. B* **73**, 34–41 (2007)
47. Brenier, R., Mugnier, J., Mirica, E.: XPS study of amorphous zirconium oxide films prepared by sol-gel. *Appl. Surf. Sci.* **143**, 85–91 (1999)



## Supplementary information

Synthesis optimization of carbon supported ZrO<sub>2</sub> nanoparticles from different organometallic precursors

Pankaj Madkikar<sup>a\*</sup>, Xiaodong Wang<sup>b</sup>, Thomas Mittermeier<sup>a</sup>, Alessandro H.A. Monteverde Videla<sup>c</sup>, Christoph Denk<sup>a</sup>, Stefania Specchia<sup>c</sup>, Hubert A. Gasteiger<sup>a</sup>, Michele Piana<sup>a</sup>

<sup>a</sup>Chair of Technical Electrochemistry, Department of Chemistry and Catalysis Research Center, Technische Universität München, D-85748 Garching, Germany

<sup>b</sup>Johnson Matthey Catalysts (Germany) GmbH, Bahnhofstr. 43 + 96257 Redwitz, Germany

<sup>c</sup>Politecnico di Torino, Department of Applied Science and Technology, Corso Duca degli Abruzzi 24, 10129 Torino, Italy

---

\*[pankaj.madkikar@tum.de](mailto:pankaj.madkikar@tum.de) / +498928913835



## Structural characterization of synthesized ZrOPc

### ○ *Elemental analysis of ZrOPc*

**CHN-analyses was done on a Hekatech EURO EA analyzer which is based on dynamic flash combustion technique. Zr content was analyzed by photometric method on Shimadzu UV-160 photometer.** Elemental analysis reveals that the elements contained in the product are close to the theoretical values of ZrOPc (Table 1). The deviation from the theoretical values is likely because of phthalocyanine sublimation due to its high thermal stability, causing systematic errors in its analysis and because of unreacted starting impurities which were also confirmed in the FTIR and proton NMR spectroscopy [1].

**Table S1:** CHN (by combustion) and Zr (by photometry) analysis on synthesized ZrOPc.

$C_{32}H_{16}N_8OZr$	Theoretical	Experimental
C	62.0	$58.6 \pm 0.3$
H	2.6	$2.6 \pm 0.3$
N	18.1	$16.0 \pm 0.3$
O	2.6	---
Zr	14.7	$13.0 \pm 0.6$

### ○ *UV-Vis spectroscopy*

**UV-Vis spectroscopy was performed on PerkinElmer LAMBDA 35 UV-Vis spectrophotometer. Concentrated sulphuric acid ( $H_2SO_4$ ) (96% Ultrapur) was used as the solvent in analysis of ZrOPc.** We observed strong absorption bands centered at 308 and 809 nm, attributable to electronic transitions of the inner pyrrole ring in the phthalocyanine (Pc) macrocycle (Fig. S1). The band at 308 nm (B or Soret band –  $a_{2u} \rightarrow e_g$ ) is due to the increase of electronic density at the bridging atoms of azamethine group, whereas the band at 809 nm (Q band –  $a_{1u} \rightarrow e_g$ ) originates from the electronic

charge transfer from pyrrole to benzene functional group [2]. **The peak at 719 nm is the splitted component of Q band [3, 4]. Peak at 445 nm is possibly because of the symmetry of Pc complex [5].** The recorded spectra are in agreement with the results by Tomachynski et al. [6].

**Fig. S1** UV-Vis absorption spectra of ZrOPc in concentrated H<sub>2</sub>SO<sub>4</sub>

○ *NMR spectroscopy*

**Proton (<sup>1</sup>H) NMR spectra of ZrOPc was recorded in CDCl<sub>3</sub> solution with a *Bruker AV500 (500 MHz) spectrometer. MestReNova software was used in post-run analysis of data files including background correction, solvent referencing, and phase correction.*** Two predominant sets of protons are detected in <sup>1</sup>H NMR analysis. Their chemical shifts are in the region of 9.35-9.15 ppm and 8.25-8.05 ppm, consistently with the literature values for the Pc protons at H<sup>1,4</sup> and H<sup>2,3</sup>, respectively (Fig. S2) [7].

**Fig. S2** <sup>1</sup>H NMR spectra of ZrOPc (H<sup>1,4</sup> and H<sup>2,3</sup>) and un-reacted C<sub>6</sub>H<sub>4</sub>(CN)<sub>2</sub> (red asterisk) in CDCl<sub>3</sub>

Proton signals at 7.8 ppm and 7.7 ppm (marked by red asterisk) are assignable to un-reacted 1,2 dicyanobenzene (C<sub>6</sub>H<sub>4</sub>(CN)<sub>2</sub>) [8].

○ *FTIR spectroscopy*

**Fourier transform infrared (FTIR) spectroscopy was used for identification of characteristic vibrational frequencies in ZrOPc. *PerkinElmer Spectrum Two* FTIR spectrometer with ATR mode was used here. Sample was pressed on the ATR-crystal by a mini-hand press prior to measurement.** The fingerprint region of the synthesized complex is shown in Fig. S3. The band appearing at 1331 cm<sup>-1</sup> can be assigned to C–C symmetric stretching of isoindole. Another band at 1286 cm<sup>-1</sup> is due to C–N *asymmetric* stretching vibrations in isoindole. The absorption band at 1071 cm<sup>-1</sup> originates from C–N *asymmetric* stretching vibration in pyrrole. The absorption band at 891 and 729 cm<sup>-1</sup> is related to C–H bending out of plane deformation. These typical

absorption bands fit very well to the characteristic bands of Pc macrocycle [9]. In addition, band at  $1161\text{ cm}^{-1}$  fits to C-N in plane stretching,  $1116\text{ cm}^{-1}$  corresponds to C-H bending in plane deformation,  $778\text{ cm}^{-1}$  is due to C-N stretching vibration. Band at  $631\text{ cm}^{-1}$  corresponds to C-C macrocycle ring deformation. Besides, Zr coordination in the Pc ring is confirmed by the absence of the very strong absorption band at  $1006\text{ cm}^{-1}$  originating from the N-H bending vibration in metal-free Pc compounds as reported by Seoudi et al [9].

**Fig. S3** IR absorption spectra of ZrOPc (fingerprint region)

No distinct dicyanobenzene peaks were identified due to low concentration.

In this supplementary information we would like to conclude that elemental analysis, UV-Vis,  $^1\text{H-NMR}$ , and FTIR spectroscopies confirm the successful synthesis of ZrOPc.

○ *X-ray diffractograms of ZrOPc and Zr(acac)<sub>4</sub> residue*

ZrO<sub>2</sub> is clearly seen in the XRDs of ZrOPc and Zr(acac)<sub>4</sub> residue which remains after TGA in pure Ar (Fig. S4).

**Fig. S4** XRDs of ZrOPc and Zr(acac)<sub>4</sub> residue after TGA in pure Ar

#### References

1. Cook M and Chambrier I.: Phthalocyanine Thin Films: Deposition and Structural Studies. In: The Porphyrin Handbook: Elsevier, (2003)
2. Mack J and Stillman M.: Electronic Structures of Metal Phthalocyanine and Porphyrin Complexes from Analysis of the UV-Visible Absorption and Magnetic Circular Dichroism Spectra and Molecular Orbital Calculations. In: The Porphyrin Handbook: Elsevier, (2003)
3. Mack J and Stillman M.: Band Deconvolution Analysis of the Absorption and Magnetic Circular Dichroism Spectral Data of ZnPc(-2) Recorded at Cryogenic Temperatures. J. Phys. Chem. **99**, 7935–7945 (1995)
4. Gerasymchuk Y, Chernii V, Tomachynski L, Legendziewicz J, St. Radzki.: Spectroscopic characterization of zirconium(IV) and hafnium(IV) gallate phthalocyanines in monolithic silica gels obtained by sol-gel method. Opt. Mater **27**, 1484–1494 (2005)
5. Edwards L and Gouterman M.: Porphyrins. J. Mol. Spectrosc. **33**, 292–310 (1970)

6. Tomachynski L, Chernii V, Volkov S.: Synthesis of dichloro phthalocyaninato complexes of titanium, zirconium, and hafnium. *Russ. J. Inorg. Chem.* **47**, 208-211 (2002)
7. Guillard R, Dormond A, Belkalem M, Anderson J, Liu Y, Kadish K.: First example of 1:1 actinide-phthalocyanine complexes: synthesis, electrochemical, and spectral characterization of bis(diketonato)thorium(IV) and -uranium(IV) phthalocyaninates. *Inorg. Chem.* **26**, 1410–1414 (1987)
8. Laulhé S, Gori S, Nantz M.: A chemoselective, one-pot transformation of aldehydes to nitriles. *J. Org. Chem.* **77**, 9334–9337 (2012)
9. Seoudi R, El-Bahy G, El Sayed Z.: FTIR, TGA and DC electrical conductivity studies of phthalocyanine and its complexes. *J. Mol. Struct.* **753**, 119–126 (2005)

### 3.2. ZrO<sub>2</sub> Based Oxygen Reduction Catalysts for PEMFCs: Towards a Better Understanding

T. Mittermeier, P. Madkikar, X. Wang, H. A. Gasteiger, and M. Piana

Journal of The Electrochemical Society 2016, Volume 163, Issue 14, Pages F1543 - F1552

Permanent weblink: <http://dx.doi.org/10.1149/2.0901614jes>

This is an open access article distributed under the terms of the Creative Commons Attribution Non-Commercial No Derivatives 4.0 License (CC BY-NC-ND, <http://creativecommons.org/licenses/by-nc-nd/4.0/>), which permits non-commercial reuse, distribution, and reproduction in any medium, provided the original work is not changed in any way and is properly cited. For permission for commercial reuse, please email: [oa@electrochem.org](mailto:oa@electrochem.org).

This chapter comprises of a detailed electrochemical characterisation of carbon supported ZrO<sub>2</sub> nanoparticles synthesised by different precursors as mentioned in the previous chapter. This electrochemical screening was of utmost importance, since it was necessary to investigate the possible descriptors towards high ORR activity. Three potential sources for high ORR activity were proposed:

- Zr and N together (ZrOPc/KB)
- Zr and N separate (Zr(acac)<sub>4</sub> + Melamine)/KB)
- Zr only (Zr(acac)<sub>4</sub>/KB)

The first two mainly focus on the concurrent presence of Zr and N during heat-treatment of the samples. It is already reported that N could possibly dope the ZrO<sub>2</sub> structure, forming oxygen vacancies [123], which are possibly ORR active [27]. The third descriptor focuses on the ORR active sites which can be formed without the presence of N, e.g., specific oxide phases, nanoparticle size, etc.

### 3. Noble-Metal-Free Electrocatalysts

Screening of the samples was first done by thin-film RDE measurements, from which a dependence of the ORR activity on the used precursors and the heat-treatment conditions was established. The sample with the highest catalytic activity (ZrOPc/KB 1000 PO) was subjected to Tafel analysis and apparent activation energy determination. A mechanistic study is conducted via R(R)DE voltammetry which is performed in both acidic (0.1 M HClO<sub>4</sub>) and alkaline (0.1 M NaOH) electrolyte. The catalyst is also tested in a single-cell PEMFC configuration. Both Tafel analysis and apparent activation energy determined from the PEMFC data are correlated with that from the RDE measurements. A comparison of the ORR mass activities of ZrOPc/KB 1000 PO with the state-of-the-art ZrO<sub>2</sub> catalysts and with the 2017 DOE target was done.

It is unambiguously shown that one requirement for increasing ORR activity of the catalysts is to have both Zr and N species present simultaneously during heat treatment, while presence of only Zr yields samples with negligible catalytic activity. It is also seen that a very small amount of N (0.2 – 1.5 wt%) is enough to develop measurable ORR activity in ZrO<sub>2</sub> based catalysts. The mechanistic study reveals that the ORR in acid electrolyte presumably runs through a 2e<sup>-</sup> reduction to H<sub>2</sub>O<sub>2</sub>, while in alkaline electrolyte the ORR seems to go through a 4e<sup>-</sup> reduction at high potentials. Tafel slopes from RDE and PEMFC measurements are quite consistent (≈200 mV/decade), with a cathodic ORR transfer coefficient of  $\alpha = 0.3 - 0.4$ . After evaluating the activation energy from RDE (5 – 60 °C) and PEMFC (40 – 120 °C) data, it is confirmed that the measured activation energies are clearly too low to meet the DOE target. When extrapolated to 0.8 V<sub>RHE</sub>, ZrOPc/KB 1000 PO exhibits values of ≈0.04 A/g<sub>cat</sub>, translating into ≈0.04 A/cm<sup>3</sup><sub>cat</sub>. This is an ≈1 order of magnitude lower mass activity than the highest value reported in the literature (≈0.4 A/g<sub>cat</sub>) and almost four orders of magnitude lower than the DOE target for PGM-free catalysts (300 A/cm<sup>3</sup><sub>cat</sub>). The reason for the low activity of our catalysts could be due to the fact that they were not synthesised in a similar way as done by Ota et al., who obtained the ZrO<sub>2</sub> based materials with the highest reported ORR activities. However, it seems probable that this ≈10× higher mass activity reported by Ota et al. is due to Fe impurities, which could possibly form the well-known Fe-N-C centres that are ORR active [124, 125]. This hypothesis is based on the conditions used in the synthesis approach reported by Ishihara et al., where multi-wall carbon nanotubes (MWCNTs) are used (known to have some Fe remnants) and are heat-treated in NH<sub>3</sub> atmosphere between 700 – 900 °C, favouring formation of Fe-N-C centres [125].

### **Author contributions**

P. M., X. W., and C. D. performed the syntheses and the structural/morphological characterisation with support of M. P. (for details, see Madkikar et al. [126]). T. M. performed the electrochemical measurements and analyses. T. M. and H. A. G. interpreted the PEMFC activation energy data and wrote the manuscript. All authors discussed the results and commented on the manuscript.

### 3. *Noble-Metal-Free Electrocatalysts*

This page is left intentionally blank.





# ZrO<sub>2</sub> Based Oxygen Reduction Catalysts for PEMFCs: Towards a Better Understanding

T. Mittermeier,<sup>\*,z</sup> P. Madkikar,<sup>\*</sup> X. Wang, H. A. Gasteiger,<sup>\*\*</sup> and M. Piana<sup>\*\*\*</sup>

Chair of Technical Electrochemistry, Department of Chemistry and Catalysis Research Center, Technische Universität München, Munich, Germany

The oxygen reduction reaction (ORR) activity of ZrO<sub>2</sub> based, carbon-supported nanoparticles is not conclusively reported in literature. This study examines the dependence of the ORR activity on the used precursors as well as on the heat-treatment atmosphere and temperature. We further determine the ORR activation energy and the ORR mechanism. Various precursors containing Zr and/or N were employed in the synthesis, and the ORR activity was measured by rotating (ring) disk electrode (R(R)DE) voltammetry in both acidic and alkaline electrolyte as well as by measurements in a single-cell polymer electrolyte membrane fuel cell (PEMFC) configuration. We show that even the most active ZrO<sub>2</sub> based ORR catalysts exhibit an activity gap of ca. two orders of magnitude compared to the DOE target of 300 A/cm<sup>2</sup> for PGM-free ORR catalysts, thus requiring further development. Our RRDE analysis suggests a primarily 2-electron ORR mechanism in the case of the tested catalysts in acid, which in turn provides a consistent temperature dependence between RDE and PEMFC experiments, allowing also for a mechanistic (re-) interpretation of experimental results in the literature.

© The Author(s) 2016. Published by ECS. This is an open access article distributed under the terms of the Creative Commons Attribution Non-Commercial No Derivatives 4.0 License (CC BY-NC-ND, <http://creativecommons.org/licenses/by-nc-nd/4.0/>), which permits non-commercial reuse, distribution, and reproduction in any medium, provided the original work is not changed in any way and is properly cited. For permission for commercial reuse, please email: [oa@electrochem.org](mailto:oa@electrochem.org). [DOI: 10.1149/2.0901614jes] All rights reserved.



Manuscript submitted August 8, 2016; revised manuscript received October 12, 2016. Published November 15, 2016.

Catalysts based on nitrogen and carbon-coordinated 3d transition metals (mostly Fe and Co), commonly referred to as TM-N-Cs, have been in the focus of research in PGM-free electrocatalysis for the oxygen reduction reaction (ORR) over the past decades. Without further distinction, their promises and drawbacks are that they offer reasonable activities, but that they generally lack long-term stability in the acidic environment of a proton exchange membrane fuel cell (PEMFC).<sup>1</sup> In an approach to improve the stability of non-noble-metal ORR electrocatalysts, valve-metal oxide based analogues that exhibit high stability against chemical dissolution in acidic environment have been explored<sup>2-7</sup> mostly by Ota and co-workers, who studied the ORR activity of sputtered oxides based on Nb, Ta, Ti and Zr.<sup>8-10</sup> with Zr based oxides exhibiting the highest ORR activity so far. Surprisingly, beyond their work, only very few studies on this class of catalysts have been published,<sup>11-13</sup> although a benefit of this class of materials was found in their robustness against methanol poisoning.<sup>11,13</sup> Ota and co-workers also investigated the ORR activity of micrometric Ta and Zr oxides produced by heat-treatment of carbides,<sup>11,14</sup> nitrides,<sup>14</sup> or carbonitrides,<sup>6,10,15,16</sup> concluding that the formation of understoichiometric or defective oxides (i.e., of oxygen vacancies) would enhance their ORR activity, which was based on the observation that partial reduction of the formed oxides lead to improved ORR activity.<sup>15,16</sup> The same group also applied surface sensitive X-Ray absorption spectroscopy, which suggested a correlation between ORR activity and defect-induced strain of the Ta<sub>2</sub>O<sub>5</sub> oxide layer formed on top of a μm-sized TaCN core upon high-temperature oxidation.<sup>10</sup>

In order to increase the very low catalyst dispersion (i.e., the electrochemically active surface area per gram of catalyst) obtained with the above synthesis approaches, methods to synthesize highly dispersed Zr oxide nanoparticles supported on carbon black were investigated.<sup>12,17-19</sup> For these materials, the ORR activity was correlated with synthesis-specific parameters, such as temperature, gas composition, and heat-treatment time during synthesis,<sup>4,5,9,20-23</sup> but a systematic quantitative comparison of the effect of the synthesis conditions on the ORR activity has not yet been conducted and is subject of the present work.

This study focuses on the ORR activity of ZrO<sub>2</sub> nanoparticles supported on Ketjenblack (ZrO<sub>2</sub>/KB) that are produced from two different

organo-metallic precursors via heat-treatment at different temperatures in various gas atmospheres. The interplay of Zr, N and C species are thus investigated vs. the applied heat-treatment procedure in order to facilitate a direct comparison of catalysts produced from different precursors and under various synthesis conditions. Additionally, comparative measurements of the ORR activity in alkaline electrolyte and in a PEMFC configuration allow for further mechanistic insights into the ORR mechanism.

## Experimental

**Synthesis of materials.**—The detailed synthesis procedures and in-depth morphological characterization of the ZrO<sub>x</sub>/C based ORR catalysts tested in this study can be found in a forthcoming publication from our group.<sup>24</sup> In short, catalysts were produced by wet impregnation of Ketjenblack (KB) with one of the following precursors: i) zirconium oxyphthalocyanine (ZrOPc); ii) hydrogen phthalocyanine (H<sub>2</sub>Pc); iii) zirconium acetylacetonate (Zr(acac)<sub>4</sub>); or, iv) Zr(acac)<sub>4</sub> together with melamine (Zr(acac)+Mel). Subsequently, different heat treatments under controlled temperature and gas atmosphere were conducted in a conventional tubular furnace (HTM Reetz, Germany), as outlined in the following.

**ZrOPc/KB and H<sub>2</sub>Pc/KB.**—After impregnation of the carbon with the respective precursor, either one of the following heat-treatment procedures were applied. i) Reductive heat-treatment (further on referred to as RED): ≈ 300 mg of the precursor were put into an alumina crucible, heated to the desired heat-treatment temperature under a flow of 5% H<sub>2</sub> in Ar (flow rate of 1.0 slpm), and held there for 2 h. ii) Partial oxidation (further on referred to as PO): after procedure i), an additional treatment at the same temperature was applied under a flow of 2.5% H<sub>2</sub> + 0.5% O<sub>2</sub> in an Ar/N<sub>2</sub> background (flow rate of 2.1 slpm) for another 1 h. Both procedures were followed by cooling the sample to room temperature under a flow of 5% H<sub>2</sub> in Ar (flow rate of 1.0 slpm).

**Zr(acac)<sub>4</sub>/KB and (Zr(acac)<sub>4</sub>+Mel)/KB.**—After impregnation of the carbon with the respective precursor, either one of the following procedures was applied. i) Reductive heat-treatment as described above for ZrOPc/KB and H<sub>2</sub>Pc/KB (identical with procedure i) above, but being held at nominal temperature for 1 h; further on labeled as RED). ii) Partial oxidation (further on referred to as PO): heating of the sample under 5% H<sub>2</sub> in Ar until the desired heat-treatment

\*Electrochemical Society Student Member.

\*\*Electrochemical Society Fellow.

\*\*\*Electrochemical Society Member.

<sup>z</sup>E-mail: [thomas.mittermeier@tum.de](mailto:thomas.mittermeier@tum.de)

temperature was reached and then immediate change of the gas atmosphere to 2.5% H<sub>2</sub> + 0.5% O<sub>2</sub> in Ar/N<sub>2</sub> background, where the samples were held for 1 h. As above, samples were subsequently cooled to room temperature under 5% H<sub>2</sub> in Ar flow.

Throughout this work, the thus synthesized catalysts are denominated by the precursor, the applied heat-treatment temperature, and the heat-treatment conditions. For example, ZrOPc/KB catalyst heat treated at 900°C in partially oxidizing gas atmosphere (PO) will be referred to as ZrOPc/KB 900 PO.

**Structural and morphological characterization.**—XRD measurements were performed using a Stadi MP diffractometer (STOE, Germany) equipped with a one dimensional silicon strip detector Mythen 1 K (Dectris, Switzerland). The diffractometer uses monochromatized Mo(K $\alpha$ 1) radiation ( $\lambda = 0.7093$  Å, 50 kV, 40 mA) in Debye–Scherrer geometry in a  $2\theta$  range from 2–50°. TEM micrographs were obtained with a JEM 2010 microscope (JEOL, Germany) with a tungsten cathode. The carbon, hydrogen, and nitrogen content of the samples were determined using a CHNS analyzer (EURO EA by Hekatech, Germany). The total zirconium content was evaluated by thermogravimetric analysis (TGA; TGA/DSC 1, Mettler-Toledo, Germany) from the residual sample weight after ramping the temperature to 1000°C under 67% O<sub>2</sub> in Ar atmosphere, considering that the only remaining species is ZrO<sub>2</sub>. For all catalysts heat treated between 750 and 1000°C, the so determined ZrO<sub>2</sub> equivalent loading on the KB support ranged between 12 and 18 wt%. Only the partially oxidized catalyst at the highest temperature of 1100°C (ZrOPc/KB 1100 PO) had a ZrO<sub>2</sub> loading of 26 wt%, due to the substantial loss of carbon, while catalysts treated at  $\leq 500^\circ\text{C}$  under reducing conditions exhibited loadings as low as 10 wt% ZrO<sub>2</sub> equivalent (ZrOPc/KB 350 RED and ZrOPc/KB 500 RED), due to large remaining fractions of the organometallic precursor. Further details are given in the forthcoming publication by Madkikar et al.<sup>24</sup>

**Electrochemical characterization.**—*Rotating (ring) disk electrode (R(R)DE) measurements.*—For the preparation of electrolytes and for the rinsing of components, 18.2 M $\Omega$ ·cm deionized water (Milli-Q Integral 5, Merck Millipore, Germany) was used. For measurements in acidic environment, a conventional two-compartment glass cell was assembled, with a heat jacket allowing for temperature control of the electrolyte via a thermostat (Model F12-ED, Julabo, Germany). 70% HClO<sub>4</sub> (double distilled, GFS Chemicals, USA) was diluted in water to 0.1 M concentration. An anodized 1 mm Ag wire (99.999%, Alfa Aesar; Germany) immersed in a solution saturated with both AgCl (99.999% trace metals, Sigma Aldrich, Germany) and KCl (Merck, Germany) served as reference electrode (RE). However, all potentials are reported on the reversible hydrogen electrode scale ( $V_{\text{RHE}}$ ), whereby the RE was calibrated vs. the RHE scale after every measurement by purging the electrolyte with H<sub>2</sub> and averaging the anodic and cathodic zero-current potential intercepts of the cyclic voltammogram of a Pt electrode. In order to avoid chloride contamination of the electrolyte, the RE was separated from the working electrode compartment: first, a Vycor 7930 glass frit separated the RE's saturated KCl solution from an electrolyte bridge filled with 0.1 M HClO<sub>4</sub>; second, another Vycor glass frit served as further barrier between the electrolyte bridge and the actual measurement electrolyte; third, the electrolyte bridge connected to a Luggin-Haber capillary reaching 1.0–1.5 cm below the working electrode. E6-series rotating-ring-disk electrode assemblies (Pine Research Instrumentation, USA) with interchangeable glassy carbon (GC) disk working electrodes (WEs) with 5.0 mm diameter were used. The ring electrode was made of either Au or Pt (6.5/7.5 mm inner/outer diameter) and remained unpolarized unless stated otherwise. No difference in ORR activity could be observed between measurements conducted with Pt-ring or Au-ring electrodes, confirming that no contamination of the PGM-free catalysts with Pt from the ring electrode took place. An Au mesh (6.3 cm<sup>2</sup>, 82 mesh, 99.99%, Advent Research Materials, UK) fused together with a 0.5 mm Au wire (99.999%, Alfa Aesar, Germany) served as a counter electrode (CE) and was separated by

a glass frit from the actual WE compartment. Electrolyte solutions were purged through a glass-frit-type bubbler with either Ar, O<sub>2</sub> or H<sub>2</sub> (grade 6.0, Westfalen, Germany). Each experiment was conducted at least two times and the depicted data points and error bars represent the mean value and standard deviation, respectively.

In order to perform RRDE voltammetry in alkaline electrolyte, a PTFE cell was used, utilizing an Au mesh CE and an Ag|AgCl|KCl RE. A detailed description of this experimental set-up, in which any contact between glass and the electrolyte is avoided in order to prevent electrolyte contamination, is given by Rheinländer et al.<sup>25</sup>

Preparation of the electrodes involved hand polishing of the disassembled GC disks with a 0.05  $\mu\text{m}$  finish with Al<sub>2</sub>O<sub>3</sub> suspension (Bühler, Germany), followed by 2  $\times$  3 min ultrasonic treatment in ultrapure water before re-assembly of the electrode holder. Thereafter, two further ultrasonication steps were conducted, followed by soaking periods in 5 M KOH (semiconductor grade, Sigma Aldrich, Germany), ultrapure water (2x), 2 M HClO<sub>4</sub>, and finally in ultrapure water (2x). Each soaking step was carried out over timespans of  $\geq 15$  min to assure a contaminant-free and reproducible GC substrate surface prior to each individual experiment. Catalyst inks for coating the glassy carbon WEs were prepared by mixing a defined amount of catalyst powder (6–10 mg) with a 3:7 v/v 2-propanol (Chromasolv, Sigma Aldrich, Germany) and water solution, followed by dispersing with an ultrasonic probe (S-250D, Branson, Germany) at a power output of 15% and a pulse time of 1.0/0.5 s on/off for 15 min, whereby the sample was immersed in ice-water. This was followed by the addition of Nafion solution (5% Nafion in lower aliphatic alcohols + H<sub>2</sub>O, Sigma Aldrich, Germany) and further sonication in an ultrasonic bath for 10 min. From the resulting ink, an aliquot of 10  $\mu\text{l}$  was pipetted onto the electrode substrate and then dried under a mild air stream, or under an IR lamp. Uniformity of the resulting catalyst layers was controlled using an optical microscope. All Zr containing catalysts had a loading of 8–9  $\mu\text{g}_{\text{Zr}}/\text{cm}^2$ , corresponding to total catalyst loadings between 0.05 and 0.12  $\text{mg}_{\text{Catalyst}}/\text{cm}^2$ , depending on the wt% ZrO<sub>2</sub> on the KB support. The KB loadings of the electrodes were kept within 0.04–0.07  $\text{mg}/\text{cm}^2$ , yielding thin electrodes (average thickness of  $\approx 1$ –2  $\mu\text{m}$ ) in order to minimize oxygen mass transport effects inside the electrode layer.

R(R)DE measurements were conducted either with a Autolab PGSTAT302N (Metrohm, Germany) equipped with an analog potential scan module, a frequency response analyzer, and a bipotentiostat module (acidic measurements) or with a CBP bipotentiostat (alkaline measurements; Pine Research Instrumentation, USA). In the latter case, an additional portable BioLogic SP-200 potentiostat (GAMEC, Germany) was used in order to determine the uncompensated solution resistance by AC impedance. The uncompensated solution resistance between WE and RE was determined for each experiment by potential controlled electrochemical impedance spectroscopy (EIS) measurements (10 mV root-mean-square perturbation) from the high-frequency intercept of the Nyquist plots. Potentials corrected this way are denominated *iR-free* throughout this work and the reported capacitively corrected ORR activities were determined from the positive-going potential scans.

**Proton exchange membrane fuel cell (PEMFC) measurements.**—For measurements in the temperature range 40–120°C, a PEMFC 5 cm<sup>2</sup> single cell configuration was employed, operated with a customized fuel cell test station (Greenlight Innovation, Canada), equipped with a Gamry Reference 3000 potentiostat/frequency response analyzer. Membrane electrode assemblies (MEAs) based on a 50  $\mu\text{m}$  thick Nafion 212 membrane (Quintech, Germany) were prepared by the decal transfer method. The catalyst loading of the tested ZrOPc/KB 1000 PO (16 wt% ZrO<sub>2</sub>) was obtained by weighing the decals before and after hot-pressing (0.22  $\text{mg}_{\text{Catalyst}}/\text{cm}^2$ , corresponding to an electrode thickness of  $\approx 5$   $\mu\text{m}$ , assuming a packing of the Ketjenblack support of 28  $\mu\text{m}/(\text{mg}\cdot\text{cm}^{-2})$ <sup>26</sup>). ZrO<sub>2</sub> based catalysts were coated on an ETFE substrate, whereby the ionomer to carbon ratio was  $\approx 0.84/1$  g/g. The anode had a Pt loading of 0.4  $\text{mg}/\text{cm}^2$ . A commercial 5 cm<sup>2</sup> single

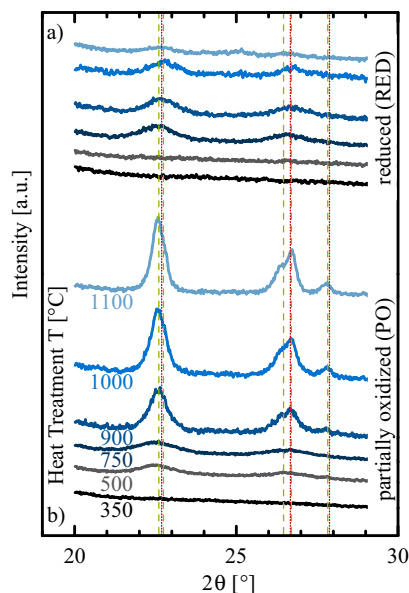


**Figure 1.** X-Ray diffraction patterns of ZrOPc/KB heat treated at various temperatures: a) reduced only (RED); b) partially oxidized (PO). The dashed green drop lines indicate tetragonal  $\text{ZrO}_2$  (PDF 00-050-1089, S. G.: P42/nmc (137)) and the dotted red drop lines cubic  $\text{ZrO}_2$  (PDF 01-071-4810, S. G.: Fm-3m).

cell hardware with single serpentine flow field (Fuel Cell Technologies, USA) sandwiched the MEA between two gas diffusion layers (25BC, SGL Carbon, Germany), which were compressed to ca. 20% strain as defined by the thickness of PTFE coated fiberglass subgaskets (Fiberflon, Germany).

Conditioning of the MEA consisted of eight sequences of holding the cell potential at 0.05 V for 45 min, then at 0.35 V for 5 min, and at 0.25 V for 10 min, all under  $\text{H}_2/\text{air}$  (400/600 nccm flows) at 60°C, 100% relative humidity, and 50 kPa<sub>gauge</sub>. The ORR activity vs. temperature was measured with  $\text{H}_2/\text{O}_2$  (400/400 nccm flows), whereby the total cell pressure was adjusted such that the  $\text{H}_2$  and  $\text{O}_2$  partial pressures remained at 0.10 MPa at a relative humidity of 90% (further on denominated as “0.9” rather than 90%). At each temperature, the cell was equilibrated for 10 min prior to recording a cyclic voltammogram at 1 mV/s. Subsequently, the high frequency resistance (HFR) was determined and the cell potentials were iR-corrected using the HFR of typically between  $\approx 90 \text{ m}\Omega \cdot \text{cm}^2$  (at 120°C) and  $\approx 120 \text{ m}\Omega \cdot \text{cm}^2$  (at 40°C). This was followed by repeating the same procedure with  $\text{N}_2$  instead of  $\text{O}_2$  on the cathode and the thus obtained capacitive currents (in  $\text{H}_2/\text{N}_2$ ) were subtracted from the currents obtained in  $\text{H}_2/\text{O}_2$ , yielding the catalyst’s ORR currents. The capacitively corrected ORR activities were determined from positive-going potential scans.

## Results and Discussion

**Structural and morphological characterization.**—X-ray diffraction (XRD).—The X-Ray diffractograms obtained on ZrOPc/KB derived catalysts in Figure 1 show that in case of reduced (RED) samples (Figure 1a) an oxide phase is formed  $\geq 750^\circ\text{C}$ , but with the broadened reflections from the nanoparticles a distinction between the tetragonal and cubic  $\text{ZrO}_2$  structure is not possible. Practically, the most prominent differentiation between these two structures would be a shoulder at  $2\theta \approx 26.4^\circ$ , which is present in the case of the tetragonal but absent in the case of the cubic phase, stemming from the lower symmetry of the former. For partially oxidized (PO) samples (Figure 1b), an oxide phase is observed already at  $\geq 500^\circ\text{C}$  and can clearly be assigned to tetragonal for catalysts heat treated at  $\geq 900^\circ\text{C}$ .

Figure 2 depicts representative XRD patterns of the mechanistically most relevant samples derived from the precursors  $\text{Zr}(\text{acac})_4/\text{KB}$

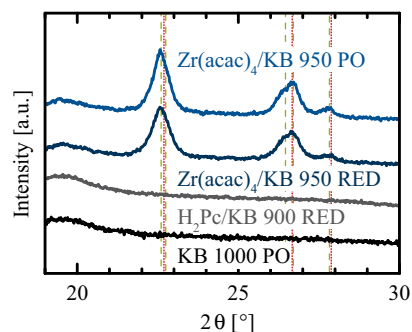


**Figure 2.** Representative XRD patterns of (from bottom to top) heat treated Ketjenblack (KB),  $\text{H}_2\text{Pc}/\text{KB}$  and  $\text{Zr}(\text{acac})_4/\text{KB}$ . Reference reflections of tetragonal (dashed green) and cubic (dotted red)  $\text{ZrO}_2$  as in Figure 1.

and  $\text{H}_2\text{Pc}/\text{KB}$ , as well as of the pure heat treated Ketjenblack (KB 1000 PO) as a reference (their ORR activity will be discussed below). In Figure 2, heat-treated metal-free phthalocyanine supported on Ketjenblack ( $\text{H}_2\text{Pc}/\text{KB}$  900 RED; second line from the bottom) does not exhibit any difference from bare KB partially oxidized at  $1000^\circ\text{C}$  (lower-most line), indicating that pyrolysis of metal-free phthalocyanine does not result in any crystalline phase. In contrast, the two depicted catalysts based on  $\text{Zr}(\text{acac})_4/\text{KB}$  precursor clearly exhibit tetragonal  $\text{ZrO}_2$  phases. Generally, in a forthcoming study within our group, it was found that  $\text{Zr}(\text{acac})_4$  precursor tends to develop crystalline  $\text{ZrO}_2$  phases already at lower heat-treatment temperatures compared to  $\text{ZrOPc}/\text{KB}$ . Nevertheless, both precursors lead to isostructural  $\text{ZrO}_2$  nanoparticles for heat treatments at  $\geq 750^\circ\text{C}$ .<sup>24</sup>

Exemplary transmission electron microscopy (TEM) micrographs are shown for  $\text{ZrOPc}/\text{KB}$  1000 PO and  $\text{Zr}(\text{acac})_4/\text{KB}$  950 PO (Figure 3). The average particle sizes of  $9 \pm 2 \text{ nm}$  for the former and of  $10 \pm 2 \text{ nm}$  for the latter are virtually identical (number based averages obtained by counting at least 100 particles in each case). All materials in this study which are based on ZrOPc precursor exhibit particle sizes ranging from  $\approx 4 \text{ nm}$  at low heat-treatment temperatures (500 PO and 750 RED) to  $\approx 9 \text{ nm}$  at higher temperatures (1000 PO). Those stemming from  $\text{Zr}(\text{acac})_4$  precursors range from  $\approx 4 \text{ nm}$  (500 PO and RED) to  $\approx 10 \text{ nm}$  (950 PO). For catalysts heat treated below  $500^\circ\text{C}$  (as well as for  $\text{ZrOPc}/\text{KB}$  500 RED), no evidence for particle formation was found by TEM and/or XRD. In the case of the metal free precursor  $\text{H}_2\text{Pc}/\text{KB}$ , no particles were found even for heat-treatment at  $1100^\circ\text{C}$  (RED or PO). More detailed morphological evaluation on these materials can be found elsewhere.<sup>24</sup>

**Comparative ORR activity assessment.**—A common baseline for comparing the ORR activity of PGM-free electrocatalysts is the volumetric or gravimetric current density at an electrode potential of 0.8 V<sub>RHE</sub>.<sup>27</sup> Considering 0.8 V<sub>RHE</sub> in the case of  $\text{ZrOPc}/\text{KB}$  1000 PO

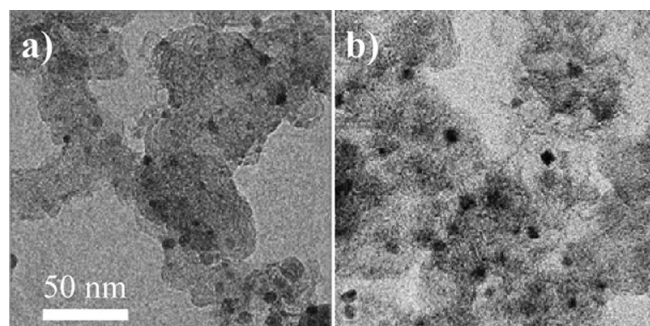


**Figure 3.** Exemplary TEM micrographs: a) of  $\text{ZrOPc}/\text{KB}$  after partial oxidation at  $1000^\circ\text{C}$  (1000 PO); b) of  $\text{Zr}(\text{acac})_4/\text{KB}$  after partial oxidation at  $950^\circ\text{C}$  (950 PO).



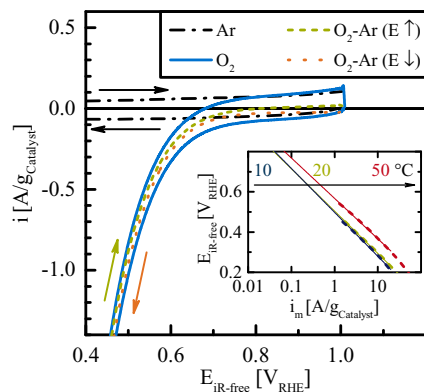


**Figure 4.** Exemplary RDE raw data for  $72 \mu\text{g}/\text{cm}^2$  ZrOPc/KB 1000 PO in  $0.1 \text{ M HClO}_4$  at 1600 rpm,  $5 \text{ mV}/\text{s}$ , and  $20^\circ\text{C}$ : CV in Ar (dash-dotted black line), in  $\text{O}_2$  atmosphere (full blue line), and subtraction of Ar CV from  $\text{O}_2$  CV (for the positive-going (green dashed) and negative-going (orange dotted) scans) in terms of mass-specific current density. Inset: Tafel plot of potential vs. mass-specific kinetic current  $i_m$ .  $i_m$  was obtained by Koutecký-Levich analysis (400–2500 rpm, see e.g., chapter 9.3.4 in Ref. 33) of capacitively corrected measured currents. Extrapolations to  $0.8 V_{\text{RHE}}$  are depicted by the thin full lines in the inset.

from this study, the overall current obtained under oxygen is very small compared to the capacitive currents under Ar (compare solid blue line and black dash-dotted line in Figure 4). Since the true ORR currents are obtained by subtracting the capacitive currents (under Ar) from the overall measured currents (under  $\text{O}_2$ ), the resulting error by subtracting two nearly identical numbers at/near  $0.8 V_{\text{RHE}}$  would result in a rather inaccurate determination of the true ORR current. Therefore, two approaches to compare ORR activities are used in this work.

i) In order to compare the ORR activities of the various produced catalysts, the measured potential at a current of  $-1 \text{ A}/\text{g}_{\text{Catalyst}}$  is used, subtracting the currents recorded under Ar atmosphere from those under  $\text{O}_2$ , as is shown for an example in Figure 4 (see dotted/dashed lines for negative- and positive-going scans). At  $-1 \text{ A}/\text{g}_{\text{Catalyst}}$  and a scan rate of  $5 \text{ mV}/\text{s}$ , the overall measured current under  $\text{O}_2$  is generally ca. 10 times larger than the corresponding capacitive current. At the same time, the overall current density ( $0.05\text{--}0.12 \text{ mA}/\text{cm}^2$ ) is still  $< 5\%$  of the oxygen mass transport limited current  $i_{\text{lim}}$  (for the catalyst loadings used in this study), which in  $0.1 \text{ M HClO}_4$  at  $20^\circ\text{C}$  is  $\approx 5.7 \text{ mA}/\text{cm}^2$  for the 4-electron reduction ( $n = 4$ ) to water (measured, e.g., for polycrystalline  $\text{Pt}^{28}$ ) or  $\approx 2.9 \text{ mA}/\text{cm}^2$  for the 2-electron reduction ( $n = 2$ ) to hydrogen peroxide (as  $i_{\text{lim}} \propto n$ ). Thus, when comparing potentials at a mass specific current density of  $-1 \text{ A}/\text{g}_{\text{Catalyst}}$ , the contributions from both capacitive currents and of mass transport limitations can be neglected.

ii) In order to compare activities with literature data, kinetic current densities of the measured catalysts are extrapolated to  $0.8 V_{\text{RHE}}$  by means of a Tafel extrapolation from the measured ORR activities at lower potentials, namely from currents between  $-1$  to  $-10 \text{ A}/\text{mg}_{\text{Catalyst}}$  (cf., inset of Figure 4). While the extrapolation of the Tafel lines to the roughly one to two orders of magnitude smaller currents at  $0.8 V_{\text{RHE}}$  is not without error, we believe that it will yield more reliable ORR activity values than via capacitive corrections at such low currents, even though the latter approach has been followed in most of the literature concerned with these types of catalysts. The apparent Tafel slopes for all conducted RDE experiments lie between  $180\text{--}210 \text{ mV}/\text{decade}$  (see, e.g., inset of Figure 4), similar to what was observed previously for Zr oxide based materials.<sup>12</sup> The Tafel slopes observed here correspond to values for the cathodic ORR transfer coefficient of  $\alpha = 0.3\text{--}0.4$ , which is reasonably consistent with the values reported for magnetron sputtered  $\text{ZrO}_x\text{N}_y$  ( $\alpha = 0.37\text{--}0.46$ , depending on the exact preparation of each sample<sup>4</sup>).

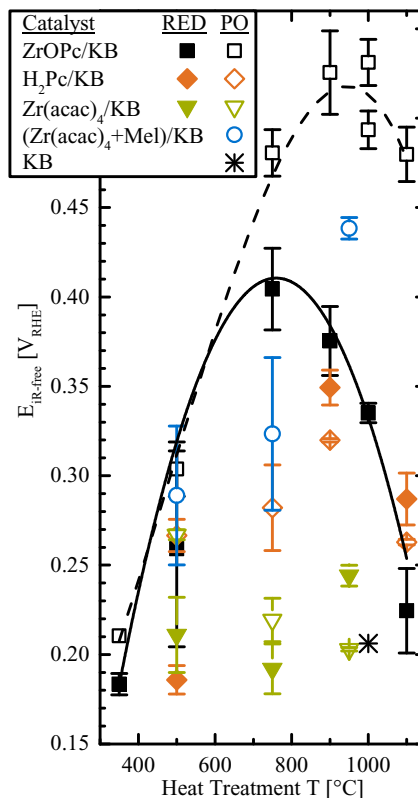


**Figure 5.** ORR activity at  $-1 \text{ A}/\text{g}_{\text{Catalyst}}$  of heat treated ZrOPc/KB (squares),  $\text{Zr}(\text{acac})_4/\text{KB}$  (triangles),  $\text{H}_2\text{Pc}/\text{KB}$  (diamonds) and  $\text{Zr}(\text{acac})_4+\text{Melamine}/\text{KB}$  (circles), and Ketjenblack (asterisk) evaluated by RDE in  $0.1 \text{ M HClO}_4$ ,  $20^\circ\text{C}$  1600 rpm, anodic scans at  $5 \text{ mV}/\text{s}$ , capacitively corrected. Data point at ZrOPc/KB 350 PO and KB 1000 PO are single measurements.

Figure 5 shows a comparison of the electrocatalytic ORR activities in terms of electrode potential at a faradaic (i.e., capacitively corrected) ORR current of  $-1 \text{ A}/\text{g}_{\text{Catalyst}}$  exhibited by the tested catalysts (error bars represent standard deviations of at least two independent experiments). First, comparing partially oxidized (open black squares) and reduced (solid black squares) ZrOPc/KB, one common trend is apparent. The ORR activity in each case exhibits a maximum, which in the case of reducing heat-treatment (RED) occurs at ca.  $750^\circ\text{C}$ , whereas it appears at around  $950^\circ\text{C}$  for partially oxidizing heat-treatment (PO). With the latter being more favorable for ordered crystallite formation (see Figure 1), this may be a hint that crystallinity, specifically the formation of tetragonal  $\text{ZrO}_2$  nanocrystallites (see Figure 1), may play an important role in the ORR activity. However, catalysts derived from  $\text{Zr}(\text{acac})_4$  precursor (open and solid green triangles), which more easily formed a well ordered tetragonal crystallite phases (even at lower temperatures compared to ZrOPc/KB), show a much lower activity for the ORR, requiring potentials of  $\approx 0.20\text{--}0.25 V_{\text{RHE}}$  to reach  $-1 \text{ A}/\text{g}_{\text{Catalyst}}$ . In fact, the activity exhibited by bare heat treated carbon (KB 1000 PO) is very similar to that of the  $\text{Zr}(\text{acac})_4$ -derived catalysts (see black asterisk symbol in Figure 5). Also, there is no apparent correlation between heat-treatment temperature/atmosphere and ORR activity within the  $\text{Zr}(\text{acac})_4/\text{KB}$  catalysts. Therefore, the fact that the  $\text{ZrO}_2/\text{KB}$  catalysts derived from both ZrOPc and  $\text{Zr}(\text{acac})_4$  precursors are iso-structural but display a difference of up to  $\approx 0.3 \text{ V}$  in their maximum ORR activity suggests that the  $\text{ZrO}_2$  morphology is not decisive for their ORR activity.

A decisive difference between ZrOPc and  $\text{Zr}(\text{acac})_4$  derived catalysts is likely the presence of nitrogen in the former and its absence in the latter. To investigate the influence of nitrogen alone, we examined the ORR activities of  $\text{H}_2\text{Pc}/\text{KB}$  derived catalysts, which are depicted in Figure 5 (orange diamonds). As in the case of  $\text{Zr}(\text{acac})_4$  based

catalysts, little impact of gas conditions (RED or PO) is found (compare to open and solid green triangles). While at heat-treatment temperatures of  $\geq 900^\circ\text{C}$ , the observed activities of heat treated  $\text{H}_2\text{Pc}/\text{KB}$  are comparable to those of  $\text{ZrOPc}/\text{KB}$  treated under reducing conditions (black solid symbols), they remain considerably lower compared to those of  $\text{ZrOPc}/\text{KB}$  treated under partially oxidizing conditions (open black symbols). This proves that the presence of Zr is necessary for high ORR activity. However, a comparison of the ORR activities of catalysts derived from Zr-containing but N-free precursors (i.e., the  $\text{Zr}(\text{acac})_4/\text{KB}$  based catalysts; green triangles) with those derived from Zr-free but N-containing precursors (i.e.,  $\text{H}_2\text{Pc}/\text{KB}$  based catalysts; orange diamonds), indicates that nitrogen plays an equally important role in the formation of electrocatalytically active centers for the ORR, whereby the most active catalysts are based on both Zr and N-containing precursors.

To further elucidate the beneficial impact of Zr and N on the ORR activity, we examined the catalysts based on using N-free  $\text{Zr}(\text{acac})_4$  in combination with N-containing metal-free melamine as precursors, supported on Ketjenblack and heat treated under partially oxidizing conditions. Figure 5 reveals that melamine as additional precursor, i.e., as nitrogen source, positively impacts the ORR activity of nanosized  $\text{ZrO}_2/\text{KB}$  catalysts (blue circles), approaching the activity of the  $\text{ZrOPc}$  derived catalysts. Two possible reasons for the ORR enhancement resulting from the combination of  $\text{Zr}(\text{acac})_4$  and melamine precursors can be proposed. One hypothesis is that nitrogen provided by melamine reacts with  $\text{Zr}(\text{acac})_4$  or with the already formed  $\text{ZrO}_2$ . Thermogravimetric analysis shows that both  $\text{Zr}(\text{acac})_4$  and melamine are fully decomposed at already  $500^\circ\text{C}$ ,<sup>24,29</sup> so that, regardless of the actual nature of the interaction between melamine and  $\text{Zr}(\text{acac})_4$ , it should occur already at  $500^\circ\text{C}$ . Indeed, the  $(\text{Zr}(\text{acac})_4+\text{Mel})/\text{KB}$  sample produced by partial oxidation at  $500^\circ\text{C}$  (blue circle in Figure 5) exhibits comparable ORR activity as the  $\text{ZrOPc}/\text{KB}$  samples produced by reduction or partial oxidation at  $500^\circ\text{C}$  (black squares in Figure 5). A reaction of nitrogen with pre-formed  $\text{ZrO}_2$  was also proposed by Liu et al.,<sup>12</sup> who claimed that a reaction of  $\text{ZrO}_2/\text{C}$  with  $\text{NH}_3$  at  $950^\circ\text{C}$  would lead to low levels of nitrogen doping into the oxide lattice, analogous to the reported sub-oxide formation in the gas phase heat-treatment of  $\text{TiO}_2$  in acetylene.<sup>30</sup> The other hypothesis is that nitrogen from melamine interacts with the carbon support to form active centers upon heat-treatment, similar to the interactions of gaseous N-precursors with carbons that are reported in the literature.<sup>12,31</sup> This would also be consistent with the slightly elevated ORR activities of heat treated  $\text{H}_2\text{Pc}/\text{KB}$  catalysts (orange diamonds in Figure 5) compared to the  $\text{Zr}(\text{acac})_4/\text{KB}$  catalysts based on a N-free precursor (green triangles in Figure 5). While it is not possible to distinguish between these two hypotheses based on the available data, it is very clear that the presence of both Zr and N is required for maximizing the ORR activity.

In the following we will examine whether there might be a correlation between the nitrogen content and the ORR activity. Figure 6 shows the measured electrode potential at a current density of  $-1 \text{ A/g}_{\text{Catalyst}}$  vs. nitrogen content, determined by elemental analysis for partially oxidized as well as reduced  $\text{ZrOPc}/\text{KB}$  catalysts and for partially oxidized  $(\text{Zr}(\text{acac})_4+\text{Mel})/\text{KB}$  catalysts. An apparent trend is the peaking ORR activity of  $\text{ZrOPc}/\text{KB}$  catalysts at  $\approx 0.5$  and  $\approx 1.5 \text{ wt}\% \text{ N}$  content for partially oxidized (open black squares) and reduced (solid black squares) catalysts, respectively. For  $(\text{Zr}(\text{acac})_4+\text{Mel})/\text{KB}$  catalysts, the optimum N content is at  $\approx 0.2 \text{ wt}\%$  (blue circles), whereby it should be noted that at such low levels, the uncertainty of the N analysis is relatively large (ca.  $\pm 0.1\%$ ). In general, as shown by the inset of Figure 6, the nitrogen content decreases with increasing heat-treatment temperature for all the catalysts. However, the nature of nitrogen sites in the resulting  $\text{ZrO}_2/\text{KB}$  catalysts remains unclear at this point. In another study of our group, X-Ray photoelectron spectroscopy (XPS) analysis could not provide any evidence for a possible N-doping of  $\text{ZrO}_2$ .<sup>24</sup> An assessment of the presence as well as of the possible influence of oxide defects on the ORR activity has been reported in the literature,<sup>3,4,9,10,14–16,22,23</sup> but the conclusions are still rather ambiguous.

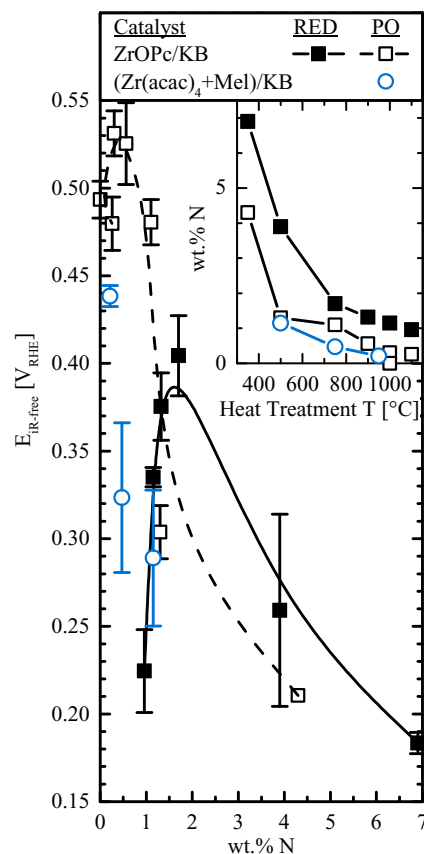


**Figure 6.** ORR activity at  $-1 \text{ A/g}_{\text{Catalyst}}$  vs. nitrogen content of heat treated  $\text{ZrOPc}/\text{KB}$  (squares) and  $(\text{Zr}(\text{acac})_4+\text{Mel})/\text{KB}$  (circles) evaluated by RDE in  $0.1 \text{ M HClO}_4$  at  $20^\circ\text{C}$  (1600 rpm, positive-going scans at  $5 \text{ mV/s}$ , capacitively corrected). The nitrogen content was determined by CHNS analysis.

**ORR mechanistic studies by RRDE.**—The most active sample of all the catalysts ( $\text{ZrOPc}/\text{KB}$  1000 PO) was additionally examined in alkaline and acid environment by RRDE using a Pt ring to quantify the extent of hydrogen peroxide formation. For a rigorous comparison, a prepared electrode was first measured in alkaline environment, and subsequently transferred and measured in a cell with acidic electrolyte. To validate that the Pt ring held at  $1.2 V_{\text{RHE}}$  does not influence the measured ORR activity, we compared the measured potential at  $-1 \text{ A/g}_{\text{Catalyst}}$  in  $0.1 \text{ M HClO}_4$  in the RRDE configuration ( $539 \text{ mV}_{\text{RHE}}$  obtained from Figure 7 after normalization by the given catalyst loading) with the average potential at that current in the previous measurements ( $531 \pm 13 \text{ mV}_{\text{RHE}}$ , see Figure 5). The difference within the standard deviation of the previously determined mean value proves that the polarized Pt ring does not affect the ORR activity. Figure 7 shows the ORR polarization curves of  $\text{ZrOPc}/\text{KB}$  1000 PO and, for comparison, of  $\text{KB}$  1000 PO in both acidic and alkaline electrolytes. Quite obviously, much higher ORR activities are obtained in alkaline compared to acid electrolytes. In fact,  $\text{KB}$  1000 PO exhibits only negligible ORR activity in acid, but shows a rather high half-wave potential of  $651 \text{ mV}_{\text{RHE}}$  with respect to the current plateau at  $\approx 2.5 \text{ mA/cm}^2$  in  $0.1 \text{ M NaOH}$ , which is only  $\approx 40 \text{ mV}$  more negative than that of the  $\text{ZrOPc}/\text{KB}$  1000 PO catalyst. Thus, while the presence of Zr and low levels of N derived from the  $\text{ZrOPc}$  precursor lead to a clear enhancement of the ORR activity in alkaline environment over that of heat treated carbon black, the catalytic gain is much lower than the  $\approx 300 \text{ mV}$  observed in acid (see Figure 5).

A closer inspection of the data in Figure 7a also reveals that mass transport limiting currents in  $0.1 \text{ M NaOH}$  of  $\approx 3 \text{ mA/cm}^2$  are much lower than one would expect for a 4-electron oxygen reduction reaction in alkaline electrolyte ( $\approx 5.5 \text{ mA/cm}^2$  as measured for a Pt(111)

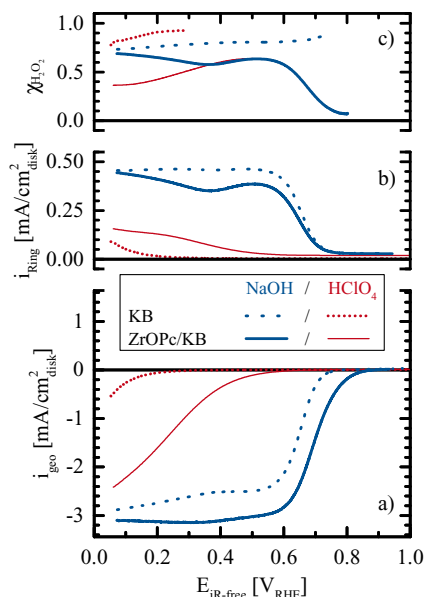
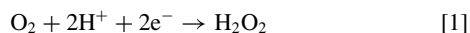


**Figure 7.** RRDE data set for the positive-going potential scans under  $O_2$  of ZrOPc/KB 1000 PO (full lines) and pure KB 1000 PO (dotted lines) in 0.1 M NaOH (blue) or 0.1 M  $HClO_4$  (red) at 20°C, 5 mV/s, and 1600 rpm: a) disk currents vs.  $iR$ -free potential (vs. RHE); b) ring currents at  $E_{Ring} = 1.2 V_{RHE}$ ; c)  $H_2O_2$  yield calculated with Equation 2 from the ring currents after offset-correction and using a collection efficiency of  $N = -0.255$  (derived from Equations 9.4.8, 9.4.16, 9.4.17 in Ref. 33). The loadings are  $54 \mu g_{Carbon}/cm^2$  (KB 1000 PO) and  $66 \mu g_{Catalyst}/cm^2$  (ZrOPc/KB 1000 PO), corresponding to a carbon content of  $\approx 55 \mu g_{Carbon}/cm^2$ .

surface in 0.1 M KOH<sup>28</sup>). This points toward a 2-electron oxygen reduction reaction to  $H_2O_2$  rather than to  $H_2O$ :



This is demonstrated more clearly by examining the simultaneously recorded ring currents  $i_{Ring}$  (Figure 7b). For example, considering both KB 1000 PO and ZrOPc/KB 1000 PO in acid (red lines), oxidative currents are observed at the ring electrode whenever ORR currents are detected on the disk, indicating the formation of  $H_2O_2$  during the ORR. In alkaline electrolyte (blue lines), considerable ring currents appear negative of approximately the same potential ( $\leq 0.75 V_{RHE}$ ) for both KB 1000 PO and ZrOPc/KB 1000 PO, even though the corresponding ORR currents are separated by almost 100 mV. This is due to the fact that there is a potential region ( $0.75 V_{RHE} < E < 0.85 V_{RHE}$ ), where ZrOPc/KB 1000 PO exhibits substantial ORR activity while showing no or very small ring currents, suggesting a preference for the 4-electron reduction to  $H_2O$ . This difference in alkaline electrolyte between KB 1000 PO ( $H_2O_2$  always detected at the ring) and ZrOPc/KB 1000 PO (no/little  $H_2O_2$  detection at high potentials) suggests separate ORR current contributions from the bare KB support (mostly leading to  $H_2O_2$ ) and from the heat treated, N containing, ZrOPc (mostly leading to  $H_2O$ ).

For a better quantification of the extent of  $O_2$  reduced to  $H_2O_2$  or  $H_2O$ , the measured ring currents can be translated into hydrogen peroxide yields  $\chi_{H_2O_2}$  (see Figure 7), according to Equation 2:<sup>32</sup>

$$\chi_{H_2O_2} = (2 \cdot i_{Ring}/N) / (i_{geo} + i_{Ring}/N) \quad [2]$$

where  $i_{Ring}$  and  $i_{geo}$  are ring and disk current, respectively and  $N = -0.255$  the collection efficiency as derived by Equations 9.4.8, 9.4.16 and 9.4.17 in Bard and Faulkner.<sup>33</sup> As shown in Figure 7c, both materials exhibit high  $H_2O_2$  yields in alkaline electrolyte, amounting to  $\chi_{H_2O_2} \approx 0.6$  (ZrOPc/KB 1000 PO) and  $\approx 0.8$  (KB 1000 PO) at potentials of  $\leq 0.6 V_{RHE}$ . As expected from the above discussion, the  $H_2O_2$  yield for ZrOPc/KB 1000 PO clearly decreases toward very low values at potentials above  $\approx 0.60 V_{RHE}$ . In acid, the ORR

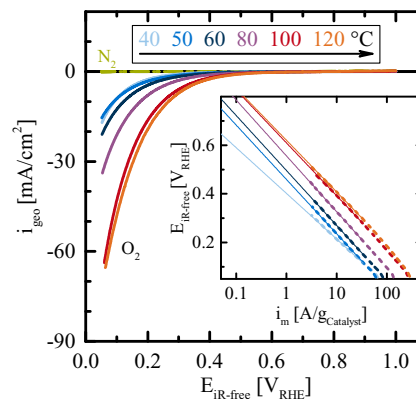


**Figure 8.** Current density vs.  $iR$ -free cell voltage of ZrOPc/KB 1000 PO cathodes measured between 40 and 120°C in a PEMFC either under  $N_2$  (green line) or under  $O_2$  (bluish to orange lines); the anodes were operated with pure  $H_2$ . All gases are supplied at flow rates of 400 nccm ( $H_2/N_2$  or  $O_2$ ) at gas partial pressures of  $p_{H_2} = p_{N_2} = p_{O_2} = 0.10$  MPa and humidified to a relative humidity of 0.9. The data were recorded at 1 mV/s and shown for the positive-going scan. Inset: Tafel plot of  $iR$ -free potential vs. mass-specific kinetic current  $i_m$  (dashed lines, extrapolations are fine full lines).  $i_m$  was obtained by subtracting the current measured in  $N_2$  from that measured current in  $O_2$ , dividing the result by the catalyst loading ( $0.22 mg_{Catalyst}/cm^2$ ).

activity is much smaller for the ZrOPc/KB 1000 PO catalyst and essentially negligible for the KB 1000 PO reference. At potentials at which  $\chi_{H_2O_2}$  can be evaluated in acid (red lines), it is  $\approx 0.4$  and  $\approx 0.8$  for ZrOPc/KB 1000 PO and KB 1000 PO, respectively. Generally, a high  $\chi_{H_2O_2}$  suggests that the ORR mainly proceeds through a 2-electron path (Equation 1). On Fe-N-C catalysts, Bonakdarpour et al. showed that the experimentally determined  $\chi_{H_2O_2}$  is generally strongly dependent on the electrode thickness and can approach a value of zero for thick electrodes, even for a pure 2-electron ORR mechanism.<sup>34</sup> This was rationalized by invoking the chemical decomposition of  $H_2O_2$  into  $H_2O$  and  $0.5 O_2$ , which leads to an apparent 4-electron reaction, if the residence time of the initially electrochemically formed  $H_2O_2$  (via Equation 1) in the electrode is sufficiently long to allow for its subsequent chemical decomposition to  $H_2O$  and  $O_2$ , which is the more likely the thicker the electrode.<sup>34</sup> While we aimed at thin catalyst layers in this study ( $< 2 \mu m$  for the here used carbon loadings of  $\leq 0.07 mg_{Carbon}/cm^2$ ), the electrode thickness is still in a range where the measured values for  $\chi_{H_2O_2}$  represent a lower limit rather than an intrinsic property of the catalyst. Unfortunately, due to the already low ORR activities of the ZrOPc/KB 1000 PO catalyst, measurements at lower loadings were experimentally not feasible. In summary, however, we believe that the intrinsic electrochemical ORR mechanism on the tested ZrOPc/KB 1000 PO (and on the KB 1000 PO reference) proceeds via a 2-electron reduction in acidic electrolyte. On the other hand, as discussed above, there are indications for a direct 4-electron mechanism in alkaline electrolyte, at least at high potentials.

**Temperature dependence of the ORR.**—Most studies on the ORR activity of valve-metal oxide based catalysts were conducted at room temperature, and there is very little literature available about the ORR activity of  $ZrO_2$  based catalysts at higher temperatures (one study in liquid electrolyte up to 50°C,<sup>4</sup> and one up to 80°C in a PEMFC<sup>12</sup>). Therefore, we will explore the apparent activation energy of our catalysts to temperatures as high as 120°C, which represents the long-term DOE target for PEMFC operation. Figure 8 depicts the positive-going voltammetric scans of cycles on ZrOPc/KB 1000 PO in a 5  $cm^2$  PEMFC under both  $N_2$  and  $O_2$  atmosphere. The raw data in  $N_2$  atmosphere exhibit basically a flat horizontal line (see green line) at virtually zero current. This not only demonstrates that ZrOPc/KB 1000 PO does not catalyze the oxidation of hydrogen permeating through the membrane, but also that the capacitive corrections of the currents



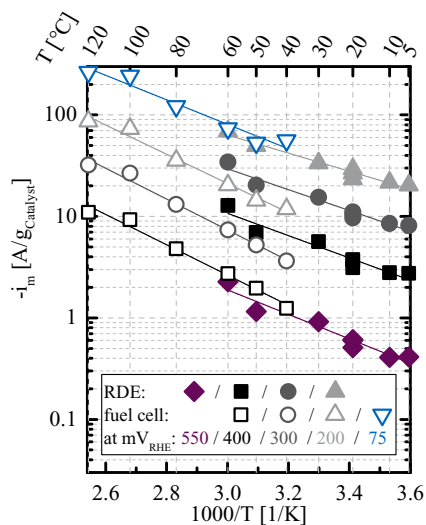


**Figure 9.** ORR activity of ZrOPc/KB 1000 PO at constant cathode potential, measured in an RDE (5–60°C, full symbols) and in a PEMFC (40–120°C, hollow symbols). RDE measurements in 0.1 M HClO<sub>4</sub>, with mass-specific currents obtained by Koutecký-Levich analysis at 400–2500 rpm (5 mV/s, positive-going scans, capacitively corrected). PEMFC measurements at relative humidity of 0.9 under H<sub>2</sub>/O<sub>2</sub> (400/400 nccm) with partial pressures maintained at 0.10 MPa (1 mV/s, positive-going scans, corrected by the capacitive currents obtained in H<sub>2</sub>/N<sub>2</sub> configuration at otherwise identical conditions).

under O<sub>2</sub> atmosphere are negligibly small. As expected, the ORR currents increase significantly with increasing temperature. The inset of Figure 8 shows a Tafel plot of mass-specific ORR currents, with Tafel slopes (obtained by fitting the data between 5–50 A/g<sub>Catalyst</sub>) ranging between 190–230 mV/decade, corresponding to cathodic transfer coefficients between 0.3–0.4. These values are consistent with those observed in RDE experiments (cf., discussion of Figure 4).

Figure 9 depicts mass-specific ORR currents as a function of temperature in an Arrhenius representation for cathode potentials between 75 and 550 mV<sub>RHE</sub>, obtained in both RDE (5–60°C; solid symbols) and PEMFC (40–120°C; open symbols) experiments. Surprisingly, at potentials where RDE and PEMFC data can be compared (200–400 mV), the mass-specific ORR currents in RDE experiments at the same temperature are always ≈2–3 times larger than those obtained in a PEMFC (see solid vs. open squares, circles, and upward pointing triangles in Figure 9). This is reminiscent of the discrepancy between RDE and PEMFC data previously reported for several Fe-N-C catalysts.<sup>35</sup> From linear regressions of the data depicted in Figure 9, activation energies at different constant cathode potentials for both fuel cell and RDE experiment can be calculated and are shown in Figure 10. The E<sub>Act</sub> values determined from fuel cell experiments are higher than those determined from RDE experiments by ≈8–10 kJ/mol over the depicted potential range. An approach to explain this will be presented below. At 0.4 V<sub>RHE</sub>, E<sub>Act</sub> = 21 ± 2 kJ/mol (RDE) and 29 ± 2 kJ/mol (fuel cell), respectively (Figure 10). At this potential, Doi et al. report a similar activation energy of 22 kJ/mol for their most active ZrO<sub>x</sub>N<sub>y</sub> (sputtered on a glassy carbon substrate heated at 800°C) measured in 0.1 M H<sub>2</sub>SO<sub>4</sub>.<sup>4</sup>

Over the potential ranges, over which we could determine E<sub>Act</sub> (75–400 mV<sub>RHE</sub> in PEMFC and 200–550 mV<sub>RHE</sub> in RDE experiments), a linear increase of E<sub>Act</sub> with potential is observed for both RDE and PEMFC experiments (see Figure 10). While an extensive discussion of the various definitions of activation energies can be found in a publication by Neyerlin et al.,<sup>36</sup> their Equation [22] can be applied to the experimental data of the present study to yield a correlation of E<sub>Act</sub> at a constant cathode potential E in relation to a value obtained at an (arbitrarily chosen) reference potential E<sub>reference</sub>:

$$E_{\text{Act}}(E) = E_{\text{Act}}(E_{\text{reference}}) - \alpha F \cdot (E_{\text{reference}} - E) \quad [3]$$

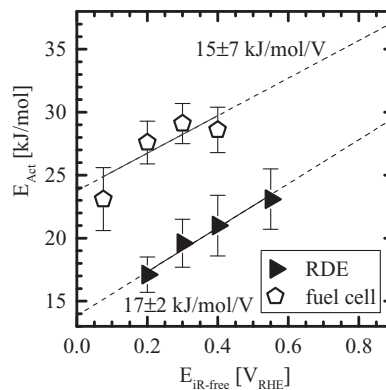


**Figure 10.** Activation energy E<sub>Act</sub> for the ORR at constant cathode potential as calculated from the data shown in Figure 9.

where,  $\alpha$  is the transfer coefficient as already defined above, and  $F$  is the Faraday constant. Equation 3 predicts a linear increase of E<sub>Act</sub>(E) with potential E, qualitatively consistent with the linear trend lines plotted in Figure 10, with slopes of 17 ± 2 and 15 ± 7 kJ/mol/V for the RDE and the PEMFC derived data, respectively. This is roughly 2-fold smaller than what would be predicted from the transfer coefficients observed in our study ( $\alpha \approx 0.3$ –0.4; see above), which based on Equation 3 would result in slopes ranging from ≈29–38 kJ/mol/V. The origin of this discrepancy is not yet clear.

Based on the mechanistic findings from the RRDE experiments, we will now try to provide a possible explanation for the above described discrepancy of a factor of ≈2–3 at any given cathode potential between the mass-specific activity obtained in RDE vs. PEMFC experiments (see Figure 9), which we believe might be due to very different local H<sub>2</sub>O<sub>2</sub> concentrations in the electrode. RRDE analysis suggests that at least the major fraction of oxygen (if not all) is electrochemically reduced to H<sub>2</sub>O<sub>2</sub> rather than H<sub>2</sub>O on the ZrOPc/KB 1000 PO catalyst (i.e., following Equation 1), so that the actual overpotential,  $\eta_{\text{O}_2|\text{H}_2\text{O}_2}$ , at any given cathode voltage would depend on the reversible potential for the electrochemical reduction of O<sub>2</sub> to H<sub>2</sub>O<sub>2</sub>, E<sup>rev</sup><sub>O<sub>2</sub>|H<sub>2</sub>O<sub>2</sub></sub>, which in this case also depends on the H<sub>2</sub>O<sub>2</sub> concentration in the electrode:

$$E_{\text{O}_2|\text{H}_2\text{O}_2}^{\text{rev}} = E_{\text{O}_2|\text{H}_2\text{O}_2}^{\text{rev},0} + RT / (2F) \cdot \ln([\text{O}_2] \cdot [\text{H}^+]^2 \cdot [\text{H}_2\text{O}_2]^{-1}) \quad [4]$$

with square brackets indicating activity of reactants and products, and E<sup>rev,0</sup><sub>O<sub>2</sub>|H<sub>2</sub>O<sub>2</sub></sub> being the reversible potential at temperature T and standard activities. At the applied O<sub>2</sub> pressure of ≈0.10 MPa, referencing to the reversible hydrogen electrode (RHE) scale (i.e., [H<sup>+</sup>] drops out), and approximating the H<sub>2</sub>O<sub>2</sub> activity by its concentration (i.e., [H<sub>2</sub>O<sub>2</sub>] ≈ c<sub>H<sub>2</sub>O<sub>2</sub>}/(1 M)), Equation 4 simplifies to:</sub>

$$E_{\text{O}_2|\text{H}_2\text{O}_2}^{\text{rev}} \approx E_{\text{O}_2|\text{H}_2\text{O}_2}^{\text{rev},0} + 2.303 \cdot RT / (2F) \cdot \log(1M/c_{\text{H}_2\text{O}_2}) \quad [5]$$

Owing to the different mass transport properties in RDE and PEMFC experiments, the local H<sub>2</sub>O<sub>2</sub> concentration in the electrode, c<sub>H<sub>2</sub>O<sub>2</sub></sub>, would be expected to be different: i) in our R(R)DE experiments with thin catalyst layers (≈1–2 μm), the removal of H<sub>2</sub>O<sub>2</sub> product into the electrolyte should be rather facile, keeping its concentration at the electrode a very low levels; ii) in PEMFCs, the removal of H<sub>2</sub>O<sub>2</sub> product can only proceed by its rather slow permeation through the membrane to the anode, where it would be reduced to H<sub>2</sub>O, and by evaporation and diffusion into the cathode exhaust, which owing to the low vapor pressure of H<sub>2</sub>O<sub>2</sub><sup>37</sup> is also expected to be low. Based on these considerations, c<sub>H<sub>2</sub>O<sub>2</sub></sub> in the PEMFC electrode is likely much larger than in the RRDE electrode, which would result in lower E<sup>rev</sup><sub>O<sub>2</sub>|H<sub>2</sub>O<sub>2</sub></sub> values (see Equation 5) and thus lower |η<sub>O<sub>2</sub>|H<sub>2</sub>O<sub>2</sub></sub>| values at the same cathode potential for the former.

In the RRDE configuration, the actual H<sub>2</sub>O<sub>2</sub> concentration can be estimated from the offset of i<sub>ring</sub> that occurs at high disk potentials, where no ORR takes place (cf., Figure 7b), and where only residual H<sub>2</sub>O<sub>2</sub> in solution is oxidized at the Pt ring (polarized at 1.2 V<sub>RHE</sub>).

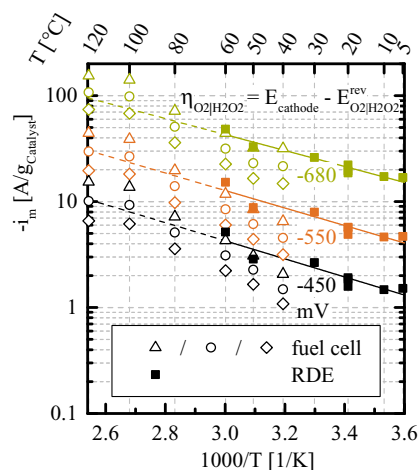


**Figure 11.** ORR activity of ZrOPc/KB (1000°C PO) at constant overpotential for the 2 e<sup>-</sup> ORR (Equation 4), measured in RDE (5–60°C, full squares for estimated c<sub>H<sub>2</sub>O<sub>2</sub></sub> = 0.03 mM) and in fuel cell (40–120°C, hollow triangles/circles/diamonds for assumed c<sub>H<sub>2</sub>O<sub>2</sub></sub> = 300/30/3 mM). RDE measurements in 0.1 M HClO<sub>4</sub>, kinetic currents by Koutecký-Levich analysis at 400–2500 rpm, 5 mV/s, positive-going scans, capacitively corrected. Fuel cell at relative humidity of 0.9, H<sub>2</sub>O<sub>2</sub> partial pressures maintained at 0.10 MPa, 400/400 nccm, cyclic voltammetry 1 mV/s, anodic scans corrected with same CVs, where cathode is under N<sub>2</sub> at otherwise identical conditions. Linear inter-/extrapolations of RDE data are shown as full/dashed lines.

limited only by mass transfer. At constant rotation rate, temperature and electrolyte composition,  $i_{\text{Ring}} = C \cdot c_{\text{H}_2\text{O}_2}$ , where  $C$  is a constant. Thus, for a known reference measurement at the same conditions, it is possible to eliminate  $C$ , yielding:

$$i_{\text{Ring}}/i_{\text{Ring,reference}} = c_{\text{H}_2\text{O}_2}/c_{\text{H}_2\text{O}_2,\text{reference}} \quad [6]$$

The H<sub>2</sub>O<sub>2</sub> transport limited ring currents can be calculated from the H<sub>2</sub>O<sub>2</sub> transport limited disk currents by the geometrical correlation between ring and disk limiting currents in an RRDE,  $i_{\text{Ring}} = i_{\text{Disk}} \cdot (r_3^3 - r_2^3)^{2/3} / r_1^{2.33}$ . For our RRDE geometry ( $r_1 = 2.50$  mm (disk radius),  $r_2 = 3.25$  mm (inner ring radius) and  $r_3 = 0.375$  mm (outer ring radius)), the measured limiting disk current of 1.8 mA/cm<sup>2</sup> at 1 mM H<sub>2</sub>O<sub>2</sub>, 1600 rpm and 20°C in 0.1 M HClO<sub>4</sub> (data not shown) thus translates to a limiting ring current at 1 mM H<sub>2</sub>O<sub>2</sub> of  $i_{\text{Ring,reference}} = 2.0$  mA/cm<sup>2</sup>. Using Equation 6 and the ring current offset at high potentials shown in Figure 7b, the effective H<sub>2</sub>O<sub>2</sub> concentration in the RRDE experiments at 20°C equates to  $c_{\text{H}_2\text{O}_2} \approx 0.03$  mM, which represents an order of magnitude estimate of the effective local H<sub>2</sub>O<sub>2</sub> concentration at the cathode catalyst in the RDE experiments.

Unfortunately, a similar estimate of c<sub>H<sub>2</sub>O<sub>2</sub></sub> in the electrode is not possible for the PEMFC configuration, but based on the above arguments, it is likely substantially larger than in the RDE configuration, particularly at low PEMFC temperatures where H<sub>2</sub>O<sub>2</sub> vapor pressure and permeability are low. In the following, we will evaluate the order of magnitude of the H<sub>2</sub>O<sub>2</sub> concentration in the PEMFC electrode that would be required to result in ORR activities which are consistent with those obtained by RDE. Thus, we assume c<sub>H<sub>2</sub>O<sub>2</sub></sub> ≈ 0.03 mM for the RDE configuration (see above) and several much higher H<sub>2</sub>O<sub>2</sub> concentrations for the PEMFC (c<sub>H<sub>2</sub>O<sub>2</sub></sub> values of 3, 30, and 300 mM), from which we then calculate the respective values of E<sup>rev</sup><sub>O<sub>2</sub>|H<sub>2</sub>O<sub>2</sub></sub> (from Equation 5). From this we then determine the overpotentials for the reduction of O<sub>2</sub> to H<sub>2</sub>O<sub>2</sub> ( $\eta_{\text{O}_2|\text{H}_2\text{O}_2} = E_{\text{cathode}} - E^{\text{rev}}_{\text{O}_2|\text{H}_2\text{O}_2}$ ) and now plot the mass-specific activity obtained in RDE and PEMFC experiments at constant values of  $\eta_{\text{O}_2|\text{H}_2\text{O}_2}$  rather than at constant cathode potentials as was done in Figure 9.

Figure 11 shows the resulting Arrhenius representation of the activities of ZrOPc/KB 1000 PO at several values of constant  $\eta_{\text{O}_2|\text{H}_2\text{O}_2}$  (i.e., green, orange, and black solid squares at  $\eta_{\text{O}_2|\text{H}_2\text{O}_2}$  of -680, -550, and -450 mV) for the RDE experiments assuming, c<sub>H<sub>2</sub>O<sub>2</sub></sub> = 0.03 mM

and for the PEMFC experiments assuming c<sub>H<sub>2</sub>O<sub>2</sub></sub> = 3/30/300 mM (open diamonds/circles/triangles). If one now compares the RDE based activities projected to the higher temperatures of the PEMFC measurements (dashed lines) with the PEMFC data, consistent activities would be obtained if the local H<sub>2</sub>O<sub>2</sub> concentrations in the PEMFC were high at 40°C (i.e., c<sub>H<sub>2</sub>O<sub>2</sub></sub> = 300 mM, see open triangles), where H<sub>2</sub>O<sub>2</sub> removal rates should be slow (see above; vapor pressure at 40°C ≈ 1 kPa<sup>37</sup>), and if they were low at 120°C (i.e., c<sub>H<sub>2</sub>O<sub>2</sub></sub> = 3 mM, see open diamonds), where H<sub>2</sub>O<sub>2</sub> removal rates should be fast (vapor pressure at 120°C ≈ 34 kPa<sup>37</sup>). While this explanation is grantedly very tentative, we believe that it is nevertheless a feasible explanation for the discrepancy observed between our RDE and PEMFC data for the ZrOPc/KB 1000 PO catalyst, which, however, would also explain similar discrepancies reported for Fe-N-C catalysts by Jaouen et al.<sup>35</sup> in their comparison of RDE and PEMFC based activities.

**Literature comparison of the ORR Activity of ZrO<sub>2</sub> Based catalysts.**—At a potential of 0.8 V<sub>RHE</sub>, a practical comparison of ORR activities on ZrO<sub>2</sub> based catalysts in acid can be found in Table I, prepared either from the same precursor as in our case (i.e., from ZrOPc) or from ZrO(NO<sub>3</sub>)<sub>2</sub> and supported on either XC-72 Vulcan carbon, Ketjenblack, carbon nanotubes (CNTs), or multi-walled carbon nanotubes (MWCNTs). Unfortunately, most data reported in the literature are not recorded in an experimental set-up allowing for the exact quantification of kinetic currents like in an RDE configuration,<sup>4,8,17–19,38</sup> so that the kinetic data at 0.8 V<sub>RHE</sub> were obtained by the subtracting large capacitive currents under Ar or N<sub>2</sub> from only slightly larger overall currents under oxygen (see above discussion under Comparative ORR Activity Assessment). A first observation from Table I is that the reported mass-specific activities at 0.8 V<sub>RHE</sub> vary by three orders of magnitude, ranging from 0.04–40·10<sup>-2</sup> A/g<sub>Catalyst</sub>, which may be compared to 4.0 ± 0.6·10<sup>-2</sup> A/g<sub>Catalyst</sub>, for our ZrOPc/KB 1000 PO catalyst (see last row; activity averaged over three independent experiments). When using either N-containing ZrOPc precursor or using N-free precursor together with NH<sub>3</sub> as nitrogen source, the activities are clearly higher, with a much more narrow range of activities from 2.4–40·10<sup>-2</sup> A/g<sub>Catalyst</sub> (except for one exception with 0.77·10<sup>-2</sup> A/g<sub>Catalyst</sub>).

Compared to the best catalysts, the ORR activity of our most active catalyst (i.e., of ZrOPc/KB 1000 PO) is roughly one order of magnitude lower. While we cannot exclude the possibility that we may not have found the optimum treatment conditions, the lower activity may be caused by ppm-level impurities of Fe (≈100–1000 ppm), which when heat treated in the presence of N-rich substances (e.g., phthalocyanines or NH<sub>3</sub>) can lead to significant ORR activity (see e.g., Kramm et al.<sup>39</sup>). Iron impurities could be introduced through the (MW)CNTs support materials, which generally have high levels of impurities,<sup>40</sup> especially Fe; similarly, iron could also be introduced when ballmilling catalyst precursors in iron/steel based vessel with iron/steel beads (done, e.g., in Reference 38). Thus, we believe that there is a finite possibility that the very high ORR activities of some ZrO<sub>2</sub> based catalysts may derive from Fe-N-C active sites and were possibly mistakenly ascribed to ZrO<sub>2</sub> based species.

Considering the technical target for PGM-free ORR catalysts of the US Department of Energy (DoE) for 2017,<sup>41</sup> namely 300 A/cm<sup>3</sup> at 0.8 V<sub>RHE</sub> and 80°C, it is necessary to convert the measured mass-specific currents to volume-specific currents. This can be done easily for our catalysts, assuming a packing of the Ketjenblack support of 28 μm/(mg·cm<sup>-2</sup>),<sup>26</sup> and using the PEMFC based ORR activity of ≈9·10<sup>-2</sup> A/g<sub>Catalyst</sub> at 80°C obtained by extrapolating the PEMFC data to 0.8 V<sub>RHE</sub> (see inset of Figure 8). This yields a volume-specific current of ≈0.04 A/cm<sup>3</sup>, which is almost four orders of magnitude lower than the above specified DoE target. Unfortunately, the same analysis cannot be done for the most catalysts listed in Table I (≈30·10<sup>-2</sup> A/g<sub>Catalyst</sub><sup>18</sup> and ≈40·10<sup>-2</sup> A/g<sub>Catalyst</sub><sup>38</sup> at 30°C), since the packing density, the wt% ZrO<sub>2</sub>, and the activation energies are not given, but assuming a similar packing density as in our case, a maximum of 50 wt% ZrO<sub>2</sub>, and similar activation energies, a maximum of ≈3 A/cm<sup>3</sup>, i.e., 10<sup>2</sup>-fold higher than obtained for our ZrOPc/KB



**Table I.** ORR activities of ZrO<sub>2</sub> nanoparticle based catalysts at 0.8 V<sub>RHE</sub>. Kinetic data at 0.8 V<sub>RHE</sub>, unless stated otherwise, are extrapolated from kinetic data measured at lower potentials, positive-going potential scans at 5 mV/s. A “t” indicates the heat-treatment time for calcination, an “x” a value not given in the respective reference.

Precursor	Treatment T*	Balance H <sub>2</sub>  O <sub>2</sub>	t	i <sub>m</sub> × 10 <sup>2</sup>	Ref.
	[°C]	[%]	[h]	[A/gCatalyst]	
XC-72, ZrO(NO <sub>3</sub> ) <sub>2</sub>	500	N <sub>2</sub>  0 0	3	0.04 <sup>1,i</sup>	12
XC-72, ZrO(NO <sub>3</sub> ) <sub>2</sub>	1.: 500	N <sub>2</sub>  0 0	3	2.4 <sup>1,i</sup>	12
	2.: 950	NH <sub>3</sub>	3		
CNT, ZrOPc	900	Ar 2 x	x	16 <sup>2,ii</sup>	17
CNT, ZrOPc	1000	Ar 2 x	x	9 <sup>2,ii</sup>	17
MWCNT, ZrOPc	900	Ar 2 0.05	3.3	30 <sup>2,ii</sup>	18
MWCNT, ZrOPc	900	Ar 2 0.05	2	24 <sup>2,ii</sup>	18
MWCNT, ZrOPc	900	Ar 2 0.5	2	0.77 <sup>2,ii</sup>	18
MWCNT, ZrOPc	900	Ar 2 0.5	1	5.3 <sup>2,ii</sup>	18
ball milled ZrOPc/MWCNTs	900	N <sub>2</sub>  2 0.05	x	20 <sup>2,ii</sup>	38
ball milled ZrOPc/MWCNTs	1.: 900	N <sub>2</sub>  2 0.05	x	40 <sup>2,ii</sup>	38
	2.: 700	NH <sub>3</sub>	x		
ZrOPc/MWCNTs	900	N <sub>2</sub>  2 0.05	x	24 <sup>2,ii</sup>	19
ZrOPc/MWCNTs	1.: 900	N <sub>2</sub>  2 0.05	1	12 <sup>2,ii</sup>	22
	2.: 1000	N <sub>2</sub>	1		
ZrOPc/KB	1.: 1000	Ar 5 0	2	4.0±0.6 <sup>3</sup>	this study
	2.: 1000	Ar+N <sub>2</sub>  2.5 0.5	1		

<sup>1</sup>0.5 M H<sub>2</sub>SO<sub>4</sub>, RT (2500 rpm)

<sup>2</sup>0.1 M H<sub>2</sub>SO<sub>4</sub>, 30°C (quiescent)

<sup>3</sup>0.1 M HClO<sub>4</sub>, 20°C (Koutecký-Levich analysis, 400–2500 rpm)

<sup>i</sup>applied diffusion correction with given raw data

<sup>ii</sup>no diffusion correction, given raw data

\*“1.”/“2.” indicates the first/second stage of the heat-treatment procedure

1000 PC catalyst could possibly be expected as an upper bound. Thus, the ORR activity of the best reported ZrO<sub>2</sub> based ORR catalysts is at least two orders of magnitude lower than the DOE target and substantial improvements would still be required for this class of PGM-free ORR catalysts.

### Conclusions

The comparison of catalysts derived from ZrOPc (precursor containing Zr and N), Zr(acac)<sub>4</sub> (containing Zr) and H<sub>2</sub>Pc (containing N) showed that simultaneous presence of both N and Zr is necessary to obtain high ORR activity. With a maximum volumetric ORR activity of ≈0.04 A/cm<sup>3</sup> observed in PEMFC configuration at 80°C, the DoE target of 300 A/cm<sup>3</sup> is missed by almost four orders of magnitude.<sup>41</sup> Although the highest gravimetric activities reported in literature are ≈10 times higher than the values found in this study,<sup>38</sup> they still seem far away from technical applicability, with a projected maximum volumetric current density of ≈3 A/cm<sup>3</sup> at 80°C. Moreover, in the most active materials reported in the literature, the presence of iron, which is known to form ORR active Fe-N-C species when heat treated in presence of carbon and nitrogen, appears likely, questioning the activity values ascribed to (defective) ZrO<sub>2</sub>. Rotating ring disk electrode measurements on the most active material examined in this study revealed a main ORR reaction pathway toward hydrogen peroxide in acidic environment. Using this finding to compare the Arrhenius behavior of RDE (5–60°C) and PEMFC data (40–120°C) at constant overpotential for the 2-electron ORR leads to consistent results of both experimental techniques under the likely assumption of 2–4 orders of magnitude different effective hydrogen peroxide concentrations. The favorably 2-electron ORR together with our finding that the activity of even the most active materials reported in the literature is far below DoE activity targets, in general suggests that ZrO<sub>2</sub> based materials need to be improved substantially in order to achieve a competitive status in noble-metal-free ORR electrocatalysis.

### Acknowledgments

The research leading to these results received funding from the Fuel Cells and Hydrogen Joint Undertaking under grant Agreement

Duramet n°278054 as part of the Seventh Framework Programme of the European Community for research, technological development and demonstration activities (FP7/2007-2013). In addition, we thank Dr. Marianne Hanzlik for the superb TEM images.

### References

- A. Garsuch, A. Bonakdarpour, G. Liu, R. Yang, and J. R. Dahn, in *Handbook of Fuel Cells*, John Wiley & Sons, Ltd, (2010).
- K.-i. Ota, Y. Ohgi, K. Matsuzawa, S. Mitsushima, and A. Ishihara, *ECS Trans.*, **45**(2), 27 (2012).
- A. Ishihara, Y. Ohgi, K. Matsuzawa, S. Mitsushima, and K.-i. Ota, *Electrochim. Acta*, **55**(27), 8005 (2010).
- S. Doi, A. Ishihara, S. Mitsushima, N. Kamiya, and K.-i. Ota, *J. Electrochem. Soc.*, **154**(3), B362 (2007).
- J.-H. Kim, A. Ishihara, S. Mitsushima, N. Kamiya, and K.-i. Ota, *Electrochim. Acta*, **52**(7), 2492 (2007).
- K. Matsuzawa, K. Nozawa, K. Yamauchi, A. Ishihara, S. Mitsushima, and K.-i. Ota, *J. Power Sources*, **226**(0), 16 (2013).
- J. Li Vage, K. Doi, and C. Mazieres, *J. Am. Ceram. Soc.*, **51**(6), 349 (1968).
- Y. Liu, A. Ishihara, S. Mitsushima, N. Kamiya, and K.-i. Ota, *J. Electrochem. Soc.*, **154**(7), B664 (2007).
- A. Ishihara, S. Doi, S. Mitsushima, and K.-i. Ota, *Electrochim. Acta*, **53**(16), 5442 (2008).
- H. Imai, M. Matsumoto, T. Miyazaki, S. Fujieda, A. Ishihara, M. Tamura, and K.-i. Ota, *Appl. Phys. Lett.*, **96**(19), (2010).
- T. Mittermeier, P. Madkikar, X. Wang, H. A. Gasteiger, and M. Piana, in “4th European PEFC and H<sub>2</sub> Forum,” (D. Jones, ed.), p. B07 50-63. European Fuel Cell Forum AG, Lucerne, Switzerland, 2013.
- G. Liu, H. M. Zhang, M. R. Wang, H. X. Zhong, and J. Chen, *J. Power Sources*, **172**(2), 503 (2007).
- D. Sebastián, V. Baglio, S. Sun, A. C. Tavares, and A. S. Aricó, *Chinese Journal of Catalysis*, **36**(4), 484 (2015).
- Y. Ohgi, A. Ishihara, K. Matsuzawa, S. Mitsushima, K.-i. Ota, M. Matsumoto, and H. Imai, *Electrochim. Acta*, **68**(0), 192 (2012).
- A. Ishihara, M. Tamura, Y. Ohgi, M. Matsumoto, K. Matsuzawa, S. Mitsushima, H. Imai, and K.-i. Ota, *J. Phys. Chem. C*, **117**(37), 18837 (2013).
- Y. Ohgi, A. Ishihara, K. Matsuzawa, S. Mitsushima, K.-i. Ota, M. Matsumoto, and H. Imai, *J. Electrochem. Soc.*, **160**(2), F162 (2013).
- S. Yin, A. Ishihara, Y. Kohno, K. Matsuzawa, S. Mitsushima, K.-i. Ota, M. Matsumoto, M. Arao, and H. Imai, *ECS Trans.*, **50**(2), 1785 (2013).
- S. Yin, A. Ishihara, Y. Kohno, K. Matsuzawa, S. Mitsushima, K.-i. Ota, M. Matsumoto, and H. Imai, *ECS Trans.*, **58**(1), 1489 (2013).
- Y. Okada, A. Ishihara, M. Arao, M. Matsumoto, H. Imai, Y. Kohno, K. Matsuzawa, S. Mitsushima, and K.-i. Ota, *ECS Trans.*, **64**(3), 231 (2014).

20. A. Ishihara, M. Hamazaki, M. Arao, M. Matsumoto, H. Imai, Y. Kohno, K. Matsuzawa, S. Mitsushima, and K. Ota, *J. Electrochem. Soc.*, **163**(7), F603 (2016).
21. Y. Liu, A. Ishihara, S. Mitsushima, and K.-i. Ota, *Electrochim. Acta*, **55**(3), 1239 (2010).
22. Y. Okada, A. Ishihara, M. Matsumoto, M. Arao, H. Imai, Y. Kohno, K. Matsuzawa, S. Mitsushima, and K. Ota, *J. Electrochem. Soc.*, **162**(9), F959 (2015).
23. K. Ukita, A. Ishihara, Y. Ohgi, K. Matsuzawa, S. Mitsushima, and K.-i. Ota, *Electrochemistry*, **79**(5), 340 (2011).
24. P. Madkikar, X. Wang, T. Mittermeier, A. H. A. Monteverde Videla, C. Denk, S. Specchia, H. A. Gasteiger, and M. Piana, *Comparative study of carbon-supported ZrO<sub>2</sub> nanoparticles synthesized from different organometallic precursors*, manuscript in preparation.
25. P. J. Rheinländer, J. Herranz, J. Durst, and H. A. Gasteiger, *J. Electrochem. Soc.*, **161**(14), F1448 (2014).
26. W. Gu, D. R. Baker, Y. Liu, and H. A. Gasteiger, in *Handbook of Fuel Cells - Fundamentals, Technology and Applications*, W. Vielstich, A. Lamm, and H. A. Gasteiger, eds., Vol. 6, p. 631, John Wiley & Sons, Ltd., (2009).
27. H. A. Gasteiger, S. S. Kocha, B. Sompalli, and F. T. Wagner, *Applied Catalysis B: Environmental*, **56**(1–2), 9 (2005).
28. N. M. Marković and P. N. Ross Jr, *Surf. Sci. Rep.*, **45**(4–6), 117 (2002).
29. M. Sathish, B. Viswanathan, and R. P. Viswanath, *Appl. Catal., B*, **74**(3–4), 307 (2007).
30. C. Rüdiger, F. Maglia, S. Leonardi, M. Sachsenhauser, I. D. Sharp, O. Paschos, and J. Kunze, *Electrochim. Acta*, **71**(0), 1 (2012).
31. F. Jaouen and J.-P. Dodelet, *J. Phys. Chem. C*, **113**(34), 15422 (2009).
32. U. A. Paulus, T. J. Schmidt, H. A. Gasteiger, and R. J. Behm, *J. Electroanal. Chem.*, **495**(2), 134 (2001).
33. A. J. Bard and L. R. Faulkner, *Electrochemical Methods: Fundamentals and Applications*, John Wiley & Sons, Inc. (2001).
34. A. Bonakdarpour, M. Lefevre, R. Yang, F. Jaouen, T. Dahn, J.-P. Dodelet, and J. R. Dahn, *Electrochem. Solid-State Lett.*, **11**(6), B105 (2008).
35. F. Jaouen, J. Herranz, M. Lefèvre, J.-P. Dodelet, U. I. Kramm, I. Herrmann, P. Bogdanoff, J. Maruyama, T. Nagaoka, A. Garsuch, J. R. Dahn, T. Olson, S. Pylypenko, P. Atanassov, and E. A. Ustinov, *ACS Appl. Mater. Interfaces*, **1**(8), 1623 (2009).
36. K. C. Neyerlin, W. Gu, J. Jorne, and H. A. Gasteiger, *J. Electrochem. Soc.*, **153**(10), A1955 (2006).
37. S. L. Manatt and M. R. R. Manatt, *Chem. - Eur. J.*, **10**(24), 6540 (2004).
38. A. Ishihara, S. Yin, K. Suito, N. Uehara, Y. Okada, Y. Kohno, K. Matsuzawa, S. Mitsushima, M. Chisaka, Y. Ohgi, M. Matsumoto, H. Imai, and K.-i. Ota, *ECS Trans.*, **58**(1), 1495 (2013).
39. U. I. Kramm, J. Herranz, N. Larouche, T. M. Arruda, M. Lefevre, F. Jaouen, P. Bogdanoff, S. Fiechter, I. Abs-Wurmbach, S. Mukerjee, and J.-P. Dodelet, *PCCP*, **14**(33), 11673 (2012).
40. C. Velasco-Santos, A. L. Martinez-Hernandez, and V. M. Castano, *Compos. Inter-faces*, **11**(8–9), 567 (2005).
41. U.S. Department of Energy, in "Fuel Cell Technologies Office Multi-Year Research, Development, and Demonstration Plan," Vol. 2015. U.S. Department of Energy, 2012.

### 3.3. Synergistic Effect on the Activity of ZrO<sub>2</sub>-Fe as PGM-Free ORR Catalysts for PEMFCs

P. Madkikar, T. Mittermeier, H. A. Gasteiger, and M. Piana

Journal of The Electrochemical Society 2017, Volume 164, Issue 7, F831-F833

Permanent weblink: <http://dx.doi.org/10.1149/2.1091707jes>

This is an open access article distributed under the terms of the Creative Commons Attribution Non-Commercial No Derivatives 4.0 License (CC BY-NC-ND, <http://creativecommons.org/licenses/by-nc-nd/4.0/>), which permits non-commercial reuse, distribution, and reproduction in any medium, provided the original work is not changed in any way and is properly cited. For permission for commercial reuse, please email: [oa@electrochem.org](mailto:oa@electrochem.org).

Our past study made it clear that the ORR activity of pure ZrO<sub>2</sub>-based catalysts is low and needs to be significantly improved. Nevertheless, it was also confirmed that we need both Zr and N to get relatively higher activity than pure Zr based samples. In addition, it was also seen that the density of active sites with Zr and N seems to be very low. Thus, it was concluded that there is a need to substitute ZrO<sub>2</sub> with an aliovalent cation. We chose Fe (Fe<sup>3+</sup>) as a candidate for substitution of traces of Zr (Zr<sup>4+</sup>) in ZrO<sub>2</sub>. This was mainly because of two reasons: first, Fe itself has intermediate ORR activity and second, literature reports indicate an increase in oxygen vacancies in ZrO<sub>2</sub> upon Fe doping. It was assumed that this increase in the oxygen vacancies could potentially increase the ORR activity of ZrO<sub>2</sub> catalysts, since they were hypothesized to be active sites for ORR.

Zirconium (IV) tetra-tert-butyl-dichlorophthalocyanine (ZrCl<sub>2</sub>Pc(t-Bu)<sub>4</sub>) and iron(II) tetra-tert-butyl-phthalocyanine FePc(t-Bu)<sub>4</sub> were chosen for this study. Both precursors were synthesised based on previous reports. They were further deposited on graphitized Ketjenblack (KB<sub>graph</sub>) similarly to our past study. KB<sub>graph</sub> was used to minimize the presence of oxygen surface groups. ZrO<sub>2</sub> was targeted to 12 wt% on the carbon support and the Fe amount was varied in each sample (0.1, 0.36, 1.0, and 10 wt%, referenced to the weight catalyst),

yielding a Fe/ZrO<sub>2</sub> atomic ratios of: 2/98, 7/93, 17/83, and 65/35. Pure Fe and pure ZrO<sub>2</sub> samples supported on KB<sub>graph</sub> were also synthesised, where the Fe and ZrO<sub>2</sub> loading was 0.36 and 12 wt%, respectively. All described samples were heat treated at 800 °C under partial oxidation (PO) conditions (cf. chapters 2.2.2, 3.1 and 3.2). Heat-treated catalysts were characterised by XRPD to check the phases present. They were further characterised by thin-film RDE voltammetry in order to compare their ORR activities. Finally, ZrO<sub>2</sub>-Fe (0.36 wt% Fe) was additionally characterised by the RRDE technique to obtain the H<sub>2</sub>O<sub>2</sub> yield.

Based on our study, it was confirmed that there exists a synergistic effect between Fe and ZrO<sub>2</sub>, which is evident from the ≈200 mV lower overpotential for ZrO<sub>2</sub>-Fe samples (1.0 and 0.36 wt%) in comparison to the samples with the pure Fe (0.36 wt%) and pure ZrO<sub>2</sub>.

### **Author contributions**

P. M. and M. P. conceived the project. M. P. and H. A. G. coordinated the project. P. M. synthesised and characterised the catalysts. P. M. and M. P. wrote the manuscript. T. M, M. P., and H. A. G. revised the manuscript. All authors discussed the results and commented on the manuscript.



## Communication—Synergistic Effect on the Activity of ZrO<sub>2</sub>-Fe as PGM-Free ORR Catalysts for PEMFCs

Pankaj Madkikar,<sup>\*,z</sup> Thomas Mittermeier,<sup>\*</sup> Hubert A. Gasteiger,<sup>\*\*</sup> and Michele Piana<sup>\*\*\*</sup>

Chair of Technical Electrochemistry, Department of Chemistry and Catalysis Research Center, Technische Universität München, D-85748 Garching, Germany

Here we report a new strategy to enhance the ORR activity of valve-metal-oxide electrocatalysts by combining an aliovalent cation (Fe) with ZrO<sub>2</sub> (particle size < 10 nm). This results in a strong increase of the ORR activity, which is clearly higher than that obtained by the individual components. The highest ORR activity for a carbon supported ZrO<sub>2</sub> catalyst with 12 wt% ZrO<sub>2</sub> is observed upon the addition of 0.36–1.0 wt% Fe (≡ Fe/Zr atomic ratios of 0.02–0.08).

© The Author(s) 2017. Published by ECS. This is an open access article distributed under the terms of the Creative Commons Attribution Non-Commercial No Derivatives 4.0 License (CC BY-NC-ND, <http://creativecommons.org/licenses/by-nc-nd/4.0/>), which permits non-commercial reuse, distribution, and reproduction in any medium, provided the original work is not changed in any way and is properly cited. For permission for commercial reuse, please email: [oa@electrochem.org](mailto:oa@electrochem.org). [DOI: 10.1149/2.1091707jes] All rights reserved.



Manuscript submitted March 9, 2017; revised manuscript received May 11, 2017. Published May 26, 2017.

High cost and limited availability of platinum-based catalysts for the oxygen reduction reaction (ORR) is a major hurdle toward the commercialization of proton exchange membrane fuel cell (PEMFC) systems. Potential candidates for Pt-free ORR catalyst with high stability in acids are based on partially-oxidized valve-metal oxides, which were first reported and studied by Ota's group, using different synthetic routes.<sup>1–4</sup> In a recent publication,<sup>5</sup> we compared the ORR mass activity of their various N-doped catalysts ranging from 0.0004 to 0.4 A/g<sub>catalyst</sub> (evaluated at an extrapolated potential of 0.8 V vs. the reversible hydrogen electrode (RHE) potential) with that of our optimized Ketjenblack-supported ZrO<sub>2</sub>/KB catalysts (≈ 0.04 A/g<sub>catalyst</sub>). While we could not exclude the possibility that we may not have found the optimum synthesis conditions, we hypothesized that the ≈10-fold lower activity of our catalyst compared to Ota et al. most active catalysts might be due to the presence of iron impurities.<sup>5</sup> In principle, this would be consistent with the commonly stated hypothesis that the active sites in ZrO<sub>2</sub> based ORR catalysts are due to the presence of oxygen vacancies or uncoordinated metal sites at the oxide surface,<sup>6,7</sup> so that doping of the oxide structure with aliovalent metals could enhance the ORR activity. Therefore, we have chosen to examine the effect of iron as a substituent, particularly since it is both ORR-active by itself<sup>8–11</sup> and is known to be able to substitute Zr in the ZrO<sub>2</sub> structure.<sup>12,13</sup> To our knowledge, this is a novel approach to increase the ORR activity of valve-metal-oxide-based catalysts while trying to keep their acid stability.

### Experimental

All chemicals were obtained from Sigma-Aldrich, unless specified otherwise. Zirconium (IV) tetra-tert-butyl-dichlorophthalocyanine (ZrCl<sub>2</sub>Pc(t-Bu)<sub>4</sub>) was synthesized as reported by Tomachynski et al.,<sup>14</sup> using 4-tert-butylphthalonitrile (≥98%, from TCI), ZrCl<sub>4</sub> (≥99.5%), 2-methylnaphthalene (β, 97%), 2-bromonaphthalene (97%), and chloroform (≥99.9%). Iron(II) tetra-tert-butyl-phthalocyanine (FePc(t-Bu)<sub>4</sub>) was synthesized similarly to Tomoda et al.,<sup>15</sup> starting from FeCl<sub>2</sub> (98%), 1,8-diazabicyclo[5.4.0]-5-undec-7-ene (≥99.0%), 2-ethoxyethanol (99%), and chloroform (≥99.9%). The only modification in the original procedures was the replacement of 1,2-dicyanobenzene with 4-tert-butylphthalonitrile as starting precursor, to produce soluble phthalocyanines. The formation of metal phthalocyanines was proven by Fourier transform infrared spectroscopy, based on the Pc fingerprint and the absence of NH bending to confirm the insertion of metal.<sup>16,17</sup> Metal-Pc purity was further quantified by thermogravimetric analysis under air.

ZrCl<sub>2</sub>Pc(t-Bu)<sub>4</sub> and/or FePc(t-Bu)<sub>4</sub> were deposited on graphitized Ketjenblack (KB<sub>graph</sub>) (EA-type from Tanaka Kikinokogyo K.K.) as described previously,<sup>17</sup> targeting a loading of 12 wt% ZrO<sub>2</sub>/KB<sub>graph</sub>. KB<sub>graph</sub> was used to minimize the presence of oxygen surface groups. The corresponding amount of ZrCl<sub>2</sub>Pc(t-Bu)<sub>4</sub> and/or FePc(t-Bu)<sub>4</sub> for the desired metal-based Fe content was impregnated on carbon using CHCl<sub>3</sub> as solvent. The Fe content of the ZrO<sub>2</sub>-Fe/KB<sub>graph</sub> catalysts based on the amount of precursors was 0.1, 0.36, 1.0 and 10 wt% (Fe/ZrO<sub>2</sub> atomic ratios: 2/98, 7/93, 17/83, and 65/35, respectively); as a reference, 0.36 wt% Fe/KB<sub>graph</sub> were also prepared. After impregnation, the solvent was removed by rotovaporation (Heidolph, Hei-VAP Value). The mixture was further dried overnight at RT and then heat-treated in a quartz tube furnace (HTM Reetz) by heating the samples in 5% H<sub>2</sub>/Ar until 800°C (at a rate of ≈10°C min<sup>-1</sup> to ≈700°C and 2°C min<sup>-1</sup> to 800°C), then holding the temperature for 2 h in the same gas-mixture, followed by switching to a mixture of 2.5% H<sub>2</sub> and 0.5% O<sub>2</sub> in Ar (all gases supplied by Westfalen AG) for 1 h. Finally, the sample was cooled to RT in 5% H<sub>2</sub>/Ar.

The final catalysts were analyzed using a STOE X-ray powder diffractometer, equipped with a monochromatized molybdenum (Mo) K<sub>α1</sub> X-ray source (λ = 0.7093 Å, 50 kV, 40 mA). The measurements were performed in Debye-Scherrer geometry with a 2θ range of 2–50° and a step size of 0.015° 2θ. The procedure to determine the ORR activity and H<sub>2</sub>O<sub>2</sub> yield of the catalysts is reported in Ref. 5, 18, 19. The only difference was in the ink preparation, here done by dispersing the catalysts in pure N,N-dimethylformamide (≥99.8%, Fisher Scientific) by sonication in a cold-bath for 1 h. After this, a Nafion solution (5 wt% Nafion) was added to obtain a Nafion/carbon mass ratio of ≈1/4 and the mixture was further sonicated for 5 min.

### Results and Discussion

The X-ray diffraction (XRD) analysis of the synthesized electrocatalysts shown in Figure 1 confirms the formation of zirconia (ZrO<sub>2</sub>) in all Zr-containing samples. Phase assignment between tetragonal (PDF no. 01-072-7115) or cubic (PDF no. 01-071-4810) is not possible, as these two phases are very similar and the reflections are extremely broadened. The ZrO<sub>2</sub> crystallite size was estimated by the Scherrer equation, comparing the full width at half maximum of the ZrO<sub>2</sub>-Fe/KB<sub>graph</sub> catalysts with that of the ≈10 nm ZrO<sub>2</sub>/KB catalyst prepared previously,<sup>17</sup> yielding a crystallite size on the order of several nanometers for the ZrO<sub>2</sub>-Fe/KB<sub>graph</sub> catalysts. In addition, no evident Fe compounds are detected for the samples with 0.1, 0.36, and 1.0 wt% Fe. This is either due to the formation of very small (<3 nm) or amorphous nanoparticles, and/or to Fe<sup>3+</sup> substitution into the ZrO<sub>2</sub> structure. Unfortunately, the latter cannot be determined from shifts in the ZrO<sub>2</sub> diffractions, due to the very broad diffraction peaks.

\*Electrochemical Society Student Member.

\*\*Electrochemical Society Fellow.

\*\*\*Electrochemical Society Member.

<sup>z</sup>E-mail: [pankaj.madkikar@tum.de](mailto:pankaj.madkikar@tum.de)

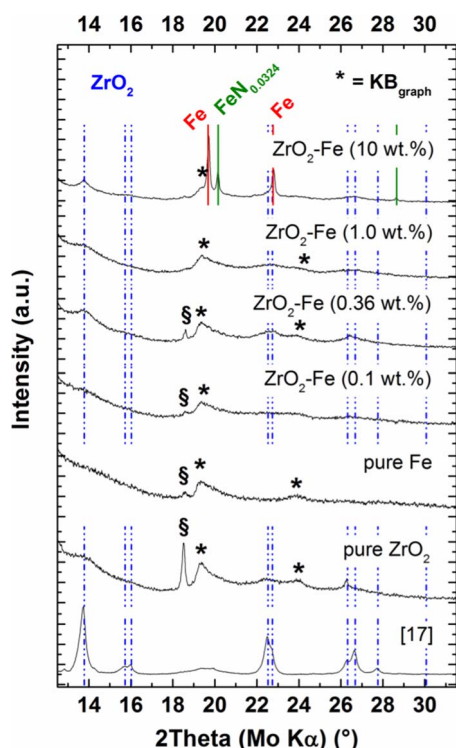


**Figure 1.** X-ray diffractograms of 0.36 wt% Fe/ $\text{KB}_{\text{graph}}$ , 12 wt%  $\text{ZrO}_2/\text{KB}_{\text{graph}}$ , and  $\text{ZrO}_2\text{-Fe}/\text{KB}_{\text{graph}}$  catalysts (with 0.1, 0.36, 1.0, or 10 wt% Fe and 12 wt%  $\text{ZrO}_2$ ) and 13 wt%  $\text{ZrO}_2/\text{KB}$  from Reference 17. The reflections marked with § are instrument-based artefacts.

On the other hand, the  $\text{ZrO}_2\text{-Fe}/\text{KB}_{\text{graph}}$  catalyst with 10 wt% Fe shows clear Fe (PDF no. 00-006-0696) and  $\text{FeN}_{0.0324}$  (PDF no. 01-075-2127) phases (crystallite size of  $\approx 30$  and  $\approx 40$  nm, respectively, estimated by the Scherrer equation), whereby the formation of metallic Fe probably occurs during the final cooling phase in 5%  $\text{H}_2/\text{Ar}$ . A more detailed structural characterization of the samples is the focus of future work.

Figure 2a shows the activities of the various catalysts in 0.1 M  $\text{HClO}_4$  at 1600 rpm under pure  $\text{O}_2$ , whereby the current density range ( $< 0.5$   $\text{mA}/\text{cm}^2$ ) was far below the limiting current densities for the 4-electron reduction to  $\text{H}_2\text{O}$  ( $\approx 6$   $\text{mA}/\text{cm}^2$ ) and the 2-electron reduction to  $\text{H}_2\text{O}_2$  ( $\approx 3$   $\text{mA}/\text{cm}^2$ ), so that the shown ORR activities reflect the kinetic mass activities of the catalysts. It shows that the  $\text{ZrO}_2\text{-Fe}/\text{KB}_{\text{graph}}$  catalysts (0.1, 0.36, 1.0, and 10 wt% Fe) have a much higher ORR activity in comparison to pure 0.36 wt%  $\text{Fe}/\text{KB}_{\text{graph}}$ , 12 wt%  $\text{ZrO}_2/\text{KB}_{\text{graph}}$ , and our previously published 13 wt%  $\text{ZrO}_2/\text{KB}$ ,<sup>5</sup> clearly indicating the strong synergistic effect of Fe on the ORR activity of  $\text{ZrO}_2$ . The highest ORR activities are observed for the  $\text{ZrO}_2\text{-Fe}/\text{KB}_{\text{graph}}$  catalysts with 0.36 and 1 wt% Fe ( $\equiv \text{Fe}/\text{Zr}$  atomic ratios of 0.02 and 0.08), which show  $\approx 200$  mV lower overpotentials compared to pure  $\text{ZrO}_2$  at  $-1$   $\text{A}/\text{g}_{\text{cat}}$ , whereby their mass activities of  $\approx 0.15\text{--}0.20$   $\text{A}/\text{g}_{\text{cat}}$  at 0.8  $\text{V}_{\text{RHE}}$  are very close to the best  $\text{ZrO}_2/\text{carbon}$  catalysts reported so far.<sup>5</sup> The decrease in ORR activity for 10 wt% Fe is likely due to the formation of less active compounds, namely metallic Fe and  $\text{FeN}_{0.0324}$ <sup>10,11</sup> (s. Figure 1); on the other hand, the lowered ORR activity for the 0.1 wt% Fe is probably due to a decreasing density of active sites. While the nature of the active sites is still under investigation (e.g., whether Fe is being substitute into the structure of  $\text{ZrO}_2$ ), it is obvious that the presence of small amounts of Fe species substantially improves the ORR activity of  $\text{ZrO}_2/\text{carbon}$  catalysts, as we had hypothesized previously.<sup>5</sup>

The RRDE data analysis in Figure 2b shows that the  $\text{H}_2\text{O}_2$  yield of the best catalyst  $\text{ZrO}_2\text{-Fe}/\text{KB}_{\text{graph}}$  (0.36 wt% Fe) at a loading of 72  $\mu\text{g}_{\text{cat}}/\text{cm}^2$  is  $\approx 20\%$ , somewhat lower than the  $\approx 40\text{--}50\%$  ob-

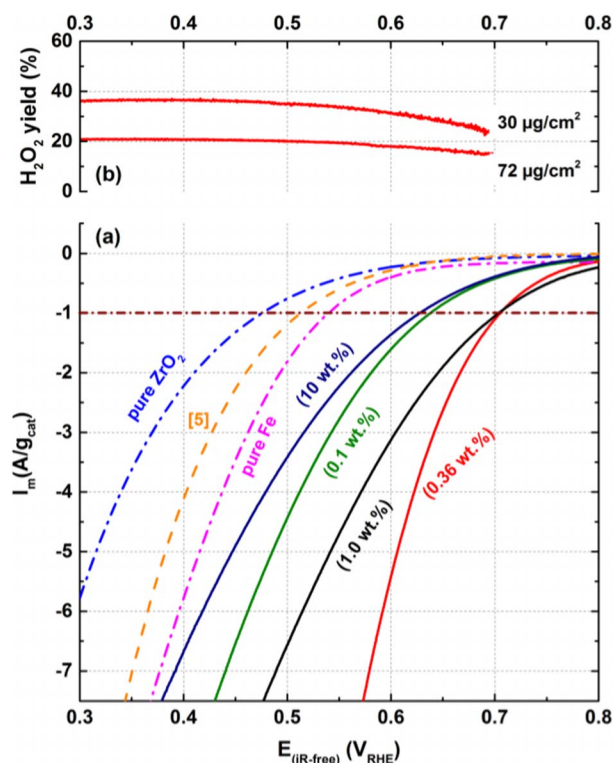


**Figure 2.** a) ORR mass activities of 0.36 wt%  $\text{Fe}/\text{KB}_{\text{graph}}$ , 12 wt%  $\text{ZrO}_2/\text{KB}_{\text{graph}}$ , and  $\text{ZrO}_2\text{-Fe}/\text{KB}_{\text{graph}}$  catalysts (with 0.1, 0.36, 1.0, or 10 wt% Fe and 12 wt%  $\text{ZrO}_2$ ) and 13 wt%  $\text{ZrO}_2/\text{KB}$ ,<sup>5</sup> measured by thin-film RDE ( $70\text{--}76$   $\mu\text{g}_{\text{cat}}/\text{cm}^2$ ) in  $\text{O}_2$  saturated 0.1 M  $\text{HClO}_4$  at 20°C and 1600 rpm. The activities are taken from capacitively-corrected anodic scans recorded at 5 mV/s. b) Peroxide yield of  $\text{ZrO}_2\text{-Fe}$  (0.36 wt% Fe) at the catalyst loading used in a) and at a  $\approx 2.5$ -fold lower loading (collection efficiency  $N = 0.255$ ).

served for our best  $\text{ZrO}_2/\text{KB}$  catalyst reported previously.<sup>5</sup> However, as the  $\text{ZrO}_2\text{-Fe}/\text{KB}_{\text{graph}}$  loading is decreased to 30  $\mu\text{g}_{\text{cat}}/\text{cm}^2$ , the  $\text{H}_2\text{O}_2$  yield increases to  $\approx 40\%$ , which is quite comparable in behavior and magnitude to what was reported for nitrogen/carbon-coordinated iron catalysts.<sup>19</sup> Getting a better understanding about the active sites and testing the long-term stability of optimized  $\text{ZrO}_2\text{-Fe}/\text{carbon}$  catalyst is the focus of our future studies.

## Summary

Here we report the successful synthesis of carbon-supported  $\text{ZrO}_2$  nanoparticles ( $< 10$  nm) with a defined amount of Fe, as new strategy to enhance their ORR activity. A clear synergistic effect between Fe and  $\text{ZrO}_2$  is evident from the fact that  $\text{ZrO}_2\text{-Fe}$  (1.0 or 0.36 wt%) have a  $\approx 200$  mV lower overpotential compared to both samples with pure Fe (0.36 wt%) or pure  $\text{ZrO}_2$ . Lower or higher Fe loadings leads to decreased ORR activity. The  $\text{H}_2\text{O}_2$  yield for the best catalyst is, however, comparable to that of nitrogen/carbon-coordinated iron catalysts.

## Acknowledgments

The Bayerische Forschungsstiftung (Project ForOxiE<sup>2</sup>, AZ 1143-14) supported this work.

## References

- S. Yin, A. Ishihara, Y. Kohno, K. Matsuzawa, S. Mitsushima, K.-I. Ota, M. Matsumoto, M. Arai, and H. Imai, *ECS Trans.*, **50**(2), 1785 (2013).
- S. Yin, A. Ishihara, Y. Kohno, K. Matsuzawa, S. Mitsushima, K.-I. Ota, M. Matsumoto, and H. Imai, *ECS Trans.*, **58**(1), 1489 (2013).
- Y. Okada, A. Ishihara, M. Arai, M. Matsumoto, H. Imai, Y. Kohno, K. Matsuzawa, S. Mitsushima, and K.-I. Ota, *ECS Trans.*, **64**(3), 231 (2014).



4. A. Ishihara, S. Yin, K. Suito, N. Uehara, Y. Okada, Y. Kohno, K. Matsuzawa, S. Mitsushima, M. Chisaka, Y. Ohgi, M. Matsumoto, H. Imai, and K. -I. Ota, *ECS Trans.*, **58**(1), 1495 (2013).
5. T. Mittermeier, P. Madkikar, X. Wang, H. A. Gasteiger, and M. Piana, *J. Electrochem. Soc.*, **163**, F1543 (2016).
6. A. Ishihara, M. Tamura, Y. Ohgi, M. Matsumoto, K. Matsuzawa, S. Mitsushima, H. Imai, and K. -I. Ota, *J. Phys. Chem. C*, **117**, 18837 (2013).
7. Y. Ohgi, A. Ishihara, K. Matsuzawa, S. Mitsushima, K. -I. Ota, M. Matsumoto, and H. Imai, *J. Electrochem. Soc.*, **160**, F162 (2013).
8. M. Lefèvre and J. P. Dodelet, *ECS Trans.*, **45**(2), 35 (2012).
9. B. Piela, T. S. Olson, P. Atanassov, and P. Zelenay, *Electrochim. Acta*, **55**, 7615 (2010).
10. U. Kramm, J. Herranz, N. Larouche, T. Arruda, M. Lefèvre, F. Jaouen, P. Bogdanoff, S. Fiechter, I. Abs-Wurmbach, S. Mukerjee, and J-P. Dodelet, *Phys. Chem. Chem. Phys.*, **14**, 11673 (2012).
11. C. Choi, C. Baldizzone, J-P. Grote, A. Schuppert, F. Jaouen, and K. Mayrhofer, *Angew. Chem. Int. Ed.*, **54**, 12753 (2015).
12. S. Kumar, S. Bhunia, J. Singh, and A. Ojha, *J. Alloys Comp.*, **649**, 348 (2015).
13. G. Herrera, N. Montoya, A. Doménech-Carbó, and J. Alarcón, *Phys. Chem. Chem. Phys.*, **15**, 19312 (2013).
14. L. Tomachynski, V. Chernii, and S. Volkov, *Russ J Inorg Chem.*, **47**, 208 (2002).
15. H. Tomoda, S. Saito, and S. Shiraishi, *Chem. Lett.*, **12**, 313 (1983).
16. R. Seoudi, G. S. El-Bahy, and Z. A. El Sayed, *J. Mol. Struct.*, **753**, 119 (2005).
17. P. Madkikar, X. Wang, T. Mittermeier, A. Monteverde Videla, C. Denk, S. Specchia, H. Gasteiger, and M. Piana, *J. Nanostructure Chem.*, **7**, (2017).
18. U. Paulus, T. Schmidt, H. Gasteiger, and R. Behm, *J. Electroanal. Chem.*, **495**, 134 (2001).
19. A. Bonakdarpour, M. Lefevre, R. Yang, F. Jaouen, T. Dahn, J-P. Dodelet, and J. R. Dahn, *Electrochem. Solid State Lett.*, **11**, B105 (2008).

### 3.4. Nanometric Fe-Substituted ZrO<sub>2</sub> on Carbon Black as Novel PGM-Free ORR Catalyst for PEMFCs

P. Madkikar, D. Menga, G. S. Harzer, T. Mittermeier, A. Siebel, F. E. Wagner, M. Merz, S. Schuppler, P. Nagel, A. B. Muñoz-Garcia, M. Pavone, H. A. Gasteiger, and M. Piana

After we communicated that a clear synergism exists between Fe and ZrO<sub>2</sub> in the mixed catalyst compared to its single components (chapter 3.3), the open remaining question was the origin of such synergism, likely related to the catalyst structure and the nature of Fe-coordination in the catalysts, which we unveiled here. Furthermore, tests in single-cell PEMFCs were performed to evaluate the activity of the Fe-substituted ZrO<sub>2</sub> catalyst.

We selected 0.36 wt% Fe in ZrO<sub>2</sub> (Fe<sub>0.07</sub>Zr<sub>0.93</sub>O<sub>1.97</sub>), 1.0 wt% Fe in ZrO<sub>2</sub> (Fe<sub>0.17</sub>Zr<sub>0.83</sub>O<sub>1.91</sub>), pure Fe, and pure ZrO<sub>2</sub> samples for this study. They were subjected to both ICP and TGA analyses to obtain the actual content of Fe and ZrO<sub>2</sub> in the samples, since the aforementioned amounts are theoretical. Furthermore, the average particle size of the three ZrO<sub>2</sub>-containing samples was estimated from TEM micrographs. XPS analysis was performed on Fe<sub>0.07</sub>Zr<sub>0.93</sub>O<sub>1.97</sub> and Fe<sub>0.17</sub>Zr<sub>0.83</sub>O<sub>1.91</sub> samples to check the oxidation state of Fe and Zr in the samples. The same samples were further subjected to NEXAFS (Fe L<sub>2,3</sub> edge), more sensitive than XPS for the determination of oxidation and spin state. The Fe-related results from both XPS and NEXAFS were compared to those from Mössbauer analysis. In addition to its structural characterisation, a rigorous electrochemical characterisation of Fe<sub>0.07</sub>Zr<sub>0.93</sub>O<sub>1.97</sub> was performed. It included TF-RDE and PEMFC measurements at various temperatures for the determination of Tafel slopes and apparent activation energies and RRDE measurements for intrinsic activity and H<sub>2</sub>O<sub>2</sub> yield at different catalyst loadings. In complement to the various experimental characterisation techniques applied, DFT calculations were performed on the Fe-substituted ZrO<sub>2</sub> structure to obtain the oxidation state of Fe, the oxygen-vacancy formation energy and to understand the nature and activity of active site(s).



From the ICP analyses, it was observed that both the Fe and ZrO<sub>2</sub> content in the catalysts are approximately half of their theoretical value. This was attributed to the increased sample weight due to carbon produced from the Pc complex after heat-treatment. Nevertheless, the atomic ratio between Fe and ZrO<sub>2</sub> remained as theoretically expected. Using particle size distribution analyses, it is found that the (number based) average particle size of ZrO<sub>2</sub> in the catalysts (Fe<sub>0.07</sub>Zr<sub>0.93</sub>O<sub>1.97</sub> and Fe<sub>0.17</sub>Zr<sub>0.83</sub>O<sub>1.91</sub>) is ≈3 nm. Furthermore, XPS measurements confirm that the dominant oxidation state of Fe in both samples is 3+. Unfortunately, minor presence of Fe<sup>2+</sup> could not be excluded. NEXAFS analysis proved to be very helpful, since we could unambiguously confirmed that Fe is present in the high-spin Fe<sup>3+</sup> state, while Fe<sup>2+</sup> is absent. These results are in accordance with Mössbauer spectra, which also indicated that Fe is in high-spin Fe<sup>3+</sup> state and demonstrated that Fe is present as atomically dispersed species, which clearly infers the formation of Fe-substituted ZrO<sub>2</sub> (Fe<sub>x</sub>Zr<sub>1-x</sub>O<sub>2-δ</sub>). The oxidation and spin state of Fe is also confirmed by DFT calculations, which further indicates that Fe is likely present in the topmost atomic layer of the catalyst.

DFT shows that the oxygen-vacancy formation is much easier in Fe-substituted ZrO<sub>2</sub> in comparison to pure ZrO<sub>2</sub>. Furthermore, the higher ORR activity of Fe<sub>x</sub>Zr<sub>1-x</sub>O<sub>2-δ</sub> compared to pure ZrO<sub>2</sub> is supported by DFT. In addition, the type of products (H<sub>2</sub>O and H<sub>2</sub>O<sub>2</sub>) formed in the ORR on Fe<sub>0.07</sub>Zr<sub>0.93</sub>O<sub>1.97</sub> was determined by RRDE, which is in accordance to the DFT results on the most likely reaction paths. Using RRDE analysis, we also observed a clear increase in mass activity for Fe<sub>0.07</sub>Zr<sub>0.93</sub>O<sub>1.97</sub> with increased catalyst loadings, in agreement with the data on Fe-N-C catalyst reported by Bonakdarpour et al. [38]. Furthermore, also the single-cell PEMFC measurements confirm that Fe<sub>0.07</sub>Zr<sub>0.93</sub>O<sub>1.97</sub> is much more active than pure ZrO<sub>2</sub> catalysts. Higher ORR activity of Fe<sub>0.07</sub>Zr<sub>0.93</sub>O<sub>1.97</sub> vs. pure ZrO<sub>2</sub> catalysts is also supported by its lower Tafel slope (170 – 130 mV/decade) and lower activation energy (18.4 kJ/mol at 0.4 V) compared to pure ZrO<sub>2</sub> catalysts (190 – 230 mV/decade and 28.6 kJ/mol at 0.4 V).

### **Author contributions**

P. M. and M. Pi. conceived and coordinated the project. D. M. synthesised the catalysts. P. M. performed TEM and R(R)DE measurements. G. S. H. performed the fuel cell measurements and P. M. performed the data analysis. A. S. performed XPS measurements. F. E. W. performed Mössbauer analysis. M. M., S. S., and P. N. performed NEXAFS, followed by data treatment (together with M. Pi.). A. B. M-G. and M. Pa. performed DFT calculations. P. M. and M. Pi. wrote the manuscript. M. Pi., T. M., A. S., and H. A. G. revised the manuscript. All authors discussed the results and commented on the manuscript.

### 3. *Noble-Metal-Free Electrocatalysts*

This page is left intentionally blank.

# Nanomeric Fe-Substituted ZrO<sub>2</sub> on Carbon Black as Novel PGM-Free ORR Catalyst for PEMFCs

Pankaj Madkikar<sup>a</sup>, Davide Menga<sup>a</sup>, Gregor S. Harzer<sup>a</sup>, Thomas Mittermeier<sup>a,b</sup>, Armin Siebel<sup>a</sup>, Friedrich E. Wagner<sup>c</sup>, Michael Merz<sup>d</sup>, Stefan Schuppler<sup>d</sup>, Peter Nagel<sup>d</sup>, Ana Belén Muñoz-García<sup>e</sup>, Michele Pavone<sup>f</sup>, Hubert A. Gasteiger<sup>a</sup>, Michele Piana<sup>a</sup>

<sup>a</sup>Chair of Technical Electrochemistry, Department of Chemistry and Catalysis Research Center, Technische Universität München, D-85748 Garching, Germany

<sup>b</sup>Present address: BMW Group, D-80788 Munich, Germany

<sup>c</sup>Department of Physics, Technische Universität München, D-85748 Garching, Germany

<sup>d</sup>Karlsruher Institut für Technologie, Institut für Festkörperphysik, 76021 Karlsruhe, Germany

<sup>e</sup>Department of Physics “Ettore Pancini”, Università degli Studi di Napoli “Federico II”, Via Cintia 21, 80126 Naples, Italy

<sup>f</sup>Department of Chemical Sciences, Università degli Studi di Napoli “Federico II”, Via Cintia 21, 80126 Naples, Italy

---

## Abstract

In this contribution, we demonstrate the presence of high-spin Fe<sup>3+</sup> in Fe-substituted ZrO<sub>2</sub> (Fe<sub>x</sub>Zr<sub>1-x</sub>O<sub>2-δ</sub>), as deduced from X-ray photoelectron spectroscopy (XPS), near-edge X-ray absorption fine structure (NEXAFS), and <sup>57</sup>Fe Mössbauer spectroscopy measurements. The activity of this carbon-supported Fe<sub>x</sub>Zr<sub>1-x</sub>O<sub>2-δ</sub> catalyst towards the oxygen reduction reaction (ORR) was examined by both the rotating (ring) disk electrode (R(R)DE) method and in single-cell proton exchange membrane fuel cells (PEMFCs). DFT calculations suggest that the much higher ORR mass activity of Fe<sub>x</sub>Zr<sub>1-x</sub>O<sub>2-δ</sub> compared to Fe-free ZrO<sub>2</sub> is due to the enhanced formation of oxygen vacancies: their formation is favoured after Zr<sup>4+</sup> substitution with Fe<sup>3+</sup> and the oxygen vacancies create potential adsorption sites, which act as active centres for the ORR. H<sub>2</sub>O and/or H<sub>2</sub>O<sub>2</sub> production observed in RRDE measurements for the Fe<sub>0.07</sub>Zr<sub>0.93</sub>O<sub>1.97</sub> is also in agreement with the most likely reaction paths from DFT calculations. Tafel and Arrhenius analyses are performed on Fe<sub>0.07</sub>Zr<sub>0.93</sub>O<sub>1.97</sub> using both RRDE and PEMFC data, confirming Tafel slopes and activation energies lower than in Fe-free ZrO<sub>2</sub> catalysts.

---

## Introduction

Year 2015 was a landmark in the field of green energy, as 195 countries reached an agreement on the platform of the United Nations in France to lower greenhouse gas (GHG) emissions [1]. Zero emission vehicles (ZEVs) have gained paramount importance in order to decrease global GHG emissions from the transportation sector, which accounts for ≈14% of the total global emissions [2, 3]. Proton-exchange-membrane fuel cell (PEMFC) technology is currently most suitable to power fuel cell electric vehicles (FCEVs). However, its large-scale commercialization is impeded by several drawbacks, among which the high cost and limited availability of platinum-based catalysts is considered one of the most severe problems. Since ≈4 times more Pt is required for the cathode than for the anode (owing to the slow oxygen reduction reaction (ORR) kinetics in contrast to the very fast kinetics for the hydrogen oxidation reaction (HOR)), decreasing the Pt loading at the cathode is one possible approach to decrease the cost of the PEM fuel cell stack. However, low-loaded Pt electrodes are known to exhibit performance losses originating from mass-transport limitations, which have been assigned primarily to oxygen transport resistances occurring at the Pt/ionomer interface [4, 5]. In addition, Kongkanand and Mathias [6] have reported that a decrease of the noble metal loading to below 100 μg<sub>Pt</sub>/cm<sup>2</sup><sub>geo</sub> results in an increase in the stack cost since below this loading other stack components like the bipolar plates, the gas diffusion layer, the membrane as well as system components become more costly. Thus, current ORR catalyst research for PEMFCs is mainly driven by developing

either highly active Pt-alloy catalysts or active and cost-effective platinum-group-metal-free (PGM-free) catalysts. Iron-based catalysts, specifically those based on iron coordinated to nitrogen and carbon (often referred to as Fe-N-C catalysts), are currently the most advanced PGM-free catalysts and recent developments have dramatically narrowed the ORR activity gap between Fe-N-C and Pt catalysts [7-10]. However, the biggest drawback of Fe-N-C catalysts is their lack of long-term operational stability [11, 12]. Another class of PGM-free catalysts is based on valve metal compounds (nitrides, carbonitrides, and oxides of Group 4 and 5 metals); in particular valve metal oxides (ZrO<sub>2</sub>, Ta<sub>2</sub>O<sub>5</sub>, etc.), have been reported to be ORR active [13, 14]. The intrinsic thermodynamic stability against dissolution in an acidic environment of valve metal oxides and their reported ORR activity makes this class of materials very attractive. However, in our previous work, we concluded that ORR activities of pure carbon supported ZrO<sub>2</sub> nanoparticles are still far too low for practical PEMFC applications [15]. One strategy to increase their ORR activity is to increase the density of oxygen vacancies or uncoordinated metal sites, hypothesized to be sites with higher ORR activity [16, 17]. In this respect, Ishihara et al. [18] have already claimed enhanced ORR activity for titanium-niobium oxides (prepared by a sol-gel method), showing that the strength of oxygen interaction with the oxide surfaces could be tuned by substitutional ions (here, Nb in TiO<sub>2</sub>) causing valence changes and/or oxygen vacancies. Creation of oxygen vacancies in bulk ZrO<sub>2</sub> by substitution of Zr<sup>4+</sup> by Fe<sup>3+</sup> has been reported by Sangalli et al. [19]. In their study, they use both theoretical (density functional theory, DFT) and

experimental approaches (synthesis of Fe-doped ZrO<sub>2</sub> thin films) to prove the formation of oxygen vacancies by Fe<sup>3+</sup> doping into the ZrO<sub>2</sub> lattice.

Based on these positive effects of cation substitution, in 2017 we developed and communicated a novel approach to significantly increase the ORR activity of carbon-supported (graphitized Ketjenblack, KB<sub>graph</sub>) ZrO<sub>2</sub>-based catalysts [20]. Even though the nature of active sites was not clear, it was demonstrated that a very small amount of Fe (as low as 0.36 wt% referenced to the total weight of the catalyst) in 12 wt% ZrO<sub>2</sub> supported on carbon (≡ Fe/Zr atomic ratio of 7/93) significantly boosted the ORR activity. In addition, we showed that an optimum ORR activity was obtained for an Fe loading between 0.36 - 1.0 wt%, whereas the ORR activity was substantially lower at 0.1 and 10 wt% Fe loading. This lower ORR activity for the latter was hypothesized to be mainly due to a decreased density of active sites for 0.1 wt% Fe and the presence of less active compounds with 10 wt% Fe.

Understanding the nature of active sites is of utmost importance in (electro-)catalyst research; hence, the focus of the present work is to decipher the actual structure of the catalyst, i.e., to demonstrate that Fe is indeed substituted into the ZrO<sub>2</sub> structure, and the exact nature of the Fe coordination. For this reason, we here characterize our previously reported most active catalysts (assessed by the rotating (ring) disk electrode technique, R(R)DE), viz., Fe<sub>0.07</sub>Zr<sub>0.93</sub>O<sub>1.97</sub> (0.36 wt% Fe in ZrO<sub>2</sub>) and Fe<sub>0.17</sub>Zr<sub>0.83</sub>O<sub>1.91</sub> (1.0 wt% Fe in ZrO<sub>2</sub>) by X-ray photoelectron spectroscopy (XPS), near-edge X-ray absorption fine structure (NEXAFS), and <sup>57</sup>Fe Mössbauer spectroscopy. In addition, we perform particle size analyses of ZrO<sub>2</sub> nanoparticles in the catalysts by transmission electron microscopy (TEM). Furthermore, the Fe<sub>0.07</sub>Zr<sub>0.93</sub>O<sub>1.97</sub> catalyst will be subjected to further rigorous electrochemical characterization in thin-film R(R)DE and single-cell PEMFC measurements, including determination of the apparent activation energy and the Tafel slope. RRDE measurements at various electrode loadings are conducted to determine the hydrogen peroxide (H<sub>2</sub>O<sub>2</sub>) yield characteristics of the Fe<sub>0.07</sub>Zr<sub>0.93</sub>O<sub>1.97</sub> catalyst. Finally, the structural and electronic features of the Fe-substituted ZrO<sub>2</sub> surface will be investigated by first-principles simulations. While recent theoretical studies have addressed the surface chemistry of pure, non-defective zirconia [21], here we focus on the effects of Fe substitution on the catalyst's electronic structure, on the formation of surface oxygen vacancies, and on the interaction with reactive oxygen species. Our DFT-based results provide additional new insights that support the interpretation of our experimental ORR data.

## Experimental Section

### Chemicals

All commercially available chemicals were used without further purification. Zirconium tetrachloride (≥99.5%), 2-methylnaphthalene (97%), 2-bromonaphthalene (97%), 1,8-diazabicyclo[5.4.0]-5-undec-7-ene (≥99.0%), and 2-ethoxyethanol (99%) were purchased from Sigma-Aldrich. 4-tert-butylphthalonitrile (≥98%) was obtained from TCI. Zirconium (IV) tetra-tert-butyl-dichlorophthalocyanine (ZrCl<sub>2</sub>Pc(t-Bu)<sub>4</sub>) and iron(II) tetra-tert-butyl-phthalocyanine (FePc(t-Bu)<sub>4</sub>) were synthesized similarly to what is reported in previous publications [22, 23], except that 4-tert-butylphthalonitrile instead of 1,2-dicyanobenzene was used as a starting precursor in

order to obtain soluble phthalocyanines. ZrCl<sub>2</sub>Pc(t-Bu)<sub>4</sub> and FePc(t-Bu)<sub>4</sub> were characterized by Fourier transform infrared spectroscopy (to confirm metal insertion into the Pc) [24] and by thermogravimetric analysis under air (to quantify the metal content) [15]. We would also like to mention that the obtained precursor contained a significant fraction of organic impurities, resulting in a Zr content ≈3 times smaller than expected for an ideal ZrCl<sub>2</sub>Pc(t-Bu)<sub>4</sub>. Unfortunately, we were unable to remove the impurities from the precursor even after rigorous purification and then we used in the synthesis an amount ≈3 times higher. The exact origin of the presence of organic impurities in the precursor is not yet known, but it could be due to the presence of water impurities in a reactant, leading to the catalysis of an organic side reaction.

### Catalyst synthesis

For the present study, we synthesized four carbon-supported catalysts, viz., Fe<sub>0.17</sub>Zr<sub>0.83</sub>O<sub>1.91</sub> [denoted as ZrO<sub>2</sub>-Fe (1.0 wt%)], Fe<sub>0.07</sub>Zr<sub>0.93</sub>O<sub>1.97</sub> [denoted as ZrO<sub>2</sub>-Fe (0.36 wt%)], Fe, and ZrO<sub>2</sub>. All samples were supported on graphitized Ketjenblack carbon [denoted as KB<sub>graph</sub>] (EA-type from Tanaka Kikinokogyo). A graphitized carbon was chosen in order to minimize the presence and effect of surface oxygen groups, thus to have a better control of the partial oxidation during the heat-treatment step in the catalyst synthesis procedure. The ZrO<sub>2</sub> content was kept constant (theoretical 12 wt% ZrO<sub>2</sub>/KB<sub>graph</sub>) in all samples, except for the pure Fe catalyst [denoted as Fe], where no ZrO<sub>2</sub> is present. The synthesized catalysts Fe<sub>0.17</sub>Zr<sub>0.83</sub>O<sub>1.91</sub> and Fe<sub>0.07</sub>Zr<sub>0.93</sub>O<sub>1.97</sub> (Fe<sub>x</sub>Zr<sub>1-x</sub>O<sub>2-δ</sub>) are those reported in our past research, where the Fe/ZrO<sub>2</sub> atomic ratios are 7/93 (ZrO<sub>2</sub>-Fe (0.36 wt% of Fe)) and 17/83 (ZrO<sub>2</sub>-Fe (1.0 wt% of Fe)), whereby wt% of Fe is referred to the mass of metallic Fe in the final catalyst [20]. Catalysts were synthesized by first depositing the corresponding amounts of ZrCl<sub>2</sub>Pc(t-Bu)<sub>4</sub> and/or FePc(t-Bu)<sub>4</sub> onto KB<sub>graph</sub> using a similar impregnation process as described previously [25]. After impregnation, the solvent (chloroform, ≥99.9%) was removed by rotovaporation (Heidolph, Hei-VAP Value). The mixture was further dried overnight at 70 °C to remove all residual chloroform. The dried mixture was then transferred to a quartz tube furnace (HTM Reetz, LK 1300-150-600-3). Initially, the temperature was ramped up to 800 °C in 5% H<sub>2</sub>/Ar gas atmosphere. A heating rate of ≈10 °C min<sup>-1</sup> was maintained until ≈700 °C, which was then decreased to 2 °C min<sup>-1</sup> until 800 °C to avoid temperature overshoot. The temperature was then held for 2 h in the same gas-mixture, before switching to a mixture of 2.5% H<sub>2</sub> and 0.5% O<sub>2</sub> in Ar (partial oxidation, PO) (5.0 grade, all gases supplied by Westfalen AG) for another 1 h at the same temperature. Finally, the furnace was cooled to RT in 5% H<sub>2</sub>/Ar.

### Physicochemical characterization

Catalysts were subjected to inductively coupled plasma atomic emission spectrometry (ICP-AES; iCap 6500, Thermo Fisher Scientific) in order to determine the exact amount of Fe and ZrO<sub>2</sub>. The samples were first digested in hydrofluoric acid (40 wt%), and then in aqua regia by using a microwave digester. In addition to ICP-AES, the total metal oxide content (ZrO<sub>2</sub> + Fe<sub>2</sub>O<sub>3</sub>) was evaluated by thermogravimetric analysis (TGA; Mettler-Toledo, TGA/DSC 1) from the residual sample weight after complete combustion of the catalyst at 1000 °C in a

mixture of O<sub>2</sub>/Ar (67/33%) atmosphere. The particle size distribution of ZrO<sub>2</sub> was evaluated by transmission electron microscopy (TEM) measurements with a Jeol JEM 1400-Plus transmission electron microscope, operated at an acceleration voltage of 120 kV. Holey carbon-coated TEM grids were used for sample mounting. A CCD camera was employed to collect several images at 200,000× magnification. The software ImageJ® [26] was used to measure the diameter of at least 100 individual particles. From this data, the number averaged particle size ( $D_{Average}$ ) and the standard deviation (SD) were computed. The Sauter diameter ( $D_{Sauter}$ ) (surface-volume averaged diameter) was calculated as in Equation 1, where  $l_i$  is the number of particles with diameter ( $d_i$ ).

$$D_{Sauter} = \frac{\sum_{i=1}^n l_i d_i^3}{\sum_{i=1}^n l_i d_i^2} \quad \text{Equation 1}$$

Fe<sub>0.17</sub>Zr<sub>0.83</sub>O<sub>1.91</sub> and Fe<sub>0.07</sub>Zr<sub>0.93</sub>O<sub>1.97</sub> were subjected to X-ray photoelectron spectroscopy (XPS) to investigate the Fe coordination and oxidation state. Analyses of the samples were performed on a Kratos Axis Supra spectrometer using monochromated Al K<sub>α</sub> radiation at an energy of 1486.6 eV, operated at a total power of 525 W, 15 kV and 35 mA anode current. The samples were previously outgassed (overnight) in an ultrahigh vacuum chamber in order to remove atmospheric moisture and contaminants, so that the pressure in the chamber during the analysis was less than 1.0·10<sup>-8</sup> Torr. All the binding energy values were calibrated using the carbon signal from the KB<sub>graph</sub> carbon support (C 1s = 284.8 eV) as reference. The narrow Fe 2p spectra were collected between 702.5 to 745 eV binding energy (BE) using a step size of 0.1 eV and a pass energy of 40 eV. The XPS data analysis was performed by Casa XPS software. The represented data are an average of 10 spectra recorded for 10 min each.

Fe<sub>0.17</sub>Zr<sub>0.83</sub>O<sub>1.91</sub> and Fe<sub>0.07</sub>Zr<sub>0.93</sub>O<sub>1.97</sub> were also characterized by near-edge X-ray absorption fine structure (NEXAFS) data at the Fe L<sub>2,3</sub> edges. A pure ZrO<sub>2</sub> sample was also measured to demonstrate the absence of Fe. Spectra were collected at IFP's (Institut für Festkörperphysik) soft X-ray analytics facility WERA at the Karlsruhe synchrotron facility ANKA, Germany. Partial fluorescence-yield (FY) detection was used, both for its quasi-bulk probing depth of about 50 nm and for its independence from charging effects in non-conducting samples. For the Fe concentrations in this study, self-absorption and saturation effects were small and were not corrected. The photon-energy resolution was set to about 340 meV at the Fe L edges. The photon energy was calibrated to better than 30 meV by simultaneously measuring a NiO reference sample at the Ni L<sub>3</sub> edge (853.0 eV) [27]. The collected data are the sum of two distinct scans (30 min each). To obtain the simulated data, the code developed by Thole and van der Laan, Butler, and Cowan [28-30], and maintained and further developed by Stavitski and de Groot [31] was used to calculate spectra for different values of the crystal-field splitting (Delta\_CF) and charge transfer energy (Delta\_c). Hund's rule for exchange interaction was also taken into account. Charge-transfer effects were included for Fe<sup>2+</sup> (Fe<sup>3+</sup>) by admixing transitions of the type 2p<sup>6</sup> 3d<sup>7</sup>L → 2p<sup>5</sup> 3d<sup>8</sup>L (2p<sup>6</sup> 3d<sup>6</sup>L → 2p<sup>5</sup> 3d<sup>7</sup>L), where L denotes a hole at the oxygen ligand. Multiplet parameters (in eV) are: i) Fe<sup>2+</sup> HS: Delta\_CF (10Dq) = 1.0, Delta\_c = 4.0; ii) Fe<sup>2+</sup> LS: Delta\_CF (10Dq) = 2.5, Delta\_c = 4.0; iii) Fe<sup>3+</sup> HS: Delta\_CF (10Dq) = 0.8, Delta\_c = 4.5; and, iv) Fe<sup>3+</sup> LS: Delta\_CF (10Dq) = 3.0, Delta\_c = 4.5. The correlation energy U<sub>dd</sub>, the core-hole potential U<sub>pd</sub>, as well as the hopping parameters

T<sub>sigma</sub> and T<sub>pi</sub> were set for all spin and valence states to 5.0, 6.0, 2.0, and 1.0, respectively. The Slater integrals were renormalized to 80% of their Hartree-Fock values. According to the experimental resolution and the lifetime broadening, the simulations have been convoluted with a Gaussian with σ<sub>G</sub> = 0.2 eV and with a Lorentzian with σ<sub>(L\_3)</sub> = 0.2 eV (σ<sub>(L\_2)</sub> = 0.3 eV) for the L<sub>3</sub> (L<sub>2</sub>) edge. Finally, the position on the energy scale of the modelled spectra was adjusted by matching the white-line energy of experimental spectra with that of the Fe<sup>3+</sup> high-spin modelled spectrum; the correctness of this adjustment was confirmed by comparison of the experimental data with the literature (see Results and Discussion).

Finally, in addition to XPS and NEXAFS, the Fe<sub>0.17</sub>Zr<sub>0.83</sub>O<sub>1.91</sub>, Fe<sub>0.07</sub>Zr<sub>0.93</sub>O<sub>1.97</sub>, and Fe catalysts were also subjected to <sup>57</sup>Fe Mössbauer analyses to ascertain the exact nature of Fe coordination in the catalysts. Mössbauer spectra were recorded on powder samples placed in poly(methyl methacrylate) based holders at 4.2 K. For this, the absorber and the source of <sup>57</sup>Co in rhodium (ca. 1 Giga Becquerel) were cooled in a liquid helium bath cryostat. The spectra were fitted with a superposition of Lorentzian lines grouped into sextets using the MOS90 software (version 2.2). The fitted components often show broadened lines and have to be considered as representing distributions of magnetic hyperfine fields. Isomer shifts were measured with respect to the source having the same temperature as the absorber. Lastly, 0.245 mm/s was added to each isomer shift so that it can be referenced to α-Fe.

### Electrochemical characterization

*Rotating (ring) disk electrode measurements.*— The thin-film rotating (ring) disk electrode (TF-R(R)DE) technique was used to screen the ORR activity of the samples. Details of the experimental protocol and set-up can be found in a previous publication [15]. In short, catalyst inks were prepared by dispersing 7.2 mg of catalyst powder in 5.1 ml of N,N-dimethylformamide (≥99.8, Fisher Scientific), followed by sonication in an ice-bath for 50 min. Subsequently, 40 μl of 5% Nafion® 117 solution was added to the dispersion (resulting in a Nafion®/carbon ratio of ≈1/4 g/g) and the sonication was continued for another 10 min. Finally, 10 μl of ink was drop-cast onto a pre-cleaned glassy carbon electrode (Ø = 5 mm, obtained from Pine Research Instrumentation). The film was dried under an infrared heater for ≈60 min until the solvent was completely evaporated. The resulting catalyst films had a loading of 70 - 72 μg<sub>cat</sub>/cm<sup>2</sup>.

RDE measurements were performed at 20 °C in 0.1 M HClO<sub>4</sub> in a homemade three-electrode water-jacketed glass cell. 60% HClO<sub>4</sub> solution (Guaranteed Reagent, Kanto Chemical) was used to prepare 0.1 M HClO<sub>4</sub> solution. Dilution was done with deionized ultrapure water (Milli-Q Integral 5, 18.2 MΩ·cm). Electrochemical measurements were done using an Autolab PGSTAT302N (Metrohm) potentiostat, where linear sweep voltammograms (LSVs) were recorded at 1600 rpm under Ar and O<sub>2</sub> saturated electrolyte. ORR activities were determined from anodic scans in pure oxygen saturated electrolyte, whereby the here obtained currents were corrected for their capacitive contribution by subtracting the anodic LSV in Ar saturated electrolyte. The reported potentials are referenced to the reversible hydrogen electrode (RHE) scale and are corrected for the uncompensated solution resistance, which was determined by electrochemical impedance spectroscopy.

The apparent activation energy of the ORR was determined for the  $\text{Fe}_{0.07}\text{Zr}_{0.93}\text{O}_{1.97}$  sample by recording LSVs between 10 – 40 °C. In addition,  $\text{H}_2\text{O}_2$  quantification from the  $\text{Fe}_{0.07}\text{Zr}_{0.93}\text{O}_{1.97}$  catalyst was carried out using the RRDE technique, where the platinum ring was held at 1.2  $V_{\text{RHE}}$ , while the potential of the disk was swept between 1.0 - 0.1  $V_{\text{RHE}}$ . The collection efficiency of the ring ( $N$ ) was taken to be 0.255 [15]. As part of a mechanistic study, we varied the catalyst loading on the disk from 30 to 576  $\mu\text{g}_{\text{cat}}/\text{cm}^2$  and measured the hydrogen peroxide yield ( $\%\text{H}_2\text{O}_2$ ) at each loading. The limiting current used in the mass transport correction of geometric currents from  $\text{Fe}_{0.17}\text{Zr}_{0.83}\text{O}_{1.91}$  and  $\text{Fe}_{0.07}\text{Zr}_{0.93}\text{O}_{1.97}$  catalysts is calculated by weighted analysis after considering the amount of peroxide from the ring and assuming a theoretical 4 or 2  $e^-$  (5.6 or 2.8  $\text{mA}/\text{cm}^2$ , at 1600 rpm) limiting current as no limiting current is reached. Similar procedure is followed for Fe-N-C catalysts, except the limiting current is reached, thus it is considered instead of theoretical limiting current.

#### *Proton exchange membrane fuel cell measurements.*—

An in-house made 5  $\text{cm}^2$  active area single-cell PEMFC hardware with single serpentine graphite flow field channels (Fuel Cell Technologies) was used. It was operated with a customized fuel cell test station (G60, Greenlight Innovation), equipped with a Reference 3000 potentiostat/frequency response analyzer (Gamry). MEAs were produced by the decal transfer method. Catalyst inks were prepared by mixing the ink components in the following sequence in an 8 ml HDPE capped bottle containing 20.8 g of 3 mm diameter  $\text{ZrO}_2$  beads as grinding medium: catalyst, water, 1-propanol (99%, Sigma-Aldrich). The ink was pre-mixed using a roller mixer at 250 rpm for 1 h. Subsequently, the low equivalent weight ionomer in a water-solvent dispersion was added and the mixing was continued for 18 h at 60 rpm. The water concentration in the inks was 10 wt%, while the solid content and the ionomer to carbon weight ratio were 0.03  $\text{g}_{\text{catalyst}}/\text{ml}_{\text{ink}}$  and  $\approx 0.75/1.0$  g/g, respectively. Thereafter, the ink was coated onto a 50  $\mu\text{m}$  PTFE substrate using a Mayer rod (100  $\mu\text{m}$  wet-film thickness). The electrodes were then dried at room temperature (RT) until complete solvent evaporation. Thereafter, the MEA was assembled by hot pressing (155 °C, 3 min, 0.11  $\text{kN}/\text{cm}^2$ ) a Nafion<sup>®</sup> 212 membrane (50  $\mu\text{m}$  thickness) between an anode (20 wt% Pt/Vulcan, 100  $\mu\text{g}_{\text{Pt}}/\text{cm}^2$ ) and cathode ( $\text{Fe}_{0.07}\text{Zr}_{0.93}\text{O}_{1.97}$ , 380  $\mu\text{g}_{\text{cat}}/\text{cm}^2$ ) decal. The loadings were obtained by weighing the decals before and after hot-pressing.

Finally, the MEA was sandwiched between two gas diffusion layers (GDLs) (29BC, SGL Carbon, Germany) and the cell was assembled using PTFE coated fiberglass subgaskets (Fiberflon, Germany) to adjust a nominal GDL compression of ca. 20%. The ORR activity vs. temperature was measured with  $\text{H}_2/\text{O}_2$  (400/400  $\text{nccm}$  flows), whereby the total cell pressure was adjusted such that the  $\text{H}_2$  and  $\text{O}_2$  partial pressures remained at 100 kPa at a relative humidity of 90%. At each temperature, the cell was equilibrated for 10 min prior to recording a cyclic voltammogram at 10  $\text{mV}/\text{s}$ . Subsequently, the high frequency resistance (HFR) was determined (at open circuit voltage, AC amplitude: 10 mV) and the cell potentials were corrected to obtain the so-called  $iR$ -free potential, using the HFR which ranged between  $\approx 90$   $\text{m}\Omega\cdot\text{cm}^2$  (at 100 °C) and  $\approx 150$   $\text{m}\Omega\cdot\text{cm}^2$  (at 40 °C). The same procedure was repeated with  $\text{N}_2$  instead of  $\text{O}_2$  on the cathode; the thus obtained anodic capacitive currents in  $\text{H}_2/\text{N}_2$  were then subtracted from the anodic currents obtained in  $\text{H}_2/\text{O}_2$ ,

yielding the here given capacitively corrected ORR currents.

#### DFT calculations

In order to describe the adsorption of molecular oxygen on  $\text{ZrO}_2$ , we considered the most stable surface of tetragonal  $t\text{-ZrO}_2$  i.e., the (0  $\bar{1}$  1) surface, which is equivalent to the (1 1 1) in the cubic system. Our structural model consists of a surface slab cleaved from  $t\text{-ZrO}_2$  bulk at the theoretically determined lattice constants. We included in this slab three oxygen-terminated tri-layers, each with 16  $\text{ZrO}_2$  formula units, for a total system of 144 atoms (please see supporting information (SI), Figure S1a). This model is sufficient to converge the  $\text{O}_2$  adsorption energy with respect to slab thickness within 20 meV. Moreover, we used a 2x2 lateral supercell to ensure a realistic concentration of Fe surface species in the substituted zirconia and to avoid spurious image interactions upon formation of surface oxygen vacancies or adsorption of molecular oxygen. Each tri-layer presents oxygen atoms that points up (toward the electrolyte) and down (toward zirconia bulk), as shown in Figure S1b and c; both these oxygen-atom types have been considered when modeling oxygen vacancies. All the coordinates of the bottom-most tri-layer (B in Figure S1a) have been kept fixed at the bulk values during geometry optimizations, while the other two topmost tri-layers (S and SS in Figure S1a) have been fully relaxed to their minimum-energy structure. Fe-substituted zirconia has been modeled by substitution of one Zr by one Fe atom on the surface (or on the sub-surface tri-layer), for a total Fe content of  $\approx 2$  at% with respect to all Zr atoms and of  $\approx 6$  at% considering only the surface atoms.

With these structural models, we carried out spin-polarized DFT calculations with the Vienna Ab-Initio Simulation Package (VASP) [32]. We chose as level of theory the Perdew-Burke-Ernzerhof (PBE) [33] exchange-correlation density functional and the on-site Hubbard U-J term for correcting SIE [34] associated to Zr and Fe (partially) occupied  $d$  states. In particular, as in previous works [35, 36], we have used the rotationally invariant DFT+U scheme as implemented in VASP with an effective U-J value of 4.0 eV for both Zr and Fe  $d$  electrons. Nuclei and inner core electrons were replaced by projector augmented wave potentials (PAW) as obtained from the VASP repository. The valence/outer-core electrons that are included in the KS-DFT SCF cycles are listed in parentheses for each atom: Zr (4s<sup>2</sup>, 4p<sup>6</sup>, 4d<sup>2</sup> and 5s<sup>2</sup>), O (2s<sup>2</sup> and 2p<sup>4</sup> with the intermediate core radius PAW potential), C (2s<sup>2</sup> and 2p<sup>2</sup>), Fe (3d<sup>6</sup> 4s<sup>2</sup>), and H (1s<sup>1</sup>). These electronic variables are described via a plane-wave basis set, with a kinetic energy cut-off of 800 eV and a gamma-centered 3x3x1 k-point mesh. These numerical parameters are required for convergence of the total electronic energies within a threshold of 1 meV per formula unit. Bader's Atom-In-Molecule partial charges [37] have been computed within the super-cell-based approach. Oxygen vacancies,  $\text{O}_2$  adsorption, and OOH species have been considered only on a side on the slab (S in Figure S1), thus dipole corrections have been applied to avoid long-range polarization from the periodic images along the 'z' direction. Oxygen-vacancy formation energies have been computed in vacuum, while for  $\text{O}_2$  adsorption and OOH formation energy calculations have been performed considering a PCM-like implicit solvent model for water as implemented in VASP\_sol [38].

## Results and Discussion

### Elemental analysis with ICP and TGA

Quantitative analysis was performed to obtain the amount of Fe and Zr (as  $\text{Fe}_2\text{O}_3$  and  $\text{ZrO}_2$ ) in the carbon-supported catalysts. Table 1 summarizes the ICP and TGA results. In both  $\text{Fe}_{0.17}\text{Zr}_{0.83}\text{O}_{1.91}$  and  $\text{Fe}_{0.07}\text{Zr}_{0.93}\text{O}_{1.97}$  samples, atomic percent of Fe and Zr are calculated from the ICP quantitative analysis shown in Table 1, while the oxygen content is a nominal content calculated based on the amount of Fe. For Fe and  $\text{ZrO}_2$  samples, it is clearly seen that they do not contain any  $\text{ZrO}_2$  and Fe, respectively, indicating that the catalyst synthesis did not result in any cross-contamination. It is also observed that in the pure Fe sample (first row) a higher Fe content is found analytically, compared to the nominally expected amount based on the synthesis. This is likely due to the

loss of some carbon (likely from the support) during the partial oxidation (PO). This decrease in sample amount further translates into an effective increase in the Fe wt%. In addition, the agreement between the results for 1<sup>st</sup> and 2<sup>nd</sup> row of Table 1 from two different techniques i.e., ICP and TGA, further support their validity. On the contrary, the metal content in  $\text{ZrO}_2$ ,  $\text{Fe}_{0.17}\text{Zr}_{0.83}\text{O}_{1.91}$ , and  $\text{Fe}_{0.07}\text{Zr}_{0.93}\text{O}_{1.97}$  (2<sup>nd</sup>, 3<sup>rd</sup>, and 4<sup>th</sup> row) is only approximately half of the nominally expected value. This discrepancy is likely due to the carbon produced by decomposition of the Zr precursor, which is significantly larger in comparison to that produced in the Fe sample, since the amount of  $\text{FePc}(\text{t-Bu})_4$  is  $\approx 70$  times lower than the  $\text{ZrCl}_2\text{Pc}(\text{t-Bu})_4$ . Although the absolute amount of Fe and  $\text{ZrO}_2$  in  $\text{Fe}_{0.17}\text{Zr}_{0.83}\text{O}_{1.91}$ , and  $\text{Fe}_{0.07}\text{Zr}_{0.93}\text{O}_{1.97}$  is 50% of the expected, the atomic ratios between them are still the same as theoretical.

**Table 1.** Nominal (nom.) Fe and Zr content (as oxides) in the carbon supported catalysts samples in comparison to the actual content determine by quantitative analyses via ICP and TGA. SD is the standard deviation calculated for the respective analysis based on the instrumental precision. The oxygen atomic content in the Fe-substituted samples  $\text{Fe}_{0.17}\text{Zr}_{0.83}\text{O}_{1.91}$  [ $\text{ZrO}_2\text{-Fe}$  (1.0 wt%)] and  $\text{Fe}_{0.07}\text{Zr}_{0.93}\text{O}_{1.97}$  [ $\text{ZrO}_2\text{-Fe}$  (0.36 wt%)] is calculated from the analytically quantified metals content, assuming all Fe to present as a solid solution of  $\text{Fe}_2\text{O}_3$  in  $\text{ZrO}_2$ , thus forming oxygen vacancies. While  $\text{ZrO}_2\text{-Fe}$  (1.0 wt%) and  $\text{ZrO}_2\text{-Fe}$  (0.36 wt%) is the nomenclature used in our previous paper [20], where wt% represent the nominal Fe content in the catalyst assuming Fe as metal.

Sample name	Fe as $\text{Fe}_2\text{O}_3$ (theo)	Zr as $\text{ZrO}_2$ (theo)	$\text{Fe}_2\text{O}_3$	$\text{ZrO}_2$	$(\text{ZrO}_2 + \text{Fe}_2\text{O}_3)$
	wt%	wt%	ICP $\pm$ SD <sub>ICP</sub> wt%	ICP $\pm$ SD <sub>ICP</sub> wt%	TGA $\pm$ SD <sub>TGA</sub> wt%
Fe	0.58	0	0.95 $\pm$ 0.01	0	1.1 $\pm$ 0.1
$\text{ZrO}_2$	0	12.00	0.01 $\pm$ 0.01	5.66 $\pm$ 0.06	5.7 $\pm$ 0.1
$\text{Fe}_{0.17}\text{Zr}_{0.83}\text{O}_{1.91}$ [ $\text{ZrO}_2\text{-Fe}$ (1.0 wt%)]	1.43	12.00	0.73 $\pm$ 0.01	5.69 $\pm$ 0.06	6.2 $\pm$ 0.1
$\text{Fe}_{0.07}\text{Zr}_{0.93}\text{O}_{1.97}$ [ $\text{ZrO}_2\text{-Fe}$ (0.36 wt%)]	0.51	12.00	0.29 $\pm$ 0.01	5.77 $\pm$ 0.06	5.8 $\pm$ 0.1
non-heat treated $\text{Fe}_{0.07}\text{Zr}_{0.93}\text{O}_{1.97}$	0.15	3.46	—	—	3.6 $\pm$ 0.1

The last row in Table 1 shows the analytical results from a non-heat treated  $\text{Fe}_{0.07}\text{Zr}_{0.93}\text{O}_{1.97}$  sample (5<sup>th</sup> row), which served as a reference to determine whether there is any loss of metal precursors before the heat treatment step. The TGA analysis reveals that the theoretical and

actual metal loadings are in very close agreement with each other, which clearly confirms that no precursors were lost until the heat treatment. On the other hand, we could not completely exclude some loss of precursors during the heat treatment due to sublimation.

### Morphological characterization

XRD characterization of the above samples can be found in a previously published article by Madkikar et al. [20], which clearly indicated the formation of nanometric  $\text{ZrO}_2$  in all samples. From the broadening of reflexes, a crystallite size of  $<10$  nm was clearly confirmed after comparing the XRD data with our past study [25]. From the here conducted TEM image analysis (Figure 1), it was found that the (number based) average particle size of

$\text{ZrO}_2$  in  $\text{Fe}_{0.17}\text{Zr}_{0.83}\text{O}_{1.91}$  and  $\text{Fe}_{0.07}\text{Zr}_{0.93}\text{O}_{1.97}$  is very similar ( $\approx 3$  nm) (black and red bars in Figure 1a, b). On the other hand, the  $\text{ZrO}_2$  particle size in the pure  $\text{ZrO}_2$  sample was  $\approx 6.5$  nm (blue bar in Figure 1c), which is in accordance with our past study on nanometric carbon-supported  $\text{ZrO}_2$  catalysts [25]. The smaller  $\text{ZrO}_2$  particle size in the samples where Fe is introduced could be a combined effect of increased nucleation rate and/or hindered growth due to crystal strain generated in Fe-substituted  $\text{ZrO}_2$ . These hypotheses are based on the



past papers by Leite et al. [39] and Chen et al. [40], which also observed that oxide nanoparticles with a dopant (Nb-doped SnO<sub>2</sub> and Al-doped ZnO) have smaller particle size than undoped oxide nanoparticles.

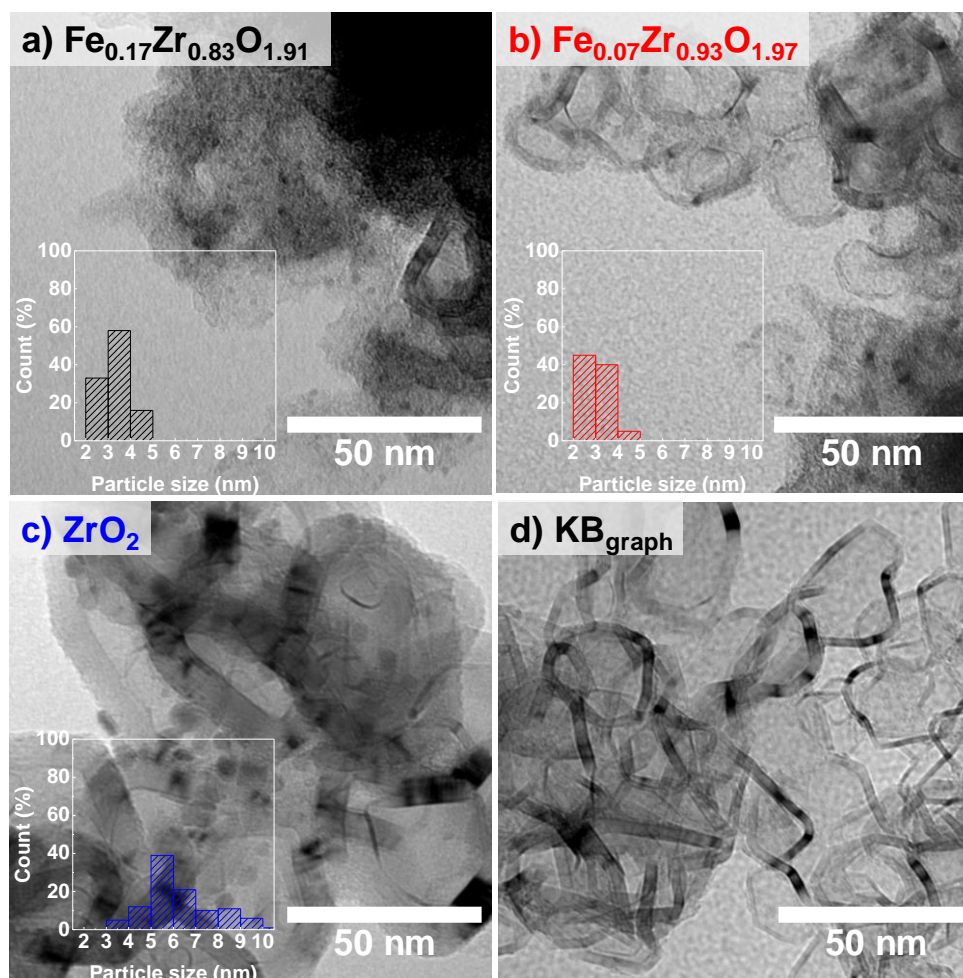


**Figure 1.** TEM micrographs of  $\text{KB}_{\text{graph}}$ -supported catalysts along with the histogram depicting  $\text{ZrO}_2$  particle size distribution in: **a)**  $\text{Fe}_{0.17}\text{Zr}_{0.83}\text{O}_{1.91}$ ; **b)**  $\text{Fe}_{0.07}\text{Zr}_{0.93}\text{O}_{1.97}$ ; **c)**  $\text{ZrO}_2$ ; and finally the support **d)** pristine  $\text{KB}_{\text{graph}}$ .

### Unveiling Fe coordination

**XPS analysis.**— High-resolution XP spectra of the Fe 2p region for the  $\text{Fe}_{0.17}\text{Zr}_{0.83}\text{O}_{1.91}$  and  $\text{Fe}_{0.07}\text{Zr}_{0.93}\text{O}_{1.97}$  samples are shown in Figure 2. Since the signal-to-noise ratio is unfortunately rather low due to the low amount of iron in the samples, reliable deconvolution of the spectra is impossible. Instead, we compare the binding energy of the Fe 2p<sub>3/2</sub> signal to known binding energy values of Fe<sup>3+</sup>, Fe<sup>2+</sup>, and Fe<sup>0</sup> species reported in the literature (cf. green, blue and brown markers in Figure 2, respectively) [41, 42].

The observed binding energy range for the Fe 2p<sub>3/2</sub> signals reveals clearly that the dominant oxidation state of Fe in both samples is 3+ (711.8 - 710.8 eV, green region) [41]. Owing to the rather low signal/noise ratio, however, the simultaneous presence of Fe<sup>2+</sup> as minor phase cannot be completely ruled out (709.5 - 707.1 eV, blue region). Metallic Fe (Fe<sup>0</sup>, 707.2 - 706.7 eV, brown region) is clearly absent in both catalysts. Additionally,  $\text{ZrO}_2$  formation was also confirmed (data not shown) by comparing the narrow Zr 3d spectra to a previous study from our group [25].

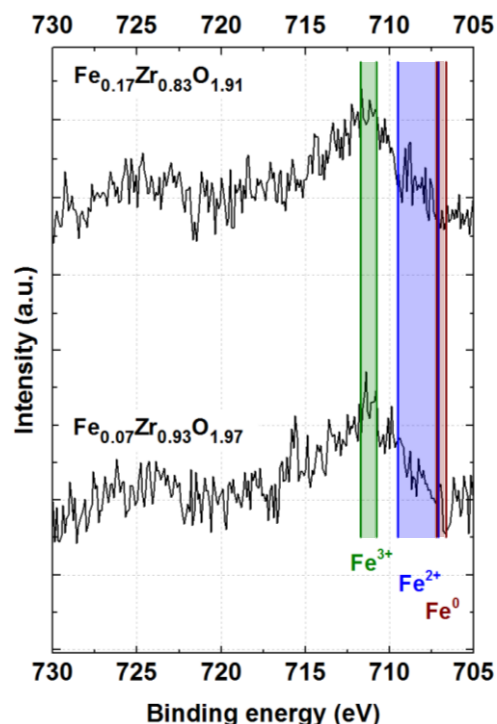


**Figure 2.** High-resolution narrow-scan XPS Fe 2p signals for the  $\text{Fe}_{0.17}\text{Zr}_{0.83}\text{O}_{1.91}$  and  $\text{Fe}_{0.07}\text{Zr}_{0.93}\text{O}_{1.97}$  samples. Different oxidation states of Fe [Fe<sup>3+</sup> (711.8 - 710.8 eV), Fe<sup>2+</sup> (709.5 - 707.1 eV), Fe<sup>0</sup> (707.2 - 706.7 eV)] [41, 42] belong to the areas marked with specific colors.



**NEXAFS analysis.**— From Figure 3 it is evident that the experimental spectra at the Fe  $L_{2,3}$  edges of  $\text{Fe}_{0.17}\text{Zr}_{0.83}\text{O}_{1.91}$  and  $\text{Fe}_{0.07}\text{Zr}_{0.93}\text{O}_{1.97}$  (light and dark blue lines, bottom panel of Figure 3) closely resemble in shape the simulated multiplet structure of high-spin  $\text{Fe}^{3+}$  (bold red line, middle panel). This is further corroborated by the close match of the position of the  $L_3$  white-line energy of our experimental spectra with previously-reported Fe in hematite ( $\text{Fe}^{3+}$ ) [43].

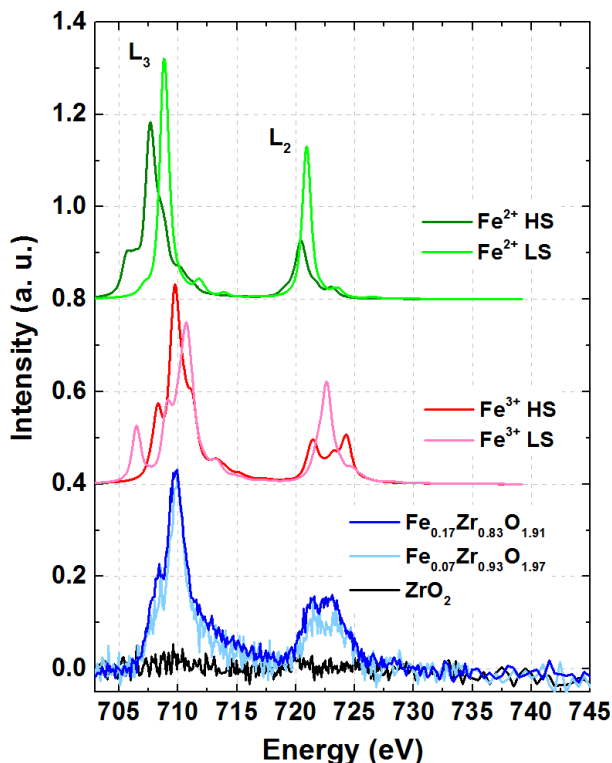


**Figure 3.** Bottom panel: Room temperature NEXAFS spectra at the Fe  $L_{2,3}$  edge recorded in fluorescence mode for  $\text{Fe}_{0.17}\text{Zr}_{0.83}\text{O}_{1.91}$  (dark blue line),  $\text{Fe}_{0.07}\text{Zr}_{0.93}\text{O}_{1.97}$  (light blue line), and  $\text{ZrO}_2$  samples (black line). Middle and top panels: multiplet analyses of the different Fe oxidation and spin states (HS = high-spin, LS = low-spin).

It is also observed that the shapes of the  $L_3$  and  $L_2$  edge are similar to that of goethite  $\text{FeO}(\text{OH})$  and hematite  $\alpha\text{-Fe}_2\text{O}_3$ , where Fe is present as high-spin  $\text{Fe}^{3+}$  at ambient temperatures and pressures [44, 45]. Thus, it can be stated quite unambiguously that Fe exists as high-spin  $\text{Fe}^{3+}$  in both  $\text{Fe}_{0.17}\text{Zr}_{0.83}\text{O}_{1.91}$  and  $\text{Fe}_{0.07}\text{Zr}_{0.93}\text{O}_{1.97}$ . Lastly, the pure  $\text{ZrO}_2$  sample (containing negligibly small amount of Fe, ICP (Table 1)) serves as a baseline and confirms the absence of significant amounts of Fe (Figure 3).

**Mössbauer analysis.**— Based on the Mössbauer spectra (Figure 4), only one type of Fe is present in the  $\text{Fe}_{0.17}\text{Zr}_{0.83}\text{O}_{1.91}$  and  $\text{Fe}_{0.07}\text{Zr}_{0.93}\text{O}_{1.97}$  catalysts (top and middle panel). The isomer shift ( $\delta$ ) and quadrupole splitting (QS) of the primary doublet are 0.5 and 1.0 mm/s, respectively. These values indicate that Fe is present in high-spin isolated  $\text{Fe}^{3+}$  state [46]. Both the primary and the secondary doublet belong to the same Fe species. In addition, some paramagnetic relaxation related to the same  $\text{Fe}^{3+}$  are also identified. On the contrary, Mössbauer spectra of the catalyst sample containing only iron (denoted as Fe) looks completely different (bottom panel in Figure 4). In this case, three phases, viz., metallic Fe (bcc and fcc), along with  $\gamma\text{-Fe}_2\text{O}_3$  and  $\text{Fe}_3\text{C}$  are identified, while isolated  $\text{Fe}^{3+}$  is not detected. This clearly indicates that the formation of

metallic Fe, iron carbide, and iron oxide is hindered when  $\text{ZrO}_2$  is present.

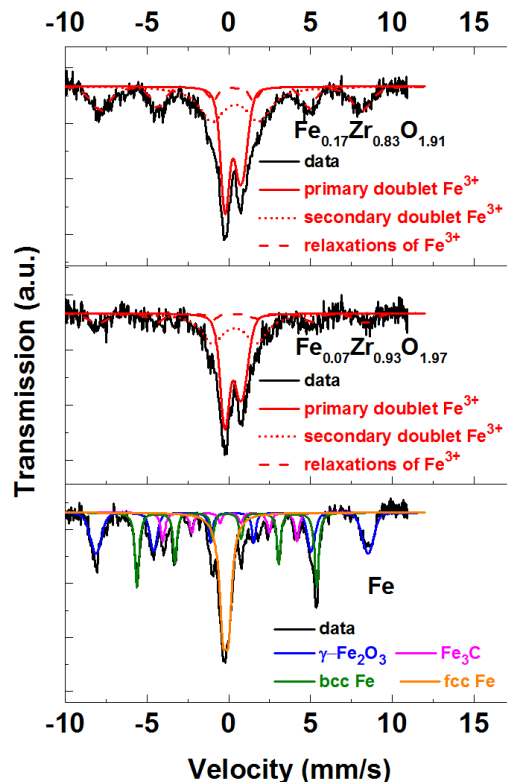


**Figure 4.**  $^{57}\text{Fe}$  Mössbauer spectra of the  $\text{Fe}_{0.17}\text{Zr}_{0.83}\text{O}_{1.91}$ ,  $\text{Fe}_{0.07}\text{Zr}_{0.93}\text{O}_{1.97}$ , and Fe catalysts measured at 4.2 K. The Fe oxidation state and the various phases are also depicted in each spectra. Secondary doublets and paramagnetic relaxations of  $\text{Fe}^{3+}$  are observed only in  $\text{Fe}_{0.17}\text{Zr}_{0.83}\text{O}_{1.91}$  and  $\text{Fe}_{0.07}\text{Zr}_{0.93}\text{O}_{1.97}$ .

The finding that iron is present exclusively in form of isolated  $\text{Fe}^{3+}$  in our  $\text{Fe}_{0.17}\text{Zr}_{0.83}\text{O}_{1.91}$  and  $\text{Fe}_{0.07}\text{Zr}_{0.93}\text{O}_{1.97}$  catalysts may be compared to reports in the literature that iron in the active sites of Fe-N-C catalysts is mainly in the  $\text{Fe}^{2+}$  oxidation state [47, 48] (with only traces of  $\text{Fe}^{3+}$  possible [49]). Thus; since we do not detect any  $\text{Fe}^{2+}$  in our NEXAFS and in our XPS analysis, we can exclude the presence of ORR active Fe-N-C moieties in our  $\text{Fe}_{0.17}\text{Zr}_{0.83}\text{O}_{1.91}$  and  $\text{Fe}_{0.07}\text{Zr}_{0.93}\text{O}_{1.97}$  catalysts. The high-spin state of  $\text{Fe}^{3+}$ , evident in NEXAFS data, indicates that Fe is likely coordinated by oxygen, typically observed for this spin configuration [44, 45]. On the other hand, from the Mössbauer analysis we observe only isolated  $\text{Fe}^{3+}$ . Combining these two observations, we can conclude that  $\text{Fe}^{3+}$  substitutes  $\text{Zr}^{4+}$  in the  $\text{ZrO}_2$  structure, forming the solid solution  $\text{Fe}_x\text{Zr}_{1-x}\text{O}_{2-\delta}$ .

**Oxidation state of Fe from DFT.**— Sangalli et al. [19] have reported the presence of Fe as  $\text{Fe}^{3+}$  in the bulk of Fe-substituted  $\text{ZrO}_2$  (oxide phase, tetragonal). We have studied here the electronic structure of the material considering Fe as substituent at the catalyst surface. First, the computed energy difference between the slabs containing Fe in the surface and subsurface positions ( $E_{(\text{Fe-ZrO}_2\text{S})} - E_{(\text{Fe-ZrO}_2\text{SS})} = -2.4$  eV) indicates that Fe is likely to be found at the topmost atom layer, i.e., at the surface of the  $\text{Fe}_x\text{Zr}_{1-x}\text{O}_{2-\delta}$  catalyst. The computed atomic magnetic moment of the Fe atom ( $4.17 \mu_B$ , thus more than four unpaired electrons in Fe [50]) and the projected density of states (PDOS) (Figure S2 in the SI) provide further evidence of a high-spin 3+ valence state for the Fe atom at the catalyst surface, with a full occupation (d5) of d states in the  $\alpha$  channel (spin-up) and no occupation of d states in the  $\beta$  channel (spin-down).

### TF-R(R)DE data and mechanistic interpretation:

In the following, we compare the ORR activity of our catalysts by comparing the potential at a fixed current ( $E_{iR-free}$  @  $-1$  A/g<sub>cat</sub>) at which the faradaic current is 3 - 5 times higher than the capacitive current but still <5% of the diffusion limited current. This implies capacitive correction errors will be small and oxygen transport resistances are negligible at our chosen mass-specific reference current of  $-1$  A/g<sub>cat</sub>.

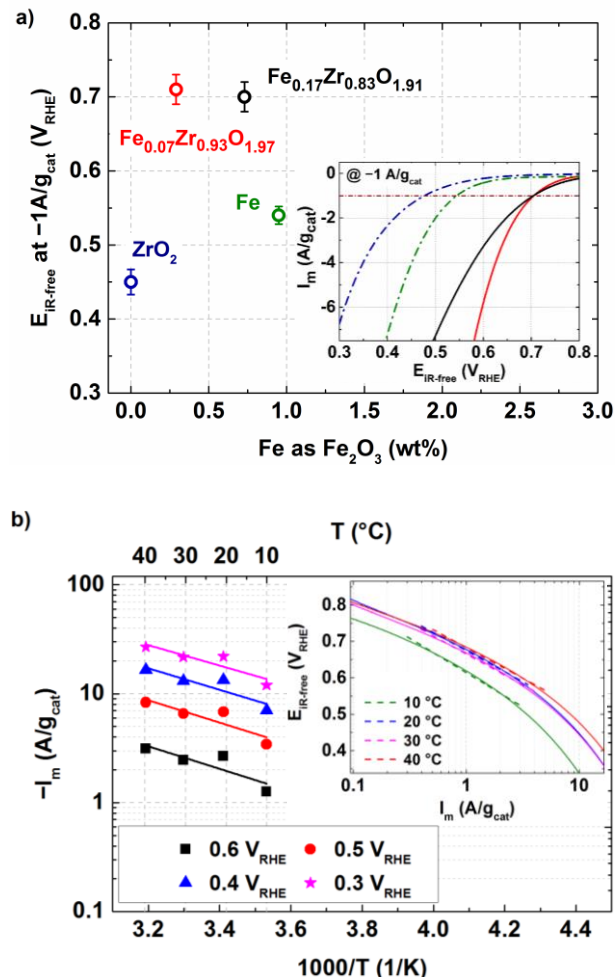


**Figure 5.** a)  $iR$ -free potential ( $E_{iR-free}$  in V<sub>RHE</sub>) at  $-1$  A/g<sub>cat</sub> as function of Fe amount (on the basis of Fe<sub>2</sub>O<sub>3</sub>) for the carbon-supported catalysts specific in Table 1. Inset: Zoom into the capacitively corrected TF-RDE data (anodic scans) in 0.1 M HClO<sub>4</sub> at 1600 rpm, 5 mV/s, and 20 °C; oxygen transport resistance correction was made, by considering a theoretical 2-electron limiting current (2.8 mA/cm<sup>2</sup>) for Fe and ZrO<sub>2</sub> samples, while a limiting current of 5.04 mA/cm<sup>2</sup> was considered (obtained based on the amount of H<sub>2</sub>O<sub>2</sub> content from the ring) for Fe<sub>0.17</sub>Zr<sub>0.83</sub>O<sub>1.91</sub> and Fe<sub>0.07</sub>Zr<sub>0.93</sub>O<sub>1.97</sub> samples. b) ORR activities of Fe<sub>0.07</sub>Zr<sub>0.93</sub>O<sub>1.97</sub> measured at constant cathode potentials in a TF-RDE at various temperatures ( $T = 10 - 40$  °C) in 0.1 M HClO<sub>4</sub> at 1600 rpm, 5 mV/s. Inset: Tafel plot ( $E_{iR-free}$  vs.  $-I_m$ ) of Fe<sub>0.07</sub>Zr<sub>0.93</sub>O<sub>1.97</sub> (10 - 40 °C), where dashed lines represent the linear regression used to calculate Tafel slopes; oxygen transport resistance correction was made, by considering a limiting current of 5.04 mA/cm<sup>2</sup> at all temperatures.

Determination of ORR currents is always performed after subtraction of the capacitive current contribution (measured in Ar-saturated electrolyte) from the overall currents measured in oxygen-saturated solution. Clearly, Fe<sub>0.17</sub>Zr<sub>0.83</sub>O<sub>1.91</sub> and Fe<sub>0.07</sub>Zr<sub>0.93</sub>O<sub>1.97</sub> are much more active than the catalysts containing only Fe or ZrO<sub>2</sub> (Figure 5a). This indicates a strong synergism between

Fe and ZrO<sub>2</sub>. It should be also noted that, since Fe is confirmed to be in Fe<sup>3+</sup> oxidation state (see above), it is assumed that Fe is present as Fe<sub>2</sub>O<sub>3</sub> for the ease of quantification. In addition, from our previous work, we concluded that the optimum ORR activity lies between 0.3 - 0.75 wt% Fe<sub>2</sub>O<sub>3</sub> (7 - 17 at% Fe) [20]. However, based on durability considerations, we decided to use the catalyst with lowest amount of Fe (i.e., 0.3 wt% Fe<sub>2</sub>O<sub>3</sub> (7 at% Fe)  $\equiv$  Fe<sub>0.07</sub>Zr<sub>0.93</sub>O<sub>1.97</sub>) as a benchmark catalyst for further analyses and characterizations. This is because Fe could be leached from the catalyst in the strongly acidic environment of a PEMFC. These liberated iron cations can not only replace protons in the electrode layer and in the membrane, but can also act as Fenton's reagent which leads to the decomposition of locally formed hydrogen peroxide to hydroxyl and hydroperoxyl radicals which lead to membrane degradation and are thus detrimental to PEMFC long-term performance [51, 52].

From our DFT-based results, the much higher mass activity of Fe-substituted ZrO<sub>2</sub> with respect to ZrO<sub>2</sub> can be ascribed to the different surface patterns and, hence, potential oxygen (intermediate) adsorption sites. Besides surface Zr and Zr/Fe atoms in pure and Fe-substituted ZrO<sub>2</sub>, respectively, we must consider the presence of oxygen vacancies (V<sub>O</sub>). In pure ZrO<sub>2</sub>, the concentration of V<sub>O</sub> is very small, since the oxygen vacancy formation energy ( $\Delta E_{form}$ ) both in the bulk [53] and in the surface [35, 54] is quite high. It is well known that  $\Delta E_{form}$  can be dramatically decreased, and hence, V<sub>O</sub> can be increased by aliovalent substitution of Zr<sup>4+</sup> cations with trivalent species like Y, La, or Al [55, 56]. While Sangalli et al. have studied oxygen vacancies in bulk Fe-substituted ZrO<sub>2</sub> [19], we focus here on surface vacancies, due to their possible implication on the ORR catalysis. As detailed in Figure S3 and Table S1 of the SI, the presence of Fe atoms dramatically decreases  $\Delta E_{form}$ . For any possible surface vacancy position in ZrO<sub>2</sub>,  $\Delta E_{form}$  ranges between 5.6 and 5.9 eV, while in Fe-substituted ZrO<sub>2</sub>  $\Delta E_{form}$  decreases to in between 0.07 and 0.8 eV. It is noteworthy here that  $\Delta E_{form}$  decreases not only for the generation of oxygen vacancies which are directly linked to Fe (along Fe-O-Zr bonds), but also for the other Zr-O-Zr bonds along the surface slab. This effect arises from the strong hybridization of Fe  $d$ - $e_g$  states and O  $p$  states, which significantly lowers  $\Delta E_{form}$  by allowing the convenient delocalization of the extra charge ( $2 e^-$  left by the leaving oxygen atom) onto the O sublattice [57].

Figure 5b shows mass activities at 0.3, 0.4, 0.5, and 0.6 V<sub>RHE</sub> as a function of temperature in an Arrhenius representation. Via a linear regression, the activation energy ( $E_{act}$ ) and its standard deviation at each electrode potential were determined, which will be discussed in the last part of this manuscript. A Tafel analysis (Figure 5b, inset) of the Fe<sub>0.07</sub>Zr<sub>0.93</sub>O<sub>1.97</sub> catalyst in the range of  $\approx 0.3 - 3$  A/g<sub>cat</sub> reveals a Tafel slope (TS) between 190 - 160 mV/decade (from 10 - 40 °C). These TS values are slightly lower compared to pure ZrO<sub>2</sub> based catalysts (180 - 210 mV/decade), which were reported in an extensive study by Mittermeier et al. [15].

To gain more mechanistic insights, the influence of catalyst loading on H<sub>2</sub>O<sub>2</sub> yield and the apparent mass activity of the Fe<sub>0.07</sub>Zr<sub>0.93</sub>O<sub>1.97</sub> catalyst was investigated by RRDE. Four catalyst loadings were tested (30, 72, 288, and 576  $\mu$ g/cm<sup>2</sup>) and the H<sub>2</sub>O<sub>2</sub> yield at each loading was evaluated (Figure 6). The loadings were selected such that the difference between consecutive loadings should be at least a factor of two, with the lowest and highest loading differing by a factor of  $\approx 20$ . Peroxide yield is only shown within the potential window where a meaningful signal-to-noise ratio is obtained, i.e., where

capacitive corrections to the disk currents were small (see above). It is readily observed that an increase in the catalyst loading is accompanied by a decrease of the H<sub>2</sub>O<sub>2</sub> yield. At the lowest loading of 30 μg/cm<sup>2</sup>, the fraction of oxygen being reduced to hydrogen peroxide amounts to ≈37%, while at the highest loading of 576 μg/cm<sup>2</sup> it decreases to <10%. Bonakdarpour et al. [58] and Muthukrishnan et al. [59] have reported a similar trend for Fe-N-C type catalysts.

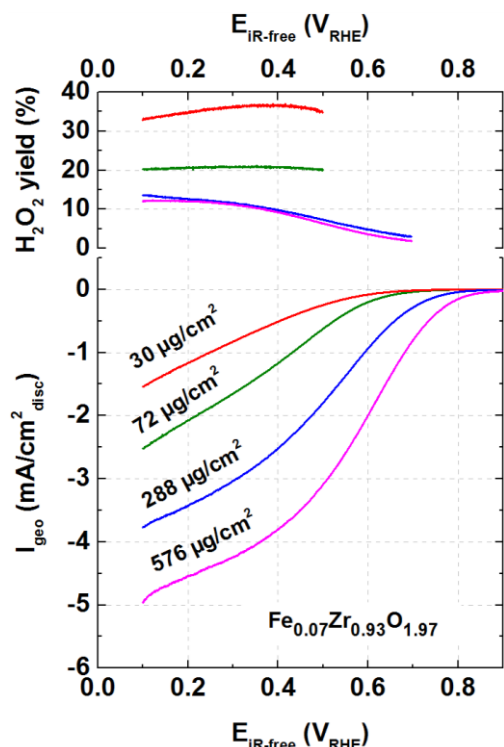


**Figure 6.** Upper panel: RRDE-derived H<sub>2</sub>O<sub>2</sub> yield vs. potential for different loadings of the carbon-supported Fe<sub>0.07</sub>Zr<sub>0.93</sub>O<sub>1.97</sub> catalyst. Lower panel: disk current versus potential for different catalyst loadings. Shown are the data for anodic scans at 5 mV/s (capacitively corrected) in O<sub>2</sub> saturated 0.1 M HClO<sub>4</sub> at 20 °C and 1600 rpm. The collection efficiency (N) of the ring (potentiostated at 1.2 V<sub>RHE</sub>) is taken to be -0.255 [15].

It is also worth mentioning that, for similar loadings, the H<sub>2</sub>O<sub>2</sub> yield from Fe<sub>0.07</sub>Zr<sub>0.93</sub>O<sub>1.97</sub> is approximately half compared to the Fe-N-C catalysts in the study by Bonakdarpour et al. [58]. When compared to pure ZrO<sub>2</sub> catalysts which produce mainly peroxide, it is hypothesized that Fe<sub>0.07</sub>Zr<sub>0.93</sub>O<sub>1.97</sub> has two sites for the ORR [15]: ZrO<sub>2</sub> producing mainly H<sub>2</sub>O<sub>2</sub>, while Fe and/or oxygen vacancies convert the generated H<sub>2</sub>O<sub>2</sub> to H<sub>2</sub>O. This hypothesis is underpinned by the fact that the H<sub>2</sub>O<sub>2</sub> yield decreases with increasing catalyst layer thickness, i.e., as the residence time of generated H<sub>2</sub>O<sub>2</sub> within the catalyst layer increases, providing more time for H<sub>2</sub>O<sub>2</sub> decomposition inside the layer.

Another interesting point to discuss here is that when the ORR mass activities of Fe<sub>0.07</sub>Zr<sub>0.93</sub>O<sub>1.97</sub> are compared for different loadings (30-576 μg/cm<sup>2</sup>), an increase in mass activity (≈1.8 times at 0.6 V<sub>RHE</sub>) for thick films (576 μg/cm<sup>2</sup>) is observed (Figure 7). When a similar analysis is being performed on the data for the Fe-N-C catalyst by Bonakdarpour et al., a mass activity increase of ≈2.4 times at 0.6 V<sub>RHE</sub> can be noted when the loading is increased from 80 and 800 μg/cm<sup>2</sup> [58].

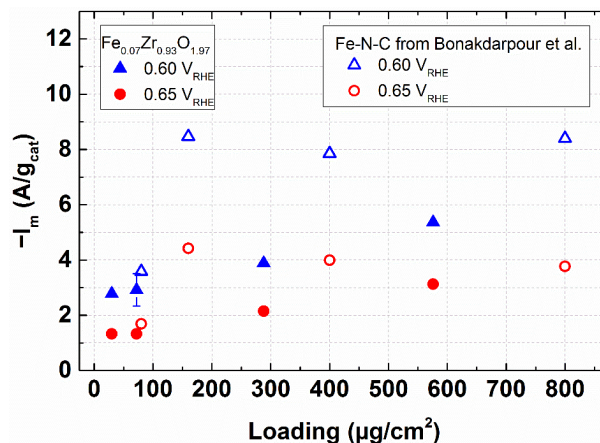


**Figure 7.** Comparison of the RDE-derived ORR mass activity of Fe-N-C (open symbols, extracted from ref. [58]) and Fe<sub>0.07</sub>Zr<sub>0.93</sub>O<sub>1.97</sub> (solid symbols) catalysts at 0.60 and 0.65 V<sub>RHE</sub> as a function of catalyst loadings on the disk electrode.  $I_m$  for Fe-N-C [58] and Fe<sub>0.07</sub>Zr<sub>0.93</sub>O<sub>1.97</sub> catalyst;  $I_m$  is extracted by mass-transport correcting the measured current calculated as described in the experimental section.

This increase of the mass activity of PGM-free catalysts with film thickness is counter-intuitive if compared to Pt-based catalysts, where the mass activity would decrease with increasing catalyst layer thickness due to mass transport limitations [60, 61]. Together with the lower hydrogen peroxide yield observed at higher electrode loadings (equivalent to a higher number of electrons utilized per O<sub>2</sub> molecule), this behavior may be characteristic for ORR catalysts which primarily reduce oxygen to hydrogen peroxide, but at the same time catalyze the chemical decomposition of hydrogen peroxide to O<sub>2</sub> and H<sub>2</sub>O [15, 58].

#### Nature of active sites from DFT study

In order to elucidate the origin of the different products obtained with pure ZrO<sub>2</sub> and Fe-substituted ZrO<sub>2</sub> (defective and non-defective), we have considered adsorption of O<sub>2</sub> on all possible catalytic active sites for both materials. In non-defective ZrO<sub>2</sub>, we consider only Zr sites due to the very low concentration of V<sub>O</sub> expected from the high  $\Delta E_{form}$  value (see Table S1 (SI)). In Fe-substituted ZrO<sub>2</sub>, we have considered Fe and Zr and non-equivalent Fe-V<sub>O</sub>-Zr and Zr-V<sub>O</sub>-Zr, which present a very low  $\Delta E_{form}$  and are likely to occur under operating conditions. As shown in Table S2 (SI), O<sub>2</sub> adsorbs weakly on top of Zr atoms both in non-defective pure and Fe-substituted ZrO<sub>2</sub> with a negligible associated surface-molecule charge transfer. Without oxygen vacancies, O<sub>2</sub> is not expected to be adsorbed on top of Fe atoms in non-defective Fe-substituted ZrO<sub>2</sub>. Regarding defective Fe-ZrO<sub>2</sub>, O<sub>2</sub> adsorption is favored on either Fe-V<sub>O</sub>-Zr or Zr-V<sub>O</sub>-Zr, due to a direct charge transfer from the reduced surface to O<sub>2</sub> antibonding orbitals, which results in stable bridge-like peroxide/superoxide species (Figure S4c and d in the SI). We must note that only for molecular oxygen adsorption on the Fe-V<sub>O</sub>-Zr we obtain an overall favorable energy balance (i.e., negative enthalpy) for the two subsequent processes of oxygen vacancy formation and O<sub>2</sub> adsorption (data listed in Table S2 in the SI).

On these stable species, we have considered the two proton-coupled electron transfer (PCET) steps of the ORR, leading to the formation of H<sub>2</sub>O<sub>2</sub> or H<sub>2</sub>O via a first \*OOH intermediate. In pristine zirconia, where V<sub>O</sub> are difficult to form, our calculations predict a stable Zr-bound \*OOH species (Figure 8a). On the other hand, by considering the active sites made by the formation of different oxygen vacancies created around a Fe cation,



our results show the formation of both a stable \*OOH species (Figure 8b) and a dissociated intermediate made of \*OH and \*O species (Figure 8c). This dissociation does not occur for Zr-V<sub>O</sub>-Zr sites in Fe-substituted ZrO<sub>2</sub> (Figure 8d).

The species in Figure 8c can conveniently form only water after the second PCET step, because the oxygen-oxygen bond has already been dissociated in the first PCET. When the \*OOH species is stable, the second protonation step can lead to H<sub>2</sub>O<sub>2</sub>, if the second proton goes to the un-protonated oxygen atom, or to H<sub>2</sub>O via the

dissociation of the oxygen-oxygen bond and the formation of a surface bound \*O species. We computed the total energy variations related to the reactions (R1) and (R2), considering the equivalence at zero bias between the energy of the proton-electron couple and half the energy of molecular hydrogen (H<sup>+</sup> + e<sup>-</sup> → ½ H<sub>2</sub>) as in the common Nørskov theoretical standard hydrogen reference approach [62]. Our results are listed in Table 2.

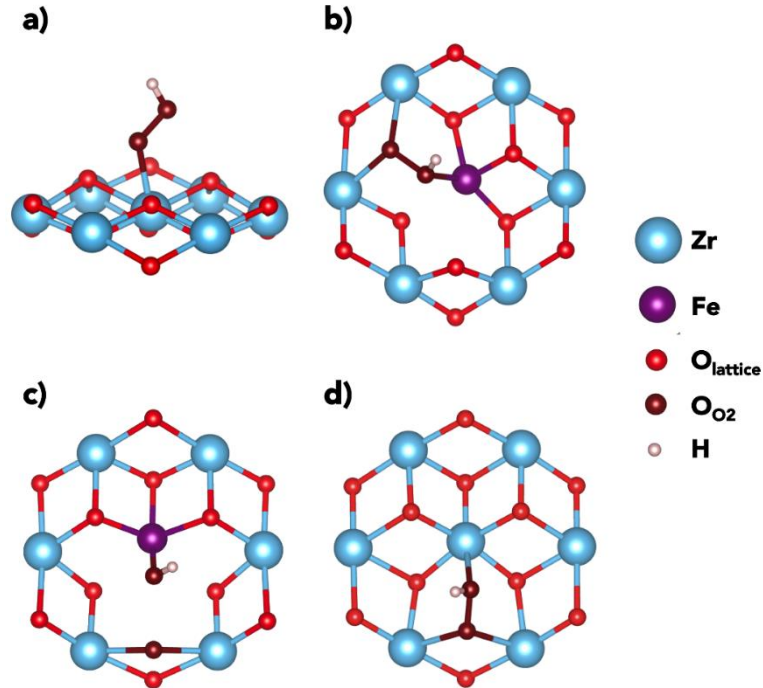


**Figure 8.** **a)** Lateral view of \*OOH species on Zr sites in pure non-defective ZrO<sub>2</sub>. Surface sites in Fe-substituted ZrO<sub>2</sub>; **b)** top view of \*OOH species on Fe-V<sub>O</sub>-Zr vacancies; **c)** top view of \*OOH species, dissociated as \*OH + \*O on Fe-V<sub>O</sub>-Zr vacancies; **d)** top view of \*OOH species on Zr-V<sub>O</sub>-Zr vacancies. Only neighbours and next-neighbouring atoms to the active sites are shown for the ease of viewing.



**Table 2.** Total energy variation (in eV) for reactions (R1) and (R2) (second PCET step of the oxygen reduction reaction), considering the two possible products. The reactions are computed in water via the PCM-like implicit solvation scheme; the energy of the proton-electron couple is considered to be equal to half the energy of H<sub>2</sub>. Negative values correspond to thermodynamically favorable process.

Catalytic site	Products	
	H <sub>2</sub> O <sub>2</sub> (via R1)	H <sub>2</sub> O (via R2)
Zr at ZrO <sub>2</sub> (Figure 8a)	-0.558	0.271
Fe-V <sub>O</sub> -Zr at Fe:ZrO <sub>2</sub> (Figure 8b)	1.227	-1.321
Fe-V <sub>O</sub> -Zr at Fe:ZrO <sub>2</sub> (Figure 8c)	-	-1.355
Zr-V <sub>O</sub> -Zr at Fe:ZrO <sub>2</sub> (Figure 8d)	-0.444	-0.994

According to these results, pure defective ZrO<sub>2</sub> leads mainly to H<sub>2</sub>O<sub>2</sub> production, which is in agreement with our previous findings with Fe-free ZrO<sub>2</sub>/C catalysts [15]. On the other hand, in Fe-substituted ZrO<sub>2</sub> all oxygen vacancies around Fe will lead to a strong preference for the formation of H<sub>2</sub>O, while at these active sites the formation of H<sub>2</sub>O<sub>2</sub> is unfavorable. A small amount of H<sub>2</sub>O<sub>2</sub>

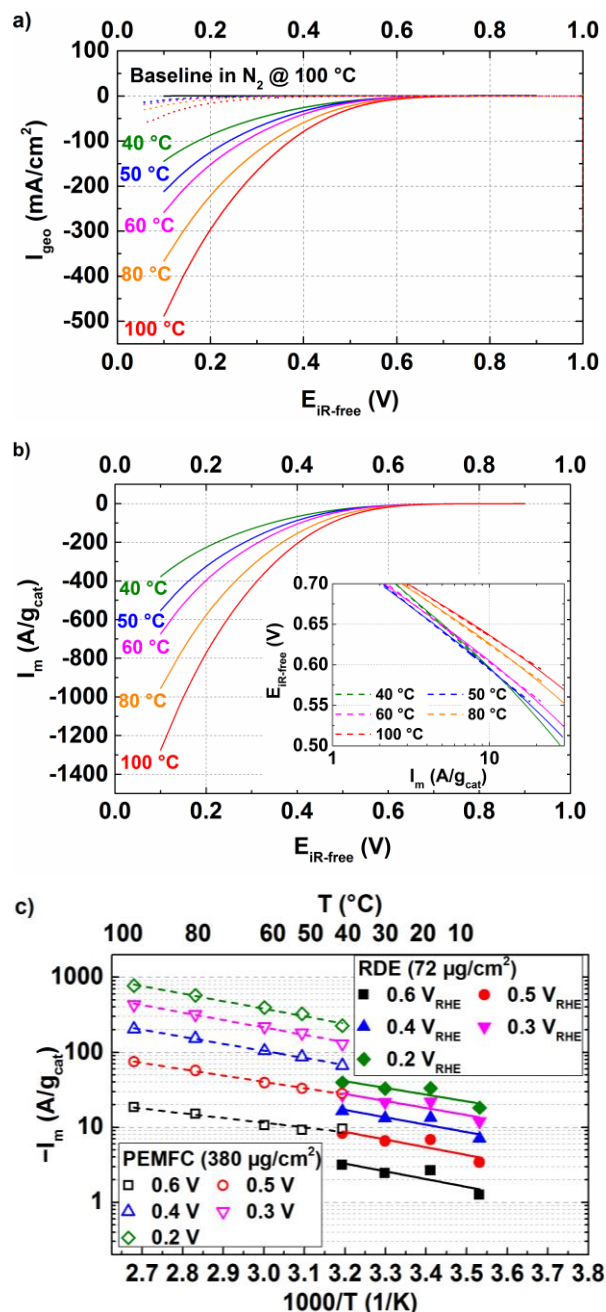
production in Fe-substituted ZrO<sub>2</sub> is to be ascribed to oxygen vacancy active sites in the proximity of Zr atoms. These DFT-based results provide a likely mechanism which is in agreement with the experimental selectivity data from RRDE (see Figure 6).

## PEMFC measurements

Figure 9a. depicts the measured geometric currents ( $I_{\text{geo}}$ ) recorded in anodic scans (at 10 mV/s) in  $\text{H}_2/\text{O}_2$  configuration in a 5  $\text{cm}^2$  active area single-cell PEMFC for the  $\text{Fe}_{0.07}\text{Zr}_{0.93}\text{O}_{1.97}$  catalyst (solid lines) vs. HFR-corrected potential ( $E_{\text{iR-free}}$ ). These data are not corrected for the capacitive contribution (measured in  $\text{N}_2$ ), since it is very small over the relevant potential window between 0.1 - 0.7 V (see black solid line in Figure 9a). Furthermore, a closer inspection of the  $\text{H}_2/\text{N}_2$  data shows that  $\text{Fe}_{0.07}\text{Zr}_{0.93}\text{O}_{1.97}$  does not seem to catalyze the hydrogen oxidation in this potential range, as is evident from the absence of oxidative currents for cross-over  $\text{H}_2$  (i.e.,  $\text{H}_2$  permeating from the anode to the cathode compartment). The oxidative currents are ( $<0.5 \text{ mA}/\text{cm}^2$ ), while typical Pt/C cathode catalysts would show an oxidative current in the range of a few  $\text{mA}/\text{cm}^2$  depending on the pressure, temperature, and relative humidity [63]. After comparison of  $I_{\text{geo}}$  for the  $\text{Fe}_{0.07}\text{Zr}_{0.93}\text{O}_{1.97}$  catalyst with that of a Fe-free carbon-supported  $\text{ZrO}_2$  catalyst (dotted lines in Figure 5a, taken from ref. [15]), we can conclude that the  $\text{Fe}_{0.07}\text{Zr}_{0.93}\text{O}_{1.97}$  catalyst is clearly more active than the Fe-free  $\text{ZrO}_2$  catalyst from our past study [15], as one would have already expected from RDE data (Figure 5a).

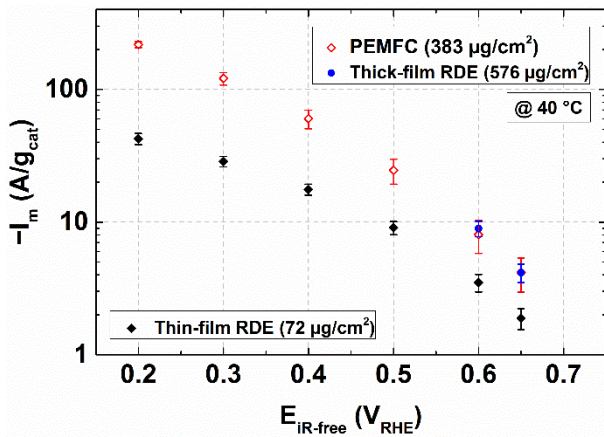
Figure 9b depicts the mass normalized and capacitively corrected polarization curves at different temperatures, whereas the inset in Figure 9b depicts the Tafel analysis for mass-specific ORR currents between 40 – 100  $^\circ\text{C}$  determined between ca. 2 - 20  $\text{A}/\text{g}_{\text{cat}}$ . The Tafel analysis yields TS values of 170 - 130 mV/decade, which are slightly lower than those determined by TF-RDE measurements. From this data, the mass activity at any given iR-free potential is extracted and compared in Figure 9c for PEMFC and RDE measurements in an Arrhenius type representation. At first glance, it is easily observed that the mass activities determined from PEMFC measurements are higher compared to the ones obtained from RDE measurements. When compared at same temperature of 40  $^\circ\text{C}$ ,  $I_{\text{m}}$  from the PEMFC measurement is  $\approx 3$ -fold higher compared to the RDE results at a potential of 0.6  $V_{\text{iR-free}}$  (black symbols); this factor increases to  $\approx 5$ -fold as the potential decreases to 0.2  $V_{\text{iR-free}}$  (green symbols). From Figure 7, an estimate of the difference in mass activity with respect to the catalyst loading, i.e., between 72  $\mu\text{g}/\text{cm}^2$  (in RDE) and 380  $\mu\text{g}/\text{cm}^2$  (in PEMFC) can be obtained and would be around 1.5 times at 0.6  $V_{\text{iR-free}}$ . However, the RRDE analysis reported in Figure 7 was performed at 20  $^\circ\text{C}$ , while the above PEMFC and RDE data are compared at 40  $^\circ\text{C}$ . Thus to confirm whether there is any additional increase in mass activity at higher temperature for a thicker film, a further RDE measurement was performed at 40  $^\circ\text{C}$  with a higher catalyst layer loading of 576  $\mu\text{g}/\text{cm}^2$ .

Figure 10 compares the mass activity at 40  $^\circ\text{C}$  for the thin- and thick-film RDE with the results obtained from PEMFC measurements. It becomes evident that  $I_{\text{m}}$  from a thick-film RDE measurement closely matches the  $I_{\text{m}}$  from PEMFC measurement with a similar loading at 0.6  $V_{\text{iR-free}}$ . This indicates that the increase of the apparent mass activity of the  $\text{Fe}_{0.07}\text{Zr}_{0.93}\text{O}_{1.97}$  catalyst with increasing electrode thickness/loading increases ( $\approx$ factor 2) when the temperature is increased from 20 to 40  $^\circ\text{C}$ . From the RRDE and DFT calculations, it is clear that the  $\text{Fe}_{0.07}\text{Zr}_{0.93}\text{O}_{1.97}$  catalyst generates both  $\text{H}_2\text{O}$  and  $\text{H}_2\text{O}_2$ , whereas the apparent  $\text{H}_2\text{O}_2$  yield decreases with increasing catalyst loading. Thus, one could hypothesize that, at 40  $^\circ\text{C}$ , this increase in  $I_{\text{m}}$  is due to the chemical decomposition of  $\text{H}_2\text{O}_2$ , yielding  $\text{H}_2\text{O}$  and  $\text{O}_2$ ; the latter is in turn electrochemically reduced within the thick layer, as



**Figure 9.** a)  $\text{H}_2/\text{O}_2$  (400/400 nccm) polarization curves for the carbon-supported  $\text{Fe}_{0.07}\text{Zr}_{0.93}\text{O}_{1.97}$  (solid lines) and the Fe-free  $\text{ZrO}_2$  catalysts (dotted lines, taken from ref. [15]) in 5  $\text{cm}^2$  active area single-cell PEMFCs at various temperatures (color coded), 90% RH, and 100 kPa gas partial pressure (absolute pressure varying with temperature due to the changing water partial pressure). The cathode and anode loadings were 380  $\mu\text{g}_{\text{cat}}/\text{cm}^2$  and 100  $\mu\text{g}_{\text{Pt}}/\text{cm}^2$ , respectively. b) Capacitively corrected and mass normalized polarization curve vs. the HFR-corrected cell voltage ( $E_{\text{iR-free}}$ ) for the  $\text{Fe}_{0.07}\text{Zr}_{0.93}\text{O}_{1.97}$  catalyst at 40, 50, 60, 80, and 100  $^\circ\text{C}$  (Inset: Tafel analysis); c) Arrhenius representation for the  $\text{Fe}_{0.07}\text{Zr}_{0.93}\text{O}_{1.97}$  catalyst at various iR-free electrode potentials from RDE and PEMFC data.

mentioned in the previous sections. The strong activity of  $\text{Fe}_{0.07}\text{Zr}_{0.93}\text{O}_{1.97}/\text{KB}_{\text{graph}}$  for the  $\text{H}_2\text{O}_2$  chemical decomposition is confirmed experimentally.



**Figure 10.** Comparison of ORR mass activities ( $I_m$ ) at 40 °C vs. the HFR-corrected cathode potentials ( $E_{iR-free}$ ) obtained from thin-film (72  $\mu\text{g}/\text{cm}^2$ ) and thick-film (576  $\mu\text{g}/\text{cm}^2$ ) RDE, and PEMFC (380  $\mu\text{g}/\text{cm}^2$ ) measurements.

In Figure 11 we show the activation energy ( $E_{act}$ ) of the  $\text{Fe}_{0.07}\text{Zr}_{0.93}\text{O}_{1.97}$  catalyst at different cathode potentials ( $E_{iR-free}$ ), determined from PEMFC and thin-film RDE measurements. Here it is evident that  $E_{act}$  of  $\text{Fe}_{0.07}\text{Zr}_{0.93}\text{O}_{1.97}$  from RDE and PEMFC measurements lie in a similar range (12-20 kJ/mol). On the other hand,  $E_{act}$  of Fe-free  $\text{ZrO}_2$  obtained from RDE and PEMFC measurements, lay on different ranges (PEMFC: 20-30 kJ/mol, thin-film RDE: 15-25 kJ/mol). Mittermeier et al. [15] justified this discrepancy by claiming that PEMFC and RDE have different local  $\text{H}_2\text{O}_2$  concentrations in the electrode which changes the actual overpotential,  $|\eta_{O_2|H_2O_2}|$  since for this catalyst  $\text{H}_2\text{O}_2$  is the major ORR product. Since  $\text{Fe}_{0.07}\text{Zr}_{0.93}\text{O}_{1.97}$  produces  $\approx 2$ -3 times lower peroxide at low catalyst loadings than Fe-free  $\text{ZrO}_2$  and its concentration further decreases with higher loadings, it is reasonable that the  $E_{act}$  from RDE and PEMFC measurements are in better agreement with each other. In addition it is also observed that  $E_{act}$  of the  $\text{Fe}_{0.07}\text{Zr}_{0.93}\text{O}_{1.97}$  catalyst is lower than that of a Fe-free  $\text{ZrO}_2$  catalyst [15].

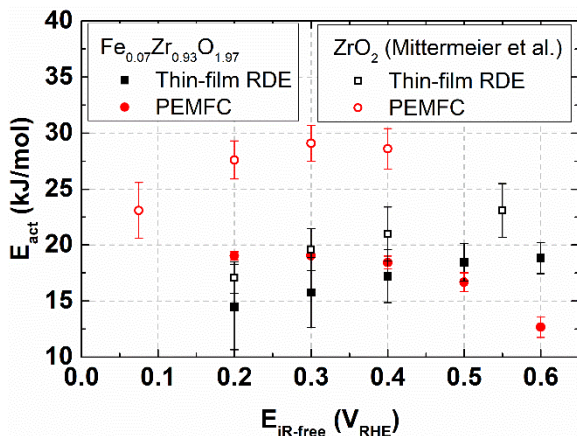


**Figure 11.** Activation energy ( $E_{act}$ ) of the carbon-supported  $\text{Fe}_{0.07}\text{Zr}_{0.93}\text{O}_{1.97}$  and Fe-free  $\text{ZrO}_2$  catalysts (from Mittermeier et al. [15]) measured at different cathode potentials ( $E_{iR-free}$ ) in an RDE and a single-cell PEMFC.

Furthermore, we observe a clear linear correlation between  $E_{act}$  and  $E_{iR-free}$  in RDE data, but not in PEMFC data. A similar behavior was also reported by Mittermeier et al. [15] in the case of pure  $\text{ZrO}_2$  catalysts, where a perfect linear regression for the RDE data was obtained in comparison to a different behavior for PEMFC data. Unfortunately, at this point we can only speculate that this discrepancy stems from the difference in layer

thickness and operating temperatures, i.e., 2  $\mu\text{m}$  in thin-film RDE (10–40 °C) vs.  $\approx 10 \mu\text{m}$  in PEMFC (40–100 °C). It is already shown in the above sections that the increase in  $I_m$  depends on temperature and loading. Therefore, it would be quite reasonable to assume that there is a complex mixture of multiple reactions (oxygen reduction to hydrogen peroxide, chemical decomposition of peroxide) and a very different experimental environment (gas phase in PEMFC and aqueous phase in RDE), which gives rise to this non-linearity.

## Conclusions

While we had already reported on the high ORR activity of carbon-supported nanometric Fe-substituted  $\text{ZrO}_2$  in a previous communication [20], it remained unclear what the nature of the active site(s) would be, how Fe is coordinated in this catalyst, and how it would perform in a single-cell PEMFC. In this contribution we have successfully unveiled the nature of Fe and its coordination in the Fe-substituted  $\text{ZrO}_2$  catalyst, together with the possible active sites. NEXAFS and  $^{57}\text{Fe}$  Mössbauer spectroscopy analysis revealed that Fe exists as high-spin, isolated  $\text{Fe}^{3+}$  in the structure of  $\text{ZrO}_2$ , a finding which was also supported by DFT calculations. In addition, we collected RDE data to determine the ORR mass activity of Fe-substituted  $\text{ZrO}_2$  catalysts, which is much improved in comparison to Fe-free  $\text{ZrO}_2$ . DFT has shed light on the structural origin of this increased ORR activity of  $\text{Fe}_x\text{Zr}_{1-x}\text{O}_{2-\delta}$  catalysts, showing that  $\text{Zr}^{4+}$ -substitution with  $\text{Fe}^{3+}$  highly favors the formation of oxygen vacancies both along Fe-O-Zr and Zr-O-Zr bonds, which are the active sites in these catalysts. The oxygen reduction selectivity ( $\text{H}_2\text{O}$  vs.  $\text{H}_2\text{O}_2$ ) of the carbon supported  $\text{Fe}_{0.07}\text{Zr}_{0.93}\text{O}_{1.97}$  catalyst observed from RRDE measurements are in agreement with the most likely reaction paths emerging from DFT calculations. Also PEMFC measurements on  $\text{Fe}_{0.07}\text{Zr}_{0.93}\text{O}_{1.97}$  show a much higher activity vs. the Fe-free  $\text{ZrO}_2$  catalyst. This increase in activity is further related to lower Tafel-slopes (170–130 vs. 190–230 mV/decade) and lower activation energies (at 0.4 V, 18.4 vs. 28.6 kJ/mol) of  $\text{Fe}_{0.07}\text{Zr}_{0.93}\text{O}_{1.97}$  compared with Fe-free  $\text{ZrO}_2$  catalysts [15]. We also evaluated the variation of mass activity of the best catalyst as a function of loading in RRDE measurements and compared the results with PEMFC data. From this comparison, we observed in both electrochemical techniques a significant increase in mass activity with catalyst loading.

## Acknowledgments

This work was supported by the Bayerische Forschungsstiftung (Project ForOxiE<sup>2</sup>, AZ 1143-14). We thank the Karlsruhe Nano Micro Facility (KNMF) and KARA for the provision of beamtime. The efforts of Dr. Carsten Peters in acquiring TEM images and guidance of Johannes Sicklinger with the peroxide decomposition experiment are greatly acknowledged.

## References

- [1] UNFCCC: Historic Paris Agreement on Climate Change: 195 Nations Set Path to Keep Temperature Rise Well Below 2 Degrees Celsius, Paris, 2015, <https://unfccc.int/news/finale-cop21>. (Accessed on 05/05/2018).
- [2] <http://www.zevalliance.org/international-zev-alliance-announcement/>. (Accessed on 05/05/2018).

- [3] Climate Change 2014: Mitigation of Climate Change. Contribution of Working Group III to the Fifth Assessment Report of the Intergovernmental Panel on Climate Change, Cambridge University Press, Cambridge and New York, 2015.
- [4] S. Jomori, K. Komatsubara, N. Nonoyama, M. Kato, T. Yoshida, An Experimental Study of the Effects of Operational History on Activity Changes in a PEMFC, *Journal of The Electrochemical Society* 160(9) (2013) F1067-F1073.
- [5] A. Orfanidi, P. Madkikar, H.A. El-Sayed, G.S. Harzer, T. Kratky, H.A. Gasteiger, The Key to High Performance Low Pt Loaded Electrodes, *Journal of The Electrochemical Society* 164(4) (2017) F418-F426.
- [6] A. Kongkanand, M.F. Mathias, The Priority and Challenge of High-Power Performance of Low-Platinum Proton-Exchange Membrane Fuel Cells, *The Journal of Physical Chemistry Letters* 7(7) (2016) 1127-1137.
- [7] M. Lefèvre, E. Proietti, F. Jaouen, J.-P. Dodelet, Iron-Based Catalysts with Improved Oxygen Reduction Activity in Polymer Electrolyte Fuel Cells, *Science* 324(5923) (2009) 71-74.
- [8] J.Y. Cheon, T. Kim, Y. Choi, H.Y. Jeong, M.G. Kim, Y.J. Sa, J. Kim, Z. Lee, T.-H. Yang, K. Kwon, O. Terasaki, G.-G. Park, R.R. Adzic, S.H. Joo, Ordered mesoporous porphyrinic carbons with very high electrocatalytic activity for the oxygen reduction reaction, *Scientific Reports* 3 (2013) 2715.
- [9] D. Sebastián, A. Serov, K. Artyushkova, P. Atanassov, A.S. Aricò, V. Baglio, Performance, methanol tolerance and stability of Fe-aminobenzimidazole derived catalyst for direct methanol fuel cells, *Journal of Power Sources* 319 (2016) 235-246.
- [10] Z. Qiao, H. Zhang, S. Karakalos, S. Hwang, J. Xue, M. Chen, D. Su, G. Wu, 3D polymer hydrogel for high-performance atomic iron-rich catalysts for oxygen reduction in acidic media, *Applied Catalysis B: Environmental* 219 (2017) 629-639.
- [11] V. Goellner, C. Baldizzone, A. Schuppert, M.T. Sougrati, K. Mayrhofer, F. Jaouen, Degradation of Fe/N/C catalysts upon high polarization in acid medium, *Physical Chemistry Chemical Physics* 16(34) (2014) 18454-18462.
- [12] C.H. Choi, C. Baldizzone, J.-P. Grote, A.K. Schuppert, F. Jaouen, K.J.J. Mayrhofer, Stability of Fe-N-C Catalysts in Acidic Medium Studied by Operando Spectroscopy, *Angewandte Chemie International Edition* 54(43) (2015) 12753-12757.
- [13] Y. Okada, A. Ishihara, M. Arao, M. Matsumoto, H. Imai, Y. Kohno, K. Matsuzawa, S. Mitsushima, K.-i. Ota, Improvement of the Electrocatalytic Activity of Zirconium Oxide-Based Catalyst for ORR, *ECS Transactions* 64(3) (2014) 231-238.
- [14] Y. Ohgi, A. Ishihara, K. Matsuzawa, S. Mitsushima, K.-i. Ota, M. Matsumoto, H. Imai, Oxygen reduction reaction on tantalum oxide-based catalysts prepared from TaC and TaN, *Electrochimica Acta* 68(Supplement C) (2012) 192-197.
- [15] T. Mittermeier, P. Madkikar, X. Wang, H.A. Gasteiger, M. Piana, ZrO<sub>2</sub> Based Oxygen Reduction Catalysts for PEMFCs: Towards a Better Understanding, *Journal of The Electrochemical Society* 163(14) (2016) F1543-F1552.
- [16] A. Ishihara, M. Tamura, Y. Ohgi, M. Matsumoto, K. Matsuzawa, S. Mitsushima, H. Imai, K.-i. Ota, Emergence of Oxygen Reduction Activity in Partially Oxidized Tantalum Carbonitrides: Roles of Deposited Carbon for Oxygen-Reduction-Reaction-Site Creation and Surface Electron Conduction, *The Journal of Physical Chemistry C* 117(37) (2013) 18837-18844.
- [17] Y. Ohgi, A. Ishihara, K. Matsuzawa, S. Mitsushima, K.-i. Ota, M. Matsumoto, H. Imai, Factors for Improvements of Catalytic Activity of Zirconium Oxide-Based Oxygen-Reduction Electrocatalysts, *Journal of The Electrochemical Society* 160(2) (2013) F162-F167.
- [18] A. Ishihara, Y. Tamura, M. Chisaka, Y. Ohgi, Y. Kohno, K. Matsuzawa, S. Mitsushima, K.-i. Ota, Titanium-Niobium Oxides as Non-Noble Metal Cathodes for Polymer Electrolyte Fuel Cells, *Catalysts* 5(3) (2015) 1289.
- [19] D. Sangalli, A. Lamperti, E. Cianci, R. Ciprian, M. Perego, A. Debernardi, Role of oxygen vacancies on the structure and density of states of iron-doped zirconia, *Physical Review B* 87(8) (2013) 085206.
- [20] P. Madkikar, T. Mittermeier, H.A. Gasteiger, M. Piana, Communication—Synergistic Effect on the Activity of ZrO<sub>2</sub>-Fe as PGM-Free ORR Catalysts for PEMFCs, *Journal of The Electrochemical Society* 164(7) (2017) F831-F833.
- [21] G. Wang, F. Huang, X. Chen, S. Wen, C. Gong, H. Liu, F. Cheng, X. Zheng, G. Zheng, M. Pan, Density functional studies of zirconia with different crystal phases for oxygen reduction reaction, *RSC Advances* 5(103) (2015) 85122-85127.
- [22] L.A. Tomachynski, V.Y. Chernii, S.V. Volkov, Synthesis of dichloro phthalocyaninato complexes of titanium, zirconium, and hafnium, *Russian journal of inorganic chemistry* 47(2) (2002) 208-211.
- [23] T. Haruhiko, S. Shojiro, S. Shinsaku, Synthesis of Metallophthalocyanines from Phthalonitrile with Strong Organic Bases, *Chemistry Letters* 12(3) (1983) 313-316.
- [24] R. Seoudi, G.S. El-Bahy, Z.A. El Sayed, FTIR, TGA and DC electrical conductivity studies of phthalocyanine and its complexes, *Journal of Molecular Structure* 753(1-3) (2005) 119-126.
- [25] P. Madkikar, X. Wang, T. Mittermeier, A.H.A. Monteverde Videla, C. Denk, S. Specchia, H.A. Gasteiger, M. Piana, Synthesis optimization of carbon-supported ZrO<sub>2</sub> nanoparticles from different organometallic precursors, *Journal of Nanostructure in Chemistry* 7(2) (2017) 133-147.
- [26] C.A. Schneider, W.S. Rasband, K.W. Eliceiri, NIH Image to ImageJ: 25 years of image analysis, *Nature Methods* 9 (2012) 671-675.
- [27] M. Merz, D. Fuchs, A. Assmann, S. Uebe, H. v. Löhneysen, P. Nagel, S. Schuppler, Spin and orbital states in single-layered La<sub>2-x</sub>CaxCoO<sub>4</sub> studied by doping- and temperature-dependent near-edge x-ray absorption fine structure, *Physical Review B* 84(1) (2011) 014436.
- [28] B.T. Thole, G.v.d. Laan, Systematics of the Relation between Spin-Orbit Splitting in the Valence Band and the Branching Ratio in X-Ray Absorption Spectra, *EPL (Europhysics Letters)* 4(9) (1987) 1083.
- [29] P.H. Butler, *Point Group Symmetry Applications: Methods and Tables*, Plenum, New York, 1962.



- [30] R.D. Cowan, *The Theory of Atomic Structure and Spectra*, University of California Press, Berkeley, 1981.
- [31] E. Stavitski, F.M.F. de Groot, The CTM4XAS program for EELS and XAS spectral shape analysis of transition metal L edges, *Micron* 41(7) (2010) 687-694.
- [32] G. Kresse, J. Furthmüller, *Vienna Ab-initio Simulation Package (VASP): The Guide*, VASP Group, Universität Wien, Vienna, 2003.
- [33] J.P. Perdew, K. Burke, M. Ernzerhof, Generalized Gradient Approximation Made Simple, *Physical Review Letters* 77(18) (1996) 3865-3868.
- [34] I.A. Vladimir, F. Aryasetiawan, A.I. Lichtenstein, First-principles calculations of the electronic structure and spectra of strongly correlated systems: the LDA + U method, *Journal of Physics: Condensed Matter* 9(4) (1997) 767.
- [35] A.B. Muñoz-García, F. Sannino, G. Vitiello, D. Pirozzi, L. Minieri, A. Aronne, P. Pernice, M. Pavone, G. D'Errico, Origin and Electronic Features of Reactive Oxygen Species at Hybrid Zirconia-Acetylacetonate Interfaces, *ACS Applied Materials & Interfaces* 7(39) (2015) 21662-21667.
- [36] A.B. Muñoz-García, M. Pavone, K-doped Sr<sub>2</sub>Fe<sub>1.5</sub>Mo<sub>0.5</sub>O<sub>6</sub>-[small delta] predicted as a bifunctional catalyst for air electrodes in proton-conducting solid oxide electrochemical cells, *Journal of Materials Chemistry A* 5(25) (2017) 12735-12739.
- [37] R.F.W. Bader, *Atoms in Molecules—A Quantum Theory*, Oxford University Press, New York, 1990.
- [38] K. Mathew, R. Sundararaman, K. Letchworth-Weaver, T.A. Arias, R.G. Hennig, Implicit solvation model for density-functional study of nanocrystal surfaces and reaction pathways, *The Journal of Chemical Physics* 140(8) (2014) 084106.
- [39] E.R. Leite, I.T. Weber, E. Longo, J.A. Varela, A New Method to Control Particle Size and Particle Size Distribution of SnO<sub>2</sub> Nanoparticles for Gas Sensor Applications, *Advanced Materials* 12(13) (2000) 965-968.
- [40] K.J. Chen, T.H. Fang, F.Y. Hung, L.W. Ji, S.J. Chang, S.J. Young, Y.J. Hsiao, The crystallization and physical properties of Al-doped ZnO nanoparticles, *Applied Surface Science* 254(18) (2008) 5791-5795.
- [41] S.L. Gojković, S. Gupta, R.F. Savinell, Heat-Treated Iron(III) Tetramethoxyphenyl Porphyrin Supported on High-Area Carbon as an Electrocatalyst for Oxygen Reduction: I. Characterization of the Electrocatalyst, *Journal of The Electrochemical Society* 145(10) (1998) 3493-3499.
- [42] N.S. McIntyre, D.G. Zetaruk, X-ray photoelectron spectroscopic studies of iron oxides, *Analytical Chemistry* 49(11) (1977) 1521-1529.
- [43] M. Sassi, C.I. Pearce, P.S. Bagus, E. Arenholz, K.M. Rosso, First-Principles Fe L<sub>2,3</sub>-Edge and O K-Edge XANES and XMCD Spectra for Iron Oxides, *The Journal of Physical Chemistry A* 121(40) (2017) 7613-7618.
- [44] K. Otte, R. Pentcheva, W.W. Schmahl, J.R. Rustad, Pressure-induced structural and electronic transitions in FeOOH from first principles, *Physical Review B* 80(20) (2009) 205116.
- [45] T.J. Regan, H. Ohldag, C. Stamm, F. Nolting, J. Lüning, J. Stöhr, R.L. White, Chemical effects at metal/oxide interfaces studied by x-ray-absorption spectroscopy, *Physical Review B* 64(21) (2001) 214422.
- [46] T.R. Sahoo, S.S. Manoharan, S. Kurian, N.S. Gajbhiye, Mössbauer spectroscopic study of iron-doped zirconia synthesized by microwave route, *Hyperfine Interactions* 188(1) (2009) 43-49.
- [47] U.I. Kramm, I. Herrmann-Geppert, J. Behrends, K. Lips, S. Fiechter, P. Bogdanoff, On an Easy Way To Prepare Metal–Nitrogen Doped Carbon with Exclusive Presence of MeN<sub>4</sub>-type Sites Active for the ORR, *Journal of the American Chemical Society* 138(2) (2016) 635-640.
- [48] A. Zitolo, V. Goellner, V. Armel, M.-T. Sougrati, T. Mineva, L. Stievano, E. Fonda, F. Jaouen, Identification of catalytic sites for oxygen reduction in iron- and nitrogen-doped graphene materials, *Nature Materials* 14 (2015) 937.
- [49] U.I. Koslowski, I. Abs-Wurmbach, S. Fiechter, P. Bogdanoff, Nature of the Catalytic Centers of Porphyrin-Based Electrocatalysts for the ORR: A Correlation of Kinetic Current Density with the Site Density of Fe–N<sub>4</sub> Centers, *The Journal of Physical Chemistry C* 112(39) (2008) 15356-15366.
- [50] M. Pavone, A.M. Ritzmann, E.A. Carter, Quantum-mechanics-based design principles for solid oxide fuel cell cathode materials, *Energy & Environmental Science* 4(12) (2011) 4933-4937.
- [51] E. Endoh, S. Terazono, H. Widjaja, Y. Takimoto Degradation Study of MEA for PEMFCs under Low Humidity Conditions, *Electrochemical and Solid-State Letters* 7(7) (2004) A209-A211.
- [52] T. Kinumoto, M. Inaba, Y. Nakayama, K. Ogata, R. Umebayashi, A. Tasaka, Y. Iriyama, T. Abe, Z. Ogumi, Durability of perfluorinated ionomer membrane against hydrogen peroxide, *Journal of Power Sources* 158(2) (2006) 1222-1228.
- [53] J.X. Zheng, G. Ceder, T. Maxisch, W.K. Chim, W.K. Choi, First-principles study of native point defects in hafnia and zirconia, *Physical Review B* 75(10) (2007) 104112.
- [54] O.A. Syzgantseva, M. Calatayud, C. Minot, Revealing the Surface Reactivity of Zirconia by Periodic DFT Calculations, *The Journal of Physical Chemistry C* 116(11) (2012) 6636-6644.
- [55] C. Ricca, A. Ringuede, M. Cassir, C. Adamo, F. Labat, Revealing the properties of the cubic ZrO<sub>2</sub> (111) surface by periodic DFT calculations: reducibility and stabilization through doping with aliovalent Y<sub>2</sub>O<sub>3</sub>, *RSC Advances* 5(18) (2015) 13941-13951.
- [56] H. Zhang, B. Gao, B. Sun, G. Chen, L. Zeng, L. Liu, X. Liu, J. Lu, R. Han, J. Kang, B. Yu, Ionic doping effect in ZrO<sub>2</sub> resistive switching memory, *Applied Physics Letters* 96(12) (2010) 123502.
- [57] A.B. Muñoz-García, A.M. Ritzmann, M. Pavone, J.A. Keith, E.A. Carter, Oxygen Transport in Perovskite-Type Solid Oxide Fuel Cell Materials: Insights from Quantum Mechanics, *Accounts of Chemical Research* 47(11) (2014) 3340-3348.
- [58] A. Bonakdarpour, M. Lefevre, R. Yang, F. Jaouen, T. Dahn, J.-P. Dodelet, J.R. Dahn, Impact of Loading in RRDE Experiments on Fe–N–C Catalysts: Two- or Four-Electron Oxygen Reduction?, *Electrochemical and Solid-State Letters* 11(6) (2008) B105-B108.



- [59] A. Muthukrishnan, Y. Nabaie, T. Okajima, T. Ohsaka, Kinetic Approach to Investigate the Mechanistic Pathways of Oxygen Reduction Reaction on Fe-Containing N-Doped Carbon Catalysts, *ACS Catalysis* 5(9) (2015) 5194-5202.
- [60] S.L. Gojković, S.K. Zečević, R.F. Savinell, O<sub>2</sub> Reduction on an Ink-Type Rotating Disk Electrode Using Pt Supported on High-Area Carbons, *Journal of The Electrochemical Society* 145(11) (1998) 3713-3720.
- [61] K.J.J. Mayrhofer, D. Strmcnik, B.B. Blizanac, V. Stamenkovic, M. Arenz, N.M. Markovic, Measurement of oxygen reduction activities via the rotating disc electrode method: From Pt model surfaces to carbon-supported high surface area catalysts, *Electrochimica Acta* 53(7) (2008) 3181-3188.
- [62] J.K. Nørskov, J. Rossmeisl, A. Logadottir, L. Lindqvist, J.R. Kitchin, T. Bligaard, H. Jónsson, Origin of the Overpotential for Oxygen Reduction at a Fuel-Cell Cathode, *The Journal of Physical Chemistry B* 108(46) (2004) 17886-17892.
- [63] H.A. Gasteiger, W. Gu, R. Makharia, M.F. Mathias, B. Sompalli, Beginning-of-life MEA performance — efficiency loss contributions, *Handbook of Fuel Cells — Fundamentals, Technology and Applications*, Wiley, UK, 2003, pp. 593-610.

## Supplementary information

### Nanometric Fe-Substituted ZrO<sub>2</sub> on Carbon Black as Novel PGM-Free ORR Catalyst for PEMFCs

Pankaj Madkikar<sup>a</sup>, Davide Menga<sup>a</sup>, Gregor S. Harzer<sup>a</sup>, Thomas Mittermeier<sup>a,b</sup>, Armin Siebel<sup>a</sup>, Friedrich E. Wagner<sup>c</sup>, Michael Merz<sup>d</sup>, Stefan Schuppler<sup>d</sup>, Peter Nagel<sup>d</sup>, Ana Belén Muñoz-García<sup>e</sup>, Michele Pavone<sup>f</sup>, Hubert A. Gasteiger<sup>a</sup>, Michele Piana<sup>a</sup>

<sup>a</sup>Chair of Technical Electrochemistry, Department of Chemistry and Catalysis Research Center, Technische Universität München, D-85748 Garching, Germany

<sup>b</sup>Present address: BMW Group, D-80788 Munich, Germany

<sup>c</sup>Department of Physics, Technische Universität München, D-85748 Garching, Germany

<sup>d</sup>Karlsruher Institut für Technologie, Institut für Festkörperphysik, 76021 Karlsruhe, Germany

<sup>e</sup>Department of Physics “Ettore Pancini”, Università degli Studi di Napoli “Federico II”, Via Cintia 21, 80126 Naples, Italy

<sup>f</sup>Department of Chemical Sciences, Università degli Studi di Napoli “Federico II”, Via Cintia 21, 80126 Naples, Italy

---

## Computational Part

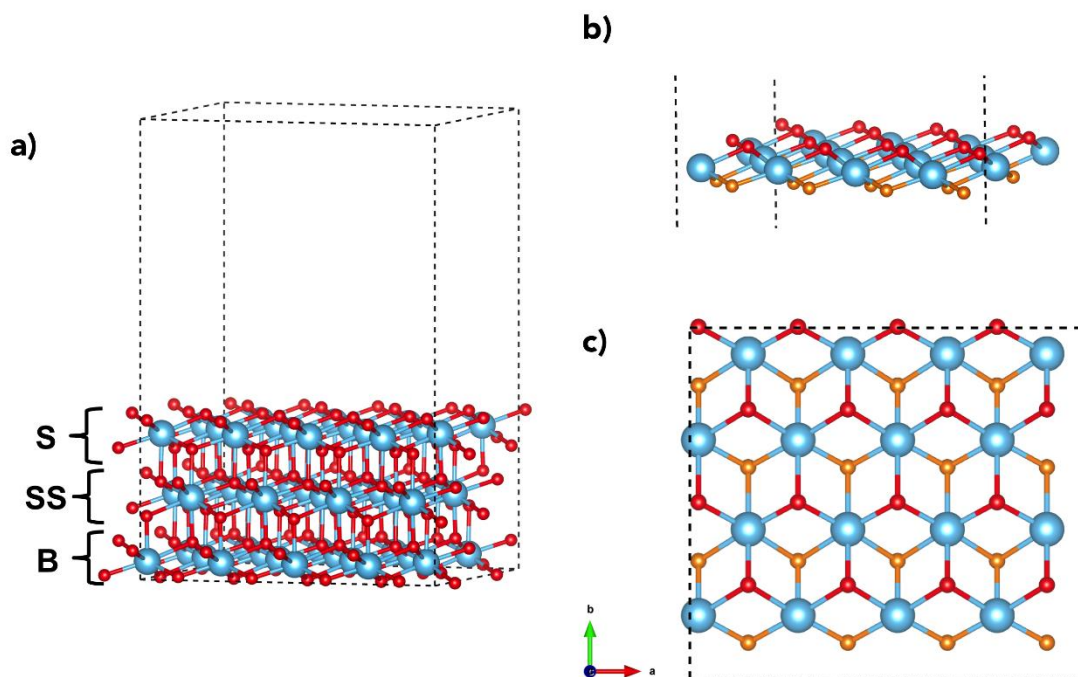


**Figure S1.** **a)** Slab model for tetragonal  $\text{ZrO}_2$  ( $0 \bar{1} 1$ ) surface corresponding to  $(1 \bar{1} 1)$  in the cubic phase. Surface (S), sub-surface (SS) and bulk-like (B) O-Zr-O tri-layers shown. Each tri-layer consist on 16 Zr atoms (blue) and 32 O atoms (red) for a total of 144 atoms; **b)** lateral view of the surface tri-layer of slab a), showing upwards- and downwards-oriented oxygen atoms in red and orange, respectively; **c)** top view of S tri-layer b). In b) and c), SS and B tri-layers have been removed for ease of viewing.

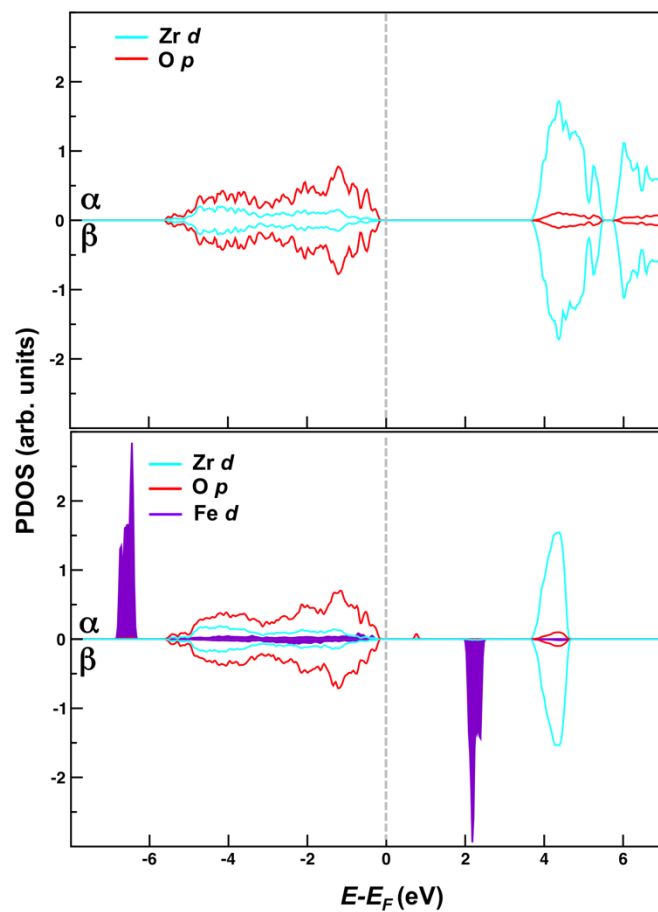


**Figure S2.** Atom- and angular-momentum- projected density of states (PDOS) of  $ZrO_2$  (top) and Fe-substituted  $ZrO_2$  (bottom). Both  $\alpha$  and  $\beta$  spin channels are shown, and Fermi energy has been set to zero.

## Oxygen vacancy formation

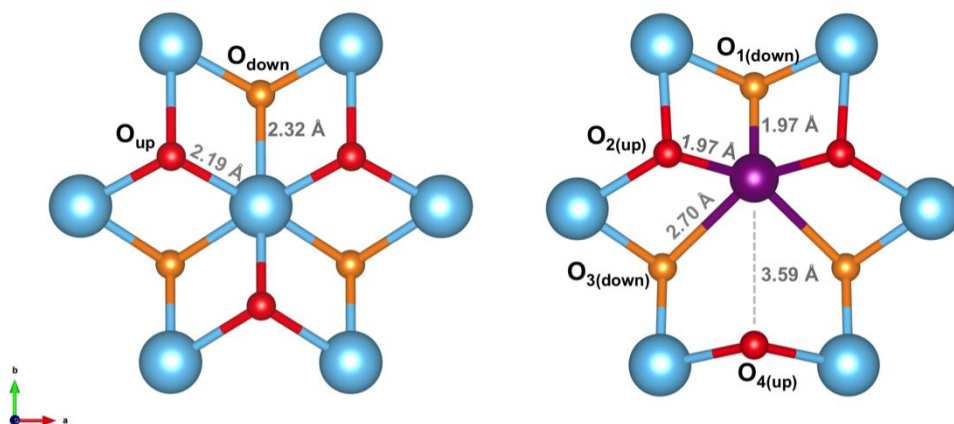


**Figure S3.** Left: Zoom around a surface Zr center on  $ZrO_2$ . Right: Zoom around a surface Fe in Fe-substituted  $ZrO_2$ .  $O_{up}$  and  $O_{down}$  are shown in red and orange, respectively. The Zr/Fe-O distances are also reported.

Figure S3 shows the great anisotropy around the cation surface position upon Fe substitution, since Fe-O bonds are significantly shorter than Zr-O ones. This anisotropy generates four non-equivalent oxygen positions around surface Fe, different from the two non-equivalent ones in pristine  $ZrO_2$ . For these non-equivalent positions, we computed the oxygen vacancy formation energies and the  $O_2$  adsorption energies. In Fe-substituted  $ZrO_2$ ,  $O_{up}$  and  $O_{down}$  oxygen vacancies around Zr atoms that are far from the substituting Fe have also been taken into account.

**Table S1.** Oxygen vacancy formation energies ( $\Delta E_{form}$ ) and charge variation on different sublattices ( $\Delta q$ ) upon formation of the oxygen vacancies  $V_O$ . Positive values in  $\Delta q$  indicates gain in electrons left from leaving structural oxygen.

		Oxygen Vacancy Formation				
		ZrO <sub>2</sub> (111)				
		$\Delta E_{form}$ (eV)	$\Delta q$ (e <sup>-</sup> )			
Zr	O		Fe			
ZrO <sub>2</sub>	V <sub>O</sub> - O <sub>up</sub>	5.84	1.25	0.13	-	
	V <sub>O</sub> - O <sub>down</sub>	5.68	1.29	0.09	-	
Fe:ZrO <sub>2</sub>	Fe-V <sub>O</sub> -Zr	O <sub>1(down)</sub>	0.60	0.30	0.69	0.30
		O <sub>2(up)</sub>	0.30	0.24	0.67	0.37
		O <sub>3(down)</sub>	0.80	0.26	0.78	0.31
		O <sub>4(up)</sub>	0.07	0.23	0.41	0.31
	Zr-V <sub>O</sub> -Zr	O <sub>up</sub>	0.54	0.31	0.77	0.29
		O <sub>down</sub>	0.74	0.29	0.80	0.29

Pure ZrO<sub>2</sub> presents a high oxygen vacancy formation energy ( $\Delta E_{form}$ ), as expected from the unfavourable local reduction of the Zr atoms next to the vacancy. In the Fe-doped material, the expected hybridization of Fe d states and O p states significantly lowers the  $\Delta E_{form}$  in all cases, since it helps the delocalization of the extra charge onto the O sublattice, besides of Zr and Fe. Oxygen vacancies are easier to form at the O<sub>up</sub> positions in all cases, in particular on the O<sub>4</sub>-position, which was not bound to Fe atom anymore after surface reconstruction (Figure S3, right).

## O<sub>2</sub> adsorption

**Table S2.** O<sub>2</sub> adsorption energies ( $E_{ads}$ ), charge variation on different sublattices ( $\Delta q$ ) upon O<sub>2</sub> adsorption (positive values in  $\Delta q$  indicates electron gain left from leaving structural oxygen, while negative  $\Delta q$  indicates electron donation to molecular oxygen) and O-O distance ( $d_{O-O}$ ) after adsorption for all the sites considered in ZrO<sub>2</sub> and Fe-substituted ZrO<sub>2</sub>. Sum of oxygen vacancy formation (Table T1) and O<sub>2</sub> adsorption is indicated for each site. Label of selected structures shown in Figure S4 also included.

		O <sub>2</sub> adsorption								
		(111) 2x2								
		$E_{ads}$ (eV)	$\Delta q$ (e <sup>-</sup> )				$d_{O-O}$ (Å)	$\Delta E_{form}$ + $E_{ads}$ (eV)	Structure (Fig. SZ)	
Zr	O		Fe	O <sub>2</sub>						
ZrO <sub>2</sub>	Non-defective	-0.02	-0.02	~0	-	0.02	1.23	-0.02	<b>a</b>	
	V <sub>O</sub> - O <sub>up</sub>	-5.62	-1.36	-0.13	-	1.49	1.42	+0.12	<b>b</b>	
	V <sub>O</sub> - O <sub>down</sub>	-4.10	-1.17	-0.32	-	1.49	1.49	+1.58	-	
Fe: ZrO <sub>2</sub>	Non-defective		On Fe: 0.85	~0	-0.01	-0.02	0.03	1.23	+0.85	-
			On Zr: 0.10	-0.02	-0.01	~0	0.03	1.23	+0.10	<b>a</b>
	Fe-V <sub>O</sub> -Zr	O <sub>1(down)</sub>	2.21	-0.12	-0.75	-0.06	0.93	1.40	+2.81	-
		O <sub>2(up)</sub>	-0.53	-0.24	-0.87	-0.22	1.33	1.46	-0.23	<b>c</b>
		O <sub>3(down)</sub>	2.19	-0.11	-0.82	-0.22	1.04	1.42	+2.99	-
		O <sub>4(up)</sub>	-0.27	-0.11	-0.27	-0.35	0.73	1.36	-0.20	<b>d</b>
	Zr-V <sub>O</sub> -Zr	O <sub>up</sub>	-0.51	-0.27	-0.90	-0.32	1.49	1.48	+0.03	<b>b</b>
O <sub>down</sub>		2.55	-0.02	-1.39	-0.08	1.49	1.49	+3.29	-	

On the pure and non-defective zirconia, O<sub>2</sub> adsorption is weak, while is extremely favored on defective ZrO<sub>2</sub>. The oxygen-vacant lattice transfers electrons to the O<sub>2</sub> anti-bonding molecular orbital, forming peroxide species.

On the Fe-substituted non-defective zirconia, O<sub>2</sub> presents a low affinity with Fe surface sites so O<sub>2</sub> adsorption is slightly less unfavored on Zr sites, with no charge transfer associated to the process.

Regarding defects, O<sub>2</sub> adsorption is only favored on vacant sites at O “up”-like oxygen positions. Charge transfer to O<sub>2</sub> can be associated to peroxide species in all cases except the O<sub>4up</sub> case, where a superoxide species is formed.

By considering the overall process of oxygen vacancy formation and O<sub>2</sub> adsorption, we can state that O<sub>2</sub> binding energies on non-defective ZrO<sub>2</sub> and Fe-substituted ZrO<sub>2</sub> are near-zero or slightly positive on Zr sites and very positive on Fe sites. Those on defects are near-zero or moderately negative on O<sub>up</sub>-like vacancies and highly positive on O<sub>down</sub>-like vacancies.



For OOH formation, we have considered all cases with near-zero or negative oxygen vacancy formation plus O<sub>2</sub> adsorption values in Table T2 (green values). Structures of adsorbed O<sub>2</sub> in these cases are shown in Figure S4.

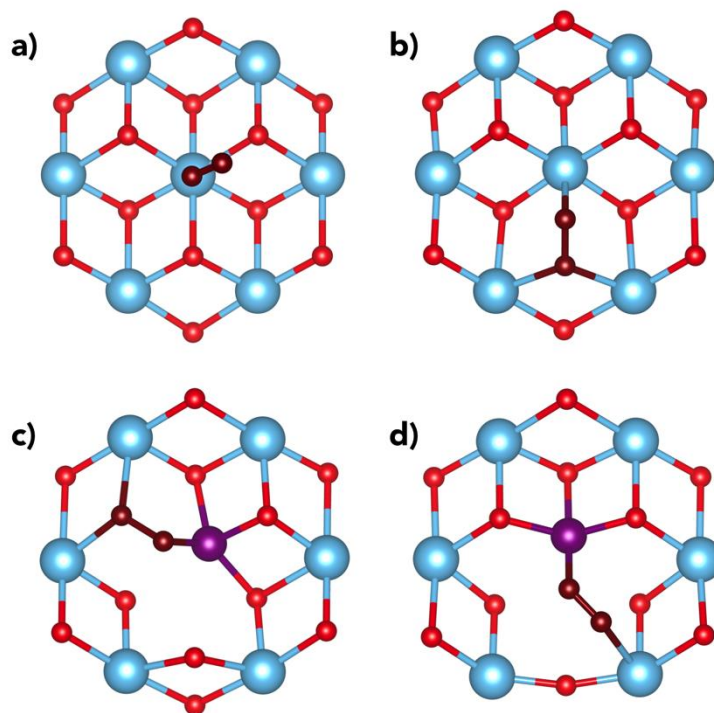


**Figure S4.** Top view of O<sub>2</sub> (dark red) adsorbed on selected adsorption sites (see text). **a)** O<sub>2</sub> on Zr sites on ZrO<sub>2</sub> and Fe-substituted ZrO<sub>2</sub>. **b)** O<sub>2</sub> on all-Zr up-like oxygen vacancies on ZrO<sub>2</sub> and Fe-substituted ZrO<sub>2</sub>. **c)** O<sub>2</sub> on up-like O<sub>2</sub> oxygen vacancy in Fe-substituted ZrO<sub>2</sub> (see Figure S3, right). **d)** O<sub>2</sub> on up-like O<sub>4</sub> oxygen vacancy in Fe-substituted ZrO<sub>2</sub> (see Figure S3, right).

In all cases, we tested the eventual dissociation of O<sub>2</sub> from these structures, but final geometries re-attached to the peroxide/superoxide-like species.

## Addendum – ORR Activity of Cu- or Co-Containing Nanometric ZrO<sub>2</sub>

After having demonstrated that substitution of Zr<sup>4+</sup> by Fe<sup>3+</sup> in ZrO<sub>2</sub> leads to the formation of oxygen vacancies, resulting in improved ORR activity, we were interested in testing different transition metals. In addition, there are already reports in the literature, which correlate the substitution of different metal cations in the ZrO<sub>2</sub> structure with oxygen vacancy formation, and show local changes in the ZrO<sub>2</sub> structure after substitution [127, 128]. Figure 17 shows the activity of Cu- and Co-containing catalyst in comparison to Fe-substituted ZrO<sub>2</sub>, all obtained using similar syntheses, i.e., via co-adsorption of soluble metal macrocycles followed by a heat treatment in a H<sub>2</sub>/O<sub>2</sub> mixture.

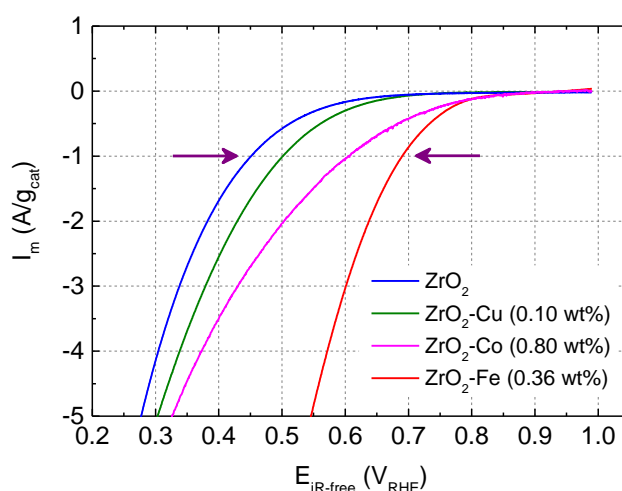


**Figure 17.** ORR mass activities of 12 wt% ZrO<sub>2</sub>/KB<sub>graph</sub>, and ZrO<sub>2</sub>-based/KB<sub>graph</sub> catalysts with Cu (0.10 wt%), Co (0.80 wt%), and Fe (0.36 wt%), measured by thin-film RDE (70-76 μg<sub>cat</sub>/cm<sup>2</sup>) in O<sub>2</sub> saturated 0.1 M HClO<sub>4</sub> at 20 °C and 1600 rpm. The activities are taken from capacitively-corrected anodic scans recorded at 5 mV/s. Here, wt% in the parentheses refers to the nominal content of Cu, Co, and Fe (assumed in metallic state) with respect to the entire catalyst.

Based on these first results, at -1 A/g<sub>cat</sub> the Cu- and Co-containing samples have higher ORR overpotential in comparison to the Fe-containing catalyst, but clearly have a lower overpotential than the metal-free ZrO<sub>2</sub> catalyst. It would be very interesting to use DFT to calculate how the oxygen-vacancy formation energy changes for the different catalysts, and comparing these predictions with X-ray absorption spectroscopy and perhaps XPS measurements. From it might be possible to correlate the absence/presence of oxygen vacancies in the catalyst structure with ORR mass activity. Such correlation would be definitely helpful in the development of oxide-based ORR catalysts.

### 3.5. Noble-Metal-Free Electrocatalysts – Conclusions

As mentioned in chapter 2.1.3, the first part of this thesis was aimed at understanding the active sites in ZrO<sub>2</sub>-based catalysts. In that process, we initially synthesised carbon-supported ZrO<sub>2</sub> nanoparticles from different precursors namely, ZrOPc (N-rich, O-poor) and Zr(acac)<sub>4</sub> (N-absent, O-rich). The synthesised catalysts were subjected to XRPD and TEM analyses. It was concluded that synthesis of a phase pure ZrO<sub>2</sub> was easier with Zr(acac)<sub>4</sub>. This finding was in accordance with the TGA-MS results, which clearly depict that the thermal degradation of Zr(acac)<sub>4</sub> is much easier in comparison to ZrOPc. XPS analysis was performed on several samples synthesised from both precursors. Unfortunately, we could just confirm the formation of ZrO<sub>2</sub>, but could not draw any correlation between Zr 3d<sub>5/2</sub> binding energy and the synthesis temperature or gas conditions, even though the ORR activity varied with these synthesis conditions.

After structural-morphological characterisation of the ZrO<sub>2</sub> catalysts, they were subjected to rigorous electrochemical characterisation. This included, TF-R(R)DE and single PEMFC cell measurements. Tafel analysis and activation energy determination was part of the analysis. From the electrochemical characterisation, it was unambiguously shown that ZrO<sub>2</sub> samples are ORR active only when both Zr and N species are present simultaneously during heat treatment. It was seen that a very small amount of N in the final catalyst (0.2 – 1.5 wt%) was enough to develop measurable ORR activity. RRDE analysis confirmed that the pure-ZrO<sub>2</sub> catalysts followed only the 2e<sup>-</sup> ORR path in acid electrolyte, i.e., produced only H<sub>2</sub>O<sub>2</sub>. Tafel analysis (both from RDE and PEMFC) yielded a Tafel slope of ≈200 mV/decade. In addition, the apparent activation energy was also determined (in a PEMFC: ≈29 kJ/mol at 0.4 V). Based on these results, it was clear that the ORR activity of pure ZrO<sub>2</sub> catalysts was insufficient, and that there was a need to increase their activity.

In pursuit to boost the ORR activity of ZrO<sub>2</sub> catalysts, we decided to use Fe to modify the ZrO<sub>2</sub> structure/activity. This was based on the past literature which claims that Fe forms oxygen vacancies, known as potential ORR active centres, in Fe-substituted ZrO<sub>2</sub>. We unambiguously confirmed that the presence of Fe together with ZrO<sub>2</sub> increases its ORR activity (≈200 mV lower overpotential than Fe-free ZrO<sub>2</sub> or pure Fe catalysts).

Although we managed to boost the activity of ZrO<sub>2</sub> catalysts, the open question was how iron would be coordinated in the catalysts and how these novel catalysts would perform in a single-cell PEMFC. After NEXAFS and Mössbauer analyses, we unambiguously confirmed that Fe in the aforementioned catalysts is present in isolated high-spin Fe<sup>3+</sup> state. This further implied

that the catalyst is indeed Fe-substituted  $\text{ZrO}_2$  ( $\text{Fe}_x\text{Zr}_{1-x}\text{O}_{2-\delta}$ ). RRDE analysis of  $\text{Fe}_{0.07}\text{Zr}_{0.93}\text{O}_{1.97}$  indicated a lower peroxide production in comparison to pure  $\text{ZrO}_2$  catalysts, and single PEMFC measurements confirmed a much higher activity vs. pure  $\text{ZrO}_2$  catalyst. This higher activity was also supported by a lower Tafel slope (170 – 130 mV/decade) and activation energy ( $\approx 18$  kJ/mol at 0.4 V). DFT studies supported these experimental results, showing that the formation of oxygen vacancies is favoured in  $\text{Fe}_x\text{Zr}_{1-x}\text{O}_{2-\delta}$  vs. pure  $\text{ZrO}_2$ , and also allowing to correlate the presence of the oxygen vacancies with the catalytic activity. The DFT predictions of the most likely ORR products ( $\text{H}_2\text{O}$  and  $\text{H}_2\text{O}_2$ ) with and without oxygen vacancies are also in agreement with the experimental selectivity data obtained from RRDE analyses.



## 4. Low-Loaded Platinum Catalysts in PEMFCs

Despite of a substantial improvement in both durability and performance of PGM-free catalysts through the last decades, these materials still have to overcome the challenge of long-term operational stability in PEMFCs. On the other hand, the production of high performing low Pt loaded electrodes in order to meet the cost target towards PEMFC commercialization is also a big challenge. Low Pt loaded electrodes exhibit unaccounted voltage losses, which until recently could not be assigned to any specific origin. Recent research has shown that a big part of these voltage losses can be ascribed to mass transport resistances at the Pt/ionomer interface or through the thin ionomer film covering the Pt nanoparticles [42, 97]. Even though these studies were able to demonstrate that these mass transport resistances have a significant contribution to this unaccounted voltage loss, the origin of a part of these unaccounted losses is still unclear. Chapter 4.1 addresses this issue by examining the effect of ionomer distribution and thickness on the oxygen mass transport resistance. As an outcome, we were successful in unambiguously assigning a part of this unassigned voltage loss to the inhomogeneity of the ionomer distribution in the electrode.

## 4.1. The Key to High Performance Low Pt Loaded Electrodes

A. Orfanidi<sup>‡</sup>, P. Madkikar<sup>‡</sup>, H. A. El-Sayed, G. S. Harzer, T. Kratky, and H. A. Gasteiger

Journal of The Electrochemical Society 2017, Volume 164, Issue 4, F418-F426

<sup>‡</sup>These authors contributed equally to this work.

Permanent weblink: <http://dx.doi.org/10.1149/2.1621704jes>

This is an open access article distributed under the terms of the Creative Commons Attribution 4.0 License (CC BY, <http://creativecommons.org/licenses/by/4.0/>), which permits unrestricted reuse of the work in any medium, provided the original work is properly cited.

In this study, we not only show and confirm that at least part of the unassigned oxygen transport losses in a low Pt loaded PEMFC cathode is related to the homogeneity of the ionomer film over the catalyst. This study is the first one that shows that improving the ionomer distribution on a nanoscale by functionalising the carbon support can substantially reduce transport related voltage losses seen in low Pt loaded electrodes.

In order to demonstrate that nanoscale homogeneity of the ionomer film is critical, we functionalised the surface of a commercially available high surface area carbon support (Vulcan XC-72) with  $-NH_x$  groups, following a previously reported procedure. In short, the carbon support was first functionalised with carboxylic, hydroxyl, and  $NO_x$  groups. This was followed by conversion of these groups into amides/imides/lactams ( $-NH_x$ ). Elemental analysis and XPS was performed on the functionalised carbon support to determine the amounts of nitrogen and the type of functional groups, respectively. This was followed by  $N_2$  adsorption measurements to investigate the microstructure of the carbon support before and after functionalisation. Pt deposition on C- $NH_x$  was performed by the polyol method in order to obtain 20 wt% Pt/C- $NH_x$ . A commercially available 20 wt% Pt/Vulcan XC-72 catalyst was used as a



reference catalyst based on the same type of carbon support, but without  $-\text{NH}_x$  surface groups. The average particle size of Pt was estimated from TEM micrographs. TF-RDE measurements were performed to confirm that functionalisation of the carbon support did not influence the intrinsic ORR activity of the catalyst. Therefore, any differences in the fuel cell performance especially in dilute oxygen (10%  $\text{O}_2$  in  $\text{N}_2$ ) at high current densities can be solely attributed to the interaction between the ionomer and carbon. Low Pt loaded electrodes ( $0.07 \text{ mg}_{\text{Pt}}/\text{cm}^2_{\text{geo}}$ ) were manufactured and tested in a single-cell PEMFC setup. This included differential flow polarization curves, limiting current measurements, and impedance measurements for the determination of both the high frequency resistance and the proton conductivity in the cathode catalyst layer. Each experiment was repeated twice to verify reproducibility.

It was unambiguously shown that the catalyst layer with  $-\text{NH}_x$  functionalised carbon support exhibited a far better high current density performance than the catalyst without any functionalisation. This has been ascribed to a more homogenous ionomer coverage of the catalyst particles, which arises from the strong coulombic interaction between  $-\text{NH}_x$  (positively charged) surface groups on the carbon support and  $\text{SO}^{3-}$  (negatively charged) groups of the ionomer during the ink manufacturing process. In addition, we were able to account for almost half of the unaccounted voltage losses after correcting for the known voltage losses. However, there was still a significant amount of losses that could not be assigned. In order to further understand the origin of these remaining unaccounted voltage losses, we lowered the ionomer to carbon (I/C) mass ratio from 0.65 to 0.40, and then to 0.25. We found that by lowering the I/C ratio to 0.40, we were able to account for almost all of the voltage losses (still unaccounted were  $\approx 40 \text{ mV}$  at  $2 \text{ A}/\text{cm}^2_{\text{geo}}$ ). This proved that the ionomer film thickness does indeed contribute to the mass transport resistance. Lowering the I/C ratio even more (I/C: 0.25), resulted in a slight reduction of the performance due to poor proton conductivity in the catalyst layer. Therefore, in order to achieve high performance with low Pt loaded electrodes, an exquisite balance between obtaining a homogeneous ionomer distribution and optimising for a low I/C ratio (but, adequate proton conductivity) is important.

### **Author contributions**

A. O. and P. M. conceived and coordinated the project. A. O. and P. M. functionalised the carbon. A. O. deposited Pt on the carbon, performed, and analysed the  $\text{N}_2$  adsorption and fuel cell measurements of the catalysts. P. M. performed and analysed TGA, elemental analyses, assisted in RDE, and XPS measurements. H. A. S. performed and analysed RDE and TEM measurements. G. S. H. analysed EIS data. A. O. and P. M. wrote the manuscript. A. O. and

#### *4. Low-Loaded Platinum Catalysts in PEMFCs*

H. A. G. revised the manuscript. All authors discussed the results and commented on the manuscript.



## The Key to High Performance Low Pt Loaded Electrodes

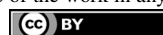
A. Orfanidi,<sup>a,\*,\*,z</sup> P. Madkikar,<sup>a,\*,\*</sup> H. A. El-Sayed,<sup>a</sup> G. S. Harzer,<sup>a,\*</sup> T. Kratky,<sup>b</sup>  
and H. A. Gasteiger<sup>a,\*\*</sup>

<sup>a</sup>Chair of Technical Electrochemistry, Department of Chemistry and Catalysis Research Center, Technische Universität München, D-85748 Garching, Germany

<sup>b</sup>Chair of Physical Chemistry with Focus on Catalysis, Department of Chemistry and Catalysis Research Center, Technische Universität München, D-85748 Garching, Germany

The effect of ionomer distribution on the oxygen mass transport resistance, the proton resistivity of the cathode catalyst layer, and the H<sub>2</sub>/air fuel cell performance was investigated for catalysts with surface modified carbon supports. By introducing nitrogen containing surface groups, it was shown that the ionomer distribution in the cathodic electrode can be optimized to decrease mass transport related voltage losses at high current density. The in house prepared catalysts were fully characterized by TEM, TGA, elemental analysis, and XPS. Thin-film rotating disk electrode measurements showed that the carbon support modification did not affect the oxygen reduction activity of the catalysts, but exclusively affects the ionomer distribution in the electrode during electrode preparation. Limiting current measurements were used to determine the pressure independent oxygen transport resistance – primarily attributed to oxygen transport in the ionomer film – which decreases for catalysts with surface modified carbon support. Systematically lowering the ionomer to carbon ratio (I/C) from 0.65 to 0.25 revealed a maximum performance at I/C = 0.4, where an optimum between ionomer thickness and proton conductivity within the catalyst layer is obtained. From this work, it can be concluded that not only ionomer film thickness, but more importantly ionomer distribution is the key to high performance low Pt loaded electrodes.

© The Author(s) 2017. Published by ECS. This is an open access article distributed under the terms of the Creative Commons Attribution 4.0 License (CC BY, <http://creativecommons.org/licenses/by/4.0/>), which permits unrestricted reuse of the work in any medium, provided the original work is properly cited. [DOI: 10.1149/2.1621704jes] All rights reserved.



Manuscript submitted November 28, 2016; revised manuscript received February 17, 2017. Published March 2, 2017.

Since 2015, proton exchange membrane fuel cell (PEMFC) electric vehicles (FCEVs) are emerging in the market. Despite the major breakthroughs in achieving the durability and performance targets for automotive applications, the cost of fuel cell stacks is still higher compared to the competing internal combustion engines, which is partly related to the cost and supply constraints of the platinum based catalysts, especially for the air cathode (the fast kinetics of the hydrogen oxidation reaction allow for low anode Pt loadings without compromising performance<sup>1</sup>). For large-scale commercial viability, it has been estimated that the Pt loading, especially at the cathode needs to be reduced below 0.1 mg<sub>Pt</sub>/cm<sup>2</sup><sub>geo</sub>.<sup>2,3</sup>

Over the past decade there have been numerous studies focusing on the optimization of the catalyst layer and seeking to gain fundamental insights into the various kinetic and transport resistances, which limit the performance of air cathodes, particularly at low Pt loadings.<sup>4-8</sup> While several methods were developed to quantify the voltage losses, there still remain unexplained voltage losses at high current density, particularly in the case of low Pt loading cathodes.<sup>9-14</sup> These have been rationalized by suggesting more complex oxygen reduction reaction (ORR) kinetics with variable Tafel slope,<sup>4</sup> by an interfacial resistance at the ionomer/platinum interface,<sup>9,15</sup> and/or by unusually high oxygen transport resistances through an assumed homogeneous thin ionomer film covering the Pt particles.<sup>16,17</sup> However, recent high-resolution transmission electron microscopy studies suggested that the ionomer coverage in the electrode may be rather inhomogeneous<sup>18</sup> and that the solvents used for preparing catalyst inks for electrode preparation influence the ionomer distribution in the final electrode, which in turn affects MEA (membrane electrode assembly) performance.<sup>19</sup> Therefore, one of the challenges in preparing MEAs is to achieve catalyst layers with a homogeneous ionomer distribution. This is not only expected to lead to maximum MEA performance, but also to allow for a more quantitative assignment of the transport related voltage losses, as all transport resistance measurements and voltage loss corrections are based on assuming uniform ionomer distribution in the electrode.

In the following, we will show that a modification of the carbon support of the platinum catalyst and an optimization of the ionomer

content of the cathode catalyst layer result in a significant improvement of the MEA performance with ultra-low Pt loadings (ca. 0.07 mg<sub>Pt</sub>/cm<sup>2</sup>). We hypothesize that this is due to achieving a more homogeneous ionomer coverage on the carbon support (Vulcan XC72) which we functionalized with amide/imide/lactam groups (–NH<sub>x</sub>), which are known to ionically interact with the ionomer's sulfonic acid groups (–SO<sub>3</sub>H).<sup>20,21</sup> This hypothesis is consistent with a very recent conference report<sup>22</sup> and with our finding that the unassigned MEA voltage losses, i.e., after correction for the measured proton and oxygen transport resistances, are reduced to unprecedentedly low values in MEAs based on NH<sub>x</sub>-functionalized carbon supports.

### Experimental

**Carbon functionalization with NH<sub>x</sub> surface groups.**—2 g of commercially available Vulcan XC72 (Tanaka Kikinokogyo K.K.) was mixed with 100 ml of 70% HNO<sub>3</sub> (Sigma Aldrich, ACS reagent) and then immersed into a pre-heated oil bath (70°C, reflux conditions) for 30 min. The carbon (further on referred to as “V-Ox”) was filtrated and washed with hot water until neutral filtrate pH; then it was dried in a vacuum oven for 12 h at 80°C. Thereafter, 1 g of the sample was placed in a tube furnace (Carbolite Gero GmbH & Co KG, Germany) for 4 h at 200°C under pure NH<sub>3</sub> gas with a flow rate of 1 l/min to prepare aminated Vulcan carbon (further on referred to as “V-NH<sub>x</sub>”). This procedure closely follows that described by Jansen et al.<sup>23</sup>

**Synthesis of ca. 20 wt% Pt/V-NH<sub>x</sub>.**—300 mg of the aminated Vulcan support, 200 ml of ethylene glycol, 100 ml of deionized water, and 1.54 ml of H<sub>2</sub>PtCl<sub>6</sub> (8 wt% H<sub>2</sub>PtCl<sub>6</sub> in H<sub>2</sub>O (≡ 0.25 mol/l) from Alfa Aesar) were placed in a round-bottom flask and stirred for 18 h at 25°C. Thereafter, the flask was immersed in a pre-heated oil bath at 120°C and stirred for 2 h. The catalyst was separated by filtration and washed with hot water until the filtrate was pH neutral and chloride free; subsequently, the catalyst was dried in a vacuum oven at 70°C for 12 h.<sup>24</sup> The final platinum loading was quantified by both TGA and elemental analysis.

**Microstructure of carbon.**—The surface areas of the commercial and aminated Vulcan carbon were evaluated by N<sub>2</sub> physisorption at 77 K using a Autosorb-iQ instrument (Quantachrome, UK). All samples were degassed under vacuum at 90°C for 15 h prior to physisorption measurements. Adsorption and desorption isotherms of all sam-

<sup>z</sup>These authors contributed equally to this work.

\*Electrochemical Society Student Member.

\*\*Electrochemical Society Fellow.

<sup>z</sup>E-mail: [alin.orfanidi@tum.de](mailto:alin.orfanidi@tum.de)

ples were recorded in the relative pressure range of  $10^{-5} \leq (p/p_0) \leq 0.995$ , where  $p$  represents the gas pressure and  $p_0$  the saturation pressure. This specific relative pressure range was chosen in order to ensure high resolution in the micro and mesopore region; to ensure high accuracy, the sample weight was adjusted to have a minimum absolute surface area of  $>10 \text{ m}^2$ . The specific surface area and pore volume distribution were calculated by the Brunauer-Emmett-Teller (BET) method and by the quenched solid density functional theory (QSDFT) method, respectively (using the ASiQwin program). The adsorption branch was used for the BET surface area (best fit within  $0.01 \leq (p/p_0) \leq 0.25$ ) using a multipoint fit. In addition, a slit/cylindrical pore and adsorption QSDFT kernel was used for the characterization of the nanopore size distribution (small mesopores and micropores with  $<30 \text{ nm}$ ) of the carbons. It should be noted that QSDFT is more accurate than other theories or non-local density functional theory (NLDFT), as it takes into consideration the heterogeneity of the carbon surface and thus gives a more realistic estimate of the micro and mesopores contribution.<sup>25,26</sup>

**Transmission electron microscopy.**—Transmission electron microscopy (TEM) was used to evaluate the Pt distribution on the carbon support. Samples for TEM analysis were prepared by dispersing a very small amount of the catalyst in deionized water and then depositing a few drops of the suspension onto carbon-coated Cu400 TEM grids (Science Services, Germany). Imaging was performed using a CM100 EM (Philips, Netherlands) operated at 100 kV and a resolution of 0.5 nm. For the evaluation of the average Pt particle size distribution, 230 individual particles were measured manually using ImageJ.

**Thermogravimetric analysis.**—Thermogravimetric analysis (TGA) of the carbons (V, V-Ox, and V-NH<sub>x</sub>; all without platinum) was performed with a TGA/DSC 1 (Mettler Toledo, Switzerland) in pure argon at 5 K/min in order to quantify the amount of functional groups on the pristine, oxidized, and aminated carbons. The Pt content was also evaluated by TGA from the residual sample weight after burning the carbon by heating the sample to 1000°C under 83% O<sub>2</sub> in Ar atmosphere.

While the nominal Pt loadings for the here prepared catalyst (supported on V-NH<sub>x</sub>) and the commercial catalyst (supported on V) is 20.0 wt%, it is critical for this study to precisely quantify the Pt loadings, which we have done by TGA. The thus determined Pt content of the here prepared Pt/V-NH<sub>x</sub> catalyst was 20.3 wt% and that of the commercial Pt/V catalyst was 19.4 wt% (which was in perfect agreement with the value provided by the manufacturing company, 19.6 wt%). For this study we used for the commercial Pt/V the Pt loading provided by the manufacturing company.

**Elemental analysis.**—CHNS analyses were done using a EURO EA analyzer (Hekatech, Germany), which is based on the dynamic flash combustion technique. The Pt content was analyzed photometrically using a UV 160 photometer (Shimadzu, Japan).

**X-ray photoelectron spectroscopy.**—Surface chemical analysis was accomplished by X-ray photoelectron spectroscopy (Leybold—Heraeus LHS 10 XPS with a non-monochromatized Mg K $\alpha$  source). The powder samples were pressed and fixed onto a vacuum compatible copper foil adhesive tape. The spectra were recorded at a constant pass energy of 100 eV, corresponding to an energy resolution of  $\sim 1.1 \text{ eV}$ . The measured C 1s peak at a binding energy of 284.5 eV indicates the absence of sample charging. All spectra were recorded at a pressure below  $5 \cdot 10^{-8} \text{ mbar}$ . The core level spectra were fitted by Voigt functions after subtraction of a linear background.

**Rotating disk electrode.**—Electrochemical characterization of the catalysts was done by the thin-film rotating disk electrode (RDE) technique, comparing the intrinsic activities of commercial Vulcan XC72 supported platinum catalyst (19.6 wt% Pt/V from TKK) with that of the here synthesized Pt/V-NH<sub>x</sub> catalyst (20.3 wt% Pt). The catalyst inks were prepared by mixing 7.8 mg of Pt/V in 5.57 ml of

DMF and 7.0 mg of Pt/V-NH<sub>x</sub> in 5.0 ml of DMF (both equating to 1.4 mg<sub>catalyst</sub>/ml). Ink suspensions were bath-sonicated for 15 min. No Nafion was added to the inks in order to ascertain the true mass and specific activities of catalysts without any poisoning caused by Nafion.<sup>27</sup> 5  $\mu\text{l}$  of the ink was drop-cast onto a polished (0.05  $\mu\text{m}$  alumina, Bühler, Germany) and pre-cleaned stationary 5 mm diameter GC electrode (Pine, USA), resulting in a catalyst loading of 36  $\mu\text{g}/\text{cm}^2$ . The electrode was covered with a beaker and the catalyst film was dried overnight at room temperature in order to yield a homogeneous film. All electrochemical measurements were conducted in a home-made three-electrode jacketed glass cell. The electrode was attached to a rotator (Pine, USA), which was connected to a potentiostat (Autolab, Germany). A reversible hydrogen electrode (RHE) was used as a reference electrode, which was calibrated at the beginning of each experiment. All measurements were done at 25°C in 0.1 M HClO<sub>4</sub> which was prepared from 18 M $\Omega \cdot \text{cm}$  Milli-Q water (Merck Millipore, Germany) and HClO<sub>4</sub> (60%, analytical grade, Kanto Chemical, Japan). All gases (Ar, O<sub>2</sub>, and H<sub>2</sub>) were of 6.0 grade (Westfalen, Germany). The reported potentials are referenced to the RHE scale and are iR-free. ORR activities were extracted at 1600 rpm from 20 mV/s anodic scans. Mass and specific activities are extracted after applying the mass transport correction for RDE.<sup>28</sup>

**Membrane electrode assembly preparation.**—All 5 cm<sup>2</sup><sub>geo</sub> membrane electrode assemblies (MEAs) were fabricated using the decal transfer method. Catalyst inks were prepared by mixing the catalyst with a low-EW ionomer containing water-solvent dispersion (Asahi Kasei, Japan, 700 EW (EW  $\equiv g_{\text{polymer}}/\text{mol}_{\text{H}^+}$ )). The ink components were added into a 8 ml HDPE capped bottle containing 16.5 g of 5 mm ZrO<sub>2</sub> beads in the following sequence: catalyst, water, 1-propanol, and finally the ionomer dispersion. The water concentration in the inks was 10 wt%, while the solid content was 0.03 g/ml<sub>ink</sub> in order to obtain a suitable viscosity for the coating process. Three ionomer to carbon weight ratios (I/C) were used: 0.65, 0.40, and 0.25. The inks were mixed by placing the bottles onto a roller-mill (60 rpm) for 18 h at room temperature. Thereafter, the inks were coated onto virgin PTFE using a mayer rod coater.

The noble metal loading of the cathode electrodes was ca. 0.07 mg<sub>Pt</sub>/cm<sup>2</sup><sub>geo</sub> (see details in Table III) for all cases. The loading of the electrodes was determined by weighting the decals before and after the catalyst layer transfer. The same anodes were used for all measurements: 0.1 mg<sub>Pt</sub>/cm<sup>2</sup><sub>geo</sub> consisting of 19.6 wt% Pt/V (TKK) with an I/C ratio of 0.65. The MEAs were assembled by hot pressing a 15  $\mu\text{m}$  membrane (Asahi Kasei) placed between the anode and cathode decals at 155°C for 3 min with an applied force of 0.11 kN/cm<sup>2</sup>. All inks and decals were manufactured twice to verify reproducibility. For each MEA type, two independent fuel cell measurements were conducted; the average value of the measurements with error bars corresponding to the standard deviation are depicted in all figures.

**Fuel cell operation.**—The electrochemical measurements were performed using a single-cell hardware purchased from Fuel Cell Technologies Inc., fitted with 5 cm<sup>2</sup><sub>geo</sub> active area graphite flow-fields<sup>29</sup> (0.5 mm lands/channels; made by Poco Graphite). The assembling torque applied was 12 Nm and the compression of the gas diffusion media (Freudenberg H14C7) was set to 20% by using incompressible fiber-glass PTFE sub-gaskets.

Fuel cell tests were performed on an automated Greenlight Innovation fuel cell test station (type G60). All MEAs were conditioned before each test using the same voltage-controlled ramp-in procedure (H<sub>2</sub>/air flows of 1390/3320 nccm at 80°C, 100% relative humidity, and 150 kPa<sub>abs,inlet</sub>): 0.6 V for 45 min, 5 min at OCV, and 10 min at 0.85 V. This sequence was repeated 10 times, after which constant performance was reached. Differential-flow polarization curves were recorded in current-control mode at 80°C, 170 kPa<sub>abs</sub> inlet controlled pressure, 100% relative humidity (RH) for both reactants, and constant flows of 2000 nccm of H<sub>2</sub> and 5000 nccm of air or O<sub>2</sub> (at these conditions, the inlet to outlet pressure drop in anode and cathode are 2 and 22 kPa, respectively). Prior to recording a polarization curve from

low to high current densities, MEAs were conditioned at 0.75 V for 15 min; each current density point was held for 10 min. and the resulting voltage was averaged over the final 30 s. AC impedance spectra were collected at each current density to determine the respective high frequency resistance (Gamry Ref3000 potentiostat).

**Fuel cell diagnostic measurements.**—The electrochemically active surface area (ECSA) of the cathode electrode was evaluated via cyclic voltammetry, averaging the H-desorption and H-adsorption charge and using a reference value of  $210 \mu\text{C}/\text{cm}_{\text{Pt}}^2$ . The counter/reference electrode was fed with 200 nccm of fully humidified 5%  $\text{H}_2$  in nitrogen, while the working electrode was first flushed with dry  $\text{N}_2$ , the flow of which was stopped during recording the CVs. The potential was cycled at 150 mV/s between 0.03 and 1.0 V (vs. RHE) at 40°C and ambient pressure. The shorting resistance and the  $\text{H}_2$  cross-over currents were measured with  $\text{H}_2/\text{N}_2$  at 170 kPa<sub>abs,inlet</sub>, 80°C, and 100% RH.

The proton conduction resistance in the cathode electrode was determined by AC impedance (Gamry Ref3000 potentiostat) under  $\text{H}_2/\text{N}_2$  (anode/cathode) at 0.2 V, following previous work<sup>43</sup> (peak-to-peak perturbation of 3.5 mV between 500 kHz and 0.2 Hz, with 20 points per decade). Three spectra were collected at each condition to verify reproducibility. Proton conduction resistances ( $R_{\text{H}^+,\text{cath}}$ ) were determined at 100, 70, 50, and 30% RH at 80°C under differential flow conditions ( $\text{H}_2/\text{N}_2$  at 1000/1000 nccm), maintaining constant gas partial pressures (i.e., at cell pressures of 270, 255, 246, and 236 kPa<sub>abs,inlet</sub> respectively). Under these operating conditions the pressure drop over the flow field was negligible (<2 kPa<sub>abs</sub>), which resulted in no change in the RH between the inlet and outlet of the cell.

The effective proton resistance  $R_{\text{H}^+,\text{cath}}^{\text{eff}}$  (in units of  $\Omega \cdot \text{cm}^2$ ) was calculated by using Equation 10 from Liu et al.<sup>42</sup> and was used to correct for the proton conduction resistance induced voltage loss. The proton resistivity  $\rho_{\text{H}^+,\text{cath}}$  (in units of  $\Omega \cdot \text{cm}$ ) was calculated by dividing the proton resistance ( $R_{\text{H}^+,\text{cath}}$ ) by the cathode electrode thickness (calculated from the well-known packing density of Vulcan carbon based electrodes of  $28 \mu\text{m}/(\text{mg}_\text{C}/\text{cm}^2)^{30}$ ).

The total mass transport resistance was derived from limiting current measurements<sup>5,11</sup> at 80°C cell temperature and at 70% RH under differential conditions (2000 nccm of  $\text{H}_2$  and 5000 nccm of  $\text{O}_2/\text{N}_2$  mixtures). The dry mole fraction of oxygen was altered from 0.5 to 24%  $\text{O}_2$  in  $\text{N}_2$ , while the cell potential was set to 0.3, 0.15, 0.1, and 0.05 V for 2 min each. To quantify pressure-independent and pressure-dependent oxygen transport resistances, limiting current measurements were conducted at 170, 270, 350, and 500 kPa<sub>abs,inlet</sub>. Under these experimental conditions there was no significant change of the RH over the whole active area of the MEA. To be more precise, the RH in the inlet of the cell was set at 70% for all cases, while the resulting RH at the outlet was 68%, 70%, 71%, and 73% for the 170, 270, 350, and 500 kPa<sub>abs,inlet</sub>, respectively, based on the measured pressure drop at a given flow rate and pressure as well as a water production corresponding to  $4 \text{ A}/\text{cm}^2_{\text{geo}}$ .

## Results

**Carbon and catalyst characterization.**—CHNS elemental analysis (see Table I) was conducted in order to determine the functionalization degree of the pristine Vulcan XC72 carbon (V), after its oxidation (V-Ox), and after its subsequent amination (V-NH<sub>x</sub>). It is well known that oxidation of carbon in concentrated  $\text{HNO}_3$  leads

**Table I. Elemental analysis (CHNS) of the different carbon supports.**

Sample	C [%]	H [%]	N [%]	S [%]
V	98.8 ± 0.3	0.0	0.2 ± 0.3	0.5 ± 0.3
V-Ox	95.1 ± 0.3	0.1 ± 0.3	0.4 ± 0.3	0.5 ± 0.3
V-NH <sub>x</sub>	96.8 ± 0.3	0.2 ± 0.0	0.9 ± 0.0	0.5 ± 0.0

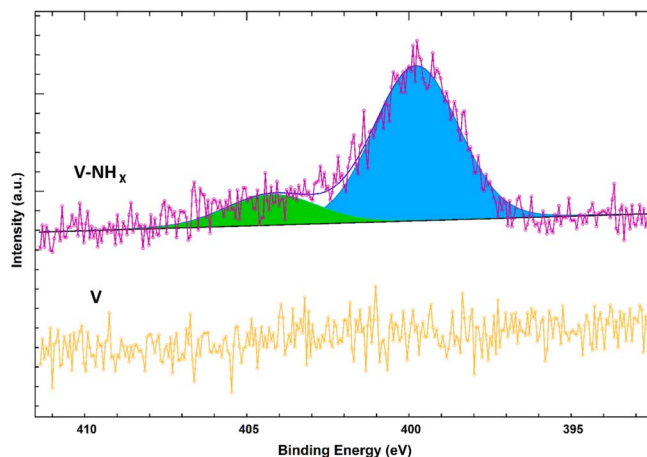


**Figure 1.** XP spectra of V and V-NH<sub>x</sub> carbons in the N 1s region.

to a surface functionalization with carboxylic, hydroxyl, and NO<sub>x</sub> groups.<sup>31,32</sup> Accordingly, the N-content of the oxidized Vulcan support is significantly higher than that of the pristine carbon (see Table I). It further increases after the heat-treatment in NH<sub>3</sub> to 0.9% (see V-NH<sub>x</sub> in Table I), owing to the formation of amides/imides/lactams upon reaction with NH<sub>3</sub>.<sup>23</sup> With the increase in N-content, a simultaneous increase in the C-content is also seen (from 95.1 to 96.8 wt%), which is due to the loss of less stable O-containing functional groups during heat-treatment. The carbon content determined by CHNS analysis (see Table I) is in excellent agreement with that determined by TGA analysis (see Figure S1).

The presence and nature of the N-containing functional groups on the V-NH<sub>x</sub> support was examined by X-ray Photoelectron Spectroscopy (XPS). The broad peak at 399.8 eV (see Figure 1) is consistent with the presence of imides/lactams/amides;<sup>33</sup> while it is not possible by XPS to distinguish between the different groups.<sup>34</sup> The pristine Vulcan XC72 carbon was also subjected to the same analysis and, as expected, no N-containing surface groups could be detected (Figure 1).

The microstructure of the pristine (V) and functionalized carbon (V-NH<sub>x</sub>) was investigated via N<sub>2</sub> adsorption isotherm, seeking to determine any potential changes in the microstructure of the support by the amination treatment, as this could affect the performance of the catalyst in low Pt loaded electrodes.<sup>35</sup> Table II depicts the results from the BET and the QSDFT analysis. The total surface area estimated by BET (first row in Table II) and QSDFT (i.e., the sum of micro and mesopore areas from QSDFT analysis) are in perfect agreement. QSDFT determines the contribution of the micropores and mesopores to the total area (see experimental for more details). Using the IUPAC classification,<sup>36</sup> the contribution of the micropores (<2 nm) and the mesopores (>2 nm) to the total surface area was quantified (see Table II and Figure S2). The area of the micropores is commonly referred to as internal surface area, while the one of the mesopores is referred to as external area of a carbon support. Functionalization of the Vulcan carbon with NH<sub>x</sub> groups clearly results in a decrease of the internal porosity of the carbon support (from 127 to 74 m<sup>2</sup>/g),

**Table II. Surface area analysis of pristine Vulcan carbon (V) and aminated carbon (V-NH<sub>x</sub>). 1<sup>st</sup> row: total surface area determined by BET; 2<sup>nd</sup> and 3<sup>rd</sup> row: meso and micropore areas determined by QSDFT.**

Carbon	Units	V	V-NH <sub>x</sub>
Surface area	m <sup>2</sup> /g <sub>C</sub>	231	175
Mesopores	m <sup>2</sup> /g <sub>C</sub>	102	101
Micropores	m <sup>2</sup> /g <sub>C</sub>	127	74



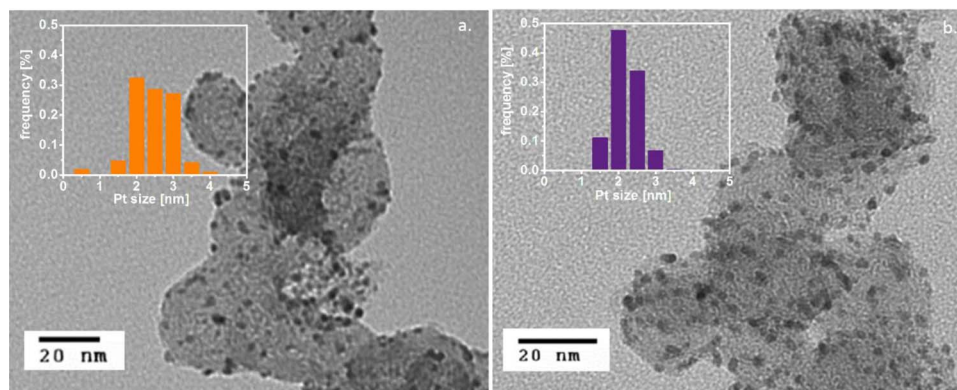


**Figure 2.** TEM micrographs and their corresponding Pt size distribution for: a. 19.6 wt% Pt/V and b. 20.3 wt% Pt/V-NH<sub>x</sub>.

without, however, affecting the external surface area of the carbon and the mesopore size distribution (see Figure S2). The observed decrease in micropore area was previously suggested to be due to the blocking of micropores by functional groups.<sup>57</sup>

TEM micrographs of the commercial Pt/V and the here prepared Pt/V-NH<sub>x</sub> catalyst were obtained to determine their Pt particle size distribution. Representative micrographs and the corresponding particle size distribution histograms are shown in Figure 2. It is clear that both catalysts exhibit a similar and reasonably narrow Pt distribution over the carbon support (see also Figure S3), as well as similar average Pt particle diameters of  $2.4 \pm 0.6$  nm for the 19.6 wt% Pt/V catalyst and of  $2.2 \pm 0.4$  nm for the 20.33 wt% Pt/V-NH<sub>x</sub> catalyst (see Table S4).

No changes of the surface functionalization are expected to occur during the Pt deposition procedure used in the present work, as was demonstrated by XPS measurements in an earlier work.<sup>24</sup>

**Evaluation of the ORR activity by RDE.**—Thin-film RDE ORR activity measurements were performed on the catalysts with functionalized and non-functionalized carbon support. These were done on a Nafion-free thin-film in order to avoid any poisoning of Pt due to Nafion and to exclude any interaction of Nafion with the functionalized catalyst. The obtained mass and specific activities are in good agreement with the literature for Nafion-free films.<sup>27</sup> Table III shows that the ORR mass activity of the catalyst with the functionalized support (Pt/V-NH<sub>x</sub>) is the same as that of the non-functionalized support (Pt/V), both also displaying the same Tafel slope (see Table III and Figure S5). The specific activity of the Pt/V-NH<sub>x</sub> catalyst is slightly higher than that of the Pt/V catalyst due to the difference in the ECSA (see Table III). This clearly confirms that both catalysts have essentially identical ORR activity and that the functionalization does not significantly influence the ORR activity. Thus, any of the below shown differences in the MEA performance of Pt/V vs. Pt/V-NH<sub>x</sub> can be unambiguously attributed to the interaction between the ionomer and the support.

**Fuel cell characterization.**—All cathode electrodes had similar Pt loading ( $68\text{--}78 \mu\text{g}_{\text{Pt}}/\text{cm}^2_{\text{geo}}$ ) and their detailed specifications, including their electrochemically active surface area (ECSA) are summa-

rized in Table IV. The ionomer to carbon weight ratio (I/C) was altered in order to highlight the role of the ionomer film thickness on the mass transport resistance, as will be discussed further on. The uncorrected H<sub>2</sub>/O<sub>2</sub> differential flow performance curves at 80°C, 100% RH, and 170 kPa<sub>abs</sub> inlet pressure as well as the corresponding HFR values are depicted in Figure 3a. Figure 3b shows the H<sub>2</sub>/O<sub>2</sub> performance vs cathode Pt-mass normalized current density (in units of A/g<sub>Pt</sub>), corrected for the HFR, the effective cathode proton transport resistance ( $R_{\text{H}^+, \text{cath}}^{\text{eff}}$ ; calculated from  $\rho_{\text{H}^+, \text{cath}}$  in Figure 6a), and the H<sub>2</sub> crossover ( $4 \pm 0.5 \text{ mA}/\text{cm}^2_{\text{geo}}$ ), i.e., an analogous correction which had been applied previously.<sup>11</sup> For each catalyst, two MEAs were prepared and tested to check for reproducibility, with the error bars corresponding to the standard deviation between those two measurements.

The ORR mass activity values ( $i_m$ ) for the 19.6 wt% Pt/V and 20.3 wt% Pt/V-NH<sub>x</sub> based cathodes were extracted from Figure 3b and are summarized in Table IV. As can be seen, the mass activities of the Pt/V and the Pt/V-NH<sub>x</sub> catalysts are essentially identical, consistent with the identical mass activities determined by RDE (see Table III). In addition, to facilitate a better comparison with the literature, the here obtained ORR mass activities at a total pressure of 170 kPa<sub>abs, inlet</sub> (i.e., O<sub>2</sub> and H<sub>2</sub> partial pressures of 123 kPa<sub>abs, inlet</sub>) were also converted to those ORR mass activities ( $i_m^*$ ) which are obtained at a cell pressure of 150 kPa<sub>abs, inlet</sub> (i.e., O<sub>2</sub> and H<sub>2</sub> partial pressures of 103 kPa<sub>abs, inlet</sub>) using Equation 12 from Ref. 38. The ORR mass activity of all MEAs are in good accordance with literature values reported for 20 wt% Pt/V<sup>39</sup> and other carbon supported catalysts.<sup>40</sup> Tafel slopes were determined from Figure 3b between 50 and 800 mA/cm<sup>2</sup> ( $\sim 850$  and  $\sim 12500 \text{ A}/\text{g}_{\text{Pt}}$  in Figure 3b), following the approach by Neyerlin et al.,<sup>38</sup> to only use current densities greater than 10 times the H<sub>2</sub> crossover current density and up to below 1 A/cm<sup>2</sup>. The Tafel slopes of all electrodes range between 72 and 76 mV/dec. (see Table IV),

**Table IV.** Cathode electrode Pt loadings ( $L_{\text{Pt}}$ ) and I/C mass ratios, their electrochemically active surface area (ECSA) determined by cyclic voltammetry, and their ORR mass activity at 0.9 V, 80°C, and 100% RH at the experimentally used H<sub>2</sub> and O<sub>2</sub> partial pressures of 123 kPa<sub>abs, inlet</sub> ( $i_m$ ) as well as extrapolated to H<sub>2</sub> and O<sub>2</sub> partial pressures of 103 kPa<sub>abs, inlet</sub> ( $i_m^*$ ). The last column shows the Tafel slopes. Mass activities and Tafel slopes were obtained from Figure 3b, i.e., after correction for the HFR, the effective proton conduction resistance in the electrodes, and H<sub>2</sub> crossover correction. The indicated variation represents the standard deviation from two independent measurements.

Catalyst	I/C	$L_{\text{Pt}}$ [ $\mu\text{g}_{\text{Pt}}/\text{cm}^2_{\text{geo}}$ ]	ECSA [ $\text{m}^2/\text{g}_{\text{Pt}}$ ]	$i_m$ [ $\text{A}/\text{g}_{\text{Pt}}$ ]	$i_m^*$ [ $\text{A}/\text{g}_{\text{Pt}}$ ]	TS [mV/dec.]
Pt/V	0.65	$68 \pm 1$	$52 \pm 2$	$119 \pm 2$	$93 \pm 2$	$76 \pm 1$
Pt/V-NH <sub>x</sub>	0.65	$78 \pm 2$	$55 \pm 1$	$110 \pm 6$	$86 \pm 6$	$76 \pm 0$
Pt/V-NH <sub>x</sub>	0.40	$74 \pm 2$	$56 \pm 3$	$127 \pm 2$	$100 \pm 2$	$72 \pm 1$
Pt/V-NH <sub>x</sub>	0.25	$68 \pm 4$	$59 \pm 4$	$146 \pm 8$	$105 \pm 8$	$74 \pm 1$

**Table III.** Electrochemically active surface area (ECSA), ORR mass ( $i_m$ ), and specific ( $i_s$ ) activity at 0.9 V, and Tafel slope (TS) determined by RDE measurements (from the anodic going scan at 20 mV/s and 1600 rpm in O<sub>2</sub> saturated 0.1 M HClO<sub>4</sub> at 25°C). All data are corrected for iR and oxygen mass transport; the errors represent the standard deviations from 3 independent experiments.

Catalyst	ECSA [m <sup>2</sup> /g <sub>Pt</sub> ]	$i_m$ [mA/mg <sub>Pt</sub> ]	$i_s$ [ $\mu\text{A}/\text{cm}^2_{\text{Pt}}$ ]	TS [mV/dec.]
Pt/V	$74 \pm 2.4$	$548 \pm 37$	$828 \pm 26$	$56 \pm 3.0$
Pt/V-NH <sub>x</sub>	$60 \pm 0.5$	$614 \pm 36$	$1036 \pm 65$	$56 \pm 2.0$

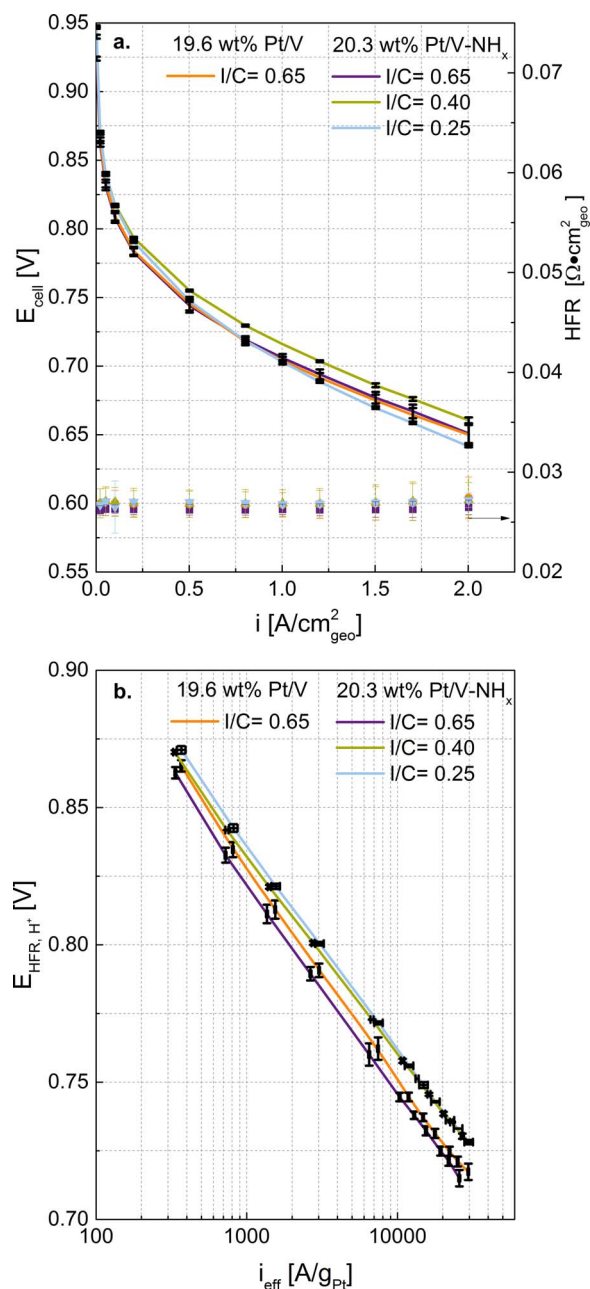


**Figure 3.**  $\text{H}_2/\text{O}_2$  (2000/5000 ncm) differential flow performance of MEAs with ultra-low Pt cathode loadings ( $68\text{--}78 \mu\text{g}_{\text{Pt}}/\text{cm}^2_{\text{geo}}$ ; see Table IV) at  $80^\circ\text{C}$ , 100% RH, and  $P_{\text{cell}} = 170 \text{ kPa}_{\text{abs, inlet}}$  for the 19.6 wt% Pt/V cathode catalyst at an I/C mass ratio of 0.65 (orange curves) and for the 20.3 wt% Pt/V- $\text{NH}_x$  cathode catalyst at I/C mass ratios of 0.65 (purple), 0.40 (green), and 0.25 (light blue): a. uncorrected performance curves (left y-axis) with their corresponding HFR (right y-axis); b. performance curves referenced to the Pt-mass normalized current density corrected for HFR,  $\text{H}^+$  conduction resistance in the cathode ( $R_{\text{H}^+, \text{cath}}^{\text{eff}}$ ), and the  $\text{H}_2$  crossover current. Anode Pt loading were  $0.1 \text{ mg}_{\text{Pt}}/\text{cm}^2_{\text{geo}}$  and the error bars correspond to the standard deviation between two independent measurements on two different MEAs.

and are thus quite close to their theoretical value of  $70 \text{ mV}/\text{dec}$ . (i.e., based on a transfer coefficient of  $\alpha = 1$ ), as reported by Neyerlin et al.<sup>38</sup> Larger Tafel slopes of  $\sim 80 \text{ mV}/\text{dec}$ . for  $0.05 \text{ mg}_{\text{Pt}}/\text{cm}^2$  cathodes were observed by Owejan et al.<sup>11</sup> (evaluated from their transport-corrected  $\text{H}_2/\text{O}_2$  polarization curves between 40 and  $800 \text{ mA}/\text{cm}^2_{\text{geo}}$ ). Considering that residual and/or not accurately corrected for transport resistances always lead to higher apparent Tafel slopes, we ascribe the slightly higher Tafel slopes in their study to unaccounted transport

losses, possibly due to not fully optimized electrodes (e.g., inhomogeneous ionomer distribution), which were shown to yield higher Tafel slopes.<sup>39</sup>

To estimate  $\text{H}_2/\text{air}$  performance of MEAs by differential flow experiments, the stack inlet conditions and the stack outlet conditions are commonly simulated by using 21% and 10%  $\text{O}_2$ , respectively<sup>41</sup> (the latter corresponds to an air stoichiometry of  $\sim 1.9$ ). Thus, polarization curves were measured under differential flows of 21% and 10%  $\text{O}_2$  in  $\text{N}_2$  at  $80^\circ\text{C}$ , 100% RH, and  $170 \text{ kPa}_{\text{abs, inlet}}$ . Figure 4 shows the effect of the carbon support functionalization on the MEA performance for 21%  $\text{O}_2$  (dashed lines) and 10%  $\text{O}_2$  (solid lines). The performance at 0.6 V for the 19.6 wt% Pt/V catalyst (orange lines) is in excellent agreement with recently published data under essentially identical conditions (differential flow,  $80^\circ\text{C}$ , 100% RH, and  $150 \text{ kPa}_{\text{abs, outlet}}$ ) for a graphitized carbon supported Pt catalyst at the same loading<sup>41</sup>:  $1.4 \text{ A}/\text{cm}^2_{\text{geo}}$  (our data) vs  $1.3 \text{ A}/\text{cm}^2_{\text{geo}}$  at 21%  $\text{O}_2$  and  $0.78 \text{ A}/\text{cm}^2_{\text{geo}}$  (our data) vs  $0.83 \text{ A}/\text{cm}^2_{\text{geo}}$  at 10%  $\text{O}_2$ . Significantly better performance, however, is observed with our  $\text{NH}_x$ -functionalized catalyst ( $1.65 \text{ A}/\text{cm}^2_{\text{geo}}$  at 21%  $\text{O}_2$  and  $0.91 \text{ A}/\text{cm}^2_{\text{geo}}$  at 10%  $\text{O}_2$ ). Kongkanand et al.<sup>41</sup> showed that the carbon support surface area (particularly the fraction of surface in micropores) and the location of the Pt particles on the primary carbon particles can significantly influence the local  $\text{O}_2$  mass transport resistance and in turn the performance of the MEA. Pt particles that are located in the interior of the catalyst (Pt supported on a high-surface area carbon, Pt/MSC-a), versus Pt particles located exclusively on the exterior of the carbon (Pt supported on a graphitized carbon support, Pt/GrC-a) can significantly influence the performance under low  $\text{O}_2$  partial pressure and low Pt loadings.

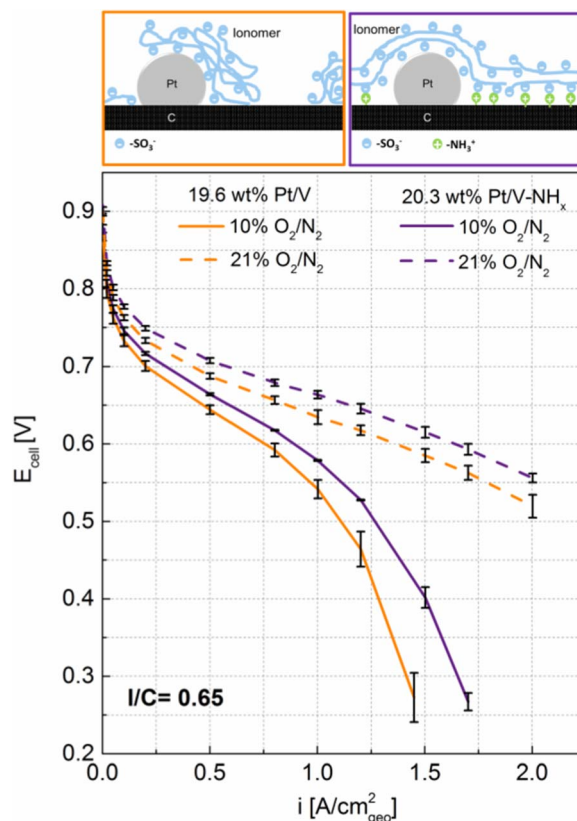


**Figure 4.** Differential flow polarization curves at  $80^\circ\text{C}$  and 100% RH of 19.6 wt% Pt/V (orange) and 20.3 wt% Pt/V- $\text{NH}_x$  (purple) cathodes with I/C of 0.65 with 21%  $\text{O}_2$  (dashed lines) and 10%  $\text{O}_2$  (solid lines) in the cathode gas feed at a cell pressure of  $170 \text{ kPa}_{\text{abs, inlet}}$ . Cathode Pt loadings were  $68 \pm 1$  and  $78 \pm 2 \mu\text{g}_{\text{Pt}}/\text{cm}^2_{\text{geo}}$  for the Pt/V and the Pt/V- $\text{NH}_x$  electrodes, respectively. The error bars correspond to the standard deviation for repeat measurements with two different MEAs. Schematics: sketch of the hypothesized ionomer distribution on the different carbon supports.



In our study, the V-NH<sub>x</sub> has a surface area of 175 m<sup>2</sup>/g<sub>C</sub>, out of which 75 m<sup>2</sup>/g<sub>C</sub> are micropores, so roughly 40% less micropores are accessible on the V-NH<sub>x</sub> compared to the V support. Part of the performance improvement which is observed for the Pt/V-NH<sub>x</sub> vs the Pt/V could be attributed to the reduced micropores of the carbon support. Nevertheless, by comparing the performance of the GrC-a (100 m<sup>2</sup>/g<sub>C</sub>) used in the study by Kongkanand et al. which has no micropores, with the V-NH<sub>x</sub> supported catalyst, the latter exhibits better performance under the same operating conditions. This indicates that the performance improvement between Pt/V-NH<sub>x</sub> and Pt/V cannot be solely attributed to the difference of microporosity of the carbon supports.

We hypothesize that this is due to a more homogeneous ionomer distribution on the NH<sub>x</sub>-functionalized carbon support (illustrated by the sketches in Figure 4), which would result in a homogeneous ionomer film thickness over the whole electrode. This hypothesis is based on the known coulombic interaction between the NH<sub>x</sub> groups on the carbon support with the SO<sub>3</sub><sup>-</sup> groups of the ionomer<sup>20,21</sup> (Figure 4, purple-framed sketch).

In the case of Pt/V, the ionomer distribution is expected to be more inhomogeneous with a more random ionomer film thickness, which would lead to a high O<sub>2</sub> transport resistance in the regions where the ionomer film is thicker and to high proton conduction resistance in the regions where the ionomer film is thinner (Figure 4, orange-framed sketch). The latter would not only be expected to result in a performance decrease at high current densities and low oxygen concentrations, but also to larger discrepancies between transport resistance corrected performance curves and the kinetically predicted performance curve.

The above hypothesis, namely that the performance difference between the Pt/V and the Pt/V-NH<sub>x</sub> is related to a difference in ionomer homogeneity and thus improved oxygen mass transport is further supported by the dependence of the performance to the I/C ratio, evaluated in Figure 5 for the 20.3 wt% Pt/V-NH<sub>x</sub> catalyst: as the I/C is decreased

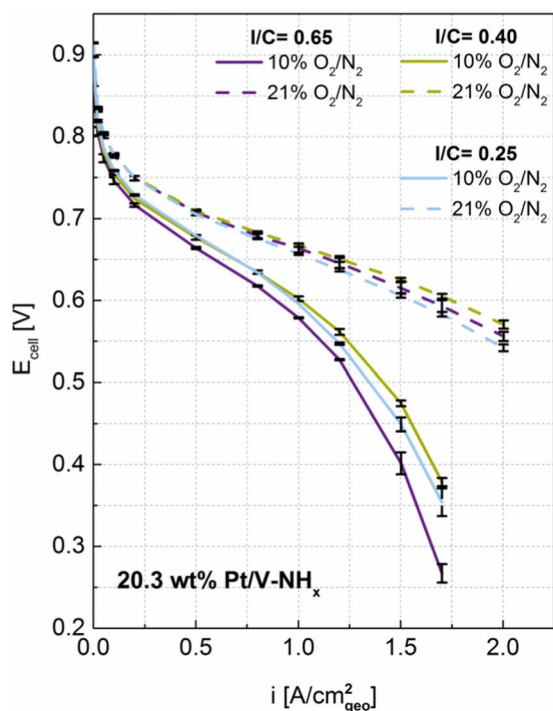


**Figure 5.** Differential flow polarization curves at 80°C and 100% RH of 20.3 wt% Pt/V-NH<sub>x</sub> cathodes with I/C mass ratios of 0.65 (purple), 0.4 (green) and 0.25 (blue) with 21% (dashed lines) and 10% O<sub>2</sub> (solid lines) in the cathode gas feed at a cell pressure of 170 kPa<sub>abs,inlet</sub>. Cathode Pt loadings were 78 ± 2, 74 ± 2, and 68 ± 4 μg<sub>Pt</sub>/cm<sup>2</sup><sub>geo</sub> for the MEAs with ionomer mass ratios of 0.65, 0.40, and 0.25, respectively. The error bars correspond to the standard deviation for repeat measurements with two different MEAs.

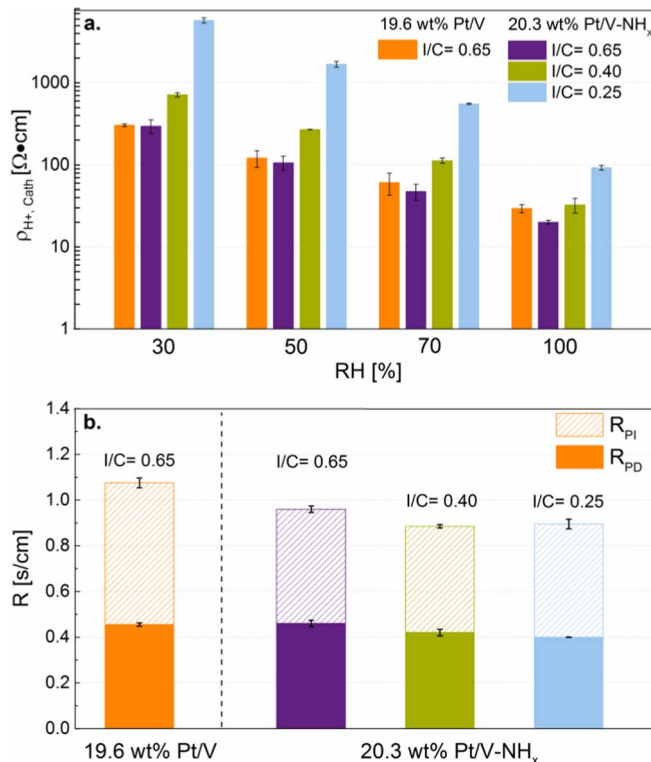


**Figure 6.** The effect of the cathode catalyst layer composition on: a. the cathode proton resistivity ( $\rho_{H^+,eff}$ ) at different relative humidities (RH) and different I/C ratios; b. the total oxygen mass transport resistance ( $R_{total} \equiv$  sum of the solid and hatched bars), which can be separated into a pressure dependent term ( $R_{PD}$ ) and a pressure independent term ( $R_{PI}$ ). The error bars correspond to the standard deviation between independent measurements with two different MEAs.

to 0.40 (green lines), the performance at 0.6 V further increases to 1.75 A/cm<sup>2</sup><sub>geo</sub> at 21% O<sub>2</sub> and 1.0 A/cm<sup>2</sup><sub>geo</sub> at 10% O<sub>2</sub>, which can only be attributed to the O<sub>2</sub> permeability through the ionomer film.<sup>9</sup> As the I/C ratio is further decreased to 0.25, the performance decreases due to poor proton conductivity in the catalyst layer, as will be quantified in the following.

The proton resistivity of the different cathodes was measured according to the method developed by Liu et al.<sup>43</sup> As shown in Figure 6a, the cathode proton resistivity strongly depends on RH and the cathode I/C ratio, as what would be expected.<sup>43</sup> Comparing the Pt/V and the Pt/V-NH<sub>x</sub> based MEAs with an I/C ratio of 0.65, the difference between their proton resistivities at the various RH values is identical within the error of the measurement. It is known that the intrusion of the ionomer into the micropores of the primary carbon particles reduces the ionomer film thickness on the external surface of the carbon support.<sup>42</sup> Thus, to estimate the average ionomer film thickness at the external carbon surface, it is necessary to determine the effective I/C ratio ( $I/C_{eff}$ ) from the overall I/C ratio, as was done by Liu et al.<sup>42</sup> Using this approach, we estimated the effective ionomer thickness ( $t_{ionomer,eff}$ ) by considering the cumulative pore volume in pores smaller than 3 nm, which was obtained from Figure S2 (highlighted). As shown in Table V, the effective ionomer film thickness at the I/C ratio of 0.65 is similar for the catalyst with the aminated (Pt/V-NH<sub>x</sub>) and the untreated carbon (Pt/V). In summary, even though one might have expected that a less homogeneous ionomer film at equal average film thickness (i.e., at equal  $t_{ionomer,eff}$ ) would lead to a higher proton resistivity, this is not the case. However, differences in proton resistivity would also be expected to be negligible for inhomogeneous ionomer films, as long as there exists a continuous ionomer pathway throughout the electrode. Therefore, the homogeneity of the ionomer on the catalyst surface cannot necessarily be deduced from proton

**Table V. Effective I/C ratio ( $I/C_{\text{eff}}$ ) and effective ionomer thickness ( $t_{\text{ionomer,eff}}$ ) for cathodes with different catalysts and overall I/C ratios, calculated by considering ionomer absorption into micropores of  $\leq 3$  nm.**

Catalyst	I/C	$I/C_{\text{eff}}$	$t_{\text{ionomer,eff}}$ [nm]
Pt/V (TKK)	0.65	0.53	2.6
Pt/V-NH <sub>x</sub>	0.65	0.58	2.8
Pt/V-NH <sub>x</sub>	0.40	0.33	1.6
Pt/V-NH <sub>x</sub>	0.25	0.18	0.9

resistivity measurements. Decreasing the I/C ratio of the Pt/V-NH<sub>x</sub> cathodes, the proton resistivity increases substantially, as expected for a decrease in the effective ionomer thickness.<sup>43,44</sup>

To quantify the oxygen mass transport resistance ( $R_{\text{total}}$ ), O<sub>2</sub> limiting current measurements were performed.<sup>5</sup> Since the same gas diffusion layer (GDL) was used for all measurements, one would expect that any differences observed originate from the changes in the catalyst layers and that the contributions from the diffusion medium and the microporous layer remain unchanged. To examine this aspect, the total oxygen mass transport resistance can be separated into a pressure dependent resistance ( $R_{\text{PD}}$ ) and a pressure independent resistance ( $R_{\text{PI}}$ ), which can be quantified by conducting limiting current measurements at various O<sub>2</sub> concentrations and at different cell pressures. Here, the  $R_{\text{PD}}$  term describes Fickian intermolecular gas diffusion through larger pores ( $>100$  nm diameter), while the  $R_{\text{PI}}$  term comprises Knudsen diffusion in small pores of the microporous layer and the catalyst layers ( $<100$  nm diameter) as well as diffusion through the ionomer film covering the Pt particles.<sup>11</sup>

Figure 6b shows the effect of the catalyst layer composition on the total transport resistance  $R_{\text{total}}$ , which is the sum of  $R_{\text{PD}}$  (solid bars) and  $R_{\text{PI}}$  (hatched bars). For all MEAs,  $R_{\text{PD}}$  was relatively constant between 0.41–0.45 s/cm, i.e., essentially identical within the error of the measurement, and thus consistent with the fact that the same diffusion media were used for all experiments. This suggests that the clearly lower total transport resistance for the 20.3 wt% Pt/V-NH<sub>x</sub> cathode with an I/C mass ratio of 0.65 (purple bars) compared to the 19.6 wt% Pt/V catalyst with the same I/C (orange bars) must be due to a lower pressure independent oxygen transport resistance ( $R_{\text{PI}}$ ) of the former, which we ascribe to a more homogeneous ionomer distribution on the NH<sub>x</sub>-functionalized carbon support. As the I/C mass ratio of 20.3 wt% Pt/V-NH<sub>x</sub> cathodes is reduced from 0.65 to 0.40, corresponding to reduction of the estimated ionomer film thickness from  $\sim 2.8$  to  $\sim 1.6$  nm (see Table V),  $R_{\text{total}}$  and  $R_{\text{PI}}$  decrease slightly, qualitatively consistent with a very recent report by Putz et al.,<sup>45</sup> who showed a decrease of  $R_{\text{PI}}$  when the effective ionomer thickness is decreased from  $\sim 3.5$  to  $\sim 2$  nm. In their study, a further decrease of the effective ionomer thickness down to  $\sim 0.5$  nm did not lead to any further decrease in  $R_{\text{PI}}$ , identical to what we observe when decreasing the I/C ratio from 0.40 to 0.25 (blue bars), i.e., from an effective ionomer film thickness of  $\sim 1.6$  nm to  $\sim 0.9$  nm. While this independence of  $R_{\text{PI}}$  from the ionomer film thickness at very low I/C ratios is not yet understood, the data in Figure 6b clearly demonstrate that cathodes prepared with NH<sub>x</sub>-functionalized carbon supports exhibit lower values of  $R_{\text{PI}}$  (and  $R_{\text{total}}$ ), which is consistent with our hypothesis that a more homogeneous ionomer distribution can be achieved by NH<sub>x</sub>-functionalized carbon supports.

## Discussion

The above presented MEA performance data clearly demonstrate superior H<sub>2</sub>/air performance at high current densities of the cathodes based on NH<sub>x</sub>-functionalized carbon supports (see dashed lines in Figures 4 and 5), which is consistent with their lower oxygen mass transport resistance (Figure 6b). Based on the above data, we hypothesize that this is due to a more homogeneous distribution of the ionomer in the MEA. In this case, however, one would expect a more quanti-

tative agreement between the ORR kinetics limited performance and the transport-corrected H<sub>2</sub>/air performance curves, as all transport resistance measurements and voltage loss corrections are based on assuming a uniform ionomer distribution in the electrode. In order to examine this assumption, we will first correct the H<sub>2</sub>/air polarization curves shown in Figures 4 and 5 (dashed lines) by the ohmic losses due to membrane and electronic resistances (i.e., by the HFR), by the total oxygen transport resistance (i.e., by  $R_{\text{total}}$  shown in Figure 6b), and by the effective proton conduction resistance in the cathode ( $R_{\text{H}^+, \text{cath}}^{\text{eff}}$ ); this will then be compared to the performance predicted by the ORR kinetics (see Table IV).

The transport-corrected H<sub>2</sub>/air cell voltage,  $E_{\text{cell,tx-corr}}$ , is described by:

$$E_{\text{cell,tx-corr}} = E_{\text{cell}} + i_{\text{geo}} \cdot \text{HFR} + \Delta E_{\text{O}_2\text{-tx}} + i_{\text{geo}} \cdot R_{\text{H}^+, \text{cath}}^{\text{eff}} \quad [1]$$

where  $U_{\text{cell}}$  is the measured H<sub>2</sub>/air cell voltage,  $\Delta U_{\text{O}_2\text{-tx}}$  is the total oxygen transport induced voltage loss, and  $R_{\text{H}^+, \text{cath}}^{\text{eff}}$  is the effective proton transport resistance in the cathode electrode. As shown by Neyerlin et al.,<sup>46</sup> the latter is related to the measured proton conduction resistance in the cathode,  $R_{\text{H}^+, \text{cath}}$ , by:

$$R_{\text{H}^+, \text{cath}}^{\text{eff}} = R_{\text{H}^+, \text{cath}} / (3 + \zeta) \quad [2]$$

where  $\zeta$  is a scaling parameter which depends on ( $i_{\text{geo}} \cdot R_{\text{H}^+, \text{cath}}$ ) divided by the ORR Tafel slope.<sup>46</sup> The voltage loss due to the total oxygen mass transport resistance ( $R_{\text{total}}$ ) is calculated using Equation 3, derived by Zihrl et al.:<sup>47</sup>

$$\Delta E_{\text{O}_2\text{-tx}} = \frac{RT}{F} \cdot \left( \frac{1}{4} + \frac{\gamma}{\alpha} \right) \cdot \ln \left( \frac{p_{\text{O}_2, \text{channel}} - \frac{RT}{4F} \cdot R_{\text{total}} \cdot i_{\text{geo}}}{p_{\text{O}_2, \text{channel}}} \right) \quad [3]$$

where,  $\gamma$  is the ORR reaction order with respect to oxygen partial pressure ( $\gamma = 0.54$ ),<sup>38</sup>  $\alpha$  is the transfer coefficient ( $\alpha = 1$ ),<sup>38</sup>  $R$  is ideal gas constant,  $T$  is the cell temperature, and  $p_{\text{O}_2, \text{channel}}$  is the partial pressure of O<sub>2</sub> in the channel of the flow field. The transport corrected H<sub>2</sub>/air performance curves calculated from the H<sub>2</sub>/air performance and HFR data as well as from the measured  $R_{\text{total}}$  and  $R_{\text{H}^+, \text{cath}}$  values (for the reader's convenience, all tabulated in the SI) using Equations 1–3 are shown in Figure 7a for the four different cathodes.

These can now be compared to the purely kinetically limited ORR performance,  $U_{\text{ORR}}$ , obtained from the reversible cell voltage,  $E_{\text{rev}}$ , and the ORR overpotential,  $\eta_{\text{ORR}}$ :

$$E_{\text{ORR}} = E_{\text{rev}} - \eta_{\text{ORR}} \quad [4]$$

whereby the reversible cell voltage at the H<sub>2</sub>/air operating conditions is  $E_{\text{rev}} = 1.17$  V (based on Equation 2 in Ref. 38. Under the assumption that the ORR kinetics follow the simple Tafel kinetics with a constant Tafel slope of  $2.303 \cdot R \cdot T / (\alpha \cdot F)$ ,  $U_{\text{ORR}}$  can be related to the ORR mass activity at the reference conditions of 0.9 V,  $T^* = 80^\circ\text{C}$ , and  $p_{\text{H}_2}^* = p_{\text{O}_2}^* = 103$  kPa<sub>abs</sub> (corresponding to  $i_m^*$  in units of A/g<sub>Pt</sub>; see Table IV) by Equation 11 in Neyerlin et al.<sup>38</sup>:

$$E_{\text{ORR}} = 0.900 \text{ V} - \frac{2.303 \cdot R \cdot T}{\alpha \cdot F} \cdot \log \left( \frac{i_{\text{eff}}}{i_m^* \cdot L_{\text{Pt}} \cdot 10^{-3} \cdot \left( \frac{p_{\text{O}_2}}{p_{\text{O}_2}^*} \right)^m \cdot \left( \frac{p_{\text{H}_2}}{p_{\text{H}_2}^*} \right)^{\alpha/2} \cdot \exp \left[ \frac{E_{\text{act}}^{(0.9\text{V})}}{RT} \cdot \left( 1 - \frac{T}{T^*} \right) \right]} \right) \quad [5]$$

where  $\alpha = 1$  ( $\equiv 70$  mV/dec. at  $80^\circ\text{C}$ ),  $L_{\text{Pt}}$  is the cathode platinum loading (in mg<sub>Pt</sub>/cm<sup>2</sup><sub>geo</sub>),  $p_{\text{O}_2}$  and  $p_{\text{H}_2}$  are the actual O<sub>2</sub> and H<sub>2</sub> partial pressures, respectively,  $m$  is the reaction order with respect to O<sub>2</sub> ( $m = 0.79$ )<sup>38</sup> and  $E_{\text{act}}^{(0.9\text{V})}$  is the activation energy at 0.9 V (note that this last term in Equation 5 vanishes for  $T = T^*$ ). The average of the ORR kinetics limited performance curves derived from Equation 5 using the ORR mass activities and Pt loadings of the different MEAs ( $i_m^*$  and  $L_{\text{Pt}}$ , see Table IV) is plotted as black line in Figure 7a, whereby the error bars represent the standard deviation between the calculated ORR curves for each MEA.

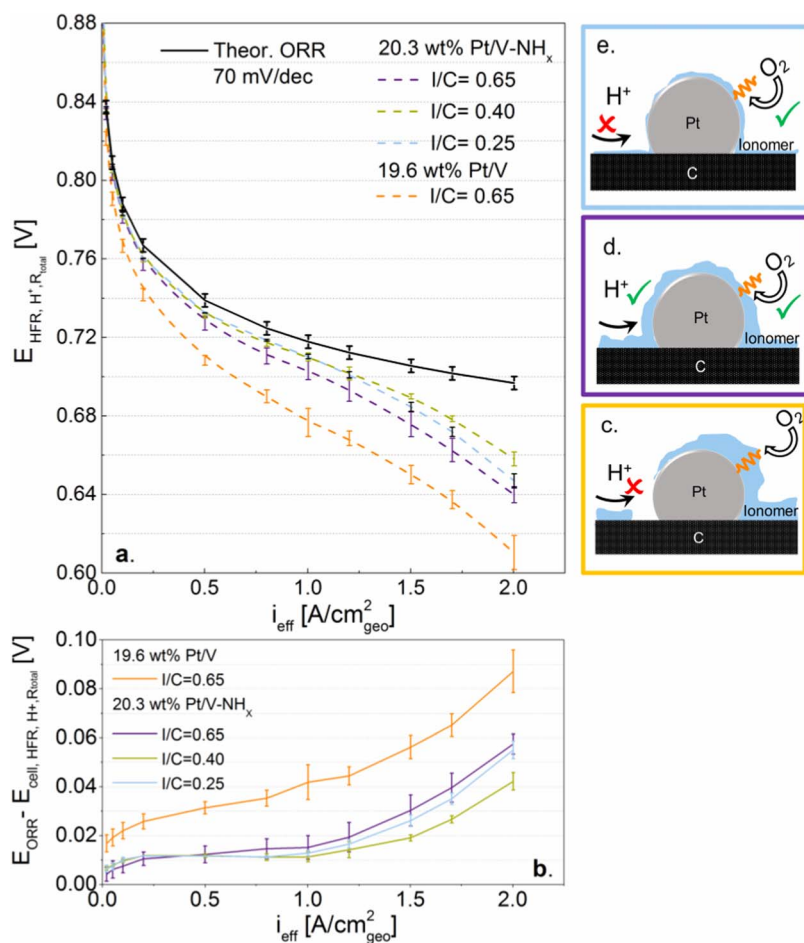


**Figure 7.** a. Transport-corrected  $H_2$ /air performance curves derived from Equation 1 for the various MEA types (dashed lines) and average value of the purely ORR kinetics limited performance curve derived from Equation 5; b. unaccounted voltage losses for each MEA type; c.-e. schematic illustration of the effect of the ionomer distribution and thickness on proton conductivity and mass transport. The error bars correspond to the standard deviation for repeat measurements with two different MEAs. Measurement conditions:  $H_2$ /air at differential flow conditions,  $80^\circ C$ , 100% RH,  $170 \text{ kPa}_{abs, inlet}$ .

We will first discuss the outcome of this analysis by comparing the two different catalysts in cathodes with the same I/C ratio of 0.65 (orange and purple lines in Figure 7a). Quite clearly, the Pt/V-NH<sub>x</sub> based MEAs exhibit lower unaccounted voltage losses, i.e., their transport-corrected performance curve is closer to the purely kinetically limited ORR performance curve (black line). To more clearly illustrate the extent of unaccounted voltage losses, Figure 7b depicts the unaccounted loss of each MEA, obtained by subtracting the transport-corrected performance curves from the ORR kinetics limited performance of the same MEA. Figure 7b illustrates that the unaccounted voltage losses of the Pt/V-NH<sub>x</sub> based MEAs (purple line) are substantially smaller than those of the MEAs based on Pt/V (orange line), which we attribute to a more homogeneous ionomer distribution and thus more homogeneous local ionomer film thickness on the former, illustrated schematically in Figures 7d (Pt/V-NH<sub>x</sub>) and 7c (Pt/V). While for the case of the V-NH<sub>x</sub> supported catalyst the unaccounted voltage losses decrease as the I/C ratio decreases.

Under the assumption of a homogeneous ionomer distribution, decreasing the I/C ratio would result in thinner ionomer film over the Pt particles, thereby facilitating higher  $O_2$  permeability to the Pt/ionomer interface. This is consistent with the lower oxygen mass transport resistance observed for the Pt/V-NH<sub>x</sub> based cathodes with an I/C ratio of 0.4 (see Figure 6b) and with their much reduced unaccounted voltage losses (see green line in Figure 7b). Therefore, from this analysis we can conclude that the ionomer distribution and thickness is a key factor in controlling oxygen mass transport resistances. On the other hand, for the Pt/V-NH<sub>x</sub> based cathodes with an I/C of 0.25, which corresponds to an effective ionomer film thickness of  $\sim 0.9$  nm (see Table V), the proton resistivity increases dramatically (see Figure 6a), which is reasonable considering that this film thickness corresponds to only  $\sim 2$  monolayers of ionomer (based on a PFSA side chain thickness of  $\sim 0.5 \text{ nm}^{48}$ ). Thus, as the ionomer film thickness

becomes very small, the contribution from oxygen mass transport to the voltage loss becomes very small in contrast to the voltage losses due to poor proton conduction in the cathode (Figure 7e). Thus, a delicate balance between good oxygen mass transport and proton conduction has to be achieved in order to obtain the highest possible performance.

In summary, the here prepared MEAs based on cathodes with NH<sub>x</sub>-functionalized carbon support show the highest cell voltage performance at ultra-low Pt loadings reported in the literature. However, even with the evidence for a more homogeneous ionomer distribution achievable with an NH<sub>x</sub>-functionalized carbon support, there still remain  $\sim 40$  mV of unaccounted voltage loss at  $2 \text{ A/cm}^2_{geo}$  (see Figure 7b). In principle, the origin of the unaccounted voltage loss could be due to: i) a not yet optimized MEA design; ii) a deviation from simple Tafel kinetics at low cathode voltages as suggested by Subramanian et al.;<sup>8</sup> and/or, iii) an oxygen mass transport resistance higher than that obtained in the currently used limiting current measurements. While we cannot exclude any of these possibilities, we consider the latter to be most probable, due to the fact that the ratio of heat flux to water generation is higher during limiting current measurements at 0.2 V than that during polarization curve measurements in  $H_2$ /air at 0.5 V, which affects the oxygen mass transport.

## Conclusions

We presented a novel concept for tailoring the ionomer distribution in the catalyst layer. We provide evidence that by functionalizing the surface of a commercially available carbon with  $-NH_x$  groups, the ionomer is homogeneously distributed throughout the catalyst layer, caused by the coulombic attraction between the sulfonate anions of the ionomer and the NH<sub>x</sub> surface groups on the carbon support. This, to our best knowledge, results in the highest  $H_2$ /air performance for



MEAs with ultra-low cathode loadings presented in the literature so far, shown to be due to reduced oxygen mass transport losses through a more homogeneous ionomer film. The presented voltage loss analysis based on proton resistivity and oxygen transport resistance measurements provided detailed insights into the major contributions to the voltage losses in MEAs with low Pt loaded cathodes. Lowering the ionomer/carbon mass ratio from 0.65 to 0.4, i.e., reducing the effective ionomer film thickness, resulted in reduced oxygen transport resistances and improved fuel cell performance. At I/C ratios of 0.25, however the performance was limited by poor proton conductivity. Therefore, the key to high performance low Pt loaded cathodes relies on the exquisite balance between good ionomer distribution and low ionomer/carbon ratio with adequate proton conductivity.

### Acknowledgments

This work has been supported by Greenerity GmbH and the German Federal Ministry of Economy (BMW project support number 03ET2058C) within the HyMotion5 research collaboration. The authors thank Prof. Dr. Sebastian Günther for his help in XPS measurements and Christoph Simon for consulting in mass transport resistance measurements.

### References

- J. Durst, A. Siebel, C. Simon, F. Hasche, J. Herranz, and H. A. Gasteiger, *Energy Environ. Sci.*, **7**, 2255 (2014).
- O. Groeger, H. A. Gasteiger, and J. P. Suchsland., *J. Electrochem. Soc.*, **162**, A2605 (2015).
- A. Kongkanand and M. F. Mathias, *J. Phys. Chem. Lett.*, **7**, 1127 (2016).
- U. Beuscher, *J. Electrochem. Soc.*, **153**, A1788 (2006).
- D. R. Baker, D. A. Caulk, K. C. Neyerlin, and M. W. Murphy, *J. Electrochem. Soc.*, **156**, B991 (2009).
- Y. Wang and C.-Y. Wang, *J. Electrochim. Acta*, **50**, 1307 (2005).
- Y. Liu, M. W. Murphy, D. R. Baker, W. Gu, C. Ji, J. Jorne, and H. A. Gasteiger, *ECS Trans.*, **11**, 473 (2007).
- N. P. Subramanian, T. A. Greszler, J. Zhang, W. Gu, and R. Makharia, *J. Electrochem. Soc.*, **159**, B531 (2012).
- A. Z. Weber and A. Kusoglu, *J. Mater. Chem. A*, **2**, 17207 (2014).
- A. Ohma, T. Mashio, K. Sato, H. Iden, Y. Ono, K. Sakai, K. Akizuki, S. Takaichi, and K. Shinohara, *Electrochim. Acta*, **56**, 10832 (2011).
- J. P. Owejan, J. E. Owejan, and W. Gu, *J. Electrochem. Soc.*, **160**, F824 (2013).
- Y. Ono, T. Mashio, S. Takaichi, A. Ohma, H. Kanesaka, and K. Shinohara, *ECS Trans.*, **28**, 69 (2010).
- T. A. Greszler, D. Caulk, and P. Sinha, *J. Electrochem. Soc.*, **159**, F831 (2012).
- R. Makharia, N. Subramanian, S. Kumaraguru, T. Greszler, B. Litteer, and Z. Liu, *Fuel Cell Seminar and Exposition, Phoenix, AZ, Presentation # GHT 33-2*, 2008.
- S. Jomori, K. Komatsubara, N. Nonoyama, M. Kato, and T. Yoshida, *J. Electrochem. Soc.*, **160**, F1067 (2013).
- K. Kudo, T. Suzuki, and Y. Morimoto, *ECS Trans.*, **33**, 1495 (2010).
- N. Nonoyama, S. Okazaki, A. Z. Weber, Y. Ikogi, and T. Yoshida, *J. Electrochem. Soc.*, **158**, B416 (2011).
- M. Lopez-Haro, L. Guétaz, T. Printemps, A. Morin, S. Escibano, P. H. Jouneau, P. Bayle-Guillemaud, F. Chandezon, and G. Gebel, *Nat. Commun.*, **5**, 5229 (2014).
- T. Ngo, T. L. Yu, and H. L. Lin, *J. Power Sources*, **225**, 293 (2013).
- K. Miyazaki, N. Sugimura, K. Kawakita, T. Abe, K. Nishio, H. Nakanishi, M. Matsuoka, and Z. Ogumia, *J. Electrochem. Soc.*, **157**, A1153 (2010).
- L. Sun and T. Okada, *J. Membr. Sci.*, **183**, 213 (2001).
- L. Xin, Y. Kang, F. Yang, A. Uzunoglu, T. Rockward, P. J. Ferreira, R. L. Borup, J. Ilavsky, L. Stanciu, and J. Xie, *ECS Conference*, Hawaii 2016, Abstract 2584.
- R. J. J. Jansen and H. van Bekkum, *Carbon*, **32**, 1507 (1994).
- A. Orfanidi, M. K. Daletou, and S. G. Neophytides, *J. Appl. Catal. B: Environ.*, **106**, 379 (2011).
- A. V. Neimark, Y. Lin, P. I. Ravikovitch, and M. Thommes, *Carbon*, **47**, 1617 (2009).
- G. Y. Gor, M. Thommes, K. A. Cychosz, and A. V. Neimark, *Carbon*, **50**, 1583 (2012).
- K. Shinozaki, Y. Morimoto, B. S. Pivovar, and S. S. Kocha, *J. Power Sources*, **325**, 745 (2016).
- K. J. J. Mayrhofer, D. Strmcnik, B. B. Bliznac, V. Stamenkovic, M. Arenz, and N. M. Markovic, *Electrochim. Acta*, **53**, 3181 (2008).
- C. Simon, F. Hasché, D. Müller, and Hubert A. Gasteiger, *ECS Trans.*, **69**, 1293 (2015).
- W. Gu, D. R. Baker, Y. Liu, and H. A. Gasteiger, in *Handbook of Fuel Cells: Advances in Electrocatalysis, Materials, Diagnostics and Durability* (editors: W. Vielstich, H. A. Gasteiger, and H. Yokokawa), John Wiley & Sons, UK Chichester, 631 (2009).
- S. Kundu, Y. Wang, W. Xia, and M. Muhler, *J. Phys. Chem. C*, **112**, 16869 (2008).
- G. Zhang, S. Sun, D. Yang, J. Dodelet, and E. Sacher, *Carbon*, **46**, 196 (2008).
- R. J. J. Jansen and H. van Bekkum, *Carbon*, **33**, 1021 (1995).
- S. Kundu, W. Xia, W. Busser, M. Becker, D. A. Schmidt, M. Havenith, and M. Muhler, *Phys. Chem. Chem. Phys.*, **12**, 4351 (2010).
- Y. Park, H. Tokiwa, and K. Kakinuma, M. Watanabe and M. Uchida, *J. Power Sources*, **315**, 179 (2016).
- J. Rouquerol, D. Avnir, C. W. Fairbridge, D. H. Everett, J. M. Haynes, N. Pernicone, J. D. F. Ramsay, K. S. W. Sing, and K. K. Unger, "Recommendations for the characterization of porous solids (Technical Report)," *Pure and Appl. Chem.*, **8**, 66 (1994).
- M. Toupin and D. Be' langer, *Langmuir*, **24**, 1910 (2008).
- K. C. Neyerlin, W. Gu, J. Jorne, and H. A. Gasteiger, *J. Electrochem. Soc.*, **153**, A1955 (2006).
- H. A. Gasteiger, S. S. Kocha, B. Sompalli, and F. T. Wagner, *J. Appl. Catal. B*, **56**, 9 (2005).
- F. T. Wagner, S. G. Yan, and P. T. Yu, *Handbook of Fuel Cells - Fundamentals, Technology and Applications* (eds.: H. Yokokawa, H. A. Gasteiger, and W. Vielstich), John Wiley & Sons Chichester, **5**, 250 (2009).
- A. Kongkanand, V. Yarlagadda, T. Garrick, T. E. Moylan, and W. Gu, *ECS Trans.*, **75**, 25 (2016).
- Y. Liu, C. Ji, W. Gu, J. Jorne, and H. A. Gasteiger, *J. Electrochem. Soc.*, **158**, B614 (2011).
- Y. Liu, M. W. Murphy, D. R. Baker, W. Gu, C. Ji, J. Jorne, and H. A. Gasteiger, *J. Electrochem. Soc.*, **156**, B970 (2009).
- Y. Liu, C. Ji, W. Gu, D. R. Baker, J. Jorne, and H. A. Gasteiger, *J. Electrochem. Soc.*, **157**, B1154 (2010).
- A. Putz, D. Susac, V. Berejnov, J. Wu, A. P. H. Hitchcock, and J. Stumper, *ECS Trans.*, **75**, 3 (2016).
- K. C. Neyerlin, W. Gu, J. Jorne, Jr. A. Clark, and H. A. Gasteiger, *J. Electrochem. Soc.*, **154**, B279 (2007).
- P. Zihrl, I. Hartung, S. Kirsch, G. Huebner, F. Hasche, and H. A. Gasteiger, *J. Electrochem. Soc.*, **163**, F492 (2016).
- M. Yamaguchi, T. Matsunaga, K. Amemiya, A. Ohira, N. Hasegawa, K. Shinohara, M. Ando, and T. Yoshida, *J. Phys. Chem. B*, **118**, 14922 (2014).

## 4.2. Low-Loaded Platinum Catalysts in PEMFCs – Conclusions

Our work has confirmed that surface functionalisation of a commercially available carbon support can result in a more homogeneous distribution of ionomer on the catalyst layer. It was observed that the catalyst with functionalised carbon support displayed significantly low oxygen mass-transport losses. In addition, by varying the ionomer to carbon mass ratio ( $I/C = 0.25, 0.40, 0.65$ ) in the cathode, it could also be concluded that a too thin ionomer film ( $\approx 0.9$  nm,  $I/C = 0.25$ ) leads to a dramatically increased proton conduction resistance in the electrode. On the other hand, for a thick ionomer film ( $I/C = 0.65$ ), the oxygen mass-transport resistance increases. Thus, it is clear that a delicate balance has to be achieved, so that the homogeneous ionomer film thickness does not inhibit oxygen mass transport, without compromising the proton conductivity.

## 5. Conclusions

The focus of this work was the development of PGM-free oxygen reduction electrocatalysts. In addition, we investigated the possible approach to minimize the voltage losses in the high current density region of standard Pt/C catalysts.

With regards to the first quest, this thesis has successfully improved the ORR activity of in-house synthesised ZrO<sub>2</sub>-based catalysts. We have also revealed synthesis parameters that can be tuned to affect and maximise the ORR activity of these types of catalysts. Chapter 3.1 and 3.2 focused on synthesis, structural, as well as electrochemical characterisation of pure carbon-supported nanometric ZrO<sub>2</sub>-based catalysts. From this we concluded that the ORR activity of pure ZrO<sub>2</sub>-based catalysts is far too low to consider their use in any practical application. Thus, in a pursuit to increase their activity, a new class of PGM-free catalysts was developed, viz., carbon-supported Fe-substituted ZrO<sub>2</sub> nanoparticles (chapter 3.3 and 3.4). It has been proven conclusively that Fe<sup>3+</sup> substitutes Zr<sup>4+</sup> in ZrO<sub>2</sub>. In addition, DFT calculations have shown the likely formation of oxygen vacancies in Fe-substituted ZrO<sub>2</sub> catalysts, which was argued to be the prime reason for its significantly improved ORR activity. It was also shown in the appendix of chapter 3.5 that there is an increase in the ORR activity when a transition metal (Fe, Cu, and Co) is present during ZrO<sub>2</sub> nanoparticle synthesis. Based on these studies, it can be easily foreseen that increasing the density of oxygen vacancies is one possible route to further increase the activity of these catalysts. Using thicker cathode catalyst layers (≈50-100 μm) in a PEMFC was found to be another way to increase the mass activity of Fe-substituted ZrO<sub>2</sub> catalysts, which is opposite to what has been observed for Pt-based catalysts, where the apparent mass activity decreases with increasing layer thickness, due to transport resistance through thick catalyst layer.

The second part of this thesis focuses on minimizing voltage losses in the high current density region of standard Pt/C catalysts by functionalising the carbon support by amide/imide/lactam groups (chapter 4.1). These groups facilitate a more homogeneous distribution of ionomer by coulombic attraction with the sulfonate anions of the ionomer. We have shown unambiguously that oxygen mass-transport losses through a homogeneous ionomer film are reduced in low-loaded cathodes. We also concluded that a homogeneous ionomer film with low ionomer/carbon ratio (with adequate proton conductivity) is a key feature to achieve high performance in low-Pt-loaded cathodes.

## *5. Conclusions*

Thus, this thesis has successfully addressed one of the important challenges in PEMFC technology, which is replacing or decreasing the PGM content in PEMFC cathodes. We hope that directions from this thesis will contribute to future developments in PEMFC technology.



## References

- [1] UNFCCC: Historic Paris Agreement on Climate Change: 195 Nations Set Path to Keep Temperature Rise Well Below 2 Degrees Celsius, Paris, 2015, <https://unfccc.int/news/finale-cop21>. (Accessed on 05/05/2018).
- [2] [https://ec.europa.eu/clima/news/articles/news\\_2015121201\\_en](https://ec.europa.eu/clima/news/articles/news_2015121201_en). (Accessed on 05/05/2018).
- [3] <https://unfccc.int/process-and-meetings/the-paris-agreement/nationally-determined-contributions-ndcs>. (Accessed on 05/05/2018).
- [4] [https://ec.europa.eu/clima/policies/international/negotiations/paris\\_en](https://ec.europa.eu/clima/policies/international/negotiations/paris_en). (Accessed on 05/05/2018).
- [5] Climate Change 2014: Mitigation of Climate Change. Contribution of Working Group III to the Fifth Assessment Report of the Intergovernmental Panel on Climate Change, Cambridge University Press, Cambridge and New York, 2015.
- [6] <https://www.epa.gov/ghgemissions/global-greenhouse-gas-emissions-data>. (Accessed on 05/05/2018).
- [7] Analysis of key trends and drivers in greenhouse gas emissions in the EU between 1990 and 2014, European Environment Agency, Copenhagen (2016) 1-31.
- [8] Roadmap 2050: A practical guide to a prosperous, low-carbon Europe, 2010. <http://www.roadmap2050.eu/project/roadmap-2050>. (Accessed on 05/05/2018).
- [9] G. Archer, 2014. <https://www.transportenvironment.org/press/transport-become-largest-source-co2-emissions-if-politicians-don%E2%80%99t-act-decisively-un-experts>. (Accessed on 05/05/2018).
- [10] J. Wansart, G. Walther, T. Spengler, Limiting motor vehicles' CO<sub>2</sub> emissions - a manufacturer's challenge, Proceedings of the 2008 International System Dynamics Conference, 2008.
- [11] O. Gröger, H.A. Gasteiger, J.-P. Suchsland, Review—Electromobility: Batteries or Fuel Cells?, Journal of The Electrochemical Society 162(14) (2015) A2605-A2622.
- [12] M.N. Eisler, A Tesla in every garage?, IEEE Spectrum 53(2) (2016) 34-55.
- [13] A portfolio of power-trains for Europe: a fact-based analysis, McKinsey & Company (2010) 1-64.
- [14] A. Yamashita, M. Kondo, S. Goto, N. Ogami, Development of High-Pressure Hydrogen Storage System for the Toyota “Mirai”, SAE Technical Paper 2015-01-1169, 2015.
- [15] M. Jacoby, Fuel-cell cars finally drive off the lot, Chemical & Engineering News 95(38) (2017) 28-32.

## References

- [16] <https://h2me.eu/about/hydrogen-refuelling-infrastructure/>. (Accessed on 05/05/2018).
- [17] <http://h2-mobility.de/en/h2-stations/>. (Accessed on 05/05/2018).
- [18] <https://www.statista.com/statistics/644545/global-sales-of-fuel-cell-vehicles/>. (Accessed on 05/05/2018).
- [19] <https://www.navigantresearch.com/newsroom/global-sales-of-fuel-cell-cars-and-buses-are-expected-to-total-more-than-580000-from-2015-to-2024>. (Accessed on 05/05/2018).
- [20] A. Kongkanand, M.F. Mathias, The Priority and Challenge of High-Power Performance of Low-Platinum Proton-Exchange Membrane Fuel Cells, *The Journal of Physical Chemistry Letters* 7(7) (2016) 1127-1137.
- [21] <http://www.autonews.com/article/20160314/OEM05/303149972>. (Accessed on 05/05/2018).
- [22] B.D. James, J.M. Huya-Kouadio, C. Houchins, D.A. DeSantis, Mass Production Cost Estimation of Direct H<sub>2</sub> PEM Fuel Cell Systems for Transportation Applications: 2016 Update, Strategic Analysis Inc, Arlington (2017) 1-244.
- [23] W. Bernhart, S. Riederle, M. Yoon, Fuel cells – A realistic alternative for zero emission?, Roland Berger Strategy Consultants (2014) 1-20.
- [24] N. Konno, S. Mizuno, H. Nakaji, Y. Ishikawa, Development of Compact and High-Performance Fuel Cell Stack, *SAE Int. J. Alt. Power.* 4(1) (2015) 123-129.
- [25] M.K. Debe, Electrocatalyst approaches and challenges for automotive fuel cells, *Nature* 486 (2012) 43-51.
- [26] E. Proietti, F. Jaouen, M. Lefèvre, N. Larouche, J. Tian, J. Herranz, J.-P. Dodelet, Iron-based cathode catalyst with enhanced power density in polymer electrolyte membrane fuel cells, *Nature Communications* 2 (2011) 416.
- [27] Y. Ohgi, A. Ishihara, K. Matsuzawa, S. Mitsushima, K.-i. Ota, M. Matsumoto, H. Imai, Factors for Improvements of Catalytic Activity of Zirconium Oxide-Based Oxygen-Reduction Electrocatalysts, *Journal of The Electrochemical Society* 160(2) (2013) F162-F167.
- [28] A. Ishihara, Y. Ohgi, K. Matsuzawa, S. Mitsushima, K.-i. Ota, Progress in non-precious metal oxide-based cathode for polymer electrolyte fuel cells, *Electrochimica Acta* 55(27) (2010) 8005-8012.
- [29] S. Yin, A. Ishihara, Y. Kohno, K. Matsuzawa, S. Mitsushima, K.-i. Ota, M. Matsumoto, M. Arao, H. Imai, Preparation of Highly Active Zr Oxide-Based Oxygen Reduction Electrocatalysts as PEFC Cathode, *ECS Transactions* 50(2) (2013) 1785-1790.

- [30] T.A. Greszler, D. Caulk, P. Sinha, The Impact of Platinum Loading on Oxygen Transport Resistance, *Journal of The Electrochemical Society* 159(12) (2012) F831-F840.
- [31] <https://www.nature.com/subjects/electrochemistry>. (Accessed on 05/05/2018).
- [32] Y. Jiao, Y. Zheng, M. Jaroniec, S.Z. Qiao, Design of electrocatalysts for oxygen- and hydrogen-involving energy conversion reactions, *Chemical Society Reviews* 44(8) (2015) 2060-2086.
- [33] D.M. Bernardi, M.W. Verbrugge, A Mathematical Model of the Solid-Polymer-Electrolyte Fuel Cell, *Journal of The Electrochemical Society* 139(9) (1992) 2477-2491.
- [34] H.A. Gasteiger, W. Gu, R. Makharia, M.F. Mathias, B. Sompalli, Beginning-of-life MEA performance — efficiency loss contributions, *Handbook of Fuel Cells – Fundamentals, Technology and Applications*, Wiley, UK, 2003, pp. 593-610.
- [35] K. Krischer, E.R. Savinova, Fundamentals of electrocatalysis, in: G. Ertl, H. Knözinger, F. Schüth, J. Weitkamp (Eds.), *Handbook of Heterogeneous Catalysis*, Wiley-VCH, Chichester, 2009, p. 1873.
- [36] H.S. Wroblowa, P. Yen Chi, G. Razumney, Electroreduction of oxygen: A new mechanistic criterion, *Journal of Electroanalytical Chemistry and Interfacial Electrochemistry* 69(2) (1976) 195-201.
- [37] H.A. Gasteiger, S.S. Kocha, B. Sompalli, F.T. Wagner, Activity benchmarks and requirements for Pt, Pt-alloy, and non-Pt oxygen reduction catalysts for PEMFCs, *Applied Catalysis B: Environmental* 56(1–2) (2005) 9-35.
- [38] A. Bonakdarpour, M. Lefevre, R. Yang, F. Jaouen, T. Dahn, J.-P. Dodelet, J.R. Dahn, Impact of Loading in RRDE Experiments on Fe–N–C Catalysts: Two- or Four-Electron Oxygen Reduction?, *Electrochemical and Solid-State Letters* 11(6) (2008) B105-B108.
- [39] C.H. Hamann, A. Hamnett, W. Vielstich, *Electrochemistry*, 2nd, Completely Revised and Updated Edition, Wiley, Weinheim, 2007.
- [40] K.C. Neyerlin, W. Gu, J. Jorne, A. Clark, H.A. Gasteiger, Cathode Catalyst Utilization for the ORR in a PEMFC: Analytical Model and Experimental Validation, *Journal of The Electrochemical Society* 154(2) (2007) B279-B287.
- [41] D.R. Baker, D.A. Caulk, K.C. Neyerlin, M.W. Murphy, Measurement of Oxygen Transport Resistance in PEM Fuel Cells by Limiting Current Methods, *Journal of The Electrochemical Society* 156(9) (2009) B991-B1003.
- [42] A.Z. Weber, A. Kusoglu, Unexplained transport resistances for low-loaded fuel-cell catalyst layers, *Journal of Materials Chemistry A* 2(41) (2014) 17207-17211.

## References

- [43] P. Zihrul, I. Hartung, S. Kirsch, G. Huebner, F. Hasché, H.A. Gasteiger, Voltage Cycling Induced Losses in Electrochemically Active Surface Area and in H<sub>2</sub>/Air-Performance of PEM Fuel Cells, *Journal of The Electrochemical Society* 163(6) (2016) F492-F498.
- [44] N.M. Markovic, H.A. Gasteiger, P.N. Ross, Oxygen Reduction on Platinum Low-Index Single-Crystal Surfaces in Sulfuric Acid Solution: Rotating Ring-Pt(hkl) Disk Studies, *The Journal of Physical Chemistry* 99(11) (1995) 3411-3415.
- [45] N.M. Marković, R.R. Adžić, B.D. Cahan, E.B. Yeager, Structural effects in electrocatalysis: oxygen reduction on platinum low index single-crystal surfaces in perchloric acid solutions, *Journal of Electroanalytical Chemistry* 377(1) (1994) 249-259.
- [46] D. Armand, J. Clavilier, Electrochemical behaviour of the (110) orientation of a platinum surface in acid medium: the role of anions, *Journal of Electroanalytical Chemistry and Interfacial Electrochemistry* 263(1) (1989) 109-126.
- [47] D. Armand, J. Clavilier, Influence of specific adsorption of anions on the electrochemical behaviour of the Pt (100) surface in acid medium: Comparison with Pt (111), *Journal of Electroanalytical Chemistry and Interfacial Electrochemistry* 270(1) (1989) 331-347.
- [48] J. Aragane, T. Murahashi, T. Odaka, Change of Pt Distribution in the Active Components of Phosphoric Acid Fuel Cell, *Journal of The Electrochemical Society* 135(4) (1988) 844-850.
- [49] E. Antolini, J.R.C. Salgado, E.R. Gonzalez, The stability of Pt–M (M=first row transition metal) alloy catalysts and its effect on the activity in low temperature fuel cells: A literature review and tests on a Pt–Co catalyst, *Journal of Power Sources* 160(2) (2006) 957-968.
- [50] S. Mukerjee, S. Srinivasan, Enhanced electrocatalysis of oxygen reduction on platinum alloys in proton exchange membrane fuel cells, *Journal of Electroanalytical Chemistry* 357(1) (1993) 201-224.
- [51] Q. Jia, W. Liang, M.K. Bates, P. Mani, W. Lee, S. Mukerjee, Activity Descriptor Identification for Oxygen Reduction on Platinum-Based Bimetallic Nanoparticles: In Situ Observation of the Linear Composition–Strain–Activity Relationship, *ACS Nano* 9(1) (2015) 387-400.
- [52] I.E.L. Stephens, A.S. Bondarenko, U. Gronbjerg, J. Rossmeisl, I. Chorkendorff, Understanding the electrocatalysis of oxygen reduction on platinum and its alloys, *Energy & Environmental Science* 5(5) (2012) 6744-6762.
- [53] C. Wang, M. Chi, D. Li, D. Strmcnik, D. van der Vliet, G. Wang, V. Komanicky, K.-C. Chang, A.P. Paulikas, D. Tripkovic, J. Pearson, K.L. More, N.M. Markovic, V.R.

- Stamenkovic, Design and Synthesis of Bimetallic Electrocatalyst with Multilayered Pt-Skin Surfaces, *Journal of the American Chemical Society* 133(36) (2011) 14396-14403.
- [54] V.R. Stamenkovic, B.S. Mun, M. Arenz, K.J.J. Mayrhofer, C.A. Lucas, G. Wang, P.N. Ross, N.M. Markovic, Trends in electrocatalysis on extended and nanoscale Pt-bimetallic alloy surfaces, *Nature Materials* 6 (2007) 241-247.
- [55] S.J. Hwang, S.-K. Kim, J.-G. Lee, S.-C. Lee, J.H. Jang, P. Kim, T.-H. Lim, Y.-E. Sung, S.J. Yoo, Role of Electronic Perturbation in Stability and Activity of Pt-Based Alloy Nanocatalysts for Oxygen Reduction, *Journal of the American Chemical Society* 134(48) (2012) 19508-19511.
- [56] L. Xiong, A. Manthiram, Effect of Atomic Ordering on the Catalytic Activity of Carbon Supported PtM (M = Fe, Co, Ni, and Cu) Alloys for Oxygen Reduction in PEMFCs, *Journal of The Electrochemical Society* 152(4) (2005) A697-A703.
- [57] P. Mani, R. Srivastava, P. Strasser, Dealloyed Pt-Cu Core-Shell Nanoparticle Electrocatalysts for Use in PEM Fuel Cell Cathodes, *The Journal of Physical Chemistry C* 112(7) (2008) 2770-2778.
- [58] L. Dubau, M. Lopez-Haro, J. Durst, L. Guetaz, P. Bayle-Guillemaud, M. Chatenet, F. Maillard, Beyond conventional electrocatalysts: hollow nanoparticles for improved and sustainable oxygen reduction reaction activity, *Journal of Materials Chemistry A* 2(43) (2014) 18497-18507.
- [59] D. Wang, H.L. Xin, R. Hovden, H. Wang, Y. Yu, D.A. Muller, F.J. DiSalvo, H.D. Abruña, Structurally ordered intermetallic platinum-cobalt core-shell nanoparticles with enhanced activity and stability as oxygen reduction electrocatalysts, *Nature Materials* 12 (2012) 81-87.
- [60] V. Stamenkovic, B.S. Mun, K.J.J. Mayrhofer, P.N. Ross, N.M. Markovic, J. Rossmeisl, J. Greeley, J.K. Nørskov, Changing the Activity of Electrocatalysts for Oxygen Reduction by Tuning the Surface Electronic Structure, *Angewandte Chemie* 118(18) (2006) 2963-2967.
- [61] V.R. Stamenkovic, B.S. Mun, K.J.J. Mayrhofer, P.N. Ross, N.M. Markovic, Effect of Surface Composition on Electronic Structure, Stability, and Electrocatalytic Properties of Pt-Transition Metal Alloys: Pt-Skin versus Pt-Skeleton Surfaces, *Journal of the American Chemical Society* 128(27) (2006) 8813-8819.
- [62] T. Yoshida, K. Kojima, Toyota MIRAI Fuel Cell Vehicle and Progress Toward a Future Hydrogen Society, *The Electrochemical Society Interface* 24(2) (2015) 45-49.
- [63] R. Jasinski, A New Fuel Cell Cathode Catalyst, *Nature* 201 (1964) 1212-1213.
- [64] H. Alt, H. Binder, G. Sandstede, Mechanism of the electrocatalytic reduction of oxygen on metal chelates, *Journal of Catalysis* 28(1) (1973) 8-19.

## References

- [65] R. Franke, D. Ohms, K. Wiesener, Investigation of the influence of thermal treatment on the properties of carbon materials modified by N<sub>4</sub>-chelates for the reduction of oxygen in acidic media, *Journal of Electroanalytical Chemistry and Interfacial Electrochemistry* 260(1) (1989) 63-73.
- [66] S. Gupta, D. Tryk, I. Bae, W. Aldred, E. Yeager, Heat-treated polyacrylonitrile-based catalysts for oxygen electroreduction, *Journal of Applied Electrochemistry* 19(1) (1989) 19-27.
- [67] J.A.R. van Veen, H.A. Colijn, J.F. van Baar, On the effect of a heat treatment on the structure of carbon-supported metalloporphyrins and phthalocyanines, *Electrochimica Acta* 33(6) (1988) 801-804.
- [68] U.I. Koslowski, I. Abs-Wurmbach, S. Fiechter, P. Bogdanoff, Nature of the Catalytic Centers of Porphyrin-Based Electrocatalysts for the ORR: A Correlation of Kinetic Current Density with the Site Density of Fe-N<sub>4</sub> Centers, *The Journal of Physical Chemistry C* 112(39) (2008) 15356-15366.
- [69] U.I. Kramm, I. Abs-Wurmbach, I. Herrmann-Geppert, J. Radnik, S. Fiechter, P. Bogdanoff, Influence of the Electron-Density of FeN<sub>4</sub>-Centers Towards the Catalytic Activity of Pyrolyzed FeTMPPCI-Based ORR-Electrocatalysts, *Journal of The Electrochemical Society* 158(1) (2011) B69-B78.
- [70] A.L. Bouwkamp-Wijnoltz, W. Visscher, J.A.R. van Veen, E. Boellaard, A.M. van der Kraan, S.C. Tang, On Active-Site Heterogeneity in Pyrolyzed Carbon-Supported Iron Porphyrin Catalysts for the Electrochemical Reduction of Oxygen: An In Situ Mössbauer Study, *The Journal of Physical Chemistry B* 106(50) (2002) 12993-13001.
- [71] G. Liu, X. Li, P. Ganesan, B.N. Popov, Studies of oxygen reduction reaction active sites and stability of nitrogen-modified carbon composite catalysts for PEM fuel cells, *Electrochimica Acta* 55(8) (2010) 2853-2858.
- [72] M. Lefèvre, J.P. Dodelet, P. Bertrand, Molecular Oxygen Reduction in PEM Fuel Cells: Evidence for the Simultaneous Presence of Two Active Sites in Fe-Based Catalysts, *The Journal of Physical Chemistry B* 106(34) (2002) 8705-8713.
- [73] G. Wu, Z. Chen, K. Artyushkova, F.H. Garzon, P. Zelenay, Polyaniline-derived Non-Precious Catalyst for the Polymer Electrolyte Fuel Cell Cathode, *ECS Transactions* 16(2) (2008) 159-170.
- [74] M. Lefèvre, E. Proietti, F. Jaouen, J.-P. Dodelet, Iron-Based Catalysts with Improved Oxygen Reduction Activity in Polymer Electrolyte Fuel Cells, *Science* 324(5923) (2009) 71-74.
- [75] F. Jaouen, J. Herranz, M. Lefevre, J.P. Dodelet, U.I. Kramm, I. Herrmann, P. Bogdanoff, J. Maruyama, T. Nagaoka, A. Garsuch, J.R. Dahn, T. Olson, S. Pylypenko,

- P. Atanassov, E.A. Ustinov, Cross-laboratory experimental study of non-noble-metal electrocatalysts for the oxygen reduction reaction, *ACS Appl Mater Interfaces* 1(8) (2009) 1623-1639.
- [76] G. Wu, K.L. More, C.M. Johnston, P. Zelenay, High-Performance Electrocatalysts for Oxygen Reduction Derived from Polyaniline, Iron, and Cobalt, *Science* 332(6028) (2011) 443-447.
- [77] C.H. Choi, C. Baldizzone, J.-P. Grote, A.K. Schuppert, F. Jaouen, K.J.J. Mayrhofer, Stability of Fe-N-C Catalysts in Acidic Medium Studied by Operando Spectroscopy, *Angewandte Chemie International Edition* 54(43) (2015) 12753-12757.
- [78] H. Schulenburg, S. Stankov, V. Schünemann, J. Radnik, I. Dorbandt, S. Fiechter, P. Bogdanoff, H. Tributsch, Catalysts for the Oxygen Reduction from Heat-Treated Iron(III) Tetramethoxyphenylporphyrin Chloride: Structure and Stability of Active Sites, *The Journal of Physical Chemistry B* 107(34) (2003) 9034-9041.
- [79] F. Jaouen, S. Marcotte, J.-P. Dodelet, G. Lindbergh, Oxygen Reduction Catalysts for Polymer Electrolyte Fuel Cells from the Pyrolysis of Iron Acetate Adsorbed on Various Carbon Supports, *The Journal of Physical Chemistry B* 107(6) (2003) 1376-1386.
- [80] H. Behret, H. Binder, G. Sandstede, Electrocatalytic oxygen reduction with thiospinels and other sulphides of transition metals, *Electrochimica Acta* 20(2) (1975) 111-117.
- [81] D. Susac, A. Sode, L. Zhu, P.C. Wong, M. Teo, D. Bizzotto, K.A.R. Mitchell, R.R. Parsons, S.A. Campbell, A Methodology for Investigating New Nonprecious Metal Catalysts for PEM Fuel Cells, *The Journal of Physical Chemistry B* 110(22) (2006) 10762-10770.
- [82] D. Susac, L. Zhu, M. Teo, A. Sode, K.C. Wong, P.C. Wong, R.R. Parsons, D. Bizzotto, K.A.R. Mitchell, S.A. Campbell, Characterization of FeS<sub>2</sub>-Based Thin Films as Model Catalysts for the Oxygen Reduction Reaction, *The Journal of Physical Chemistry C* 111(50) (2007) 18715-18723.
- [83] K. Lee, L. Zhang, J. Zhang, Ternary non-noble metal chalcogenide (W–Co–Se) as electrocatalyst for oxygen reduction reaction, *Electrochemistry Communications* 9(7) (2007) 1704-1708.
- [84] J.E. Houston, G.E. Laramore, R.L. Park, Surface Electronic Properties of Tungsten, Tungsten Carbide, and Platinum, *Science* 185(4147) (1974) 258-260.
- [85] H. Zhong, H. Zhang, G. Liu, Y. Liang, J. Hu, B. Yi, A novel non-noble electrocatalyst for PEM fuel cell based on molybdenum nitride, *Electrochemistry Communications* 8(5) (2006) 707-712.
- [86] D. Xia, S. Liu, Z. Wang, G. Chen, L. Zhang, L. Zhang, S. Hui, J. Zhang, Methanol-tolerant MoN electrocatalyst synthesized through heat treatment of molybdenum



## References

- tetraphenylporphyrin for four-electron oxygen reduction reaction, *Journal of Power Sources* 177(2) (2008) 296-302.
- [87] A. Takagaki, Y. Takahashi, F. Yin, K. Takanabe, J. Kubota, K. Domen, Highly Dispersed Niobium Catalyst on Carbon Black by Polymerized Complex Method as PEFC Cathode Catalyst, *Journal of The Electrochemical Society* 156(7) (2009) B811-B815.
- [88] A. Ishihara, Y. Shibata, S. Mitsushima, K. Ota, Partially Oxidized Tantalum Carbonitrides as a New Nonplatinum Cathode for PEFC-1-, *Journal of The Electrochemical Society* 155(4) (2008) B400-B406.
- [89] K.D. Nam, A. Ishihara, K. Matsuzawa, S. Mitsushima, K.-i. Ota, Partially Oxidized Niobium Carbonitride as Non-Platinum Cathode for PEFC, *Electrochemical and Solid-State Letters* 12(11) (2009) B158-B160.
- [90] Y. Ohgi, A. Ishihara, K. Matsuzawa, S. Mitsushima, K. Ota, Zirconium Oxide-Based Compound as New Cathode Without Platinum Group Metals for PEFC, *Journal of The Electrochemical Society* 157(6) (2010) B885-B891.
- [91] W. Schmickler, J.W. Schultze, Electron Transfer Reactions on Oxide-Covered Metal Electrodes, in: J.O.M. Bockris, B.E. Conway, R.E. White (Eds.), *Modern Aspects of Electrochemistry*, Springer US, Boston, MA, 1986, pp. 357-410.
- [92] N. Sato, CHAPTER 8 - ELECTRODE REACTIONS IN ELECTRON TRANSFER, *Electrochemistry at Metal and Semiconductor Electrodes*, Elsevier Science, Amsterdam, 1998, pp. 235-288.
- [93] W.-J. Chun, A. Ishikawa, H. Fujisawa, T. Takata, J.N. Kondo, M. Hara, M. Kawai, Y. Matsumoto, K. Domen, Conduction and Valence Band Positions of Ta<sub>2</sub>O<sub>5</sub>, TaON, and Ta<sub>3</sub>N<sub>5</sub> by UPS and Electrochemical Methods, *The Journal of Physical Chemistry B* 107(8) (2003) 1798-1803.
- [94] N.D. Leonard, K. Artyushkova, B. Halevi, A. Serov, P. Atanassov, S.C. Barton, Modeling of Low-Temperature Fuel Cell Electrodes Using Non-Precious Metal Catalysts, *Journal of The Electrochemical Society* 162(10) (2015) F1253-F1261.
- [95] S.K. Babu, H.T. Chung, P. Zelenay, S. Litster, Modeling Electrochemical Performance of the Hierarchical Morphology of Precious Group Metal-Free Cathode for Polymer Electrolyte Fuel Cell, *Journal of The Electrochemical Society* 164(9) (2017) F1037-F1049.
- [96] U. Beuscher, Experimental Method to Determine the Mass Transport Resistance of a Polymer Electrolyte Fuel Cell, *Journal of The Electrochemical Society* 153(9) (2006) A1788-A1793.

- [97] S. Jomori, K. Komatsubara, N. Nonoyama, M. Kato, T. Yoshida, An Experimental Study of the Effects of Operational History on Activity Changes in a PEMFC, *Journal of The Electrochemical Society* 160(9) (2013) F1067-F1073.
- [98] N. Nonoyama, S. Okazaki, A.Z. Weber, Y. Ikogi, T. Yoshida, Analysis of Oxygen-Transport Diffusion Resistance in Proton-Exchange-Membrane Fuel Cells, *Journal of The Electrochemical Society* 158(4) (2011) B416-B423.
- [99] A. Ishihara, M. Tamura, Y. Ohgi, M. Matsumoto, K. Matsuzawa, S. Mitsushima, H. Imai, K.-i. Ota, Emergence of Oxygen Reduction Activity in Partially Oxidized Tantalum Carbonitrides: Roles of Deposited Carbon for Oxygen-Reduction-Reaction-Site Creation and Surface Electron Conduction, *The Journal of Physical Chemistry C* 117(37) (2013) 18837-18844.
- [100] L.A. Tomachynski, V.Y. Chernii, S.V. Volkov, Synthesis of dichloro phthalocyaninato complexes of titanium, zirconium, and hafnium, *Russian journal of inorganic chemistry* 47(2) (2002) 208-211.
- [101] T. Haruhiko, S. Shojiro, S. Shinsaku, Synthesis of Metallophthalocyanines from Phthalonitrile with Strong Organic Bases, *Chemistry Letters* 12(3) (1983) 313-316.
- [102] S. Catanorchi, M. Piana, High Performance ORR (Oxygen Reduction Reaction) PGM (Pt Group Metal) Free Catalyst, ACTA S.P.A., Crespina U.S.P.a.T. Office (2011). US 2011/0034325 A1.
- [103] S. Yin, A. Ishihara, Y. Kohno, K. Matsuzawa, S. Mitsushima, K.-i. Ota, M. Matsumoto, H. Imai, Enhancement of Oxygen Reduction Activity of Zirconium Oxide-Based Cathode for PEFC, *ECS Transactions* 58(1) (2013) 1489-1494.
- [104] J.I. Langford, A.J.C. Wilson, Scherrer after sixty years: A survey and some new results in the determination of crystallite size, *Journal of Applied Crystallography* 11(2) (1978) 102-113.
- [105] C.A. Schneider, W.S. Rasband, K.W. Eliceiri, NIH Image to ImageJ: 25 years of image analysis, *Nature Methods* 9 (2012) 671-675.
- [106] P. Madkikar, X. Wang, T. Mittermeier, A.H.A. Monteverde Videla, C. Denk, S. Specchia, H.A. Gasteiger, M. Piana, Synthesis optimization of carbon-supported ZrO<sub>2</sub> nanoparticles from different organometallic precursors, *Journal of Nanostructure in Chemistry* 7(2) (2017) 133-147.
- [107] R. Seoudi, G.S. El-Bahy, Z.A. El Sayed, FTIR, TGA and DC electrical conductivity studies of phthalocyanine and its complexes, *Journal of Molecular Structure* 753(1) (2005) 119-126.

## References

- [108] T.J. Schmidt, U.A. Paulus, H.A. Gasteiger, R.J. Behm, The oxygen reduction reaction on a Pt/carbon fuel cell catalyst in the presence of chloride anions, *Journal of Electroanalytical Chemistry* 508(1) (2001) 41-47.
- [109] T.J. Schmidt, H.A. Gasteiger, R.J. Behm, Rotating Disk Electrode Measurements on the CO Tolerance of a High-Surface Area Pt/Vulcan Carbon Fuel Cell Catalyst, *Journal of The Electrochemical Society* 146(4) (1999) 1296-1304.
- [110] K. Shinozaki, J.W. Zack, R.M. Richards, B.S. Pivovar, S.S. Kocha, Oxygen Reduction Reaction Measurements on Platinum Electrocatalysts Utilizing Rotating Disk Electrode Technique: I. Impact of Impurities, Measurement Protocols and Applied Corrections, *Journal of The Electrochemical Society* 162(10) (2015) F1144-F1158.
- [111] K. Shinozaki, J.W. Zack, S. Pylypenko, B.S. Pivovar, S.S. Kocha, Oxygen Reduction Reaction Measurements on Platinum Electrocatalysts Utilizing Rotating Disk Electrode Technique: II. Influence of Ink Formulation, Catalyst Layer Uniformity and Thickness, *Journal of The Electrochemical Society* 162(12) (2015) F1384-F1396.
- [112] K.C. Neyerlin, W. Gu, J. Jorne, H.A. Gasteiger, Determination of Catalyst Unique Parameters for the Oxygen Reduction Reaction in a PEMFC, *Journal of The Electrochemical Society* 153(10) (2006) A1955-A1963.
- [113] L. Gan, C. Cui, M. Heggen, F. Dionigi, S. Rudi, P. Strasser, Element-specific anisotropic growth of shaped platinum alloy nanocrystals, *Science* 346(6216) (2014) 1502-1506.
- [114] X. Huang, Z. Zhao, L. Cao, Y. Chen, E. Zhu, Z. Lin, M. Li, A. Yan, A. Zettl, Y.M. Wang, X. Duan, T. Mueller, Y. Huang, High-performance transition metal-doped Pt<sub>3</sub>Ni octahedra for oxygen reduction reaction, *Science* 348(6240) (2015) 1230-1234.
- [115] C. Chen, Y. Kang, Z. Huo, Z. Zhu, W. Huang, H.L. Xin, J.D. Snyder, D. Li, J.A. Herron, M. Mavrikakis, M. Chi, K.L. More, Y. Li, N.M. Markovic, G.A. Somorjai, P. Yang, V.R. Stamenkovic, Highly Crystalline Multimetallic Nanoframes with Three-Dimensional Electrocatalytic Surfaces, *Science* 343(6177) (2014) 1339-1343.
- [116] J. Zhang, H. Yang, J. Fang, S. Zou, Synthesis and Oxygen Reduction Activity of Shape-Controlled Pt<sub>3</sub>Ni Nanopolyhedra, *Nano Letters* 10(2) (2010) 638-644.
- [117] J. Wu, J. Zhang, Z. Peng, S. Yang, F.T. Wagner, H. Yang, Truncated Octahedral Pt<sub>3</sub>Ni Oxygen Reduction Reaction Electrocatalysts, *Journal of the American Chemical Society* 132(14) (2010) 4984-4985.
- [118] M.K. Carpenter, T.E. Moylan, R.S. Kukreja, M.H. Atwan, M.M. Tessema, Solvothermal Synthesis of Platinum Alloy Nanoparticles for Oxygen Reduction Electrocatalysis, *Journal of the American Chemical Society* 134(20) (2012) 8535-8542.

- [119] S.-I. Choi, S. Xie, M. Shao, J.H. Odell, N. Lu, H.-C. Peng, L. Protsailo, S. Guerrero, J. Park, X. Xia, J. Wang, M.J. Kim, Y. Xia, Synthesis and Characterization of 9 nm Pt–Ni Octahedra with a Record High Activity of 3.3 A/mgPt for the Oxygen Reduction Reaction, *Nano Letters* 13(7) (2013) 3420-3425.
- [120] C. Cui, L. Gan, M. Heggen, S. Rudi, P. Strasser, Compositional segregation in shaped Pt alloy nanoparticles and their structural behaviour during electrocatalysis, *Nature Materials* 12 (2013) 765-771.
- [121] T. Mittermeier, Proton Exchange Membrane Fuel Cells Platinum-Free Oxygen Reduction and Performance Degradation by Start-Up/Shut-Down Events, Cuvillier Verlag, Göttingen, 2018.
- [122] S. Lee, Z. Zhang, X. Wang, L.D. Pfefferle, G.L. Haller, Characterization of multi-walled carbon nanotubes catalyst supports by point of zero charge, *Catalysis Today* 164(1) (2011) 68-73.
- [123] M. Lerch, O. Rahauer, Subsolidus phase relationships in the ZrO<sub>2</sub>-rich part of the ZrO<sub>2</sub>–Zr<sub>3</sub>N<sub>4</sub> system, *Journal of Materials Science* 32(5) (1997) 1357-1363.
- [124] U.I. Kramm, J. Herranz, N. Larouche, T.M. Arruda, M. Lefevre, F. Jaouen, P. Bogdanoff, S. Fiechter, I. Abs-Wurmbach, S. Mukerjee, J.-P. Dodelet, Structure of the catalytic sites in Fe/N/C-catalysts for O<sub>2</sub>-reduction in PEM fuel cells, *Physical Chemistry Chemical Physics* 14(33) (2012) 11673-11688.
- [125] A. Ishihara, S. Yin, K. Suito, N. Uehara, Y. Okada, Y. Kohno, K. Matsuzawa, S. Mitsushima, M. Chisaka, Y. Ohgi, M. Matsumoto, H. Imai, K.-i. Ota, Improving ORR Activity of Group 4 and 5 Metal Oxide-Based Cathodes for PEFCs, *ECS Transactions* 58(1) (2013) 1495-1500.
- [126] P. Madkikar, X. Wang, T. Mittermeier, A. Monteverde Videla, C. Denk, S. Specchia, H.A. Gasteiger, M. Piana, Synthesis optimization of carbon-supported ZrO<sub>2</sub> nanoparticles from different organometallic precursors, *Journal of Nanostructure in Chemistry* (2016) 1-15.
- [127] P. Li, I.W. Chen, J.E. Penner-Hahn, Effect of Dopants on Zirconia Stabilization—An X-ray Absorption Study: I, Trivalent Dopants, *Journal of the American Ceramic Society* 77(1) (1994) 118-128.
- [128] H. Kwak, S. Chaudhuri, Role of vacancy and metal doping on combustive oxidation of Zr/ZrO<sub>2</sub> core-shell particles, *Surface Science* 604(23) (2010) 2116-2128.



## List of Figures

**Figure 1.** Global GHG emissions from 2010, categorised by economic sectors. Pie chart taken from United States Environmental Protection Agency [6], and the data for these estimates can be found in the Contribution of Working Group III to the Fifth Assessment Report of the Intergovernmental Panel on Climate Change [5]..... 2

**Figure 2.** Direct GHG emissions from the respective transport modes, which rose from 2.8 Gt in 1970 to 7.0 Gt CO<sub>2</sub>eq worldwide in 2010. Graphic obtained from Sims R., R. Schaeffer, F. Creutzig, X. Cruz-Núñez, M. D'Agosto, D. Dimitriu, M.J. Figueroa Meza, L. Fulton, S. Kobayashi, O. Lah, A. McKinnon, P. Newman, M. Ouyang, J.J. Schauer, D. Sperling, and G. Tiwari, 2014: Transport. In: *Climate Change 2014: Mitigation of Climate Change. Contribution of Working Group III to the Fifth Assessment Report of the Intergovernmental Panel on Climate Change* [5]..... 3

**Figure 3.** Powertrain ranges (kilometres) versus carbon emissions (gCO<sub>2</sub> (well-to-wheel)/kilometre) 2010 – 2050. Graphic obtained from a fact-based analysis of BEVs, PHEVs, and FCEVs [13]. <sup>1</sup>ICE range for 2050 based on fuel economy improvement and assuming tank size stays constant; Assuming 6% CO<sub>2</sub> reduction due to biofuels by 2020, and 24% by 2050. Reproduced from a study made for the FCH JU with their permission [13]. ..... 6

**Figure 4.** The polarization curves from rotating disc electrode technique (not to scale) for the key energy-related electrochemical reactions. Red and blue curves refer to the hydrogen- and oxygen-involving reactions, respectively. Reproduced (in part) from [32] with permission of The Royal Society of Chemistry..... 10

**Figure 5.** General scheme of ORR. Indices (b), \*, and (a) designate the bulk, vicinity of the disc electrode, and adsorbed species, respectively. The rate constant  $k_i$  pertains to the  $i$ -th reaction according to the following index notation: (1) direct reduction to H<sub>2</sub>O (+4e<sup>-</sup>); (2) reduction to H<sub>2</sub>O<sub>2</sub> (+2e<sup>-</sup>); (-2) oxidation of H<sub>2</sub>O<sub>2</sub> to O<sub>2</sub> (-2e<sup>-</sup>); (3) reduction of H<sub>2</sub>O<sub>2</sub> to H<sub>2</sub>O (+2e<sup>-</sup>); (4) disproportionation of H<sub>2</sub>O<sub>2</sub> yielding O<sub>2</sub>; (5) desorption of adsorbed H<sub>2</sub>O<sub>2</sub>; (6) adsorption of H<sub>2</sub>O<sub>2</sub> [36]. ..... 11

**Figure 6.** Graph representing various voltage losses due to the three overpotentials (kinetic, ohmic, and mass-transport) in comparison to the theoretical cell potential calculated at the same conditions [H<sub>2</sub> (P<sub>H<sub>2</sub></sub>:150 kPa<sub>abs</sub>)/Air (P<sub>Air</sub>: 21 kPa<sub>abs</sub>), cathode: 0.1 mg<sub>Pt</sub>/cm<sup>2</sup><sub>geo</sub>, 80 °C]. Parameters considered in calculation of voltage losses are, mass activity at 0.9 V: 110 A/g<sub>Pt</sub>,

electrochemically active surface area:  $50 \text{ m}^2/\text{g}_{\text{Pt}}$ , Tafel slope:  $76 \text{ mV/decade}$ , membrane conductivity:  $0.1 \text{ S/cm}$ , membrane thickness:  $10 \text{ }\mu\text{m}$ , membrane resistance:  $0.005 \text{ }\Omega\text{cm}^2$ , contact resistance:  $0.015 \text{ }\Omega\text{cm}^2$ , oxygen transport resistance:  $1 \text{ s/cm}$ , sheet resistance:  $0.031 \text{ }\Omega\text{cm}^2$ . The voltage losses are calculated based on equations 1 and 20 from Neyerlin et al. [40] and equation 5 from Zihrul et al. [43]. ..... 12

**Figure 7.** Zirconium (IV) tetra-tert-butyl-dichlorophthalocyanine ( $\text{ZrCl}_2\text{Pc}(\text{t-Bu})_4$ ) synthesised similarly to  $\text{ZrCl}_2\text{Pc}$ . ..... 21

**Figure 8.** a) Sample holder with capillary; b) Goniometer; c) XRPD instrument; i)  $\text{Mo K}\alpha_1$  radiation source; ii) Collimator; iii) Beam stop; iv) Detector. .... 24

**Figure 9.** a) PMMA sample holder; b) Connector between motor and absorber; c) Mössbauer instrument; i) Motor; ii) Position of absorber and source; iii) Detector. .... 25

**Figure 10.** a) Sample holder with copper tapes; b) Analysis chamber of the XPS; i) X-ray beam; ii) Samples; iii) Detector; c) XPS instrument. .... 26

**Figure 11.** a) Glass tube with sample; b)  $\text{N}_2$  physisorption instrument; i) Outgassing ports; ii) Cold trap; iii) Physisorption port. .... 27

**Figure 12.** a)  $\text{Al}_2\text{O}_3$  crucible and funnel; b) Furnace with sample and reference crucible; c) TGA-MS instrument; i) TGA; ii) MS. .... 28

**Figure 13.** a) Dilute dispersion of sample; b) Copper grid with sample; c) TEM instrument; i) Electron gun; ii) Grid holder; iii) Fluorescent screen. .... 29

**Figure 14.** a) Ice-bath-sonicated homogeneous catalyst dispersion; b) Glassy carbon (GC) disc coated with a thin film of the catalyst. Here, the disc is surrounded by a Pt-ring to perform RRDE voltammetry; c) Water-jacketed electrochemical glass cell; i) working electrode contact; ii) reference electrode (RHE) along with a Luggin-Haber capillary; iii) counter electrode (Au mesh); iv) gas inlet ( $\text{Ar}$ ,  $\text{O}_2$ ,  $\text{H}_2$ ); v) rotator; vi) thermostat connections. .... 32

**Figure 15.** Schematic of a single PEMFC cell (not to scale). Components in the left figure (left to right): anode endplate with indicated gas flow path, insulating polymer, gold-coated anode current collector (CC), anode flow field, anode gasket (G) and MEA. A detailed sketch of the MEA is given in the right figure (left to right): anode gas diffusion layer (GDL), anode electrode, membrane, cathode electrode, cathode GDL. Reproduced (in part) by the permission of Cuvillier Verlag [121]. ..... 35



**Figure 16.** a) Ink preparation by roller mixing; b) Coating of the prepared ink onto a PTFE substrate using a Mayer rod; c) Preparing the decals for hot-pressing; d) Decal transfer by hot-pressing; e) Single-cell PEMFC in operation at the test station. .... 36

**Figure 17.** ORR mass activities of 12 wt% ZrO<sub>2</sub>/KB<sub>graph</sub>, and ZrO<sub>2</sub>-based/KB<sub>graph</sub> catalysts with Cu (0.10 wt%), Co (0.80 wt%), and Fe (0.36 wt%), measured by thin-film RDE (70-76 μg<sub>cat</sub>/cm<sup>2</sup>) in O<sub>2</sub> saturated 0.1 M HClO<sub>4</sub> at 20 °C and 1600 rpm. The activities are taken from capacitively-corrected anodic scans recorded at 5 mV/s. Here, wt% in the parentheses refers to the nominal content of Cu, Co, and Fe (assumed in metallic state) with respect to the entire catalyst. .... 107



## List of Schemes

<b>Scheme 1.</b> Synthesis route of $\text{ZrCl}_2\text{Pc}$ from $\text{C}_6\text{H}_4(\text{CN})_2 + \text{C}_{10}\text{H}_7\text{CH}_3 + \text{ZrCl}_4$ . .....	18
<b>Scheme 2.</b> Hydrolysis of $\text{ZrCl}_2\text{Pc}$ to $\text{ZrOPc}$ .....	20
<b>Scheme 3.</b> Synthesis of $\text{FePc}(\text{t-Bu})_4$ from $\text{C}_{12}\text{H}_{12}\text{N}_2 + \text{FeCl}_2 + \text{DBU}$ . .....	22



## List of Tables

<b>Table 1.</b> Overview over technology improvements that reduce fleet emissions as reported by Wansart et al. [10].	4
<b>Table 2.</b> Measures undertaken by OEMs to meet the emission targets as reported by Wansart et al. [10].	5
<b>Table 3.</b> XRPD scan parameters used to characterise the catalysts.	24
<b>Table 4.</b> Steps followed in the electrochemical characterisation of the catalyst by the TF-RDE technique.	33



# Acknowledgements

Its time to officially thank and acknowledge everyone who has contributed in completion of this thesis. I feel highly grateful to all of them who have contributed in this thesis, and with this acknowledgement, I would like to show my appreciation for their significant efforts.

I am grateful to Prof. Hubert A. Gasteiger for his strong commitment. His valuable guidance and time, and faith in me have an unparalleled contribution in this thesis. Prof. Gasteiger's guidance has not only made this thesis but also carved my scientific personality, which will guide me in the long run.

Many thanks to Michele who is directly supervising me from the beginning of my PhD. Without Michele, it would have been impossible for me to reach so far. Thank you very much for your time and efforts. Your push and 'Just Do It' have truly bore fruits.

I would like to thank Xiaodong and Thomas for your immense guidance in synthesis and electrochemistry, respectively. Tips and guidance from you have helped build a strong foundation and major parts of this thesis.

Special thanks to Alin, Hany, Sourov, Cuneyt, Juan, Frédéric, Cyril for your advices, which proved very useful from time to time.

I would also thank Hans, Gregor, Christoph, Timon, and Dominik for providing me insights in specific methods and analytical techniques.

Many thanks to Vroni for her efforts in taking care of all the administrative stuff, our group members for making a joyful atmosphere in the lab, and my office (Armin, Christoph, Hany, and Johannes) for all the scientific and non-scientific chats.

Special thanks to my extra 'hands' in the lab, Christoph Denk, Davide Menga, and Kevin Krempf. Thank you for your efforts and passion, which you put during your thesis and internships, which led to a win-win situation.

I would like to thank Alin especially for her valuable tips in structuring the introduction of this thesis. In addition, big thanks to Michele and Thomas for proofreading this thesis.

I acknowledge the FCHJU (n°278054) as part of FP7/2007-2013 and the Bayerische Forschungsstiftung (Project ForOxiE2, AZ 1143-14) for financial support provided for all these years.



*Acknowledgements*

Last but not the least, I thank my family and friends for their patience and support for all these years. You strengthened me emotionally, which has finally resulted in successful completion of my thesis—Thank you!

# Curriculum Vitae

Pankaj Madkikar (M.Sc.)  
Date of birth: 14<sup>th</sup> September 1988  
Nationality: Indian  
Address: Riesstr. 58, 80993 Munich  
Mobile no.: +4917641644779  
Email: pankaj.madkikar@tum.de



## Educational Qualification

---

08/2013 - present	Doctoral work at Technische Universität München (TUM) at the Chair of Technical Electrochemistry with Prof. Hubert A. Gasteiger
10/2010 - 03/2013	Master of Science in Advanced Materials Science (AMS) Technische Universität München (TUM), Ludwig-Maximilians-Universität (LMU) München, Universität Augsburg (UA) ( <i>Grade: 1.9</i> )
06/2006 - 06/2010	Bachelor of Science in Physics University of Pune (India), Fergusson College ( <i>Percentage: 89.58%</i> )
06/2006 - 06/2009	Bachelor of Science in Chemistry University of Pune (India), Fergusson College ( <i>Percentage: 86.75%</i> )

## Academic Experience

---

08/2016	'CINF 2016' summer school organized by DTU Physics (Denmark)
05/2007	'A Short Summer Course in Physics – 2007' organized by University of Pune (India)

## Research Experience

---

04/2012 - 07/2012	Internship at DENSO Europe (Eching), in 'Establishment and introduction of investigation methods in the field of carbon emission VOC/Fog tests'
03/2012	Project with UnternehmerTUM/ALTANA AG, Garching in product and business development, prototype preparation, and business planning
03/2011 - 06/2011	Research internship 'Size- and shape-selective preparation of polymer-protected metal nanoparticles supported on semiconductor surfaces' in the research group of Prof. J. A. Lercher at TUM, Garching

## Academic Achievements

---

2016	MuniCat poster award (2 <sup>nd</sup> place) at CRC Graduate Academy
2013	Won Christian Friedrich Schönbein medal for the best poster at the 4 <sup>th</sup> European PEFC & H <sub>2</sub> Forum (EFCF Conference)
2011/12	Awarded stipend by the Bavarian State Ministry for Science and Research
2009	Prof. S. K. Borgaonkar prize for achieving highest marks in chemistry at Fergusson College

## Scientific contribution

---

- Attended 6 national/international conferences/workshops
- Number of poster presentations: 4
- Number of oral presentations: 2
- Papers published: 6 (first authored: 3)
- Papers in preparation: 2 (first authored: 1)

## Teaching

---

- Worked for 700 h as practical assistant for graduate and undergraduate students
- Directly supervised 2 Masters and 3 Bachelors theses

## Skills

---

Languages known: German (B2), English (Fluent), Marathi (Native), Hindi (Fluent)

Software skills:

- Proficient with Microsoft Office and OriginLab
- Acquainted with use of 'C', Adobe Photoshop, MestReNova and ChemDraw

## Additional Courses

---

2016	'Successful Cooperation in International Teams' (2-day course, TUM)
2015	'E-Camp' (3-day course at Center for Innovation and Business Creation, TUM) 'Surviving Complex Projects' (2-day course, TUM)
2014	'Strength-based Leadership and Collaboration' (2-day course, TUM)
2011/12	'Get to Know Yourself as an Entrepreneur' at UnternehmerTUM GmbH
2011	'Principles of Entrepreneurship' by Prof. Dr. H. Patzelt at TUM, Garching

## Extracurricular Activities & Interests

---

2015 - present	Founding member of 'ECS Student Chapter Munich'
2009	Volunteer in Fergusson College fest
Interests	Cooking, reading, listening music, nature enthusiast, fitness regimes

Pankaj Madkikar



Munich, 10<sup>th</sup> May 2018

# List of Scientific Contributions

## Articles in Peer-Reviewed Journals

**1) Probing Transition-Metal Silicides as PGM-Free Catalysts for Hydrogen Oxidation and Evolution in Acidic Medium**

Mittermeier, T.; Madkikar, P.; Wang, X.; Gasteiger, H. A.; Piana, M.  
*Materials* (2017), **10**, 661

**2) Communication—Synergistic Effect on the Activity of ZrO<sub>2</sub>-Fe as PGM-Free ORR Catalysts for PEMFCs**

Madkikar, P.; Mittermeier, T.; Gasteiger, H. A.; Piana, M.  
*Journal of The Electrochemical Society* (2017), **164**, F831-F833

**3) Synthesis Optimization of Carbon-supported ZrO<sub>2</sub> Nanoparticles from Different Organometallic Precursors**

Madkikar, P.; Wang, X.; Mittermeier, T.; Monteverde Videla, A.; Denk, C.; Specchia, S.; Gasteiger, H. A.; Piana, M.  
*Journal of Nanostructure in Chemistry* (2017), **7**, 133-147

**4) The Key to High Performance Low Pt Loaded Electrodes**

Orfanidi, A.<sup>≠</sup>; Madkikar, P.<sup>≠</sup>; El-Sayed, H. A.; Harzer, G. S.; Kratky, T.; Gasteiger, H. A.  
*Journal of The Electrochemical Society* (2017), **164**, F418-F426  
(<sup>≠</sup>These authors contributed equally to this work)

**5) ZrO<sub>2</sub> Based Oxygen Reduction Catalysts for PEMFCs - Towards a Better Understanding**

Mittermeier, T.; Madkikar, P.; Wang, X.; Gasteiger, H. A.; Piana, M.  
*Journal of The Electrochemical Society* (2016), **163**, F1543-F1552

## Conference Proceedings

**1) Carbon Supported Valve Metal Oxide Based Catalysts for the Oxygen Reduction Reaction in Acidic DMFCs**

Mittermeier, T.; Madkikar, P.; Wang, X.; Gasteiger, H. A.; Piana, M.

*4<sup>th</sup> European PEFC and H<sub>2</sub> Forum*, D. Jones Editor, ISBN: 978-3-905592-17-7, Lucerne, **2013**

## Submitted Manuscripts / Manuscripts in Preparation

### 1) Nanometric Fe-substituted ZrO<sub>2</sub> on Carbon Black as Novel PGM-Free ORR Catalyst for PEMFCs

Madkikar, P.; Menga, D.; Harzer, G. S.; Mittermeier, T.; Siebel, A.; Wagner, F. E.; Merz, M.; Schuppler, S.; Nagel, P.; Muñoz-García, A. B.; Pavone, M.; Gasteiger, H. A.; Piana, M.

(manuscript in preparation)

### 2) Tailoring Catalyst Morphology Towards High Performance for Low Pt Loaded PEMFC Cathodes

Harzer, G. S.; Orfanidi, A.; El-Sayed, H. A.; Madkikar, P.; Gasteiger, H. A.

(submitted)

## List of Conferences / Workshops

Name	Level	Country	Year	Contribution
ECS 2017	International Conference	USA	2017	Oral
MSE - Kolloquium 2016	National Conference	Germany	2016	Poster
CRC Graduate Academy 2016	International Workshop	Germany	2016	Poster
MSE - Kolloquium 2015	National Conference	Germany	2015	Poster
CIMTEC 2014	International Conference	Italy	2014	Oral
EFCF 2013	International Conference	Switzerland	2013	Poster